

Michael Kaiser, BSc

**Acceleration strategies
in partitioned coupling of
fluid-structure interaction problems**

MASTER'S THESIS

to achieve the university degree of

Diplom-Ingenieur

Master's degree programme: Civil Engineering and Structural Engineering

submitted to

Graz University of Technology

Univ.-Prof. Dr.-Ing.habil Thomas-Peter Fries

Dipl.-Ing. Richard Schussnig, BSc

Institute of Structural Analysis

Graz, August 2020

AFFIDAVIT

I declare that I have authored this thesis independently, that I have not used other than the declared sources/resources, and that I have explicitly indicated all material which has been quoted either literally or by content from the sources used. The text document uploaded to TUGRAZonline is identical to the present master's thesis.

Graz, August 2020



Contents

Notation	IV
Preface	V
Abstract	VI
Zusammenfassung	VII
1 Introduction	1
1.1 Mathematical preliminaries	2
1.2 Short introduction to the Finite Element Method (FEM)	6
1.3 ALE formulation	13
2 Fluid Domain	16
2.1 Physical properties of the fluid	16
2.2 Derivation of the governing equations	17
2.3 Fluid domain in FEM	21
3 Structural Domain	27
3.1 Rigid body motion	31
4 Fluid-structure interaction	32
4.1 Computational mesh dynamics	34
4.2 Vertical flap - FSI algorithm explained on an example	36
5 Plate structure in FSI	44
5.1 Tolerance study	47
5.2 Aitken's relaxation	60
5.3 Extrapolation	68
6 Bridge structure in FSI with wind	77
6.1 Tolerance study	81
6.2 Aitken's relaxation	93
6.3 Extrapolation	99
6.3.1 Extrapolation for $\varepsilon_c = \varepsilon_F = 1 \cdot 10^{-2}$	107
6.4 Aitken's relaxation and extrapolation	108
7 Conclusion	109
Appendices	110
A More result plots for tolerance study of plate test case	110
B Iteration history of plate study reference case	119
C Results for first order extrapolation applied on plate case	123

D	Result plots for section 6.3.1	125
E	Technical properties of used parallel computer	130
	List of Figures	133
	List of Tables	133

Notation

a	Scalar
\mathbf{v}	Vector
\mathbf{A}, \mathbf{n}	Matrix or tensor
$\ \mathbf{v}\ $	Euclidean norm of \mathbf{v}
$\mathbf{v}_{i,j}$	Derivative of \mathbf{v}_i with respect to j
$\dot{\mathbf{v}}_i$	Derivative of \mathbf{v}_i with respect to time t
$\mathbf{a} \cdot \mathbf{b}$	Dot product
$\mathbf{a} : \mathbf{b}$	Contraction of \mathbf{a} and \mathbf{b}
$\nabla \cdot \mathbf{v}$	Divergence of a tensor / vector
$\nabla \mathbf{v}$	Gradient of a tensor / vector or scalar field
$f \circ g$	Composition of the functions $f \circ g = f(g(x))$
$\hat{\Omega}$	Reference domain
Ω	Real domain
Γ_D	Dirichlet boundary
Γ_N	Neumann boundary
F	Fluid, e.g. as index in Ω_F
S	Structure, e.g. as index in Ω_S
n	Time step n
i	Iteration step i

Preface

In my second year at HTL 1 Linz the subject ‘Structural Analysis’ was on the time table for the first time of my life and after the winter term I thought that I would like to study Civil Engineering because of this subject at school. Now, nearly ten years later, I write these lines for my master thesis which I worked out at the Institute of Structural Analysis at Graz University of Technology and I still think that it was absolutely the right decision to study Civil Engineering and specialise in Structural Engineering.

During my studies at TUG and an abroad term at McMaster University in Hamilton, Canada, I have got the possibility to learn a lot of new and interesting content. I found out that especially the field of mechanics and numerical mathematics applied in civil and structural engineering, in particular the finite element method (FEM), are interesting fields of study and I enrolled in subjects out of these fields as much as possible and tried to connect these topics with other fields of interest like the environment and biomechanics in my free time.

I asked Professor Dr.-Ing.habil. Fries if it would be possible to write a master’s thesis with a content of these topics and he suggested to do something about fluid-structure interaction (FSI). This topic with its interdisciplinary character contains different aspects out of different fields of mechanics and numerics. The FEM is applied in fluid mechanics and structural dynamics. Although there are some lectures about fluid mechanics and hydraulics engineering it was quite a different topic to apply FEM to fluids. This was a challenge but an interesting one.

The master’s thesis, as the last part of my studies, is also a special point in my life because I ‘finish’ my educational time. I would like to use this preface to thank all my teachers and professors at school and university for their engagement in sharing their knowledge. I would like to thank my friends and colleagues for the time we spent together, the fruitful conversations about our educational topics as well as free time activities. Special thanks to my family and here especially to my parents Christina and Wolfgang and my sister Maria. Without their support it would have never been possible to get to where I am now.

Last but not least I would like to appreciate the excellent supervision of this master’s thesis by Professor Dr.-Ing.habil. T.-P. Fries and DI R. Schussnig, BSc. It was a pleasure for me to discuss results during weekly meetings, usually online due to COVID-19. Prof. Dr. Fries had always time for me to answer my questions and he explained also the backgrounds in detail which was very interesting for me.

Michael Kaiser

Abstract

The aim of this Master's thesis about *acceleration strategies in partitioned coupling of fluid-structure interaction (FSI) problems* is to find a setting for a strongly partitioned coupled fluid-structure interaction solver which is accurate and fast.

In fluid-structure interaction problems a fluid (liquid or gas) and a solid structure interact and for a strongly partitioned coupling approach the independent solvers for fluid and solid are connected in a coupling loop.

The first part of this work describes the theoretical background of the single finite element method (FEM) solvers for the incompressible fluid flow and the solid, modelled using structural dynamics. The theory about the coupling approach is described and therefore a mesh deformation algorithm for the fluid domain (computational mesh dynamics) using a pseudo-structure based on Hooke's solid is introduced. The algorithm used in this thesis is described theoretically and applied to an example to show how it works in practice.

The second part of this thesis are two test cases. The algorithm described before is applied on a fluid-structure interaction problem concerning a thin plate as structure and in the second test case on a bridge section like the section of the famous Tacoma Narrows bridge which collapsed because of aeroelastic fluttering in 1940. This is a typical application of FSI between a civil engineering structure and wind.

The algorithm loops for the fluid solver and for the coupling procedure are solved individually. These loops have a certain prescribed tolerance to fulfil for convergence. In a tolerance study different tolerances are applied to both loops. The result of this study is a setting for which the results are accurate and the computational time is moderate. It can be shown that the tolerance for the loop in the nonlinear fluid solver can be high ($\varepsilon_F = 1 \cdot 10^{-2}$) without compromising accuracy much. The tolerance for the coupling loop should be lower ($\varepsilon_c = 1 \cdot 10^{-6}$) and the fastest convergence of the FSI problem which leads to accurate results is achieved for this case.

However, for an optimal tolerance setting calculation time is still long for both cases and so further strategies are considered to shorten the needed computational time. The first approach considered is to use *Aitken's relaxation* method. Here the improvement for the plate test case is small but for the bridge test case a shortening of nearly 25% can be achieved. The second used acceleration strategy is *extrapolation*. Different fields are extrapolated using extrapolation functions with diverse orders. It can be shown here that the results are as accurate as without extrapolation applied but the calculation time can be shortened up to nearly 50% for certain configurations.

In this thesis it can be clearly seen that an acceleration of a partitioned coupled fluid-structure interaction problem solver is possible. However, it is mentioned that the speed-up is case dependent although the used algorithm is the same for each case. The results of these studies are presented using tables and figures.

Zusammenfassung

Das Ziel dieser Masterarbeit zum Thema *Beschleunigungsstrategien in partitioniert gekoppelten Fluid-Struktur-Interaktions-Problemen* ist es, Einstellungen zu finden, um genau approximierte Lösungen im Bereich der Fluid-Struktur-Interaktion (FSI) mittels Finiter Elemente Methode (FEM) innerhalb einer angemessenen Rechenzeit zu bekommen.

Bei FSI Problemen interagiert ein Fluid (Flüssigkeit oder Gas) mit einer Struktur. In dieser Arbeit wird eine stark gekoppelte partitionierte Lösungsstrategie angewendet, bei der unabhängige FE-Löser für das Fluid und die Struktur in einer Kopplungsschleife zusammengeführt werden. Zudem ist es erforderlich eine Fluid-Netzverformung zu berücksichtigen, um die verwendeten mechanischen Modelle anwenden zu können. Für diese Netzverformung ist ein zusätzlicher Löser einer linear-elastischen Pseudostruktur nach dem Hooke'schem Gesetz im FSI-Algorithmus implementiert.

Der erste Teil der Arbeit zeigt die theoretischen Grundlagen für die verwendeten mathematisch-mechanischen Modelle und die Funktionsweise des verwendeten FSI-Lösungs-Algorithmus. Dieser wird abschließend an einem Beispiel intuitiv erklärt.

Den zweiten Teil der Arbeit bilden zwei Testfälle, für die verschiedene Studien durchgeführt wurden. Der erste Testfall ist eine dünne Platte und der zweite Testfall stellt die Tacoma-Narrows-Brücke dar, eine Hängebrücke, welche durch windinduziertes Flattern eingestürzt ist.

In dem nichtlinearen Strömungs- oder Fluid-Löser wird eine Schleife gelöst, deren Lösung eine gewisse Toleranz erfüllen muss. Die Lösung der partitionierten Kopplungsschleife muss ebenfalls eine vorgegebene Toleranz erfüllen. In der Studie werden für beide Schleifen unterschiedliche Toleranzen vorgegeben und kombiniert. Die approximierten Lösungen werden verglichen und auf Genauigkeit geprüft. Das Ergebnis der Studie ist eine Einstellung für die Toleranzen, für welche die Approximation genau genug ist und die erforderliche Rechenzeit in einem vertretbaren Bereich liegt. Für die Fluid-Schleife beträgt die gewählte Toleranz $\varepsilon_F = 1 \cdot 10^{-2}$ und für die Kopplungs-Schleife $\varepsilon_c = 1 \cdot 10^{-6}$.

Trotz dieser Einstellungen ist die benötigte Rechenzeit noch hoch. Daher wurden weitere Möglichkeiten untersucht, um den FSI-Löser zu beschleunigen. Der erste Ansatz hierzu ist die Verwendung der *Aitken-Methode*. Beim Platten-Testfall ist die erzielte Verkürzung der Rechenzeit sehr gering, beim Brücken-Testfall beträgt die Ersparnis an Rechenzeit allerdings beinahe 25%.

Der zweite verwendete Ansatz ist *Extrapolation* mit Extrapolationsfunktionen verschiedener Ordnungen. Die Extrapolation wird auf verschiedene Felder einzeln oder kombiniert angewendet (Fluid-Lösung, Strukturverformung und Netzverformung). Es gibt Konfigurationen für die keine Verkürzung oder sogar eine Verlängerung der Rechenzeit zu verzeichnen ist. Für andere Konfigurationen sind jedoch Rechenzeitverkürzungen von fast 50% erzielbar.

Die Schlussfolgerung aus dieser Arbeit ist, dass es durchaus möglich ist den verwendeten Algorithmus eines stark gekoppelten Fluid-Struktur-Interaktions-Lösers zu beschleunigen, die erzielbare Rechenzeitverkürzung jedoch sehr stark problemabhängig ist. Das heißt trotz Anwendung desselben Algorithmus auf unterschiedliche Probleme, weichen die erzielbaren Beschleunigungen voneinander ab. Die Ergebnisse der Studien sind in Tabellen und Diagrammen sowie Flächenplots dargestellt.

1 Introduction

Fluid-structure interaction (FSI) is an interdisciplinary area of research. The aim of FSI is to understand how a fluid (gas or liquid) interacts with a structure (deformable or rigid body). Therefore the sciences of mathematics, mechanics, and computer sciences, and, depending on the type of FSI, engineering (civil engineering, mechanical engineering etc.) or life sciences (biology, medicine etc.) are combined. This work is based on the book *The finite element method for fluid dynamics* by O.C. Zienkiewicz et.al. [26, pp. 423 – 450] and dissertations by T.-P. Fries [4], B. Hübner [8], E. Walhorn [24], and W. A. Wall [25].

Fluid-structure-interaction occurs in natural systems as well as in man-made technical systems. Some examples from nature are wind deforming trees and other plants, groundwater flow and its impact on soil particles and the deformation behaviour of blood vessels under pulsatile blood flow. Similar to this is the study of FSI in relation to airways and especially the lungs. Another example is the flight of insects and birds, and the relation between the movement of their wings and the surrounding air. Technical examples are aeroplane-wings and wind-turbines, interaction between sea water and off-shore-structures like foundations and pillars of wind-turbines and oil platforms. A further interesting example in Structural Engineering is the performance of a bridge under wind loads.

Fluid-structure-interaction is a phenomenon which occurs in a wide range of geometrical scales.

It is possible to divide FSI in further sub-categories. For instance the solid part (structure) could be a deformable or a rigid body but in both cases somehow moving in the fluid domain. It could be further distinguished between FSI considering a liquid or gaseous fluid, which leads to a necessary decision if the gas could be considered as an incompressible fluid or it should be modelled as a compressible one. This decision could be based on the Mach number of the occurring flow [26, p. 423].

From the short description given so far it is obvious that different physical areas are combined in FSI. On the one side is a fluid and on the other side the solid (structure). These combinations of two or more different physical fields are called *multi-physics problems*. For a long time engineers tried to reduce such multi-physics problems to a form that it could be described using only one field and the impacts from the other fields have been considered using a lot of simplifications.[25, pp. 1–2]. Because of higher calculation performance of modern computers it is nowadays much more possible than ever before to use multi-physical models to describe reality in a more accurate way.

The different considered fields are described using partial differential equations (PDEs) resulting from a modelling based on continuum mechanics. In the strongly coupled approach which is used in this work the individual fields are solved and connected through interface conditions. For each individual field, these interface conditions are on the boundary and may, therefore, also be seen as special boundary conditions (BCs). Two types of boundary conditions are considered herein:

- Dirichlet BCs: Γ_D , also called first-type, essential or fixed BCs. These are for instance displacements in structural mechanics.
- von Neumann BCs or simply Neumann BCs: Γ_N , also called natural or second-type BCs. It is used to prescribe loads in a structural mechanics problem.

Methods of Numerical Mathematics are used to solve the PDEs which describe the fluid domain and the solid domain of interest. Herein, the Finite Element Method (FEM) is used to approximate the results.

Although modern computers can solve a huge amount of equations fast and accurate, calculations in context of FSI are often very time-consuming. The aim of this thesis is to find methods and strategies how the computational time for a FSI solution could be shortened.

Choosing the parameters of the FSI algorithm carefully can lead to a decrease of calculation time with no loss of accuracy. Further it is possible to use additional mathematical tools to improve the algorithm's performance.

The following sections give a short introduction of the mathematical and physical foundations used in the following chapters. Then a description of the models and solution strategies for the fluid field, the structural field and the FSI algorithm follows. The second part of this Master's thesis ¹ demonstrates and interprets the result achieved. .

1.1 Mathematical preliminaries

Some mathematical preliminaries are given here which are used in this thesis and are not a direct part of another section.

Operators

Figure 1 shows a clockwise Cartesian coordinate system in three dimensions with unit vectors \mathbf{i} , \mathbf{j} , and \mathbf{k} . These are used for the definitions of the following operators based on [1] and [14].

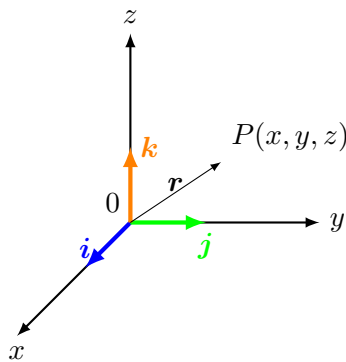


Fig. 1: Cartesian coordinate system

For the definitions of the following mathematical preliminaries an arbitrary function $\mathbf{f} = \mathbf{f}(x, y, z)$ with respect to the coordinates x , y , and z is used.

¹The calculations have been done with EduFEM [5] in Matlab [16] on a parallel computer described in Appendix E.

- Nabla operator

For Cartesian coordinates is defined as [14, p. 158]

$$\nabla \equiv \mathbf{i} \frac{\partial}{\partial x} + \mathbf{j} \frac{\partial}{\partial y} + \mathbf{k} \frac{\partial}{\partial z} \quad (1.1)$$

- Gradient

The gradient of a scalar field can be defined in different ways [1, pp. 710–711] and the vector gradient is a type of tensors which has an important role in engineering sciences [1, p. 712]. In this work the gradient is used for mathematical modelling in fluid and structural mechanics and is defined as

$$\text{grad } \mathbf{f} = \nabla \mathbf{f} = \left\{ \begin{array}{c} \frac{\partial f}{\partial x_1} \\ \vdots \\ \frac{\partial f}{\partial x_n} \end{array} \right\} \quad (1.2)$$

- Divergence

The divergence is a scalar field to a vector defined as

$$\text{div } \mathbf{f} = \nabla \cdot \mathbf{f} = \frac{\partial f_x}{\partial x} + \frac{\partial f_y}{\partial y} + \frac{\partial f_z}{\partial z} \quad (1.3)$$

- Laplace operator

It is defined as

$$\Delta = \nabla^2 = \nabla \cdot \nabla \quad (1.4)$$

which is the dot product of the Nabla operator with itself and prescribes the sum over the second derivatives of a scalar or vector function [1, p. 716].

These operators are applied several times within this thesis.

Discretization of initial value problems

For the discretization in time of a first order initial value problem, the θ -method is used (see section 2). It is a single-step method which only needs information from the previous time step n for computing quantities at time step $n + 1$ [1, p. 970]. The discretization of

$$\dot{\mathbf{u}} = f(\mathbf{u}, t) \quad (1.5)$$

is done by

$$\frac{\mathbf{u}_{n+1} - \mathbf{u}_n}{\Delta t} = \theta f(\mathbf{u}_{n+1}, t_{n+1}) + (1 - \theta) f(\mathbf{u}_n, t_n) \quad (1.6)$$

For different values of θ the method has different orders. For $\theta = \frac{1}{2}$ it is a second-order method and called *Crank-Nicolson method*, for all other θ -values only first order accuracy is possible. Two further famous values for θ are $\theta = 0$ which is the *explicit Euler method* and $\theta = 1$ which is the *implicit Euler method*. For the calculations in this thesis Crank-Nicolson is used, but in EduFEM [5] it is possible to choose other values for θ . The Crank-Nicolson method can be written as

$$u(t_{n+1}) - u(t_n) = \frac{\Delta t}{2} (f(\mathbf{u}_{n+1}, t_{n+1}) + f(\mathbf{u}_n, t_n)) \quad (1.7)$$

[3, p. 389] and [17, p. 298].

Solving of nonlinear equations

To solve nonlinear equations an iteration scheme is used. In this work the *Newton-Raphson method* and the *Picard iteration* are used. These iterative procedures search for the roots of non-linear equations.

Newton-Raphson method

The Newton-Raphson method is known for its fast convergence [1, p. 954] and the mathematical expression is

$$x_{i+1} = x_i - \frac{f(x_i)}{f'(x_i)} \quad (1.8)$$

where $f'(x_i)$ is the first derivative of the function $f(x_i)$ and $i = 0, 1, 2, \dots$ are the iteration steps until a given convergence criterium is fulfilled [3, p. 182].

Assume that a non-linear system of equations

$$\mathbf{F}(\mathbf{x}) = \mathbf{0} \quad (1.9)$$

is to be solved. The scalar Newton-Raphson method for non-linear equations given in Equation (1.8) can be easily vectorized to

$$\mathbf{x}_{i+1} = \mathbf{x}_i - \mathbf{J}^{-1}(\mathbf{x}_i) \mathbf{F}(\mathbf{x}_i) \quad (1.10)$$

where \mathbf{J} is the Jacobi matrix. This matrix is defined as

$$\mathbf{J}(\mathbf{x}) = \frac{\partial \mathbf{F}(\mathbf{x})}{\partial \mathbf{x}} \quad (1.11)$$

This definition of the Newton-Raphson method for systems of non-linear equations is based on [1, pp. 161–162]. It is easily verified that a non-linear system of equations is solved using successive solution of a linear system of equations.

Picard iteration

In the Newton-Raphson method the Jacobi matrix has to be obtained, however, it is often cumbersome to determine. It is possible to linearise the equations based on a fix-point iteration [1, p. 549]. The following algorithm is based on the so-called Oseen equations. When the non-linear problem

$$u_{n+1} \frac{\partial u_{n+1}}{\partial x} = u_{n+1} u_{,x}^{n+1} \quad (1.12)$$

should be solved, the start guess for a new time step $n + 1$ is the solution of the previous one

$$\text{start guess for } u^{n+1} = u^n \quad (1.13)$$

leading to the following algorithm:

Algorithm 1: Picard Iteration

Data: From the previous time step n the solution u^n is known and the start guess for the actual time step $n + 1$ is set as $u^{n+1} = u^n$

for $i = 1 : \infty$ **do**

solve $u^i u_{,x}^{n+1} = 0$ for u^{n+1}

break if $|u^i - u^{n+1}| \leq \varepsilon$

end

The differential equation which is to solve within the for-loop is a linear one.

The presented Algorithm 1 is one possible strategy to find a solution of a non-linear problem within each time step. Alternatively to the above example $u^{n+1} u_{,x}^i = 0$ could be used which also results in a solution. The specific linearisation chosen may have different convergence properties and therefore the optimal choice is problem dependent.

1.2 Short introduction to the Finite Element Method (FEM)

The aim of this section is to give a short overview and introduction to the FEM which is used throughout this thesis. In the following chapters it is assumed that the reader is familiar with the basics of the FEM but a short summary of fundamental aspects is provided here.

The *Finite Element Method* (FEM) ² is a tool in *numerical mathematics* to approximate boundary value problems (BVPs). A general term of this procedure is *simulation* and it is part of the scientific field of *computational engineering*. This discipline deals with modelling a real world problem using mathematics. Modelling is often based on continuum mechanics and leads to a BVP, which is composed of differential equations which have to be fulfilled in a domain of interest under certain boundary conditions. Herein, this BVP is solved using the FEM. The solution is an approximation of the analytical solution but within a certain range of accuracy which is described by certain numerical methods. Figure 2 shows a flow diagram of such a simulation process.

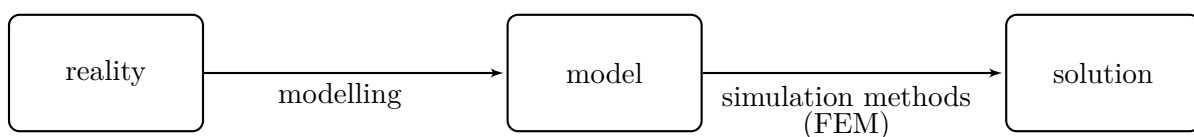


Fig. 2: Flow-diagram of a simulation

Steps in a FEM simulation

The following list shows the steps of a FEM simulation.

- pre-processing
 - Model choice including material parameters.
 - Bring the differential equation from its strong form into its weak form by multiplication with test function and application of divergence theorem.
 - Domain discretization; decompose the domain of interest (DOI) into a finite number of non-overlapping elements (meshing). The mesh often only approximates the DOI e.g. at curved boundaries and is described by elements and nodes.
- processing
 - Assembling of the system of equations.
 - Consideration of BCs in the system of equations.
 - Solve system of equations to obtain the sought solutions at the nodes.
- post-processing
 - Obtain the sought solution everywhere in the DOI use numerical interpolation routines.
 - Visualization and interpretation of the found solution.

²This section is based on the lecture notes and handouts of the lectures FEM I and FEM II taught by Prof. Dr.-Ing. T.-P. Fries at TU Graz in 2018/2019. The material is only published for students enrolled in these courses but not to the general public. [6]

The FEM mesh

In the FEM it is necessary to decompose the domain of interest into a mesh composed by elements, which are simple and uniform building blocks. A mesh is defined by the coordinates of the nodes and the connectivity matrix. This matrix defines the elements assigning each point of the reference element to a node in the mesh.

In 2d one may distinguish between triangular and quadrilateral elements and in 3d between tetrahedral and hexahedral elements. Further there are different types of elements like Lagrangian elements or Serendipity elements. The elements used in this thesis are of Lagrangian type. Elements are defined in a reference element in a ζ - η -coordinate system. For each node an element function is defined which can be linear or of higher order. Figure 3³ shows a quadratic quadrilateral element in 2d and Figure 4 shows the appropriate element functions of second order polynomials [9, pp. 126–130].

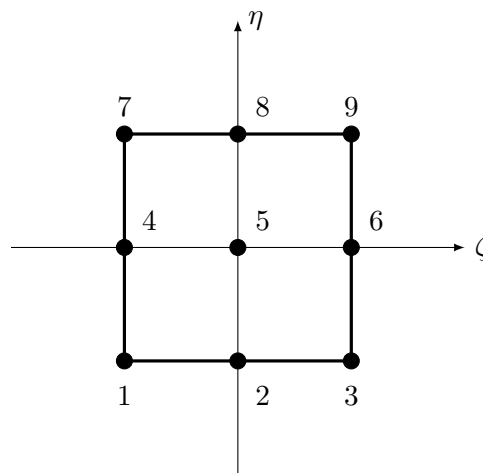


Fig. 3: Quadratic quadrilateral element in reference domain.

³Figures 3 and 4 are copied from the course paper of CE 704 - Environmental Systems Engineering - course project: Optimization by the author of this thesis submitted to Dr. Zoe Li at McMaster University in Hamilton, Canada in December 2019 [11]. This work is unpublished.

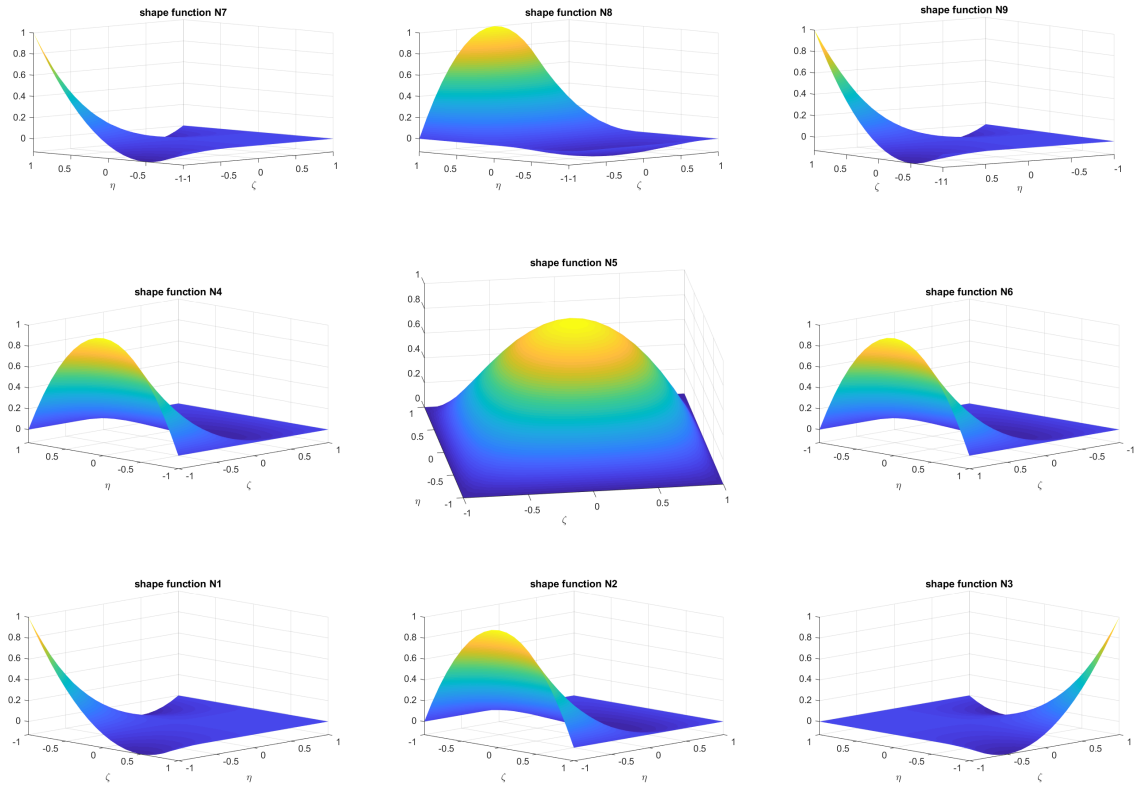


Fig. 4: Quadratic quadrilateral element shape functions.

For the discretization of a real domain of interest (e.g. structural element like a shell, a plate or a beam or a fluid domain etc.) it is necessary to perform a map

$$\mathbf{x}(\mathbf{r}) = \sum_{i=1}^n N_i(\mathbf{r}) \cdot \mathbf{x}_i \quad (1.14)$$

with n as the number of nodes per element and $\mathbf{r} = \begin{pmatrix} \zeta \\ \eta \end{pmatrix}$ as the reference coordinates. \mathbf{r} is called local coordinate system and \mathbf{x} is called global coordinate system. Equation (1.14) maps the reference element from the local coordinate system to the real element in the global coordinate system. This principle is shown in Figure 5 with the reference element on the left side and the real element on the right side. The blue lines imply the mapping function. The element function $N_i(\mathbf{r})$ fulfils the Kronecker- δ -property

$$\delta_{ik} = \begin{cases} 1, & \text{for } i = k \\ 0, & \text{for } i \neq k \end{cases} \quad (1.15)$$

which is not strictly necessary, but convenient, since prescribing essential BCs is achieved by simply prescribing nodal degrees of freedom. The Kronecker- δ -property yields conditions for the derivation of element functions.

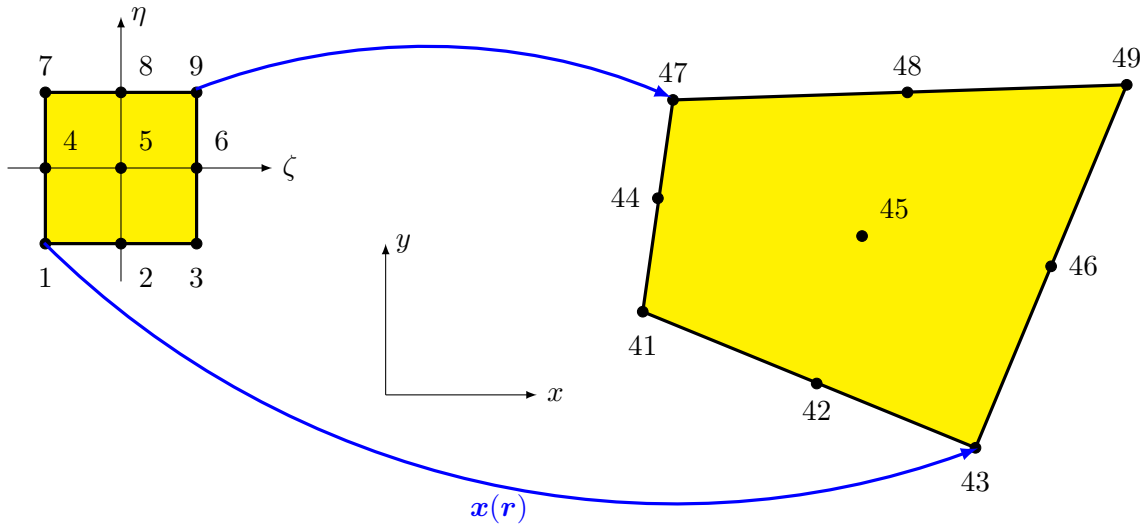


Fig. 5: Mapping of quadratic element from reference to real domain.

For the mapping of functions, vectors, and tensors, the Jacobi matrix is an important. This is the $(b \times a)$ matrix of the first derivatives of the mapping $\mathbf{x}(\mathbf{r}) : \mathbb{R}^a \rightarrow \mathbb{R}^b$.

$$\mathbf{J}(\mathbf{r}) = \frac{\partial \mathbf{x}(\mathbf{r})}{\partial \mathbf{r}} = \begin{bmatrix} \frac{\partial x_1}{\partial r_1} & \cdots & \frac{\partial x_1}{\partial r_a} \\ \vdots & \ddots & \vdots \\ \frac{\partial x_b}{\partial r_1} & \cdots & \frac{\partial x_b}{\partial r_a} \end{bmatrix} \quad (1.16)$$

It is needed when a vector is mapped from the local coordinate system to the global coordinate system

$$\mathbf{v}_x = \mathbf{J} \cdot \mathbf{v}_r \quad (1.17)$$

The derivative of a function $f(\mathbf{r})$ which is mapped by $\mathbf{x}(\mathbf{r})$ with respect to \mathbf{x} has to be calculated using the inverted transposed Jacobi matrix

$$\frac{\partial f}{\partial \mathbf{x}} = \mathbf{J}^{-T} \cdot \frac{\partial f}{\partial \mathbf{r}} \quad (1.18)$$

For the mapping of the element shape functions, this leads to

$$\frac{\partial N_i}{\partial \mathbf{x}} = \mathbf{J}^{-T} \cdot \frac{\partial N_i}{\partial \mathbf{r}}. \quad (1.19)$$

Considering $\mathbf{x}(\mathbf{r}) = \sum_{i=1}^n N_i(\mathbf{r}) \cdot \mathbf{x}_i$ the Jacobi matrix is then determined as

$$\mathbf{J}(\mathbf{r}) = \frac{\partial \mathbf{x}(\mathbf{r})}{\partial \mathbf{r}} = \sum_{i=1}^n \frac{\partial N_i(\mathbf{r})}{\partial \mathbf{r}} \cdot \mathbf{x}_i \quad (1.20)$$

In the context of the FEM it is used to modify integration weights for numerical integration and determine derivatives of element functions with respect to physical coordinates \mathbf{x} in the real domain.

For FEM calculations so-called node functions are necessary. These are the union of mapped element functions at one node. Node functions are only non-zero in the elements which share the corresponding node of a certain node function. It is important to consider that local element functions are C_∞ -continuous while global node functions are C_0 -continuous. This is the reason why first-order derivatives of the node functions have jumps at element boundaries.

Numerical interpolation and integration

Numerical interpolation and integration are two important fields of numerical mathematics used within the FEM. Because this section is only an introductory overview about the FEM these two fields are not explained in detail. The interested reader is referred to specified literature, e.g., Hughes [9] or Dahmen, Reusken [3].

When interpolating nodal values in the domain of interest, discretized by a mesh, we use

$$f(\mathbf{x}) \approx f^h(\mathbf{x}) = \sum_{i=1}^n N_i(\mathbf{r}) \cdot f_i \quad (1.21)$$

For numerical integration in EduFEM [5] Gauß quadrature is used. w_i is the integration weight and using the interpolated value at a Gauß point leads to

$$\int_{\Omega} f(\mathbf{x}) \, d\mathbf{x} \approx \sum_{i=1}^{n_Q} f^h(x_i) \cdot w_i \quad (1.22)$$

The integration weights are scaled by the determinant of the Jacobi matrix (Jacobian). The Jacobi matrix is given in Equation 1.20.

Simple FEM example

To show readers who are not so familiar with the procedures of the FEM a simple example of a tension bar ⁴ is given below. The strong form of the differential equation which describes the tension bar is

$$EA \cdot u''(x) = -p(x) \quad (1.23)$$

To obtain the weak form which is necessary to find a solution using the FEM, Equation (1.23) is multiplied with a test function $w(x)$ and integrated over the domain. Therefore the divergence theorem is applied which in one dimension is simply partial integration. These steps written as formulas are

$$w(x) \cdot EA \cdot u''(x) = -w(x) \cdot p(x) \quad (1.24)$$

$$\int_0^\ell w(x) \cdot EA \cdot u''(x) \, dx = \int_0^\ell -w(x) \cdot p(x) \, dx \quad (1.25)$$

$$-\int_0^\ell w'(x) \cdot EA \cdot u'(x) \, dx + [w(x) \cdot EA \cdot \hat{u}'(x)]_0^\ell = -\int_0^\ell w(x) \cdot p(x) \, dx \quad (1.26)$$

$$EA \int_0^\ell w'(x) \cdot u'(x) \, dx = \int_0^\ell w(x) \cdot p(x) \, dx + [w(x) \cdot \hat{N}(x)]_0^\ell \quad (1.27)$$

with $\hat{N}(x) = EA \cdot \hat{u}'(x)$ as normal force.

The system and its discretization is shown in Figure 6.

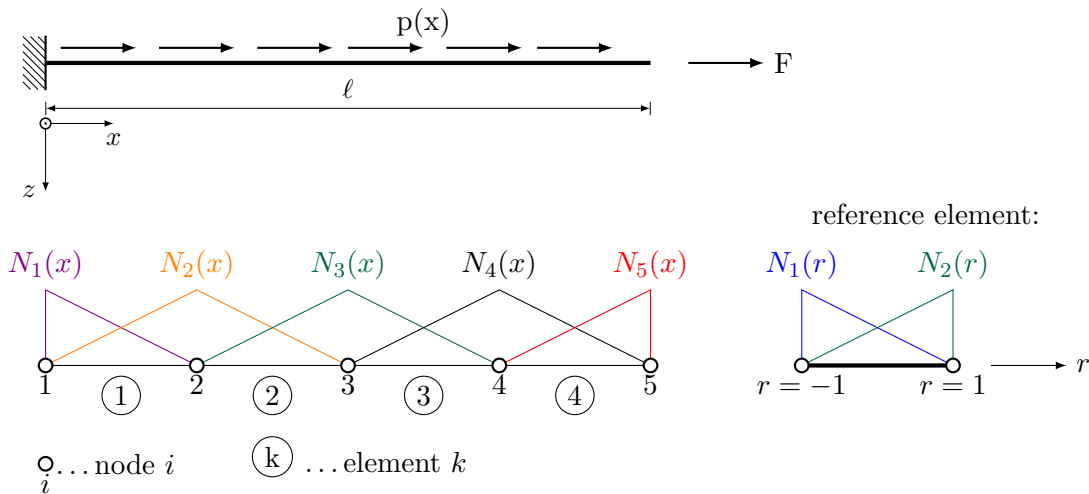


Fig. 6: FEM discretization for a tension bar using linear elements

$u(x)$ is the sought displacement field. The weak form given in Equation (1.27) is to be fulfilled for any test function $w(x)$. Because this would require an infinite number of checks, it is not possible to do this. Therefore, we restrict that $u(x)$ and $w(x)$ to be functions which can be represented by a linear

⁴This example is based on the first lecture in FEM II by Prof. Dr.-Ing. T.-P. Fries [6] and a Master's project by the author of this thesis supervised by Dipl.-Ing. D. Pölz at the Institute of Applied Mechanics (AM:BM) at TU Graz [12]. Figure 6 is a modified copy out of [12]. Both sources are not officially published.

combination of the finite element shape functions $N_i(x)$ on a given mesh used for the discretization of the tension bar. This is an ansatz for $u(x)$ and $w(x)$

$$u(x) \approx u^h(x) = \sum_{i=1}^n N_i(x) \cdot u_i = \mathbf{N}^T(x) \mathbf{u} \quad (1.28)$$

$$w(x) \approx w^h(x) = \sum_{i=1}^n N_i(x) \cdot w_i = \mathbf{N}^T(x) \mathbf{w} \quad (1.29)$$

Inserting Equations (1.28) and (1.29) into Equation (1.27) leads to

$$EA \int_0^\ell w_{,x}^h(x) u_{,x}^h(x) \, d\mathbf{x} = \int_0^\ell w^h(x) p(x) \, d\mathbf{x} + [w^h(x) \hat{N}(x)]_0^\ell \quad (1.30)$$

Now, the one $u^h(x)$ is sought for which this discrete weak form is fulfilled for any test function $w^h(x)$. When the discrete weak form is fulfilled for a finite basis of $w^h(x)$ it is also fulfilled for all linear combinations of the basis functions. The set of each individual finite element shape function $N_i(x)$ builds the canonical basis of w^h . The n equations for n nodes in the FE mesh leads to a system of equations

$$EA \cdot \begin{bmatrix} \int N_{1,x} N_{1,x} \, dx & \int N_{1,x} N_{2,x} \, dx & \dots & \int N_{1,x} N_{n,x} \, dx \\ \int N_{2,x} N_{1,x} \, dx & \int N_{2,x} N_{2,x} \, dx & \dots & \int N_{2,x} N_{n,x} \, dx \\ \vdots & \vdots & \ddots & \vdots \\ \int N_{n,x} N_{1,x} \, dx & \int N_{n,x} N_{2,x} \, dx & \dots & \int N_{n,x} N_{n,x} \, dx \end{bmatrix} \cdot \begin{bmatrix} u_1 \\ u_2 \\ \vdots \\ u_n \end{bmatrix} = \begin{bmatrix} \int N_1 p(x) \, dx + [N_1 \hat{N}] \\ \int N_2 p(x) \, dx + [N_2 \hat{N}] \\ \vdots \\ \int N_n p(x) \, dx + [N_n \hat{N}] \end{bmatrix} \quad (1.31)$$

Equation (1.31) in matrix-vector notation is

$$EA \cdot \left[\int_0^\ell \mathbf{N}_{,x} \mathbf{N}_{,x}^T \, dx \right] \cdot \mathbf{u} = \int_0^\ell \mathbf{N} p(x) \, dx + [\mathbf{N} \hat{N}]_0^\ell \quad (1.32)$$

With stiffness matrix $\mathbf{K} = EA \cdot \left[\int_0^\ell \mathbf{N}_{,x} \mathbf{N}_{,x}^T \, dx \right]$ Equation (1.32) can be written as

$$\mathbf{K} \cdot \mathbf{u} = \mathbf{b} \quad (1.33)$$

To solve this equation the boundary conditions have to be inserted into \mathbf{K} .

The following chapter deals with the fluid. It shows the physical assumptions and properties of the fluid, how it is described mathematically, and how the governing equations are solved using the FEM. Although the situation is more complex than in this simple example of a one-dimensional tension bar, the fundamental principals are the same.

1.3 ALE formulation

Mechanical models may be described with different reference settings. The settings used in this thesis are the *Lagrangian setting*, the *Eulerian setting*, and the *Arbitrary-Eulerian-Lagrangian setting* or short *ALE setting*. The difference between these formulations is the position of the observer [25, p. 9]. In the material or Lagrangian formulation the observer tracks each material point on its spatial orbital with its properties and position in space [25, p. 9]. In the spatial or Eulerian formulation the observer is fixed on a certain point in space and the properties of material points are measured which are at this point over time [25, p. 10]. In the ALE formulation the observer can move arbitrarily, which means that the observer does not have to be fixed or moving with a certain material point [25, p. 11].

Figure 7 shows these three different settings. The figure and the following mathematical formulations are based on [4, pp. 10–12].

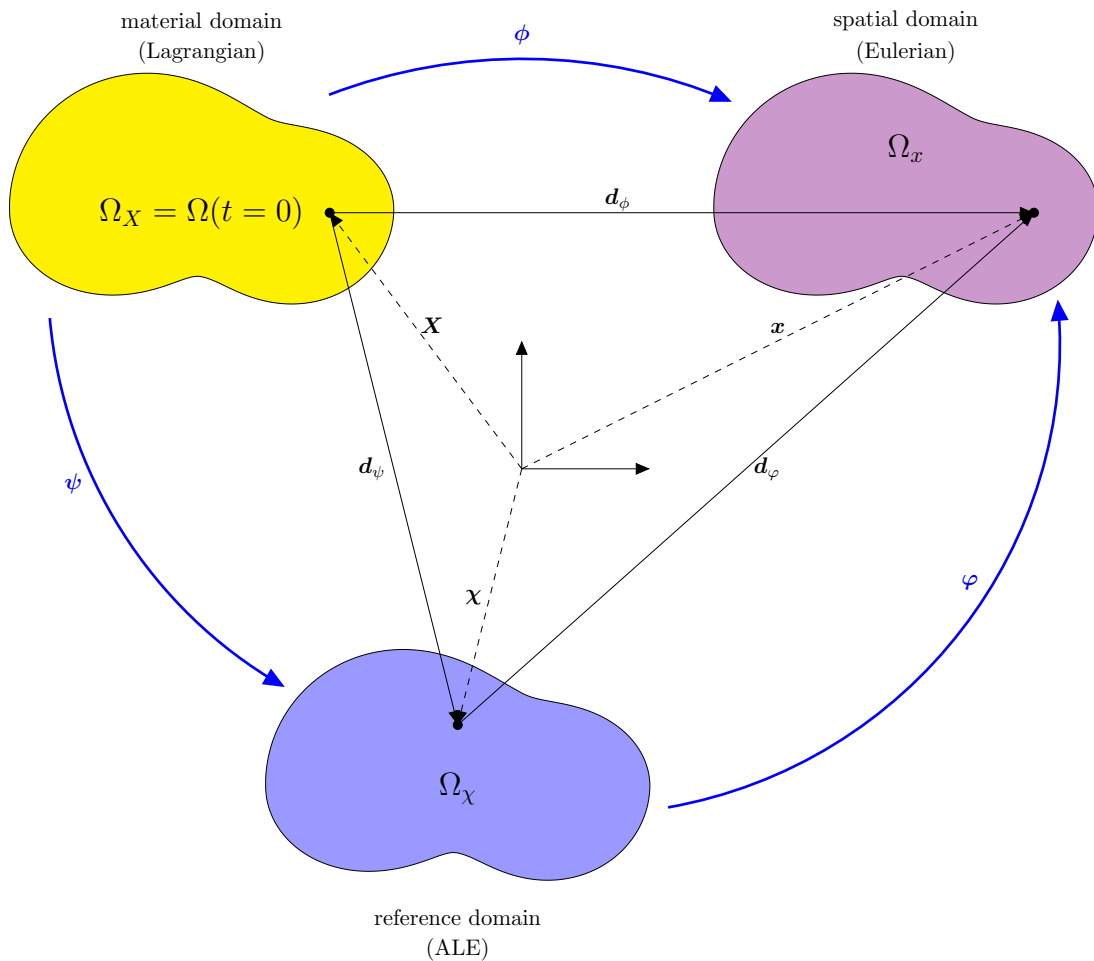


Fig. 7: Different configurations of the continuum

The initial domain is the material domain which is defined as $\Omega_X \subset \mathbb{R}^d$ where d is the space dimension. A mapping

$$\phi : \Omega_X \times (0, T) \rightarrow \mathbb{R}^d \quad (1.34)$$

describes the motion of Ω_X .

At time t the image of Ω_X is the spatial domain Ω_x . In addition to these two domains a third, so called reference domain Ω_χ is introduced. The mapping

$$\varphi : \Omega_\chi \times (0, T) \rightarrow \mathbb{R}^d \quad (1.35)$$

describes its motion. For sufficiently smooth, bijective functions ϕ and φ exists a third mapping, defined as

$$\psi : \Omega_\chi \times (0, T) \rightarrow \mathbb{R}^d, \text{ with } \psi = \varphi^{-1} \circ \phi \quad (1.36)$$

This leads for $\mathbf{x} \in \Omega_x$, $\mathbf{X} \in \Omega_X$, and $\boldsymbol{\chi} \in \Omega_\chi$ to the following relations

$$\begin{aligned} \mathbf{x} &= \phi(\mathbf{X}, t) \\ \boldsymbol{\chi} &= \psi(\mathbf{X}, t) \\ \mathbf{x} &= \varphi(\boldsymbol{\chi}, t) \end{aligned} \quad (1.37)$$

The deformations are formulated as

$$\begin{aligned} \mathbf{d}_\phi &= \mathbf{x} - \mathbf{X} \\ \mathbf{d}_\varphi &= \mathbf{x} - \boldsymbol{\chi} \\ \mathbf{d}_\psi &= \boldsymbol{\chi} - \mathbf{X} \end{aligned} \quad (1.38)$$

The velocity is the first derivative of the deformation and follows considering Equations (1.37) and (1.38) as

$$\begin{aligned} \dot{\mathbf{d}}_\phi &= \left. \frac{\partial \mathbf{d}_\phi}{\partial t} \right|_{\mathbf{X}} = \left. \frac{\partial \mathbf{x}}{\partial t} \right|_{\mathbf{X}} = \dot{\phi} \\ \dot{\mathbf{d}}_\varphi &= \left. \frac{\partial \mathbf{d}_\varphi}{\partial t} \right|_{\boldsymbol{\chi}} = \left. \frac{\partial \mathbf{x}}{\partial t} \right|_{\boldsymbol{\chi}} = \dot{\varphi} \\ \dot{\mathbf{d}}_\psi &= \left. \frac{\partial \mathbf{d}_\psi}{\partial t} \right|_{\mathbf{X}} = \left. \frac{\partial \boldsymbol{\chi}}{\partial t} \right|_{\mathbf{X}} = \dot{\psi} \end{aligned} \quad (1.39)$$

The following functions f , g , and h are defined in different domains. Defining a function in one domain leads directly to the definition of two other functions

$$\mathbf{f}(\boldsymbol{\chi}, t) = \mathbf{g}(\mathbf{x}, t) = \mathbf{h}(\mathbf{X}, t) \quad (1.40)$$

Considering chain rule, there follows for the derivative with respect to time

$$\frac{\partial \mathbf{f}}{\partial \boldsymbol{\chi}} \dot{\mathbf{d}}_\psi + \frac{\partial \mathbf{f}}{\partial t} = \frac{\partial \mathbf{g}}{\partial \mathbf{x}} \dot{\mathbf{d}}_\phi + \frac{\partial \mathbf{g}}{\partial t} = \frac{\partial \mathbf{h}}{\partial t} \quad (1.41)$$

Equation (1.39) and $\frac{\partial X}{\partial t} = 0$ are used therefore. For $\mathbf{x} = \varphi(\psi(\mathbf{X}, t), t)$ the time derivative results in

$$\dot{\mathbf{d}}_\phi = \frac{\partial \varphi}{\partial \psi} \dot{\mathbf{d}}_\psi + \dot{\mathbf{d}}_\varphi \Rightarrow \dot{\mathbf{d}}_\psi = \frac{\partial \boldsymbol{\chi}}{\partial \mathbf{x}} \left(\dot{\mathbf{d}}_\phi - \dot{\mathbf{d}}_\varphi \right) \quad (1.42)$$

Inserting this in Equation (1.41) leads to

$$\underbrace{\frac{\partial \mathbf{f}}{\partial \mathbf{x}} (\dot{\mathbf{d}}_\phi - \dot{\mathbf{d}}_\varphi)}_{\text{referential}} + \frac{\partial \mathbf{f}}{\partial t} = \underbrace{\frac{\partial \mathbf{g}}{\partial \mathbf{x}} \dot{\mathbf{d}}_\phi + \frac{\partial \mathbf{g}}{\partial t}}_{\text{spatial}} = \underbrace{\frac{\partial \mathbf{h}}{\partial t}}_{\text{material}} \quad , \quad (1.43)$$

These differences are important because it is stated here that a problem could be formulated in the reference (ALE) domain while the spatial derivatives are still used as in the spatial setting considering the difference in the convective velocity [4, p. 12]. This results in the used computational mesh dynamics (CMD) described in detail in section 4.1.

2 Fluid Domain

As explained before for the fluid structure interaction (FSI) a fluid and a structure interact. The fluid and how it is considered in the model is the topic of this chapter. At the beginning some physical properties are defined. The fluid is described using the continuity equation and the momentum equations, together representing the incompressible Navier-Stokes-equations. The derivation of these important equations in fluid mechanics is shown in this chapter and the main topic is then how the FEM model for the fluid looks like.

2.1 Physical properties of the fluid

The fluid could be a gas or a liquid. The field of fluid mechanics deals with the physical properties of the fluid and the flow of it. An example for a gaseous fluid is air and for a liquid one water but also toothpaste and honey are fluids and it is obvious to see from these examples that the properties of different fluids can be various but the fundamental equations to describe fluids mathematically are the same for all of these different fluid types although there are also differences within the models.

An important distinction between fluids and solids is that fluids cannot resist shear forces when they are in a rest position [25, p. 23]. In this thesis *Newtonian fluids* are considered. This means that the shear stresses are proportional to the change of flow velocities of the fluid [19, p. 106]. Shear stress is defined as

$$\tau = \mu \frac{du}{dt} \quad (2.1)$$

where μ is the dynamic or shear viscosity [26, p. 6] and $\frac{du}{dt}$ the derivative of the fluid velocity parallel to the shear direction. Another important quantity of a fluid is its density ρ . The kinematic viscosity ν [26, p. 15] sets it in relation to the dynamic viscosity

$$\nu = \frac{\mu}{\rho} \quad (2.2)$$

Reynolds number Re is an important parameter of a fluid. It shows the flow resistance of a viscous fluid and is defined as

$$Re = \frac{uL}{\nu} \quad (2.3)$$

where u is the fluid's velocity and L is the characteristic length. A small Reynolds number indicates that friction forces are predominant and a high Reynolds number indicates predominant inertia forces [19, p. 110].

In the fluid model used in this work the density ρ is constant and the fluid is called *incompressible*. If a flow of a gas is compressible or incompressible is characterised by Mach's number, the ratio between the characteristic velocity and acoustic velocity [19, p. 190] and [24, p. 19]. The density could depend on the temperature but this is not considered in this work.

2.2 Derivation of the governing equations

The governing equations for the fluid model used in this work are the balance of mass and linear momentum, which constitute the *Navier-Stokes equations* (NSEQ) for incompressible flow⁵. Their derivation shown here is based on [19, pp. 201 – 209].

Continuity equation

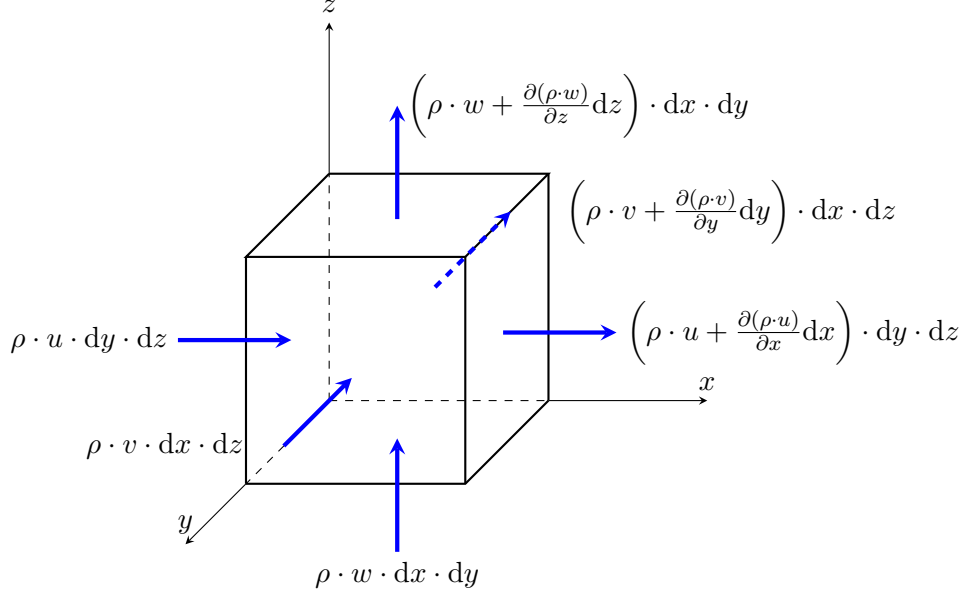


Fig. 8: Mass flow on infinitesimal volume element dV

Figure 8 shows an infinitesimal small volume element $dV = dx \cdot dy \cdot dz$. The law of conservation of mass has to be fulfilled for this element. The change of mass over time is the mass flow which flows in the volume element minus the mass flow which flows out of dV . These flows are shown in Figure 8.

The change of mass over time is

$$\frac{\partial \rho}{\partial t} \cdot dx \cdot dy \cdot dz \quad (2.4)$$

This equation combined with the equations shown in Figure 8 leads to

$$\begin{aligned} \frac{\partial \rho}{\partial t} \cdot dx \cdot dy \cdot dz = & \left(\rho \cdot u - \left(\rho \cdot u + \frac{\partial(\rho \cdot u)}{\partial x} dx \right) \right) \cdot dy \cdot dz + \\ & \left(\rho \cdot v - \left(\rho \cdot v + \frac{\partial(\rho \cdot v)}{\partial y} dy \right) \right) \cdot dx \cdot dz + \\ & \left(\rho \cdot w - \left(\rho \cdot w + \frac{\partial(\rho \cdot w)}{\partial z} dz \right) \right) \cdot dx \cdot dy \end{aligned}$$

⁵Claude Luis Maria Henry NAVIER, 1785-1836, French engineer, and George STOKES, 1819 - 1903, English mathematician and physician [21]

Some reshaping of this expression gives the continuity equation

$$\frac{\partial \rho}{\partial t} + \frac{\partial(\rho \cdot u)}{\partial x} + \frac{\partial(\rho \cdot v)}{\partial y} + \frac{\partial(\rho \cdot w)}{\partial z} = 0 \quad (2.5)$$

For an incompressible fluid with constant density follows

$$\frac{\partial u}{\partial x} + \frac{\partial v}{\partial y} + \frac{\partial w}{\partial z} = 0 \quad (2.6)$$

Equation 2.6 can be written in coordinate free notation as

$$\nabla \cdot \mathbf{u} = 0 \quad (2.7)$$

where \mathbf{u} is the fluid velocity vector.

Balance of linear momentum (Navier-Stokes equations)

The derivation of the balance of linear momentum shown here is based on laminar flow. It comes from the law of conservation of momentum on the infinitesimal volume element dV .

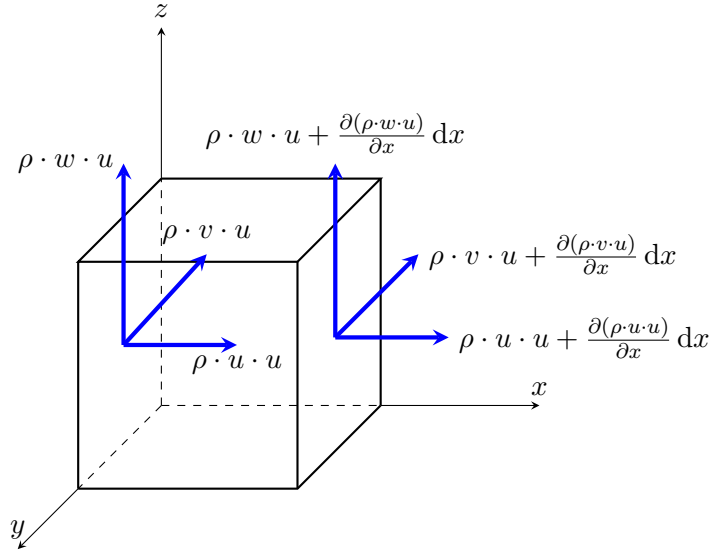


Fig. 9: Momentum flow on infinitesimal volume element dV in x -direction

The change over time of momentum in the infinitesimal volume element dV is

$$\frac{\partial(\rho \mathbf{u})}{\partial t} \cdot dx \cdot dy \cdot dz \quad (2.8)$$

Figure 9 shows dV with the necessary components in x -direction. It looks analogously for the other two coordinate directions. There are three momentum flows at each surface of the cube. In addition to the momentum also volume forces \mathbf{f} (e.g. gravitational forces) act on dV . Further normal stresses and shear stresses are considered as shown in Figure 10 for x -direction. The other two directions are considered analogously.

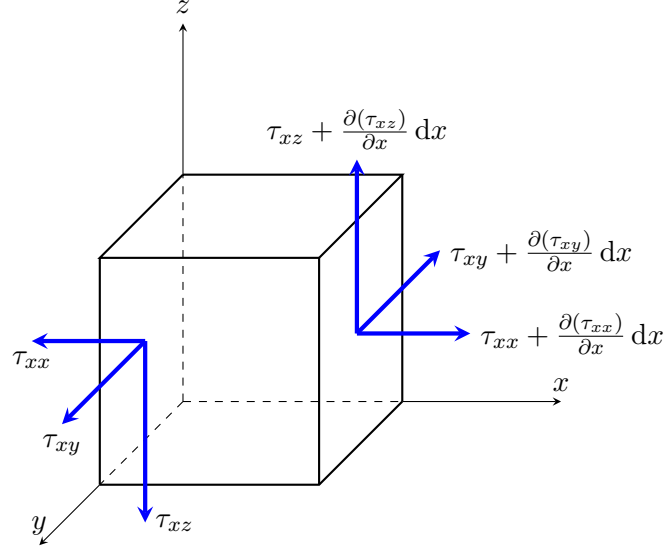


Fig. 10: Normal and shear stresses on volume element dV in x -direction

Considering for the change of the momentum over time on dV the momentum inflow, the momentum outflow, the normal and shear stresses, and the mass acting on dV follows in x -direction

$$\begin{aligned}
\frac{\partial(\rho \cdot u)}{\partial t} \cdot dx \cdot dy \cdot dz = & \left(\rho \cdot u \cdot u - \left(\rho \cdot u \cdot u + \frac{\partial(\rho \cdot u \cdot u)}{\partial x} dx \right) \right) \cdot dy \cdot dz + \\
& \left(\rho \cdot u \cdot v - \left(\rho \cdot u \cdot v + \frac{\partial(\rho \cdot u \cdot v)}{\partial y} dy \right) \right) \cdot dx \cdot dz + \\
& \left(\rho \cdot u \cdot w - \left(\rho \cdot u \cdot w + \frac{\partial(\rho \cdot u \cdot w)}{\partial z} dz \right) \right) \cdot dx \cdot dy + \\
& f_x \cdot dx \cdot dy \cdot dz + \\
& \left(-\tau_{xx} + \left(\tau_{xx} + \frac{\partial(\tau_{xx})}{\partial x} dx \right) \right) dy \cdot dz + \\
& \left(-\tau_{yx} + \left(\tau_{yx} + \frac{\partial(\tau_{yx})}{\partial y} dy \right) \right) dx \cdot dz + \\
& \left(-\tau_{zx} + \left(\tau_{zx} + \frac{\partial(\tau_{zx})}{\partial z} dz \right) \right) dx \cdot dy
\end{aligned}$$

Applying some reshaping leads to

$$\frac{\partial(\rho \cdot u)}{\partial t} + \frac{\partial(\rho \cdot u \cdot u)}{\partial x} + \frac{\partial(\rho \cdot u \cdot v)}{\partial y} + \frac{\partial(\rho \cdot u \cdot w)}{\partial z} = f_x + \frac{\partial\tau_{xx}}{\partial x} + \frac{\partial\tau_{yx}}{\partial y} + \frac{\partial\tau_{zx}}{\partial z} \quad (2.9)$$

In y -direction follows analogously

$$\frac{\partial(\rho \cdot v)}{\partial t} + \frac{\partial(\rho \cdot v \cdot u)}{\partial x} + \frac{\partial(\rho \cdot v \cdot v)}{\partial y} + \frac{\partial(\rho \cdot v \cdot w)}{\partial z} = f_y + \frac{\partial\tau_{xy}}{\partial x} + \frac{\partial\tau_{yy}}{\partial y} + \frac{\partial\tau_{zy}}{\partial z} \quad (2.10)$$

and in z -direction

$$\frac{\partial(\rho \cdot w)}{\partial t} + \frac{\partial(\rho \cdot w \cdot u)}{\partial x} + \frac{\partial(\rho \cdot w \cdot v)}{\partial y} + \frac{\partial(\rho \cdot w \cdot w)}{\partial z} = f_z + \frac{\partial\tau_{xz}}{\partial x} + \frac{\partial\tau_{yz}}{\partial y} + \frac{\partial\tau_{zz}}{\partial z} \quad (2.11)$$

Pressure p is the trace of the stress tensor

$$p = -\frac{\tau_{xx} + \tau_{yy} + \tau_{zz}}{3} \quad (2.12)$$

and is a negative normal stress. Considering Equation (2.12) it is possible to split the normal stresses into

$$\begin{aligned} \tau_{xx} &= \sigma_{xx} - p \\ \tau_{yy} &= \sigma_{yy} - p \\ \tau_{zz} &= \sigma_{zz} - p \end{aligned} \quad (2.13)$$

For Newtonian fluids consider the following relations for normal stresses

$$\begin{aligned} \sigma_{xx} &= 2 \cdot \mu \cdot \frac{\partial u}{\partial x} - \frac{2}{3} \cdot \mu \cdot \left(\frac{\partial u}{\partial x} + \frac{\partial v}{\partial y} + \frac{\partial w}{\partial z} \right) \\ \sigma_{yy} &= 2 \cdot \mu \cdot \frac{\partial v}{\partial y} - \frac{2}{3} \cdot \mu \cdot \left(\frac{\partial u}{\partial x} + \frac{\partial v}{\partial y} + \frac{\partial w}{\partial z} \right) \\ \sigma_{zz} &= 2 \cdot \mu \cdot \frac{\partial w}{\partial z} - \frac{2}{3} \cdot \mu \cdot \left(\frac{\partial u}{\partial x} + \frac{\partial v}{\partial y} + \frac{\partial w}{\partial z} \right) \end{aligned} \quad (2.14)$$

and for shear stresses with the law of complementary shear stresses

$$\begin{aligned} \tau_{yx} = \tau_{xy} &= \mu \cdot \left(\frac{\partial v}{\partial x} + \frac{\partial u}{\partial y} \right) \\ \tau_{yz} = \tau_{zy} &= \mu \cdot \left(\frac{\partial w}{\partial y} + \frac{\partial v}{\partial z} \right) \\ \tau_{zx} = \tau_{xz} &= \mu \cdot \left(\frac{\partial u}{\partial z} + \frac{\partial w}{\partial x} \right) \end{aligned} \quad (2.15)$$

Using these relations in Equations (2.14) and (2.15) together with Equation (2.6) and apply these at Equations (2.9) to (2.11) leads to the momentum equations for incompressible flows

$$\begin{aligned} \rho \left(\frac{\partial u}{\partial t} + u \frac{\partial u}{\partial x} + v \frac{\partial u}{\partial y} + w \frac{\partial u}{\partial z} \right) &= f_x - \frac{\partial p}{\partial x} + \mu \left(\frac{\partial^2 u}{\partial x^2} + \frac{\partial^2 u}{\partial y^2} + \frac{\partial^2 u}{\partial z^2} \right) \\ \rho \left(\frac{\partial v}{\partial t} + u \frac{\partial v}{\partial x} + v \frac{\partial v}{\partial y} + w \frac{\partial v}{\partial z} \right) &= f_y - \frac{\partial p}{\partial y} + \mu \left(\frac{\partial^2 v}{\partial x^2} + \frac{\partial^2 v}{\partial y^2} + \frac{\partial^2 v}{\partial z^2} \right) \\ \rho \left(\frac{\partial w}{\partial t} + u \frac{\partial w}{\partial x} + v \frac{\partial w}{\partial y} + w \frac{\partial w}{\partial z} \right) &= f_z - \frac{\partial p}{\partial z} + \mu \left(\frac{\partial^2 w}{\partial x^2} + \frac{\partial^2 w}{\partial y^2} + \frac{\partial^2 w}{\partial z^2} \right) \end{aligned} \quad (2.16)$$

In a coordinate free and vectorized notation this is

$$\rho \left(\frac{\partial \mathbf{u}}{\partial t} + (\mathbf{u} \cdot \nabla) \mathbf{u} \right) = \mathbf{f} - \nabla p + \mu \Delta \mathbf{u} \quad (2.17)$$

Considering that

$$\mu \Delta \mathbf{u} = \mu \nabla^2 \mathbf{u} = \mu \nabla \cdot (\nabla \mathbf{u} + \nabla \mathbf{u}^T)$$

Equation (2.17) can be written as

$$\rho \left(\frac{\partial \mathbf{u}}{\partial t} + (\mathbf{u} \cdot \nabla) \mathbf{u} \right) - \nabla \cdot \boldsymbol{\sigma} = \mathbf{f} \quad (2.18)$$

where $\boldsymbol{\sigma}$ is defined as

$$\boldsymbol{\sigma}(\mathbf{u}, p) = -p \cdot \mathbf{I} + \mu (\nabla \mathbf{u} + \nabla \mathbf{u}^T) \quad (2.19)$$

2.3 Fluid domain in FEM

This section is based on [6]⁶ and [26], especially chapter 4 (pages 127 to 155).

The governing equations here are the Navier-Stokes equations derived above in Equation (2.18) and Equation (2.7). With no restriction of generality this section considers a two dimensional flow with spatial coordinates $\mathbf{x} = (x, y)^T$ and velocity vector $\mathbf{u} = (u, v)^T$.

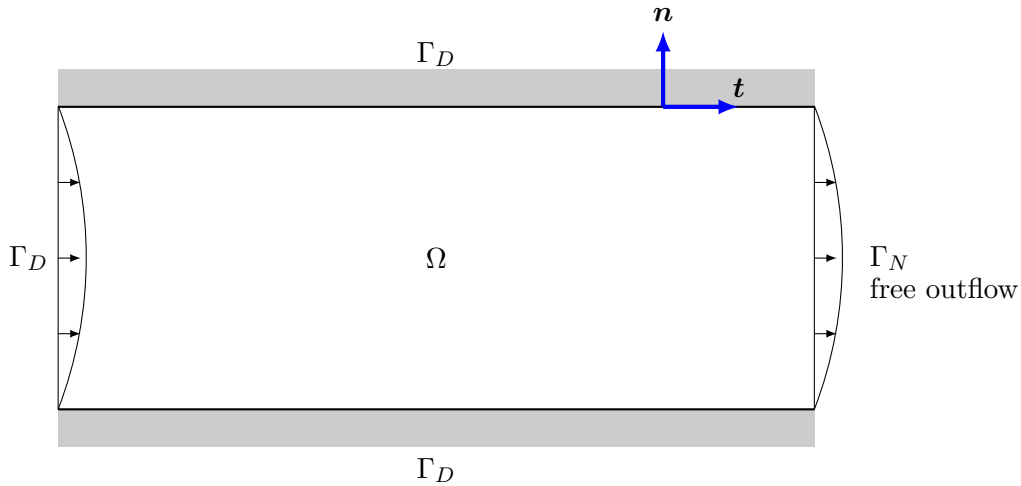


Fig. 11: Fluid domain Ω

Figure 11 shows the fluid domain of interest (fluid DOI) Ω . The figure depicts a channel flow but this is arbitrary and the principle holds true for all other possible cases. There are some boundary conditions (BCs) predefined. As mentioned before BCs are distinguished into Dirichlet or essential BCs on Γ_D and von Neumann BCs on Γ_N . In the sketch also a normal vector \mathbf{n} and a tangential vector \mathbf{t} of the edge of DOI Ω are shown.

In component-form the governing equations are

$$\rho \begin{bmatrix} \frac{\partial u}{\partial t} + (\mathbf{u} \cdot \partial_x + \mathbf{v} \cdot \partial_y) \cdot u \\ \frac{\partial v}{\partial t} + (\mathbf{u} \cdot \partial_x + \mathbf{v} \cdot \partial_y) \cdot v \end{bmatrix} - \begin{bmatrix} \sigma_{xx,x} + \sigma_{xy,y} \\ \sigma_{yx,x} + \sigma_{yy,y} \end{bmatrix} = \begin{bmatrix} f_x \\ f_y \end{bmatrix} \quad (2.20)$$

$$u_{,x} + v_{,y} = 0 \quad (2.21)$$

The velocity vector components u and v , and pressure p are the unknowns in these three equations. In this work a so-called *no-slip boundary condition* at walls is assumed for the Dirichlet BCs along the walls of Ω .

$$\mathbf{u}(\mathbf{x}, t) = \mathbf{0} \quad \forall \mathbf{x} \in \Gamma_{D,Wall} \quad t \in [0, T] \quad (2.22)$$

The von Neumann boundary condition for each case in this work is a free outflow

$$\boldsymbol{\sigma} \cdot \mathbf{n} = \mathbf{t} \quad (2.23)$$

⁶These lecture notes for FEM II are not used in the lecture and therefore not published. Prof. Dr.-Ing. T.-P. Fries gave me access to these documents in personal communication. I would like to acknowledge this here separately.

For the components of vector \mathbf{t} follows

$$\begin{aligned} t_x &= \sigma_{xx} \cdot n_x + \sigma_{xy} \cdot n_y \\ t_y &= \sigma_{yx} \cdot n_x + \sigma_{yy} \cdot n_y \end{aligned}$$

The initial condition (IC) is

$$\mathbf{u}(\mathbf{x}, t = 0) = \mathbf{u}_0 \quad (2.24)$$

with $\nabla \cdot \mathbf{u}_0 = 0$.

For discretization in time θ -method is used. For the first line of Equation (2.20) follows

$$\begin{aligned} \rho \frac{u^{n+1} - u^n}{\Delta t} &= \theta [-\rho(u^{n+1} \cdot u_{,x}^{n+1} + v^{n+1} \cdot u_{,y}^{n+1}) + \sigma_{xx,x}^{n+1} + \sigma_{xy,y}^{n+1} + f_x^{n+1}] \\ &+ (1 - \theta) [-\rho(u^n \cdot u_{,x}^n + v^n \cdot u_{,y}^n) + \sigma_{xx,x}^n + \sigma_{xy,y}^n + f_x^n] \end{aligned}$$

Reshape this to

$$\begin{aligned} \frac{\rho}{\Delta t} u^{n+1} + \rho \theta (u^{n+1} \cdot u_{,x}^{n+1} + v^{n+1} \cdot u_{,y}^{n+1}) - \theta (\sigma_{xx,x}^{n+1} + \sigma_{xy,y}^{n+1}) &= \\ \frac{\rho}{\Delta t} u^n - \rho (1 - \theta) (u^n \cdot u_{,x}^n + v^n \cdot u_{,y}^n) + (1 - \theta) (\sigma_{xx,x}^n + \sigma_{xy,y}^n) + f_x^\theta & \quad (2.25) \end{aligned}$$

with

$$f_x^\theta = \theta f_x^{n+1} + (1 - \theta) f_x^n$$

For the second line of Equation (2.20) follows analogously

$$\begin{aligned} \frac{\rho}{\Delta t} v^{n+1} + \rho \theta (u^{n+1} \cdot v_{,x}^{n+1} + v^{n+1} \cdot v_{,y}^{n+1}) - \theta (\sigma_{yx,y}^{n+1} + \sigma_{yy,y}^{n+1}) &= \\ \frac{\rho}{\Delta t} v^n - \rho (1 - \theta) (u^n \cdot v_{,x}^n + v^n \cdot v_{,y}^n) + (1 - \theta) (\sigma_{yx,x}^n + \sigma_{yy,y}^n) + f_y^\theta & \quad (2.26) \end{aligned}$$

with

$$f_y^\theta = \theta f_y^{n+1} + (1 - \theta) f_y^n$$

The continuity equation is not time-dependent. Equation 2.21 should be fulfilled at all times t . This leads to

$$u_{,x}^\theta + v_{,y}^\theta = 0 \quad \Leftrightarrow \quad \theta u_{,x}^{n+1} + (1 - \theta) u_{,x}^n + \theta v_{,y}^{n+1} + (1 - \theta) v_{,y}^n = 0 \quad (2.27)$$

Time discretization using θ -method results to time derivatives free Equations (2.25), (2.26), and (2.27) but two time-levels t^n and t^{n+1} have to be considered. At t^n all quantities are known, at t^{n+1} the fields u^{n+1} , v^{n+1} , and p^{n+1} are unknown but f^{n+1} is given. The advection terms are non-linear so a procedure to solve non-linear equations is necessary. Here the Picard iteration is used. Considering Equation (2.19) the semi-discrete Equations (2.25) and (2.26) are linearised to

$$\begin{aligned} \frac{\rho}{\Delta t} u^{n+1} + \rho \theta (u^i \cdot u_{,x}^{n+1} + v^i \cdot u_{,y}^{n+1}) - \theta (-p_{,x}^{n+1} + 2\mu u_{,xx}^{n+1}) - \theta \mu (u_{,yy}^{n+1} + v_{,xy}^{n+1}) &= \\ \frac{\rho}{\Delta t} u^n - \rho (1 - \theta) (u^n \cdot u_{,x}^n + v^n \cdot u_{,y}^n) + (1 - \theta) (-p_{,x}^n + 2\mu u_{,xx}^n) + (1 - \theta) \mu (u_{,yy}^n + v_{,xy}^n) + f_x^\theta & \quad (2.28) \end{aligned}$$

$$\begin{aligned} \frac{\rho}{\Delta t} v^{n+1} + \rho \theta (u^i \cdot v_{,x}^{n+1} + v^i \cdot v_{,y}^{n+1}) - \theta \mu (u_{,xy}^{n+1} + v_{,xx}^{n+1}) - \theta (-p_{,y}^{n+1} + 2\mu v_{,yy}^{n+1}) &= \\ \frac{\rho}{\Delta t} v^n - \rho (1 - \theta) (u^n \cdot v_{,x}^n + v^n \cdot v_{,y}^n) + (1 - \theta) \mu (u_{,xy}^n + v_{,xx}^n) + (1 - \theta) (-p_{,y}^n + 2\mu v_{,yy}^n) + f_y^\theta & \quad (2.29) \end{aligned}$$

Equation (2.27) is unchanged.

The next task is to determine the weak form of these equations. Therefore the test functions w_u , w_v , and w_p are necessary.

Multiply Equation (2.28) with test function w_u and integrate over the DOI Ω . This leads to

$$\begin{aligned} & \int w_u \left[\frac{\rho}{\Delta t} u^{n+1} + \rho\theta(u^i \cdot u_{,x}^{n+1} + v^i \cdot u_{,y}^{n+1}) - \theta(\sigma_{xx,x}^{n+1} + \sigma_{xy,y}^{n+1}) \right] d\Omega = \\ & \int w_u \left[\frac{\rho}{\Delta t} u^n + \rho(1-\theta)(u^n \cdot u_{,x}^n + v^n \cdot u_{,y}^n) + (1-\theta)(\sigma_{xx,x}^n + \sigma_{xy,y}^n) + f_x^\theta \right] d\Omega \end{aligned} \quad (2.30)$$

Apply the divergence theorem on the stress tensor leads to

$$\begin{aligned} & \frac{\rho}{\Delta t} \int w_u u^{n+1} d\Omega + \rho\theta \int w_u (u^i \cdot u_{,x}^{n+1} + v^i \cdot u_{,y}^{n+1}) d\Omega \\ & + \theta \int w_{u,x} \sigma_{xx}^{n+1} d\Omega - \theta \int w_u \sigma_{xx}^{n+1} n_x d\Gamma \\ & + \theta \int w_{u,y} \sigma_{xy}^{n+1} d\Omega - \theta \int w_u \sigma_{xy}^{n+1} n_y d\Gamma = \\ & \frac{\rho}{\Delta t} \int w_u u^n d\Omega - \rho(1-\theta) \int w_u (u^n \cdot u_{,x}^n + v^n \cdot u_{,y}^n) d\Omega \\ & - (1-\theta) \int w_{u,x} \sigma_{xx}^n d\Omega + (1-\theta) \int w_u \sigma_{xx}^n n_x d\Gamma \\ & - (1-\theta) \int w_{u,y} \sigma_{xy}^n d\Omega + (1-\theta) \int w_u \sigma_{xy}^n n_y d\Gamma + \int w_u f_x^\theta d\Omega \end{aligned} \quad (2.31)$$

Rearrange this equation and insert Equation (2.19) leads to

$$\begin{aligned} & \frac{\rho}{\Delta t} \int w_u u^{n+1} d\Omega + \rho\theta \int w_u (u^i \cdot u_{,x}^{n+1} + v^i \cdot u_{,y}^{n+1}) d\Omega \\ & + \theta \int w_{u,x} (-p^{n+1} + 2\mu u_{,x}^{n+1}) d\Omega + \theta\mu \int w_{u,y} (u_{,y}^{n+1} + v_{,x}^{n+1}) d\Omega \\ & = \frac{\rho}{\Delta t} \int w_u u^n d\Omega - \rho(1-\theta) \int w_u (u^n \cdot u_{,x}^n + v^n \cdot u_{,y}^n) d\Omega \\ & - (1-\theta) \int w_{u,x} (-p^n + 2\mu u_{,x}^n) d\Omega - (1-\theta)\mu \int w_{u,y} (u_{,y}^n + v_{,x}^n) d\Omega + \int w_u f_x^\theta d\Omega + \int w_u t_x^\theta d\Gamma \end{aligned} \quad (2.32)$$

Analogously follows for Equation (2.29)

$$\begin{aligned} & \frac{\rho}{\Delta t} \int w_v v^{n+1} d\Omega + \rho\theta \int w_v (u^i \cdot v_{,x}^{n+1} + v^i \cdot v_{,y}^{n+1}) d\Omega \\ & + \theta \int w_{v,y} (-p^{n+1} + 2\mu v_{,y}^{n+1}) d\Omega + \theta\mu \int w_{v,x} (u_{,y}^{n+1} + v_{,x}^{n+1}) d\Omega \\ & = \frac{\rho}{\Delta t} \int w_v v^n d\Omega - \rho(1-\theta) \int w_v (u^n \cdot v_{,x}^n + v^n \cdot v_{,y}^n) d\Omega \\ & - (1-\theta) \int w_{v,y} (-p^n + 2\mu v_{,y}^n) d\Omega - (1-\theta)\mu \int w_{v,x} (u_{,y}^n + v_{,x}^n) d\Omega + \int w_v f_y^\theta d\Omega + \int w_v t_y^\theta d\Gamma \end{aligned} \quad (2.33)$$

The weak form of the continuity equation is

$$\theta \int w_p u_{,x}^{n+1} d\Omega + \theta \int w_p v_{,y}^{n+1} d\Omega = -(1-\theta) \int w_p u_{,x}^n d\Omega - (1-\theta) \int w_p v_{,y}^n d\Omega \quad (2.34)$$

As described in 1.2 u^{n+1} , v^{n+1} , and p^{n+1} are sought so that Equations (2.32), (2.33), and (2.34) are fulfilled for all possible test functions w_u , w_v , and w_p . Therefore the possible functions have to be restricted to the FE basis with an ansatz of the following form

$$\begin{aligned}
u^{n+1}(\mathbf{x}) &\approx u^{h,n+1}(\mathbf{x}) = \mathbf{N}^T(\mathbf{x}) \cdot \mathbf{u}^{n+1} \\
v^{n+1}(\mathbf{x}) &\approx v^{h,n+1}(\mathbf{x}) = \mathbf{N}^T(\mathbf{x}) \cdot \mathbf{v}^{n+1} \\
p^{n+1}(\mathbf{x}) &\approx p^{h,n+1}(\mathbf{x}) = \mathbf{M}^T(\mathbf{x}) \cdot \mathbf{p}^{n+1} \\
u^n(\mathbf{x}) &\approx u^{h,n}(\mathbf{x}) = \mathbf{N}^T(\mathbf{x}) \cdot \mathbf{u}^n \\
v^n(\mathbf{x}) &\approx v^{h,n}(\mathbf{x}) = \mathbf{N}^T(\mathbf{x}) \cdot \mathbf{v}^n \\
p^n(\mathbf{x}) &\approx p^{h,n}(\mathbf{x}) = \mathbf{M}^T(\mathbf{x}) \cdot \mathbf{p}^n \\
u^i(\mathbf{x}) &\approx u^{h,i}(\mathbf{x}) = \mathbf{N}^T(\mathbf{x}) \cdot \mathbf{u}^i \\
v^i(\mathbf{x}) &\approx v^{h,i}(\mathbf{x}) = \mathbf{N}^T(\mathbf{x}) \cdot \mathbf{v}^i \\
w_u &\approx w_u^h = \mathbf{N}^T(\mathbf{x}) \cdot \mathbf{w}_u \\
w_v &\approx w_v^h = \mathbf{N}^T(\mathbf{x}) \cdot \mathbf{w}_v \\
w_p &\approx w_p^h = \mathbf{M}^T(\mathbf{x}) \cdot \mathbf{w}_p
\end{aligned} \tag{2.35}$$

For the velocity components and pressure finite elements with shape functions of different order can be used and therefore the functions are $\mathbf{N}(\mathbf{x})$ for velocities and $\mathbf{M}(\mathbf{x})$ for pressure. In this thesis Taylor-Hood-elements are used. The shape functions have different orders there [7]. This approach is also known as $Q2/Q1$, which means that the element order for the velocity field is quadratic and for the pressure field linear, two meshes have to be generated for the discretization. The reason therefore is that for incompressible flow problems the interpolation functions should be chosen for error consistency reasons so that the interpolation functions for pressure are a polynomial of one degree lower than for velocities [10].

u^n , v^n , and p^n are known from the previous time step and u^i , v^i , and p^i are known from the previous iteration step, so $u^{h,n}$, $v^{h,n}$, $p^{h,n}$, $u^{h,i}$, $v^{h,i}$, and $p^{h,i}$ can be evaluated immediately.

To get the sought discrete weak form of the equations, expressions from Equation (2.35) are applied to Equations (2.32), (2.33), and (2.34).

This leads to the following system of equations in two dimensions:

$$\begin{aligned}
& \frac{\rho}{\Delta t} \int \mathbf{N} \mathbf{N}^T d\Omega \mathbf{u}^{n+1} + \rho \theta \int (\mathbf{N}^T \mathbf{u}^i) \mathbf{N} \mathbf{N}_{,x}^T d\Omega \mathbf{u}^{n+1} \\
& + \rho \theta \int (\mathbf{N}^T \mathbf{v}^i) \mathbf{N} \mathbf{N}_{,y}^T d\Omega \mathbf{u}^{n+1} - \theta \int \mathbf{N}_{,x} \mathbf{M}^T d\Omega p^{n+1} \\
& + \theta \mu \int 2\mathbf{N}_{,x} \mathbf{N}_{,x}^T + \mathbf{N}_{,y} \mathbf{N}_{,y}^T d\Omega \mathbf{u}^{n+1} + \theta \mu \int \mathbf{N}_{,y} \mathbf{N}_{,x}^T d\Omega \mathbf{v}^{n+1} = \\
& \frac{\rho}{\Delta t} \int \mathbf{N} (\mathbf{N}^T \mathbf{u}^n) d\Omega - \rho(1-\theta) \int (\mathbf{N}^T \mathbf{u}^n) \mathbf{N} (\mathbf{N}_{,x}^T \mathbf{u}^n) d\Omega \\
& - \rho(1-\theta) \int (\mathbf{N}^T \mathbf{v}^n) \mathbf{N} (\mathbf{N}_{,y}^T \mathbf{u}^n) d\Omega + (1-\theta) \int \mathbf{N}_{,x} (\mathbf{M}^T p^n) d\Omega \\
& - (1-\theta) \mu \int \mathbf{N}_{,x} (2\mathbf{N}_{,x}^T \mathbf{u}^n) d\Omega - (1-\theta) \mu \int \mathbf{N}_{,y} (\mathbf{N}_{,y}^T \mathbf{u}^n + \mathbf{N}_{,x}^T \mathbf{v}^n) d\Omega \\
& + \int \mathbf{N} f_x^\theta d\Omega + \int \mathbf{N} t_x^\theta d\Gamma
\end{aligned} \tag{2.36}$$

$$\begin{aligned}
& \frac{\rho}{\Delta t} \int \mathbf{N} \mathbf{N}^T d\Omega \mathbf{v}^{n+1} + \rho \theta \int (\mathbf{N}^T \mathbf{u}^i) \mathbf{N} \mathbf{N}_{,x}^T d\Omega \mathbf{v}^{n+1} \\
& + \rho \theta \int (\mathbf{N}^T \mathbf{v}^i) \mathbf{N} \mathbf{N}_{,y}^T d\Omega \mathbf{v}^{n+1} - \theta \int \mathbf{N}_{,y} \mathbf{M}^T d\Omega p^{n+1} \\
& + \theta \mu \int 2\mathbf{N}_{,y} \mathbf{N}_{,y}^T + \mathbf{N}_{,x} \mathbf{N}_{,x}^T d\Omega \mathbf{v}^{n+1} + \theta \mu \int \mathbf{N}_{,x} \mathbf{N}_{,y}^T d\Omega \mathbf{u}^{n+1} = \\
& \frac{\rho}{\Delta t} \int \mathbf{N} (\mathbf{N}^T \mathbf{v}^n) d\Omega - \rho(1-\theta) \int (\mathbf{N}^T \mathbf{u}^n) \mathbf{N} (\mathbf{N}_{,x}^T \mathbf{v}^n) d\Omega \\
& - \rho(1-\theta) \int (\mathbf{N}^T \mathbf{v}^n) \mathbf{N} (\mathbf{N}_{,y}^T \mathbf{v}^n) d\Omega + (1-\theta) \int \mathbf{N}_{,y} (\mathbf{M}^T p^n) d\Omega \\
& - (1-\theta) \mu \int \mathbf{N}_{,y} (2\mathbf{N}_{,y}^T \mathbf{v}^n) d\Omega - (1-\theta) \mu \int \mathbf{N}_{,x} (\mathbf{N}_{,y}^T \mathbf{u}^n + \mathbf{N}_{,x}^T \mathbf{v}^n) d\Omega \\
& + \int \mathbf{N} f_y^\theta d\Omega + \int \mathbf{N} t_y^\theta d\Gamma
\end{aligned} \tag{2.37}$$

$$\begin{aligned}
& - \theta \int \mathbf{M} \mathbf{N}_{,x}^T d\Omega \mathbf{u}^{n+1} - \theta \int \mathbf{M} \mathbf{N}_{,y}^T d\Omega \mathbf{v}^{n+1} = \\
& (1-\theta) \int \mathbf{M} (\mathbf{N}_{,x}^T \mathbf{u}^n) d\Omega + (1-\theta) \int \mathbf{M} (\mathbf{N}_{,y}^T \mathbf{v}^n) d\Omega
\end{aligned} \tag{2.38}$$

For purposes of a shorter and clearer notation in a matrix-vector equation, the following block matrices are introduced.

- time or mass matrix ⁷

$$\mathbf{T} = \frac{\rho}{\Delta t} \int \mathbf{N}\mathbf{N}^T d\Omega \quad (2.39)$$

and shorter

$$\hat{\mathbf{T}} = \begin{bmatrix} \mathbf{T} & 0 \\ 0 & \mathbf{T} \end{bmatrix} \quad (2.40)$$

- advection matrix

$$\mathbf{A}^i = \rho \int (\mathbf{N}^T \mathbf{u}^i) \mathbf{N} \mathbf{N}_{,x}^T + (\mathbf{N}^T \mathbf{v}^i) \mathbf{N} \mathbf{N}_{,y}^T d\Omega \quad (2.41)$$

$$\mathbf{A}^n = \rho \int (\mathbf{N}^T \mathbf{u}^n) \mathbf{N} \mathbf{N}_{,x}^T + (\mathbf{N}^T \mathbf{v}^n) \mathbf{N} \mathbf{N}_{,y}^T d\Omega \quad (2.42)$$

and shorter

$$\hat{\mathbf{A}}^i = \begin{bmatrix} \mathbf{A}^i & 0 \\ 0 & \mathbf{A}^i \end{bmatrix} \quad (2.43)$$

$$\hat{\mathbf{A}}^n = \begin{bmatrix} \mathbf{A}^n & 0 \\ 0 & \mathbf{A}^n \end{bmatrix} \quad (2.44)$$

- diffusion matrix

$$\hat{\mathbf{D}} = \begin{bmatrix} \mathbf{D}_{11} & \mathbf{D}_{12} \\ \mathbf{D}_{21} & \mathbf{D}_{22} \end{bmatrix} = \mu \begin{bmatrix} \int 2\mathbf{N}_{,x}\mathbf{N}_{,x}^T + \mathbf{N}_{,y}\mathbf{N}_{,y}^T d\Omega & \int \mathbf{N}_{,y}\mathbf{N}_{,x}^T d\Omega \\ \int \mathbf{N}_{,x}\mathbf{N}_{,y}^T d\Omega & \int \mathbf{N}_{,x}\mathbf{N}_{,x}^T + 2\mathbf{N}_{,y}\mathbf{N}_{,y}^T d\Omega \end{bmatrix} \quad (2.45)$$

- constraint matrix (Lagrangian multiplier for continuity)

$$\hat{\mathbf{C}} = [\mathbf{C}_1 \quad \mathbf{C}_2] = \left[- \int \mathbf{M}\mathbf{N}_{,x}^T d\Omega \quad - \int \mathbf{M}\mathbf{N}_{,y}^T d\Omega \right] \quad (2.46)$$

This leads to

$$\begin{bmatrix} \hat{\mathbf{T}} + \theta \hat{\mathbf{A}}^i + \theta \hat{\mathbf{D}} & \theta \hat{\mathbf{C}}^T \\ \theta \hat{\mathbf{C}} & \mathbf{0} \end{bmatrix} \cdot \begin{bmatrix} \hat{\mathbf{u}}^{n+1} \\ \mathbf{p}^{n+1} \end{bmatrix} = \begin{bmatrix} (\hat{\mathbf{T}} - (1-\theta)\hat{\mathbf{A}}^n - (1-\theta)\hat{\mathbf{D}})\hat{\mathbf{u}}^n - (1-\theta)\hat{\mathbf{C}}^T \mathbf{p}^n + \mathbf{F} \\ -(1-\theta)\hat{\mathbf{C}}\hat{\mathbf{u}}^n \end{bmatrix} \quad (2.47)$$

where $\hat{\mathbf{u}} = [\mathbf{u}\mathbf{v}]^T$ and $\mathbf{F} = [F_x F_y]^T$ with

$$F_x = \int \mathbf{N} f_x^\theta d\Omega + \int \mathbf{N} t_x^\theta d\Gamma \quad (2.48)$$

$$F_y = \int \mathbf{N} f_y^\theta d\Omega + \int \mathbf{N} t_y^\theta d\Gamma \quad (2.49)$$

Equation (2.47) is the implemented system of equations in the fluid solver in EduFEM [5] for 2d cases. It is straightforwardly extended to three dimensions.

⁷ \mathbf{T} is a mass matrix and therefore often denoted as \mathbf{M} . Here \mathbf{M} stands for the shape function used in the pressure mesh, so the mass or time matrix is denoted as \mathbf{T} .

3 Structural Domain

The structural domain or solid in this model can deform with large deformations but it is assumed that only small strains will occur [25, p. 20]. Figure 12 shows an arbitrary solid in the undeformed or material configuration $\Omega_{\mathbf{X}}$ and the deformed or spatial configuration $\Omega_{\mathbf{x}}$.

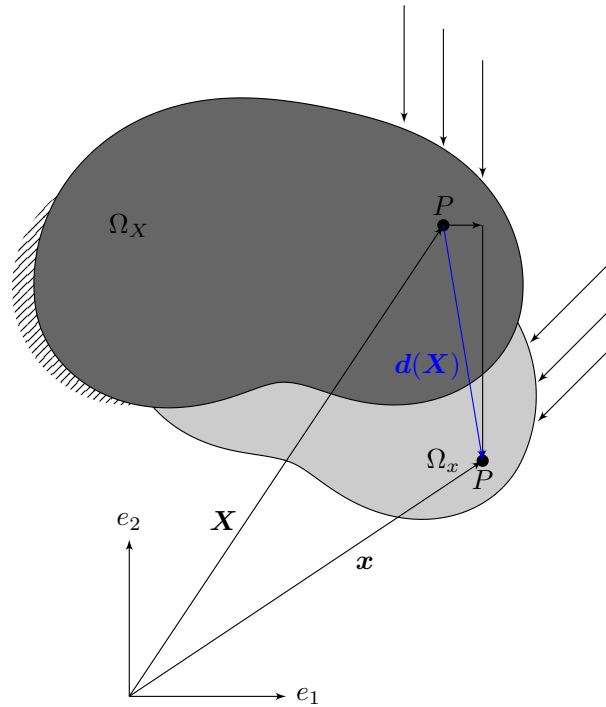


Fig. 12: Solid in material and spatial configuration

Strong form

Large displacements and rotations can occur within the structural domain and these lead to a geometrical non-linear formulation. This structural domain model is also called St. Venant solid and describes a hyper-elastic material. The following equations and descriptions leading to the strong form of the model for St. Venant solids are based on [4, pp. 12–13] with combination of [6]⁸. It is formulated in a total Lagrangian framework, that means that all quantities of the solid domain are given with respect to the material configuration \mathbf{X} .

$$\mathbf{x}(\mathbf{X}) = \mathbf{X} + \mathbf{d}(\mathbf{X}) \quad (3.1)$$

is the equation which describes the map from the undeformed configuration to the deformed configuration. \mathbf{d} is the occurring displacement. The Jacobi matrix of this map is the so-called *deformation gradient*

$$\mathbf{F} = \frac{\partial \mathbf{x}(\mathbf{X})}{\partial \mathbf{X}} = \frac{\partial \mathbf{d}}{\partial \mathbf{X}} + \mathbf{I} = \nabla_{\mathbf{X}} \mathbf{d} + \mathbf{I} \quad (3.2)$$

⁸[6] has not been necessary to work this section out, but Lecture 3 of FEM II has been used as background information.

where \mathbf{I} is the identity tensor.

$$\mathbf{C} = \mathbf{F}^T \cdot \mathbf{F} \quad (3.3)$$

is the right Cauchy-Green deformation tensor. Another important tensor is the Green-Lagrange strain tensor.

$$\begin{aligned} \mathbf{E} &= \frac{1}{2}(\mathbf{C} - \mathbf{I}) = \frac{1}{2}(\mathbf{F}^T \cdot \mathbf{F} - \mathbf{I}) \\ &= \frac{1}{2}(\nabla_{\mathbf{X}} \mathbf{d} + (\nabla_{\mathbf{X}} \mathbf{d})^T + (\nabla_{\mathbf{X}} \mathbf{d})^T (\nabla_{\mathbf{X}} \mathbf{d})) \end{aligned} \quad (3.4)$$

This is a non-linear strain tensor which describes the kinematic relations and does not generate strains considering rigid body motions.

At this stage it is necessary to connect the strains to stresses so some stress tensors are introduced: Cauchy stress tensor

$$\boldsymbol{\sigma} = \begin{bmatrix} \sigma_{xx} & \sigma_{xy} & \sigma_{xz} \\ \sigma_{yx} & \sigma_{yy} & \sigma_{yz} \\ \sigma_{zx} & \sigma_{zy} & \sigma_{zz} \end{bmatrix} \quad (3.5)$$

lives in the deformed configuration and is the only stress tensor with a concrete physical meaning. Multiplying it with the determinant of the deformation gradient gives the Kirchhoff stress tensor

$$\boldsymbol{\tau} = \det(\mathbf{F}) \cdot \boldsymbol{\sigma} \quad (3.6)$$

The first Piola-Kirchhoff stress tensor is defined as

$$\mathbf{P} = \boldsymbol{\tau} \cdot \mathbf{F}^{-T} \quad (3.7)$$

and the second Piola-Kirchhoff stress tensor as

$$\mathbf{S} = \mathbf{F}^{-1} \mathbf{P} = \det(\mathbf{F}) \mathbf{F}^{-1} \cdot \boldsymbol{\sigma} \cdot \mathbf{F}^{-T} \quad (3.8)$$

The constitutive relation is then

$$\mathbf{S} = \lambda(\text{tr} \mathbf{E}) \mathbf{I} + 2\eta \mathbf{E} \quad (3.9)$$

with Lamé constants defined as

$$\lambda = \frac{E\nu}{(1+\nu)(1-2\nu)} \quad (3.10)$$

$$\eta = \frac{E}{2(1+\nu)} \quad (3.11)$$

with Young's modulus or modulus of elasticity E and Poisson's ratio ν .

The strong form of the differential equation describing the structure in the material domain using St. Venant's model is

$$\rho_S \ddot{\mathbf{d}} - \nabla_{\mathbf{X}} \cdot (\mathbf{F} \mathbf{S}) = \mathbf{f} \quad \text{on } \Omega_S \times (0, T) \quad (3.12)$$

ρ_S is the density of the solid, \mathbf{f} is the volume force vector, and Ω_S is the undeformed structural domain.

Weak form

The continuous weak form of Equation (3.12) is then:

Find $\mathbf{d} \in [\mathcal{H}^1(\Omega_S)]^d$ with $\mathbf{d} = \hat{\mathbf{d}}$, such that for all $\mathbf{w} \in [\mathcal{H}^1(\Omega_S)]^d$ with $\mathbf{w}|_{\Gamma_D} = \mathbf{0}$

$$\int_{\Omega_S} \rho_S \mathbf{w} \cdot \ddot{\mathbf{d}} \, d\Omega + \int_{\Omega_S} \nabla_{\mathbf{X}} \mathbf{w} : (\mathbf{F}\mathbf{S}) \, d\Omega = \int_{\Omega_S} \mathbf{w} \cdot \mathbf{f} \, d\Omega + \int_{\Gamma_{S,t}} \mathbf{w} \cdot \hat{\mathbf{t}} \, d\Gamma \quad (3.13)$$

holds.

To approximate the solution of Equation (3.12) using the FEM, the weak form given in Equation (3.13) is necessary. The problem is a spatial problem as well as a time-dependent problem and therefore a spatial discretization and a time discretization of the structural domain of interest are necessary. The spatial discretization is done using the FEM as it is described in section 1.2.

In [4, p. 20] test and trial function spaces are given to approximate the displacements. The test and trial spaces are

$$\mathcal{S}_d^h = \{\mathbf{d}^h | \mathbf{d}^h \in (\mathcal{H}^{1h})^d, \mathbf{d}^h = \hat{\mathbf{d}}^h \text{ on } \Gamma_{S,d}\} \quad (3.14)$$

$$\mathcal{V}_d^h = \{\mathbf{w}^h | \mathbf{w}^h \in (\mathcal{H}^{1h})^d, \mathbf{w}^h = \mathbf{0} \text{ on } \Gamma_{S,d}\}, \quad (3.15)$$

which are constructed from the mapped element functions. For the finite dimensional space can be stated that

$$\mathcal{H}^{1h} \subseteq \mathcal{H}^1. \quad (3.16)$$

Considering these spaces, Equation (3.13) can be formulated in a Bubnov-Galerkin setting:

Find $\mathbf{d}^h \in \mathcal{S}_d^h$, such that

$$\int_{\Omega_S} \rho_S \mathbf{w}^h \cdot \ddot{\mathbf{d}}^h \, d\Omega + \int_{\Omega_S} \nabla_{\mathbf{X}} \mathbf{w}^h : (\mathbf{F}\mathbf{S}) \, d\Omega = \int_{\Omega_S} \mathbf{w}^h \cdot \mathbf{f}^h \, d\Omega + \int_{\Gamma_{S,t}} \mathbf{w}^h \cdot \hat{\mathbf{t}}^h \, d\Gamma \quad \forall \mathbf{w}^h \in \mathcal{V}_d^h \quad (3.17)$$

$\hat{\mathbf{t}}^h$ is the traction along the Neumann boundary Γ_N [4, p. 20].

The time discretization is done using *Newmark's method*. Another possible approach for time discretization is to use *HHT- α -method*. In this thesis only Newmark's method is used.

Information about time discretization using Newmark's method can be found in many books, dissertations and articles, e.g. Wall [25], Chopra [2], and Hughes [9].

The following description of Newmark's method is based on [9, pp. 490 – 504].

The equation of motion in structural dynamics is a semi-discrete system of equations of the form

$$\mathbf{M}\ddot{\mathbf{d}} + \mathbf{C}\dot{\mathbf{d}} + \mathbf{K}\mathbf{d} = \mathbf{f}(t) \quad (3.18)$$

where \mathbf{M} is the mass matrix, \mathbf{C} is the viscous damping matrix, \mathbf{K} is the stiffness matrix [9, p. 490], and \mathbf{f} is the time-dependent force vector. \mathbf{d} is the displacement vector, its first derivative is the velocity vector, and its second derivative the acceleration vector. For Equation (3.17) the considered equation of motion is [4, p. 20]

$$\mathbf{M}\ddot{\mathbf{d}}_{n+1}^h + \mathbf{C}\dot{\mathbf{d}}_{n+1}^h + \mathbf{K}(\mathbf{d}_{n+1}^h) = \mathbf{f}(t_{n+1}) \quad (3.19)$$

It is to mention that the stiffness matrix \mathbf{K} is non-linear for St. Venant solids and the damping matrix \mathbf{C} equals zero.

Newmark's method uses the following two equations [4, p. 21] and [9, pp. 490–491] together with Equation (3.19)

$$\mathbf{d}_{n+1}^h = \mathbf{d}_n^h + \Delta t \dot{\mathbf{d}}_n^h + \frac{\Delta t^2}{2} \left[(1 - 2\beta) \ddot{\mathbf{d}}_n^h + 2\beta \ddot{\mathbf{d}}_{n+1}^h \right] \quad (3.20)$$

$$\dot{\mathbf{d}}_{n+1}^h = \dot{\mathbf{d}}_n^h + \Delta t \left[(1 - \gamma) \ddot{\mathbf{d}}_n^h + \gamma \ddot{\mathbf{d}}_{n+1}^h \right] \quad (3.21)$$

The Newmark parameters β and γ are responsible for the stability and accuracy characteristics of the method. In this thesis the average acceleration scheme (implicit method or trapezoidal rule) is used. The order of accuracy is 2 and the constants are defined therefore as

$$\beta = \frac{1}{4}$$

$$\gamma = \frac{1}{2}$$

To achieve second order accuracy γ must be $\frac{1}{2}$ [9, p. 493]. For linear cases Newmark's method using these constants is unconditionally stable. For St. Venant solids described by a non-linear geometric model the energy conservation and stability properties are different compared to linear cases [4, p. 21].

In EduFEM [5] the non-linear structural domain in each time step is solved using a Newton-Raphson iteration (see section 1.1) while integrating in time is done using Newmark's method.

For the bridge test case the structure is defined as a rigid body. It is solved in EduFEM using three decoupled ODEs for horizontal and vertical displacements, and rotations. Therefore no Newton-Raphson iteration is necessary but Newmark's method is applied as well. The governing equations for the rigid body model in strong form are described in section 3.1.

3.1 Rigid body motion

The structure in the bridge test case of section 6 is modelled as a rigid body. A rigid body is a structural body in which no deformations occur and distances between two points remain constant during the entire time of analysis. In a two dimensional model three degrees of freedom - two translations and one rotation - have to be considered. Here one translation is neglected because it is blocked in the bridge case in this thesis. This section is based on [8, pp. 12–13]. In Figure 13 the rigid body considered in this model is shown. It is a modified drawing of the figure given in [8, p. 12]

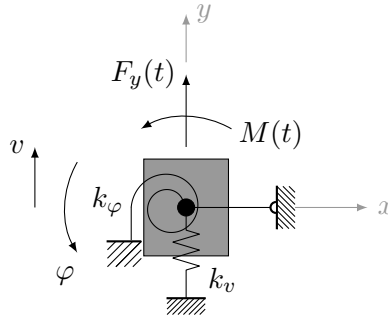


Fig. 13: Rigid body with elastic support

The vertical displacement v and the rotation φ are the components of vector \mathbf{u} . $w = \dot{v}$ is the vertical velocity of the rigid body and $\omega = \dot{\varphi}$ is the angular velocity. These are the components of the velocity vector \mathbf{w} . The mass matrix \mathbf{M} has on its main diagonal the mass m and the moment of inertia θ and the stiffness matrix has on its main diagonal the spring stiffnesses k_v and k_φ . These vectors and matrices are written as

$$\mathbf{u}(t) = \begin{bmatrix} v \\ \varphi \end{bmatrix} \quad \mathbf{w}(t) = \begin{bmatrix} w \\ \omega \end{bmatrix} \quad \mathbf{M} = \begin{bmatrix} m & 0 \\ 0 & \theta \end{bmatrix} \quad \mathbf{K} = \begin{bmatrix} k_v & 0 \\ 0 & k_\varphi \end{bmatrix}$$

The load vector and the vector of spring forces are

$$\mathbf{p}(t) = \begin{bmatrix} F_y(t) \\ M(t) \end{bmatrix} \quad \mathbf{s}(t) = \begin{bmatrix} F_s(t) \\ M_s(t) \end{bmatrix}$$

These matrices and vectors are used for a system of first order differential equations. The first one is the equation for momentum and rotational momentum given as

$$\mathbf{M}\dot{\mathbf{w}}(t) + \mathbf{s}(t) - \mathbf{p}(t) = \mathbf{0} \quad (3.22)$$

The second one is Hooke's law to describe linear spring forces and moments. It is given as

$$\mathbf{K}^{-1}\dot{\mathbf{s}}(t) - \mathbf{w}(t) = \mathbf{0} \quad (3.23)$$

To solve Equations (3.22) and (3.23) initial conditions of the form

$$\mathbf{u}(t = 0) = \mathbf{K}^{-1}\dot{\mathbf{s}}(t = 0) = \mathbf{u}_{init} \quad (3.24)$$

$$\mathbf{w}(t = 0) = \mathbf{w}_{init} \quad (3.25)$$

are necessary. Time discretization is done using Newmark's method. The mass, moment of inertia, and the spring characteristics are constant over time and therefore \mathbf{M} and \mathbf{K} are not time dependent. Two decoupled ODEs have to be solved to get the solutions for the vertical translation and the rotation.

4 Fluid-structure interaction

The topic of this chapter is how the fluid and solid interact in *fluid-structure interaction (FSI)*. The described approaches in chapter 2 for the fluid domain and chapter 3 for the solid domain can be used independently to approximate the solution of a fluid or solid problem respectively. So far these two fields have not been coupled. At first a theoretical background on generic coupling strategies is given and then it is shown how the FSI-scheme looks like using an example.

As mentioned before in chapter 1 there are several possibilities to couple two physical fields in case of FSI. Here the two fields are coupled with a partitioned coupling and a third auxiliary field is introduced which considers the movement of the fluid domain by updating the fluid mesh. This moving mesh approach is described later in 4.1.

FSI problems can be tackled using either monolithic or partitioned algorithms. In a monolithic procedure fluid and solid are treated as a unified system while in a partitioned approach both fields are treated as separate systems and coupling is done via dynamic and kinematic conditions at the interface of both systems [26, p. 440].

Using a partitioned algorithm it is possible to use independent solvers for the fluid and structural domain respectively. It is easier to change solvers individually. In practice it is possible that the spatial discretization as well as the entire modelling is done independently. The system which is to solve is usually smaller and that could have positive effects on the effort needed to solve the overall problem [25, pp. 169–170]. A disadvantage of the partitioned approach is that it is only conditionally stable, even when the solution procedures for the individual fields are unconditionally stable [25, p. 170].

It is possible to distinguish between a weakly and a strongly partitioned approach [26, p. 424]. The weakly or loosely coupled approach is more susceptible to instabilities, especially when the fluid and solid density are similar [26, p. 440]. Each single field is solved and the solution is given to the next field which goes further in time using this information. This means that coupling conditions do not have to be exactly fulfilled at each time step. This is also called one-way staggered [25, p. 170].

The interface conditions are better satisfied using a strong coupled method [26, p. 440]. The coupling conditions converge at the end of each time step because an iteration over all fields is done for each time step. This may also be called iteratively staggered. [25, p. 170]. The strongly coupled partitioned approach is used in this thesis. Figure 14 shows a flow chart diagram of the scheme applied to FSI as used in this work (compare with Figure 13.7 in [26, p. 441]).

The FSI or coupling loop contains the fluid domain solver, the solid or structural domain solver, and a computational mesh dynamics (CMD) routine. The latter is described in more detail in 4.1.

The coupling of the individually solved fields is done using a so-called Neumann-to-Dirichlet principle [4, p. 23] where the coupling is done at the level of BCs. Figure 14 shows a flowchart of the used algorithm. The first field for which the solution is approximated is the fluid field. This gives a traction $\boldsymbol{\sigma} \cdot \mathbf{n}$ along the fluid-structure interface Γ_c where c stands for *coupled* fluid-structure interface. The traction determined with the fluid solver is used as Neumann boundary condition in the structural solver. The solid solver approximates the displacements \mathbf{d} of the structure along Γ_c and these are used as Dirichlet boundary condition for the CMD. The moved mesh and the deformed structure must match each other along the interface in each time step, so the deformation of the structure must be

considered carefully. In the solid domain solver the initial structural mesh is used for each approximation during the entire calculation according to the standard Lagrangian viewpoint for the solid part. [4, p. 24]. For the convergence criteria of the partitioned coupling loop (in short notation: FSI-loop) the fluid solution with velocities u , v , and pressure p , and the structural displacements d are considered. uvp stands for the vector of the FEM approximation of the fluid domain whose components are u , v , and p .

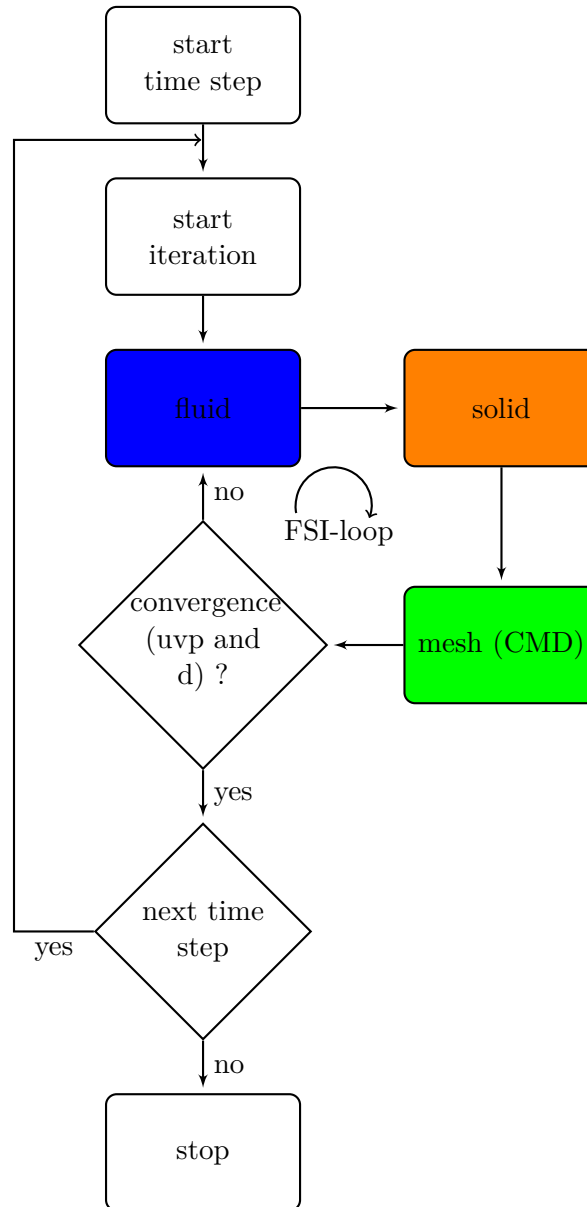


Fig. 14: Flow-diagram of FSI algorithm

Figure 14 visualizes the algorithm of the FSI partitioned coupling loop for one time step t_n with $n \in [0, N]$. Therefore the index of this loop is c . The pseudocode for this algorithm for time step t_{n+1} is:

Algorithm 2: FSI partitioned coupling loop for time step $n + 1$

Input: From time step t_n : The fluid mesh Ω_n^{fluid} with velocity \mathbf{u}_n and pressure p_n , the time independent structural domain mesh Ω_0^{solid} and time-dependent solid displacements \mathbf{d}_n .

initialization

```

while  $max(uvp_{conCrit}^c, d_{conCrit}^c) > MaxRes_c$  do
  solve fluid field - CFD to get  $\mathbf{u}_{n+1}$  and  $p_{n+1}$  using  $\Omega_{n+1}^{fluid}$ ,  $\Omega_n^{fluid}$ ,  $\mathbf{u}_n$ , and  $p_n$ 
  determine fluid forces  $\mathbf{f}_{n+1}$ 
  solve solid field - CSD using  $\Omega_0^{solid}$  and  $\mathbf{f}_{n+1}$  as BC to get  $\mathbf{d}_{n+1}$ 
  get new fluid mesh - CMD  $\Omega_{n+1}^{fluid}$  matching solid displacements  $\mathbf{d}_{n+1}$ 
end

```

Output: obtain Ω_{n+1}^{fluid} , \mathbf{u}_{n+1} , p_{n+1} , and \mathbf{d}_{n+1}

Next time step if t_{end} has not been reached.

$MaxRes_c$ is the tolerance boundary for the partitioned coupling loop, $uvp_{conCrit}^c$ and $d_{conCrit}^c$ are the test quantities (interface norms) as defined in Equations (4.7) and (4.8) respectively. In this work it is called $\varepsilon_c = \varepsilon_{FSI} = 10^{-i}$ with $i \in [1, 2, \dots, 6]$. More about this topic is described in the following chapters presenting the results of the test cases.

CFD stands for Computational Fluid Dynamics, CSD stands for Computational Solid Dynamics, CMD stands for Computational Mesh Dynamics, and Ω_{TS}^d is the spatial domain of field d at time step TS .

4.1 Computational mesh dynamics

The deformations of the structure changes the position of the fluid-structure interface in each time step and this interface must match the fluid mesh. The fluid-structure interface at the current time step must match the initial structural mesh plus the current structural deformation. Therefore the fluid mesh has to be modified to match the structural deformations correctly. This is achieved using a mesh deformation algorithm [4, p. 24]. This is also called computational mesh dynamics (CMD). The CMD solver determines the mesh position of the ALE domain over the entire simulation [25, p. 159].

There are discontinuous and continuous approaches used for mesh deformation [25, pp. 160–161]. In this work mesh deformation is implemented using a continuous approach considering a pseudo-structure. The pseudo structure is a stationary Hooke solid (linear elastic) and to determine the sought mesh deformation a system of equations has to be solved. This is a sub-problem in the fluid domain. The displacements \mathbf{d} of the structure along Γ_c are the prescribed Dirichlet BCs. For all other parts of the boundary the Dirichlet BCs are zero. [4, p. 24].

The pseudo-structure is an auxiliary field which is described by the following model [22, pp. 60–68] of a stationary Hooke solid.

As usual in structural mechanics the model consists of an equilibrium equation, kinematic relation

and constitutive or material relation which are formulated as:

kinematics:

$$\varepsilon(\mathbf{x}) = \frac{1}{2}[\nabla \mathbf{d} + (\nabla \mathbf{d})^T] \quad (4.1)$$

equilibrium:

$$\nabla \cdot \boldsymbol{\sigma}(\mathbf{x}) = 0 \quad (4.2)$$

material model or constitutive relation:

$$\boldsymbol{\sigma}(\mathbf{x}) = \lambda \text{tr}(\varepsilon) \mathbf{I} + 2\eta \varepsilon \quad (4.3)$$

With Lamé constants λ and η given in Equation (3.10) and Equation (3.11) respectively. Equation (4.2) is already the strong form of this sub-problem.

The weak form follows for Equation (4.2) analogously as Equation (3.13) as weak form for Equation 3.12) [4, p. 14]. The discretized weak form is analogously to Equation (3.17) with $\boldsymbol{\sigma}$ instead of $(\mathbf{F}\mathbf{S})$ [4, p. 20]. The element stiffness in the FE mesh for this pseudo-structure depends on the element size. Near the fluid-structure interface the fluid mesh is usually finer and built up with smaller elements around Γ_c . A higher stiffness of these elements is a strategy to avoid that invalid elements occur when the mesh deforms.

After a new mesh position has been determined using CMD the mesh velocity \mathbf{u}_M can be calculated as

$$\mathbf{u}_M = \frac{\mathbf{x}_{i+1} - \mathbf{x}_n}{\Delta t} \quad (4.4)$$

where the node positions in Ω_F of the previous time step are \mathbf{x}_n and these of the current iteration step in the FSI-loop are \mathbf{x}_{i+1} . At the end of the FSI-loop when the stopping criteria is fulfilled $\mathbf{x}_{n+1} = \mathbf{x}_{i+1}$ [4, p. 24]. The Dirichlet BCs for the flow velocities along Γ_c have to be modified so that the mesh velocity is considered. This modified Dirichlet BCs, the new node positions, and the node velocities are considered in the fluid solver as boundary data for the next fluid iteration [4, p. 24].

For $\mathbf{u} \cdot \nabla \mathbf{u}$ follows with \mathbf{u}_M

$$(\mathbf{u} - \mathbf{u}_M) \cdot \nabla \mathbf{u} \quad (4.5)$$

what is to consider in the fluid solver routine. Equation (4.5) changes the Navier-Stokes equations derived in section 2.2. As described in section 1.3 in the arbitrary Lagrangian-Eulerian approach the observer moves exactly with the mesh. The deformations of the mesh are small with respect to the mesh of the previous iteration and so many terms of the mapping can be neglected and Equation (4.5) follows.

Another approach for the mesh movement is to use Laplace's equation. Therefore the Laplace equation may be solved for each component of \mathbf{d} [4, p. 24]. The Laplace-operator is used as a smoothing or diffusion operator to get a smooth mesh movement. Throughout this work the pseudo-structure approach is used.

It may happen that the mesh deformation leads to invalid elements which is not allowed because the FEM procedure breaks down and the problem can not be solved any more. A negative Jacobian, i.e. a negative determinant of the Jacobi matrix of the finite element mapping is a result of an invalid element in a mesh.

4.2 Vertical flap - FSI algorithm explained on an example

The algorithm used to determine the solution for an FSI problem used in this work should be explained using an example in a more practical and intuitive way than above. This example was used during implementation and first tests of this algorithm. Therefore some pre-studies have been made, especially to check the mesh moving procedure used in the partitioned FSI coupling loop. Figure 15 shows the geometry of this example. The structural domain Ω_S is a vertical flap which is rounded on its top in shape of a half circle, the fluid domain Ω_F is a channel flow with a prescribed parabolic inflow on the right side of the domain of interest with a velocity of zero at the walls that is

$$\mathbf{u}(\mathbf{x}, t) = \mathbf{0} \quad \forall \mathbf{x} \in \Gamma_{D,Wall}, \quad t \in [0, T] \quad (4.6)$$

The fluid-structure interface Γ_c is shown purple in Figure 15.

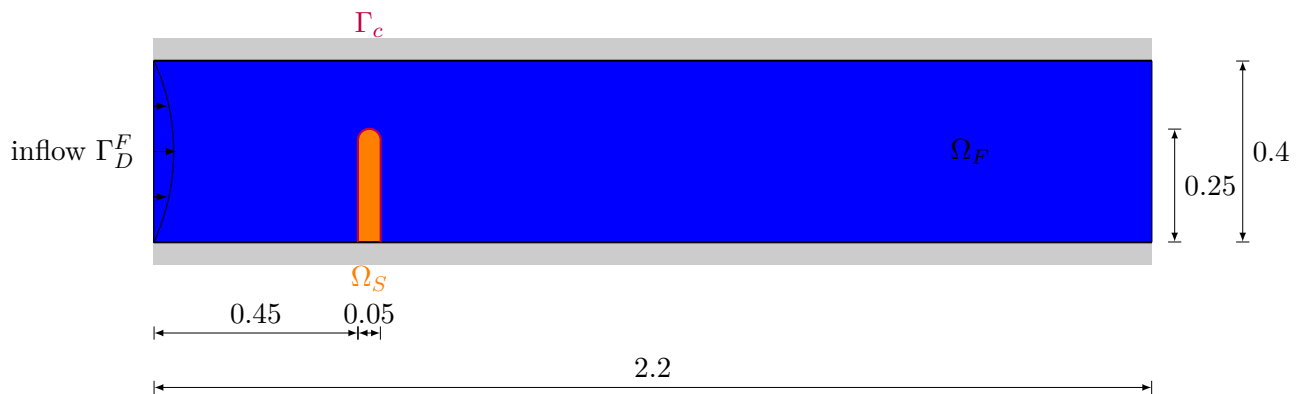


Fig. 15: Example case for explanation of FSI algorithm - Geometry and domain definition

Although, the geometry and results shown for this example depend of course on its configuration the main statements are generally valid and therefore also important for the following test cases for which detailed studies have been made. This test configuration is not considered in these further studies because the other two cases are bench-mark test cases with known results to compare the correctness of the implementation.

The mesh used in the following explanation is too rough and must be finer to get acceptable results but for more overseeable plots of the used mesh the element size has been chosen large here.

Pre-processing

Here the discretization of the three fields and the parameter input is done. Throughout this work quadrilateral elements are used. For the fluid domain three meshes are generated which are spatially identical for the initial case but the mesh to obtain the pressure field in the fluid domain has elements one order lower than the mesh used to obtain the velocity field. This is necessary because the results would be unsatisfactory if the element order for both fields would be the same without stabilization. In this work the velocity mesh has quadratic quadrilateral elements with element functions shown in Figure 4 and the pressure mesh has linear quadrilateral elements then ($Q2/Q1$ Taylor-Hood-elements, see section 2.3). It would be possible to use linear elements for the velocity mesh and constant ones for the pressure ($Q1/Q0$) but therefore a stabilization is necessary. For the structural domain, the

discretization is done using the same element order as for the fluids velocity mesh. Both meshes for fluid velocity and structure are generated together and split in a further step. Figure 16 shows the discretization of the fluid domain. The blue crosses and circles indicates that Dirichlet BCs are pre-described on these nodes.

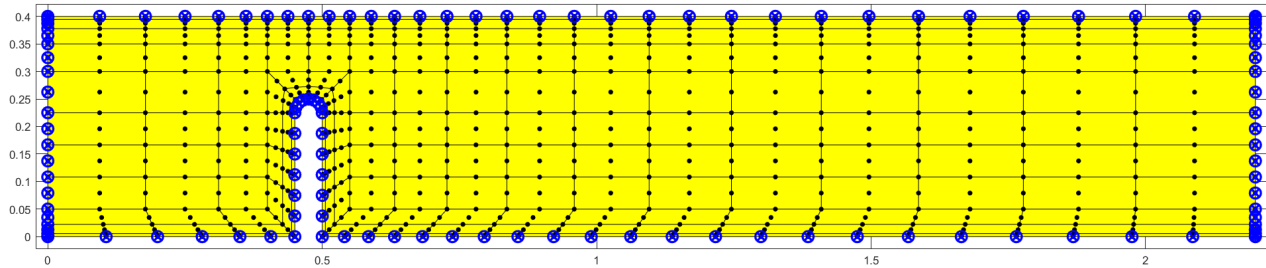


Fig. 16: FE-mesh for fluid domain

There are nine nodes per element (quadratic quadrilateral element as described in 1.2) and the elements size is smaller near the lower and upper wall and around the flap as shown in Figure 17.

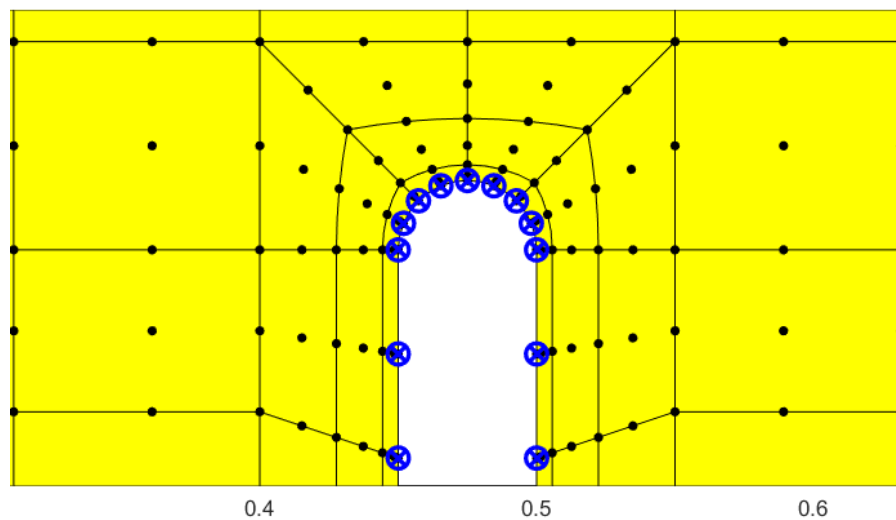


Fig. 17: Detailed FE-mesh for fluid domain around flap

Further all relevant physical and numerical parameters have to be defined in this pre-processing part. Three fields, the fluid domain, the structural domain, and the pseudo-structural domain for CMD, require definition here.

General definitions:

- start time (is 0 for all cases in this work)
- end time or number of time steps considered for entire analysis

For the fluid domain:

- the fluid density ρ_F
- the dynamic viscosity μ

For the solid domain:

- Young's modulus of elasticity E
- Poisson's ratio ν
- Lamé's constants η and λ

For numerical analysis:

- time step size for numerical analysis
- parameter to define if midpoint rule or trapezoidal rule should be used
- time for ramping
- θ and θ_{cont} for θ -method for time discretization, where θ_{cont} is used for continuity and pressure in the fluid domain and applied on the constraint matrix given in Equation (2.46).

Processing

The approximation for the sought solution of the real FSI problem is determined here. In other words the FSI model is numerically solved using the FEM. Therefore discretization of the physical domains for fluid and solid and the pseudo-structural field for the mesh movement have been done in the pre-processing step.

As stated in section 2.3 for the initial condition $\mathbf{u}(\mathbf{x}, t = 0) = \mathbf{u}_0$ the requirement $\nabla \cdot \mathbf{u}_0 = 0$ must be fulfilled. This is clearly a contradiction to the prescribed parabolic inflow shown in Figure 15. Therefore a so-called ramping is used. The higher the order of the polynomial ramping function, being a smoothed step-function, the better is the approximated FEM solution. Figure 18 shows ramping functions of first, third, and fifth order.

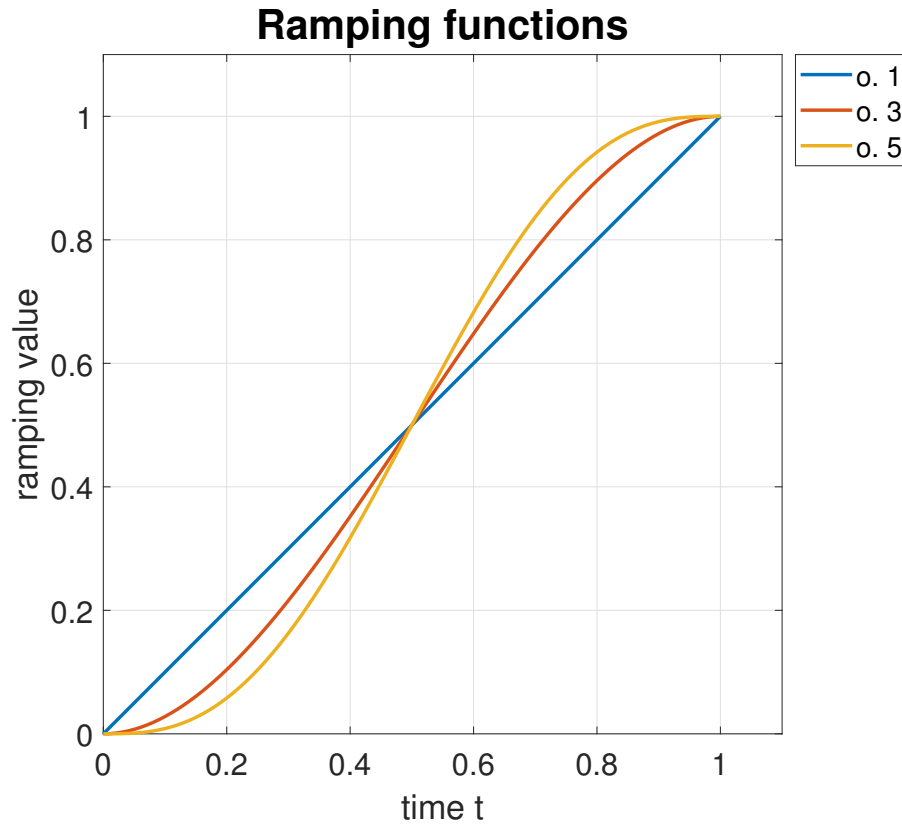


Fig. 18: Ramping functions

The order of a ramping function indicates a certain continuity as shown in table 1.

Order of ramping function	Continuity
1	C_0 -continuous
3	C_1 -continuous
5	C_2 -continuous
7	C_3 -continuous

Tab. 1: Order of ramping function and depending continuity

Ramping functions with order higher than 1 have a horizontal tangent at their beginning and ending time, which is 1 second here, leading to a smooth transition.

Another approach without a ramping function would be to evaluate the stationary solution for the FSI problem using a stationary fluid solver and a stationary solid solver respectively and use this stationary solution as the initial case for the time loop of the instationary FSI solver.

Within each time step the partitioned coupled fluid-structure iteration loop (FSI loop in Figure 14) is used. The initial values for the new iteration in time step $n + 1$ are the results of the previous time step n . For the entire FSI loop a maximum tolerance criteria $\varepsilon_{FSI} = \varepsilon_c = 10^{-i}$ is pre-described. The criteria are

$$uwp_{conCrit}^c = \frac{\|\mathbf{uwp}_{i+1}^c\| - \|\mathbf{uwp}_i^c\|}{\|\mathbf{uwp}_i^c\|} < \varepsilon_c \quad (4.7)$$

and

$$d_{conCrit}^c = \frac{\|\mathbf{d}_{i+1}^c\| - \|\mathbf{d}_i^c\|}{\|\mathbf{d}_i^c\|} < \varepsilon_c \quad (4.8)$$

where \mathbf{uwp} is the vector of the velocity components and the pressure in the FEM, and $i + 1$ is the actual iteration step and i the previous one. For the first iteration step the i stands for the start values which are the results of the last time step n . Additionally a maximum number of iteration steps is given. If this quantity should be reached the loop breaks and gives an error message that convergence was not achieved within the coupled loop. The Euclidean norm or L_2 -norm is defined as $\|\mathbf{x}\| = \|\mathbf{x}\|_2 = \sqrt{\sum_{k=1}^M |x_k|^2}$ where \mathbf{x} is a vector with M entries.

The first field solved in an independent solver is the fluid. The fluid solver solves the instationary and incompressible fluid flow using the Navier-Stokes equation described in 2 and solves the system of equations given in Equation (2.47). Within this solver are again a tolerance criteria ε_F and a maximum number of iteration steps defined. It is not necessary that these are the same as used for the partitioned FSI-loop as stated above. The convergence criterion is mathematically expressed as

$$uwp_{conCrit}^F = \frac{\|\mathbf{uwp}_{i+1}^F\| - \|\mathbf{uwp}_i^F\|}{\|\mathbf{uwp}_i^F\|} < \varepsilon_F \quad (4.9)$$

The fluid iteration scheme is a Picard iteration loop as described in 1. The mesh deformation is considered within this procedure as the Dirichlet BCs for the fluid are modified with the mesh velocities. The result of the fluid solver is the vector \mathbf{uwp} containing the velocity components u and v and the pressure p , and fluid forces on the Neumann boundary which act on the structure.

These forces are applied with negative sign (*actio et reactio*) as Neumann BCs in the solid solver. The solid solver approximates the result of the St. Venant solid as described in 3. Within the solid solver the reference mesh is the initial (undeformed) solid mesh. The non-linear structure is solved using a Newton-Raphson iteration described in 1.1. The convergence criterion is defined as

$$d_{conCrit}^S = \frac{\|\mathbf{d}_{i+1}^S\| - \|\mathbf{d}_i^S\|}{\|\mathbf{d}_i^S\|} < \varepsilon_S \quad (4.10)$$

The results of the solid solver are the approximated displacements \mathbf{d} , velocities \mathbf{v} , and accelerations \mathbf{a} of the structure and the forces on the fluid-structure interface. The displacements of the fluid-structure interface are part of \mathbf{d} and the initial quantity for the mesh movement described in 4.1.

The mesh movement is the third field considered in the coupling loop and solved with the CMD solver. It is an auxiliary structural field described by the model of a Hooke solid. It is used to determine new nodal positions inside the fluid domain and does not have any further physical meaning. The two previous solvers could be used independently to approximate solutions for dynamic fluid or solid problems. The mesh deformation is necessary for the FSI-coupling loop and therefore some pre-studies have been made to check the CMD algorithm and its ability to achieve valid and useful deformed meshes. As described in 4.1 it must be ensured that an element within the mesh remains valid. An example of an invalid linear quadratic element is shown in Figure 19. After the deformation of the element, node B (originally at B_0) is located on the left side of \overline{AC} and so inside the triangular area spanned by \overline{ACD} , which is invalid.

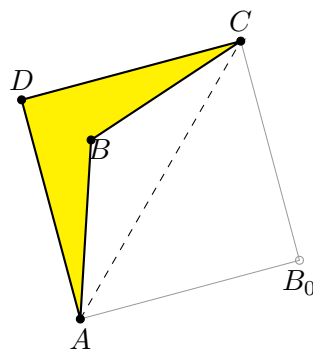


Fig. 19: Invalid linear quadrilateral element

In these pre-studies it was obvious to see that a rectangular flap with a horizontal line on its upper end instead of the half circle as used here easily leads to an invalid mesh in the area around the upper corner points. Figure 20 shows an example of an invalid mesh. The load applied to get this mesh is too high for a plausible FSI-problem and the mesh is still too rough but the purpose is to show how an invalid mesh may look like.

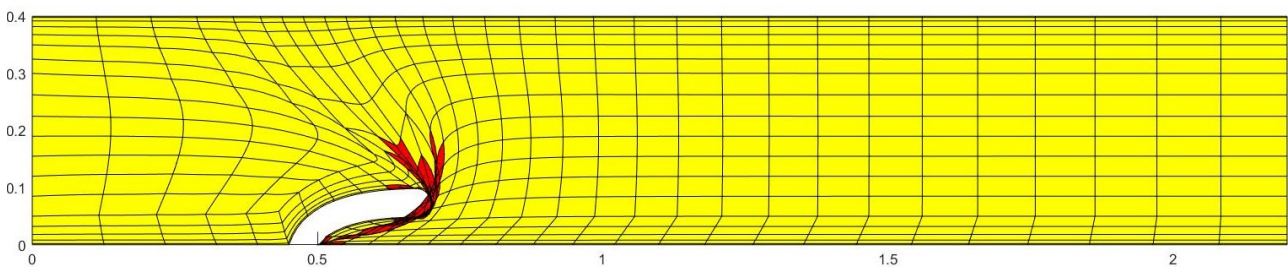


Fig. 20: Invalid fluid mesh

As described in 4.1 the mesh deformation is calculated using a linear elastic pseudo-structural approach. Therefore the stiffness of the elements has to be known and considered. In the CMD-algorithm used in this work the stiffness of the elements depends on the area of the element, the smaller an element is, the higher is its stiffness k_e . Furthermore, it has proven useful in some cases to also consider the distance of the element from the boundary of the domain or selected corner points (where the stiffness is largely increased). Figure 21 shows the stiffness distribution for this flap example. The elements around the top of the flap have the highest stiffness and the farther away an element is from the flap and the lower and upper wall, the smaller is its stiffness. Figure 21 demonstrates that the value of the elements stiffness k_e depends on the element size.

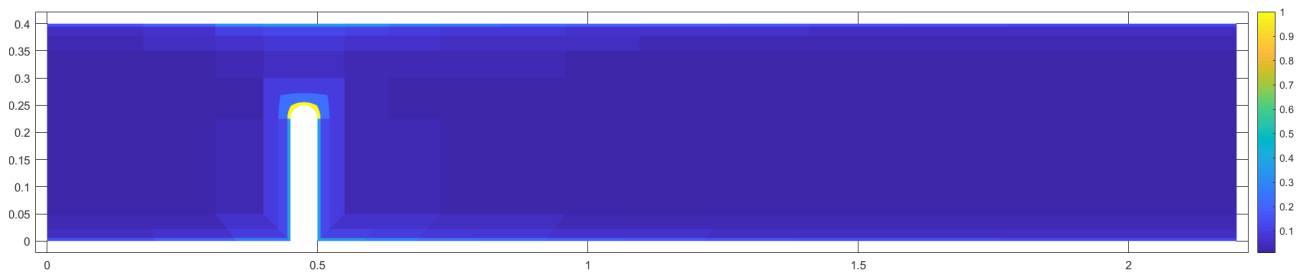


Fig. 21: Stiffness distribution in pseudo-solid field

It is also described in 4.1 that the mesh discretizing the structural domain must fit the mesh discretizing the fluid domain along the fluid-structure interface Γ_c . This is shown in Figure 22 depicting the deformed fluid and structure mesh during an instationary FSI iteration using the described algorithm shown in Figure 14.

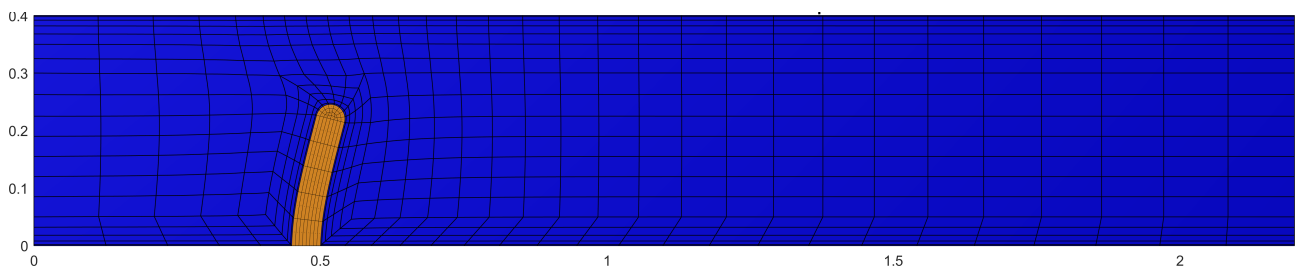


Fig. 22: Deformed fluid and structural domain during an FSI-iteration

Post-processing

Here plots of the results and further studies using the obtained results are made. The fields of the fluid quantities velocity, vorticity, and pressure can be plotted in field colour plots and movies can be generated showing the development of these fields and the deformation of the structure over time. Time measurements and counted numbers of iteration steps for different time steps and the entire calculation can be used for further interpretation. This is done for the next two test cases and shown detailed in the following chapters.

Figure 23 shows the vorticity, velocity, and pressure field respectively of the FSI flap test case at 1.84 seconds on the deformed fluid mesh.

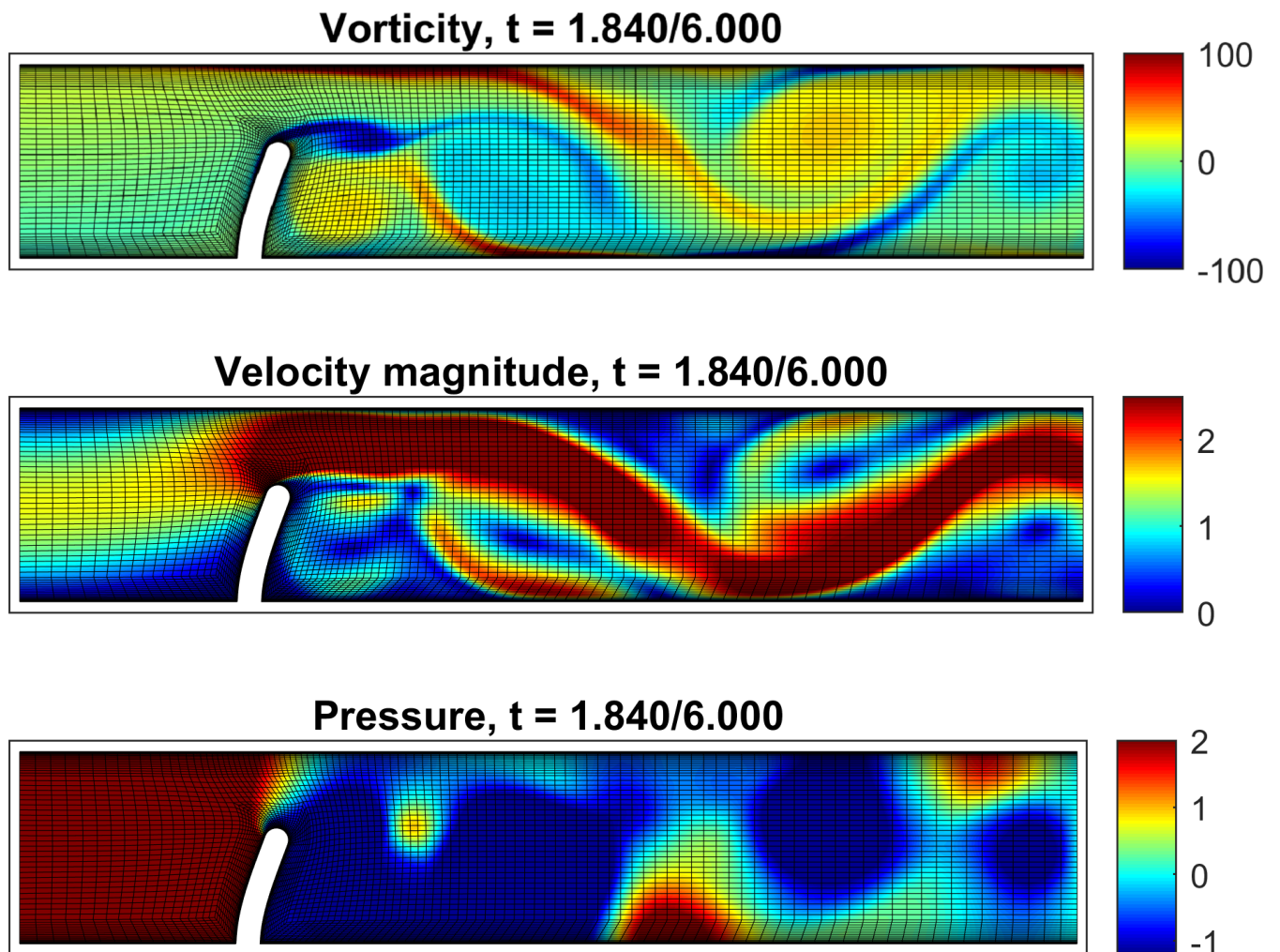


Fig. 23: Vorticity, velocity, and pressure fields respectively of flap test case - at 1.84 seconds.

To check the FSI algorithm and generate these three figures more elements are used to get more accurate results.

This test case is not considered in the following because the deformation is rather small and there are no published benchmark solutions available.

5 Plate structure in FSI

This plate case is based on the detailed description in [24, p. 101] by Walhorn it elaborating the initial test case design of Wall [25, p. 194].

Figure 24 shows the geometrical configuration of this two dimensional plate test case. *pme* (plate middle edge) is a reference point in the middle of the right edge of the plate used later to show results of the FE-calculation.

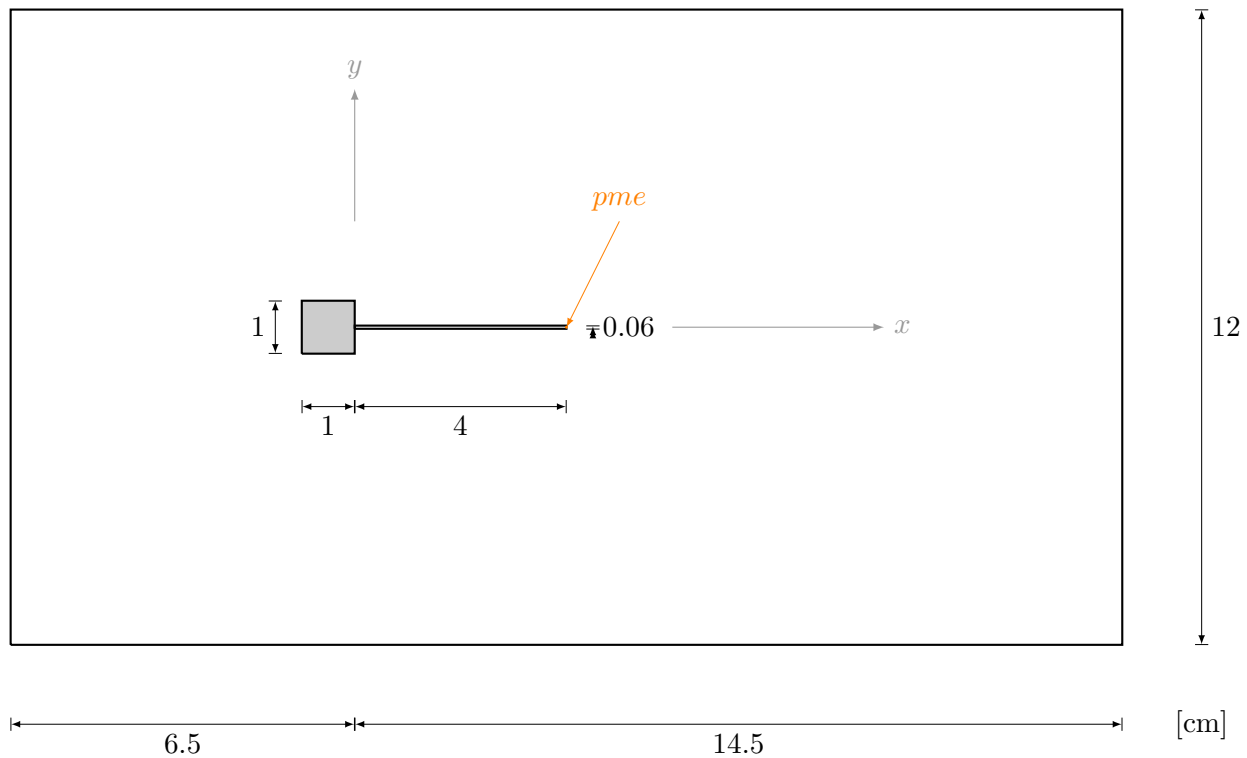


Fig. 24: Geometrical configuration of plate test case

The plate is an elastic plate which oscillates as a result of the fluid-structure interaction. The oscillation of this plate is induced by vortices which are a result of the flow around the quadratic rigid body support of the plate shown grey in Figure 24 which is fixed and not able to move [24, p. 101].

The deformations of the plate are expected to be large so that a St. Venants material model as described in chapter 3 is used to model the plate in this test case. The fluid is modelled by an incompressible instationary fluid as described in chapter 2.

Figure 25 shows the physical configuration of this test case. The prescribed inflow is constantly distributed over the height of the two-dimensional fluid domain from the left side and also constant over time. On the top and bottom domain boundaries, zero vertical velocity components are enforced, whereas on the outflow on the right side, zero-traction BCs are prescribed.

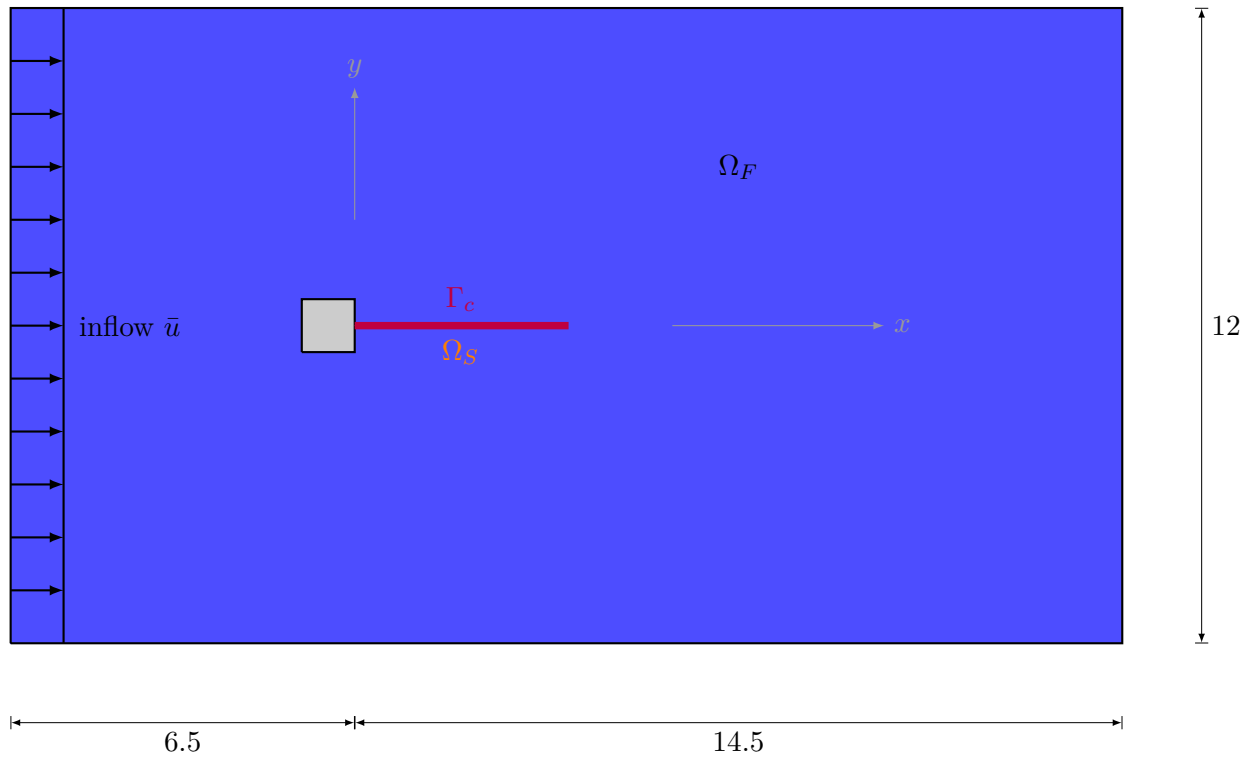


Fig. 25: FSI configuration of plate test case

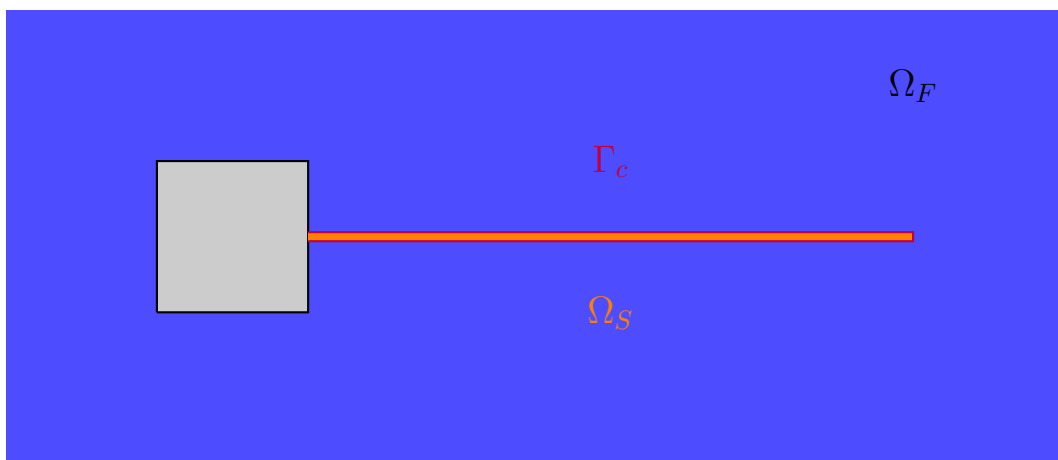


Fig. 26: Detail of the configuration of plate test case

Figure 26 is a zoomed in view of Figure 25, because the plate is very thin and so the solid domain Ω_S is seen in more detail.

The prescribed inflow velocity is $\bar{u} = 31.5$ m/s in this case. This leads to a Reynolds number of $Re = 204$.

The parameters used for the following studies for this case are given below.

General parameters: The considered time is five seconds and the time step size ts is 0.005, so 1000 time steps are used for the analysis. The tolerance of the partitioned coupled FSI loop is $\varepsilon_c = 1 \cdot 10^{-6}$, if not noted otherwise clearly within the text.

The fluid parameters are listed below and given as:

- Fluid density $\rho_F = 1.18 \cdot 10^{-3} \text{ g/cm}^3$.
- Fluid dynamic viscosity $\mu = 1.82 \cdot 10^{-4} \text{ g/cm/s}$.
- θ and θ_{cont} for the numerical analysis of the fluid domain are 0.5.
- The ramping time for the fluid due to the inflow conditions is done for 2 seconds.
- The tolerance boundary for the fluid is $\varepsilon_F = 1 \cdot 10^{-2}$ if not noted otherwise clearly within the text.

For the plate two different cases are implemented. The following studies are done with plate 2 and therefore the parameters are listed below and given as:

- Solid density $\rho_S = 2.0 \text{ g/cm}^3$.
- Solid Young's modulus of elasticity $2.0 \cdot 10^6 \text{ g/cm/s}^2$.
- Poisson's ratio $\nu = 0.35$ [-].
- Lamé's parameter λ is used for plane stress for a thin plate here, given as

$$\lambda = \frac{E \cdot \nu}{(1 - \nu^2)} \quad (5.1)$$

- Time discretization is done using Newmark's method.
- The tolerance for the solid is $\varepsilon_S = 1 \cdot 10^{-12}$ throughout this work. The reason is that the fluid and coupling tolerances and their influence on results should be investigated. The solid solver is fast and a low tolerance number⁹ which leads to better results is not expensive in relation to the number of iteration steps and calculation time. Therefore, a low ε_S is accepted here.

The physical parameters are the same as used and given in [24, p. 102].

The spatial discretization is done in the same way for all of the further shown studies. Within the program code the spatial discretization is defined. At first a mesh containing several so-called super blocks is generated for the entire spatial domain. In a further step the fluid mesh and the solid mesh are divided. For the fluid domain two meshes are generated because the element order for the mesh used to obtain the fluid pressure is one order lower than the mesh used for all other calculations in the fluid domain as described above. For this test case, as not clearly stated otherwise, the order of the

⁹Tolerances ε are positive numbers smaller than one, so the lower it is, the better. This might sound confusing sometimes.

pressure mesh is linear. For the entire spatial discretization quadrilateral elements are used. Figure 27 shows the concrete fluid mesh used for all computations of this test case.

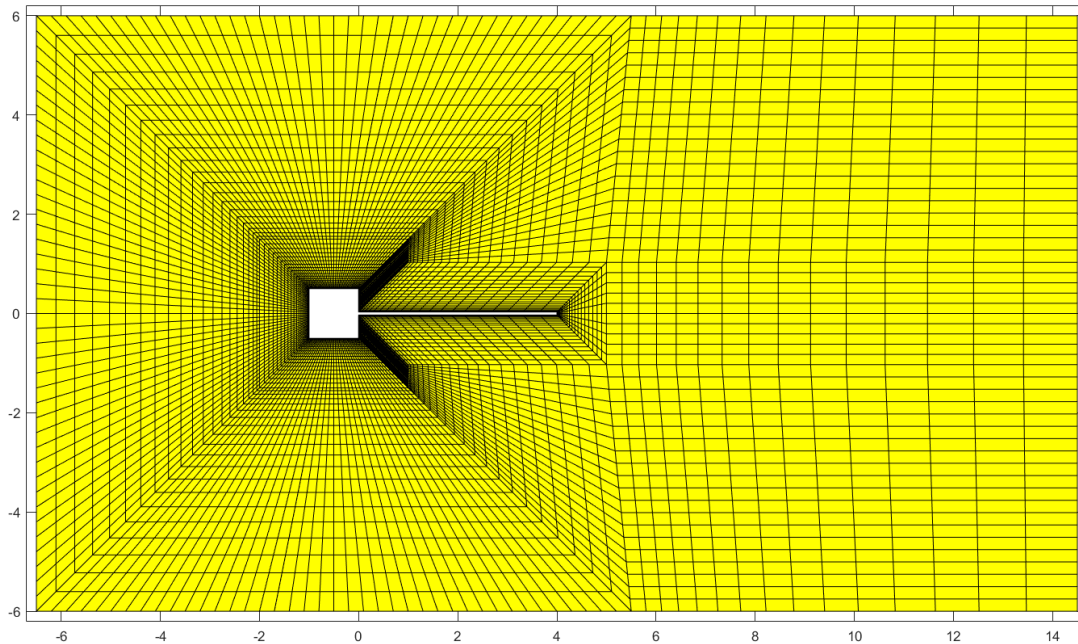


Fig. 27: FE-mesh for fluid domain

As stated in section 4.2 the mesh is finer near the fluid-structure interface Γ_c .

5.1 Tolerance study

Solving fluid-structure interaction problems often requires a large amount of time. Settings which lead to fast calculations with high accuracy are to be found but they should not be too expensive¹⁰. It is not possible that a model of a real world problem is 100% accurate. There is always a certain error to consider, called model or modelling error. This error could be estimated with about up to five per cent. Another error type in numerical analysis is the error made in the approximation of the model. There are tools and approaches used in numerical mathematics that reduce the error and leads to highly accurate approximations. However, it does not make much sense to use another method or parameters of an existing and already used method to get a results which is perhaps 0.5% better than the former one, but is much more expensive and needs a lot more time to get finished.

The aim of this study is to find settings in EduFEM [5] as algorithmically described above which leads to approximations which are accurate enough to describe the real problem correctly and without large errors and are not too expensive.

¹⁰*Expensive* in this context means a long duration of a calculation.

First, the parameters from above are used. The only two parameters which are used differently here are the tolerances ε_c and ε_F . These two parameters are given as

$$\varepsilon_c = 1 \cdot 10^{-i} \quad (5.2)$$

with

$$i \in [1, 2, 3, 4, 5, 6]$$

and

$$\varepsilon_F = 1 \cdot 10^{-j} \quad (5.3)$$

with

$$j \in \begin{cases} [1, 2, 3, 4] & \text{for } i = 1, \\ [2, 3, 4, 5, 6] & \text{for } i \in [2, 3, 4, 5, 6] \end{cases}$$

The reason therefore is that the first part of the study has been done with $i \in [2, 3, 4, 5, 6]$ and $j \in [2, 3, 4, 5, 6]$ respectively. As shown later, higher values for j and therefore smaller values for ε_F are not relevant for the sought setting so $j \in [5, 6]$ for $i = 1$ were not calculated to save time on the parallel computer for more interesting and relevant studies. In tables ‘n.c.’ stands therefore for *not calculated*.

This results in 34 entire FSI calculations for a time frame of five seconds with $t \in [0, 5]$ in the configuration described above. For this and all further studies in this thesis the calculation time on the parallel computer described in Appendix E and the number of iterations are compared. The time includes pre-processing (meshing) and processing but not post-processing. The number of iterations for the partitioned coupling loop¹¹ are the numbers for each time step, e.g. five FSI or partitioned coupling loop iterations¹². For the fluid and solid in one partitioned coupling loop, the iterations for all fluid and solid iterations respectively within the fluid solver or solid solver are summed up. This sum is used further and means that, e.g. 22 fluid iterations are the fluid iterations for the entire partitioned coupling loop.

¹¹FSI iterations and partitioned coupling loop iterations means the same. Partitioned coupling loop is the technically correct expression but FSI is shorter and means the same in diagrams, other plots, and tables.

¹²Average (avg.) FSI-iterations are the average iterations over the partitioned coupling loop needed for the entire analysis, in this example five seconds.

Table 2 shows the calculation time on the parallel computer as specified in Appendix E in hours. $\varepsilon_c = 1 \cdot 10^{-i}$ is the tolerance boundary of the partitioned coupled loop and $\varepsilon_F = 1 \cdot 10^{-j}$ of the Picard iteration loop in the fluid solver used within the partitioned coupled loop. Figure 28 shows Table 2 visualized in a bar plot.

i \ j	1	2	3	4	5	6
1	17.7	21.0	27.4	32.1	n.c.	n.c.
2	22.1	22.9	29.6	37.7	46.9	56.1
3	25.8	24.8	31.4	38.4	49.0	59.0
4	28.7	29.6	35.4	43.0	53.3	66.1
5	33.8	34.4	40.6	45.7	54.3	66.4
6	39.0	38.2	44.0	49.2	58.5	70.3

Tab. 2: Calculation time to find parallel computed solution in hours

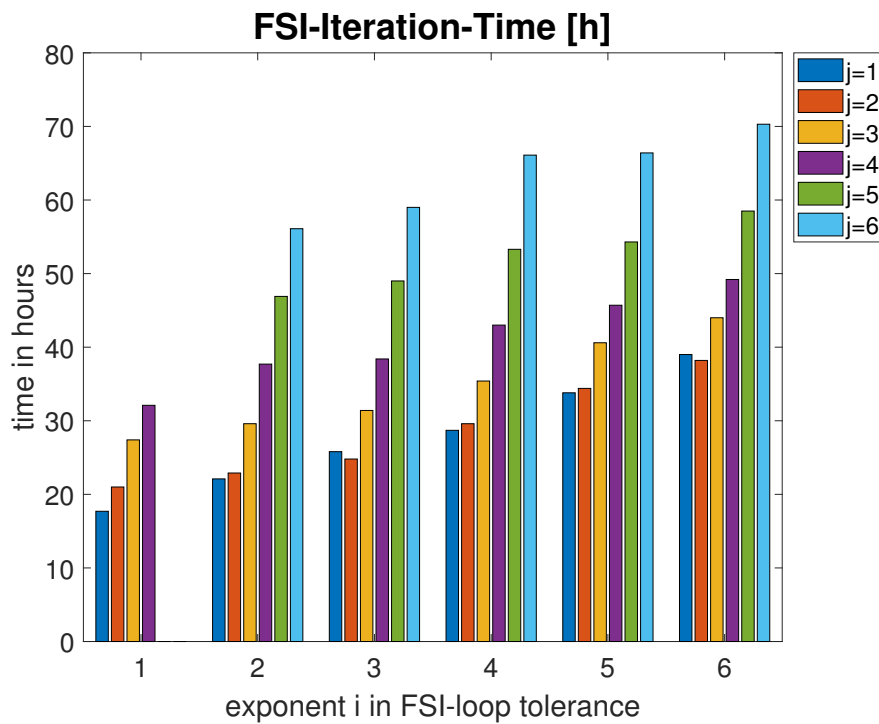


Fig. 28: Calculation time to find parallel computed solution in hours

Tables 3 and 4 show the average iterations for the partitioned coupled loop FSI , for the fluid solver F , and for the solid solver S . These tables are visualized in Figure 29 and Figure 30.

j→	1			2			3		
i↓	FSI	F	S	FSI	F	S	FSI	F	S
1	2.0	3.0	6.8	2.0	3.9	6.9	2.0	5.8	6.9
2	3.0	3.7	9.5	2.9	5.0	9.2	2.9	7.0	9.3
3	3.9	4.2	11.5	3.2	5.3	9.8	3.1	7.3	9.7
4	4.6	4.9	12.8	4.2	6.3	11.8	4.0	8.1	11.4
5	5.5	5.8	14.7	5.1	7.2	13.6	4.9	9.0	13.2
6	6.5	6.8	16.6	5.8	7.9	15.0	5.6	9.7	14.6

Tab. 3: Iteration steps to find parallel computed solution for $j \in [1, 2, 3]$

j→	4			5			6		
i↓	FSI	F	S	FSI	F	S	FSI	F	S
1	2.0	7.2	6.9	n.c.	n.c.	n.c.	n.c.	n.c.	n.c.
2	2.9	9.3	9.3	2.9	12.0	9.3	2.9	14.7	9.3
3	3.1	9.5	9.7	3.1	12.5	9.7	3.1	15.2	9.7
4	3.9	10.3	11.3	3.9	13.3	11.3	3.9	16.9	11.3
5	4.2	10.6	11.9	4.2	13.5	11.8	4.2	17.1	11.8
6	5.2	11.5	13.8	5.0	14.3	13.4	4.9	17.9	13.3

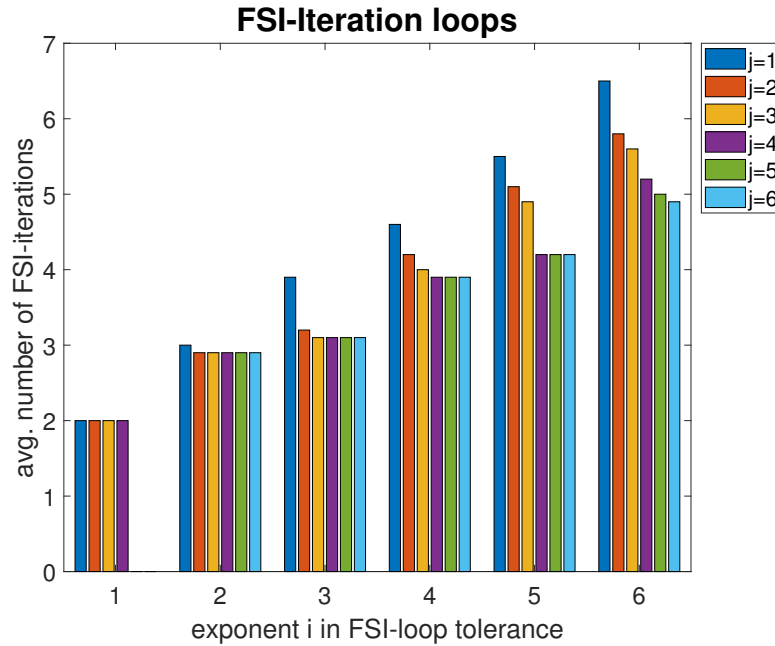
Tab. 4: Iteration steps to find parallel computed solution for $j \in [4, 5, 6]$ 

Fig. 29: Average number of FSI-Iteration loop iterations to find parallel computed solution

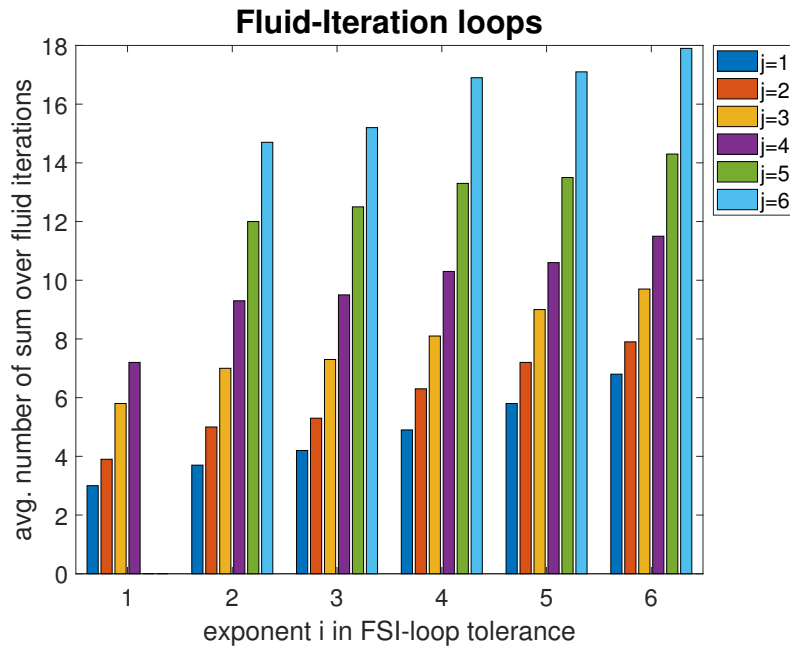


Fig. 30: Average number of summed fluid iterations to find parallel computed solution

Considering Table 2 and Figure 28 it can clearly be seen that higher exponents i and therefore smaller tolerances ε_c for the partitioned coupled loop need more time. This is expected because the higher accuracy may need more iterations of the partitioned coupled loop and therefore more time to reach convergence. For $i = 3$ and $i = 6$ the combination with $j = 2$ is slightly faster than the combination with $j = 1$ although $j = 1$ is less strict for the fluid convergence.

Figures 29 and 30 may look unexpected, viewed for the first time. Especially the averaged number of iterations over the entire time domain of the partitioned coupled loop with $i = 6$ in Figure 29 is vice versa to $i = 6$ for the calculation time in hours in Figure 28. The average number of iterations in the partitioned coupled loop decreases for increasing exponents j of the fluid tolerance boundary ε_F . In Figure 30 it can clearly be seen that the averaged number of iterations of the fluid solver increases with increasing j and i respectively.

This leads to the interpretation that the tolerance for the partitioned coupled loop is decisive. The smaller ε_F is, the more exact is the solution of the fluid solver. This needs less iterations of the partitioned coupled loop because the convergence criteria of Equation (4.7) is faster reached but the higher calculation time needed for the fluid solver can not be balanced by a decrease of the averaged number of partitioned coupled loop iterations. The tolerance defined in Equations (4.7) for the fluid domain and (4.8) for the structural domain is a relative one. It uses the solution of the last iteration step of the partitioned coupling loop and not the solution of the previous time step. Therefore the tolerance of the fluid domain is not so important any more because the used fluid solution is always the best one that exists at a certain iteration step of the partitioned coupled loop.

In the post-processing step it is further possible to visualize the vector fields of the fluid velocity and vorticity, the vector field of fluid velocity arrows shown in the midpoint of each finite element in the deformed fluid mesh, and the scalar field of fluid pressure at a certain time. Furthermore for the middle point of the right edge of the plate (point pme is shown in Figure 15) the horizontal and vertical displacements over time and the horizontal and vertical forces acting on this point over time can be plotted in a diagram. Such figures are shown and described in detail below.

To find the best setting of parameters for this plate case it is not enough to look only at the amount of required iteration steps and needed calculation time of the FEM analysis of this problem. It is necessary to consider the quality of the results when making this decision. Therefore some plots of these mentioned quantities are shown and interpreted here.

Figures 32, 31, 33, and 34¹³ show the horizontal displacement, the vertical displacement, the horizontal force, and the vertical force of point pme for $i = 1$ and appropriate $j \in [1, 2, 3, 4]$, and for $i = 6$ and appropriate $j \in [1, 2, 3, 4, 5, 6]$ over time t of analysis which is in this case 5 seconds. The plots for $i \in [2, 3, 4, 5]$ and appropriate $j \in [1, 2, 3, 4, 5, 6]$ are shown in Appendix A. In these figures it can clearly be seen that for $i = 1$ and $i = 2$ the results are different for different values of j . For the horizontal and vertical forces an oscillation occurs for $i = 1$ as shown in Figures 33 and 34. The solution for displacements are quite accurate already for $i = 1$ and $j \geq 2$. However, it is not possible to accept these tolerances for the partitioned coupling loop as a setting which is accurate enough.

Considering all results described here and the plots of the velocity, vorticity, and pressure fields of the fluid domain the setting for the tolerances of the partitioned coupling loop and the fluid solver are chosen as

$$\varepsilon_c = 1 \cdot 10^{-6} \quad (5.4)$$

and

$$\varepsilon_F = 1 \cdot 10^{-2} \quad (5.5)$$

Figures 35, 36, and 37 show the plots of the resulting fluid fields for this configuration. More of these plots are found in Appendix A. In Figure 36 some numerical errors occur, especially in the plots for $t \geq 4$ seconds. Here is noted that the vorticity field is the derivative of the velocity field. An analogy to structural engineering are the stresses which are the derivative of displacements being the primary obtained variables in a FEM approximation [13, p. 125]. Using standard C_0 -continuous FE shape functions, the vorticity of the fluid field is discontinuous across element boundaries just as the stresses in standard solid simulations. However, in the plots, the vorticity field has been smoothed, numerical oscillations can still be seen. The pressure field is a primary quantity and, hence, continuous.

The results could be different for larger or smaller time steps and other physical parameters. Therefore further investigations including more parameter studies and a larger time range could be useful. This, however, is beyond the scope of this thesis.

¹³The curves within these plots are very close together. In Appendix A in Figure 79 different line types and markers are used to show that there are different lines plotted in one diagram.

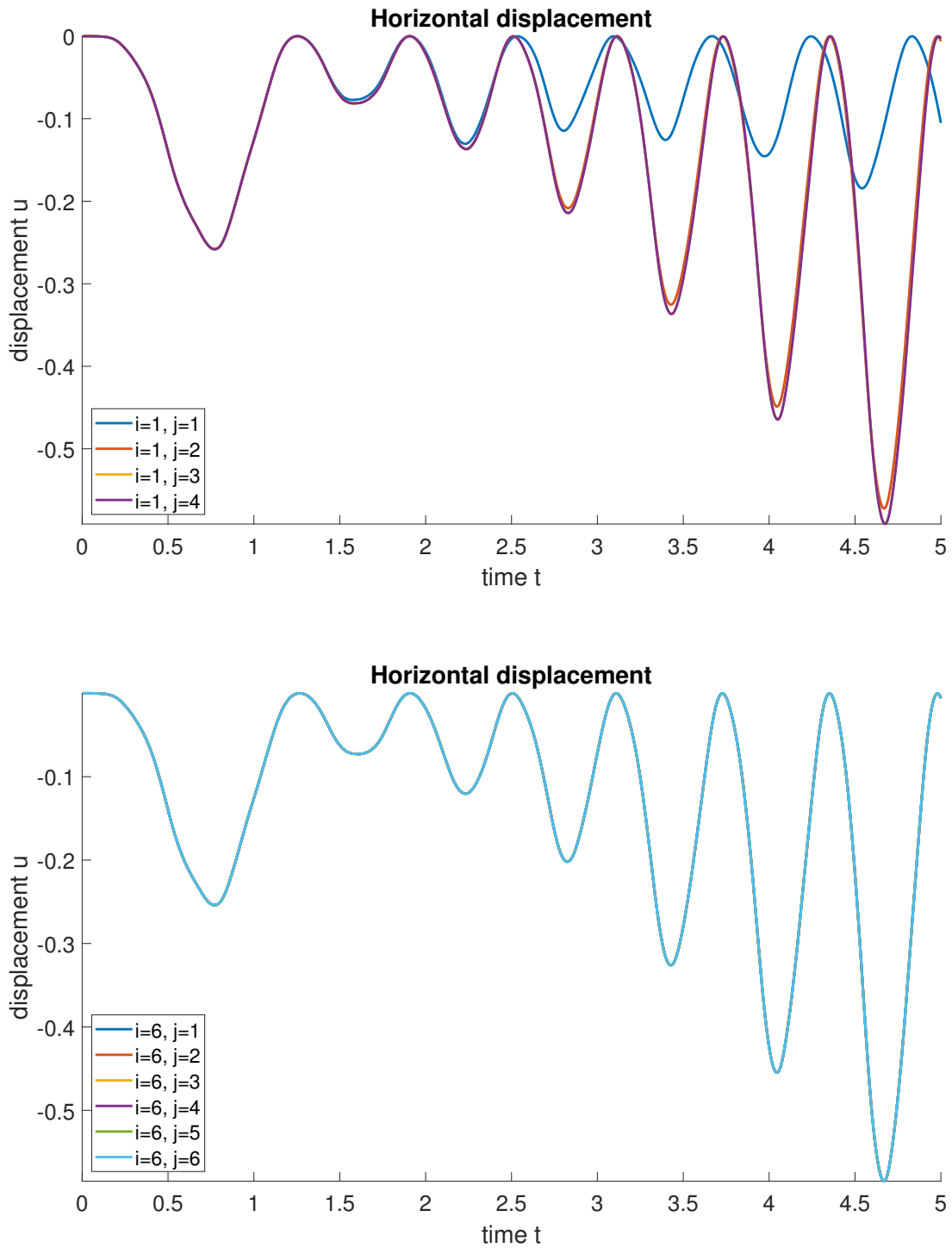


Fig. 31: Horizontal displacement of the middle point of the right edge of the plate

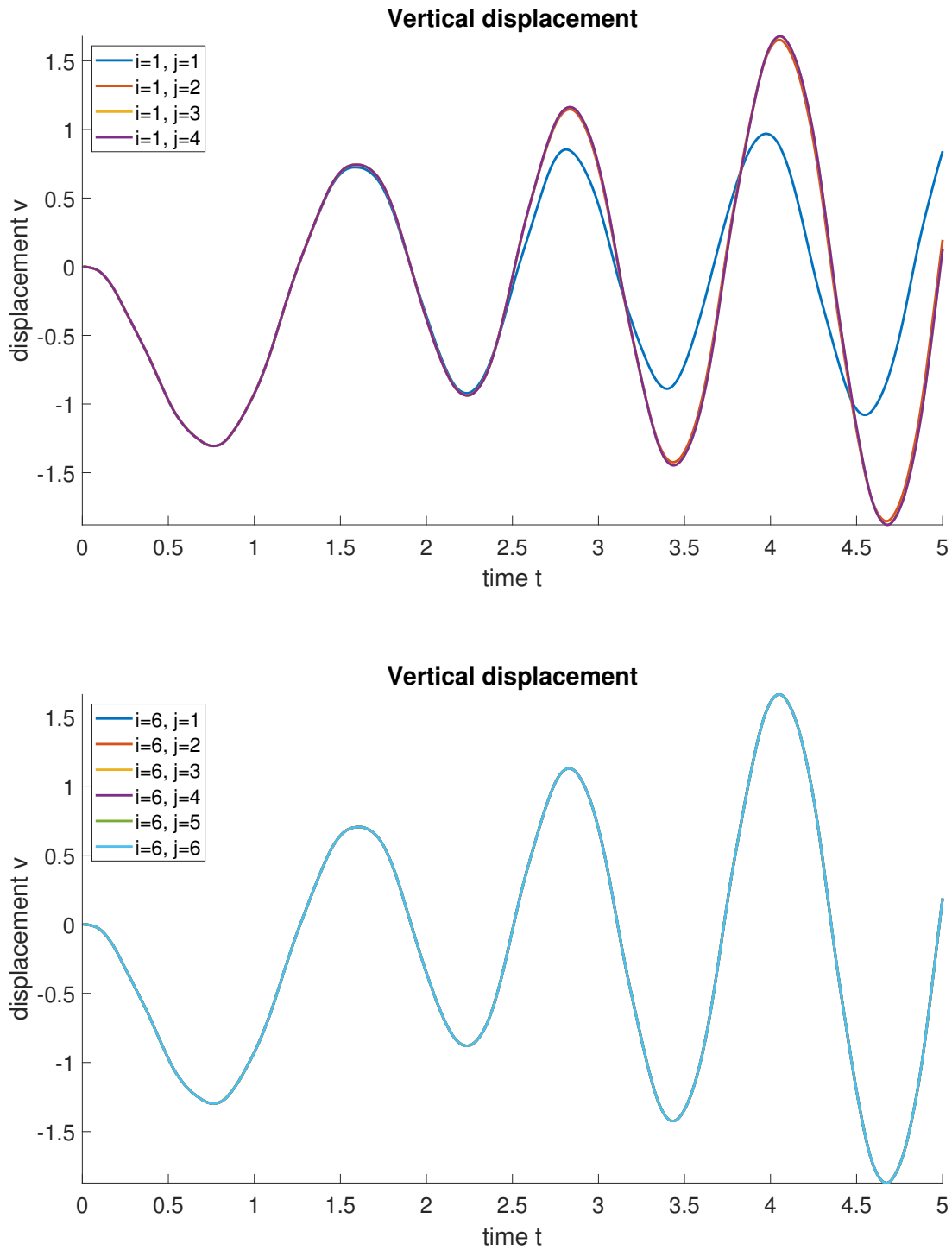


Fig. 32: Vertical displacement of the middle point of the right edge of the plate

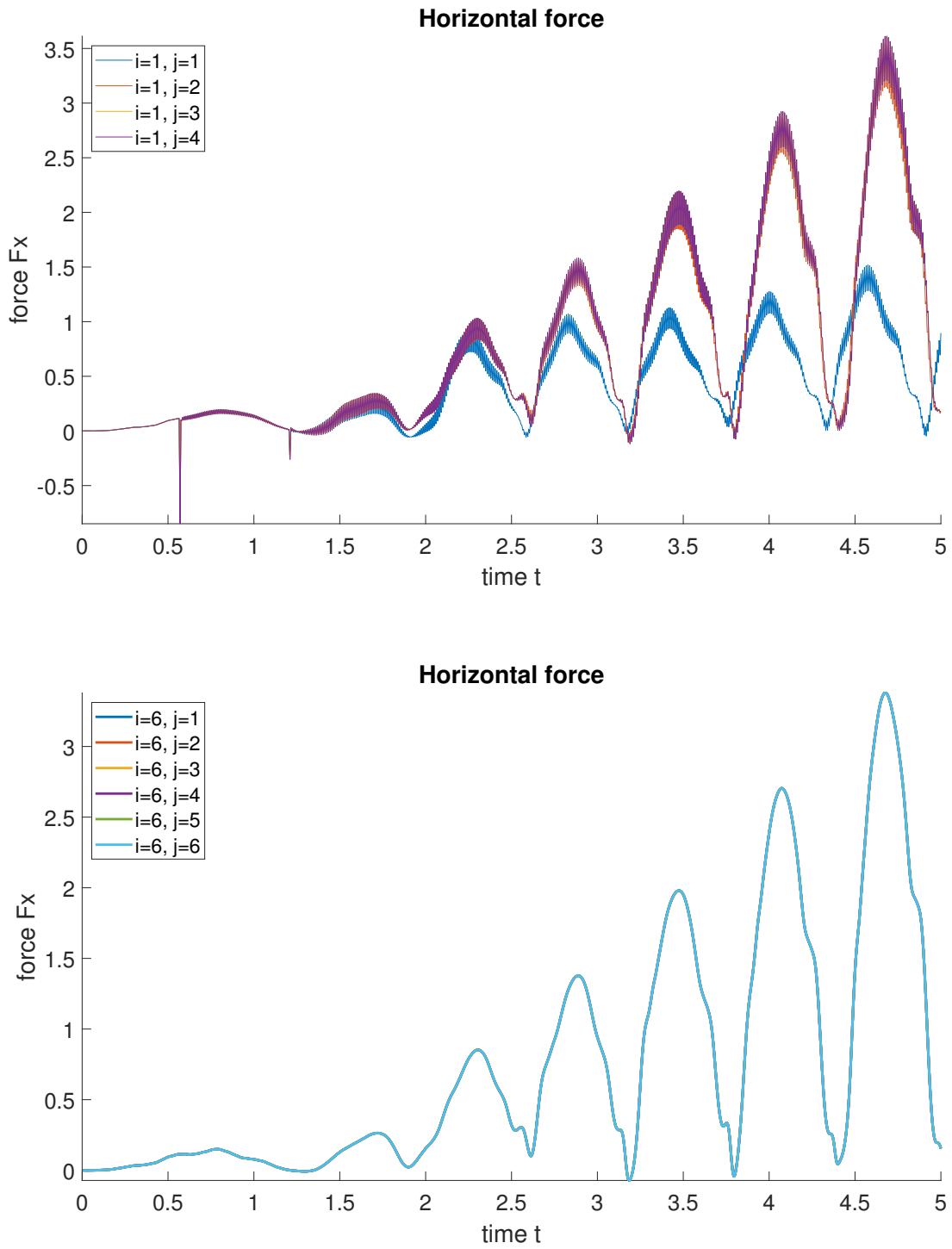


Fig. 33: Horizontal force acting on the middle point of the right edge of the plate

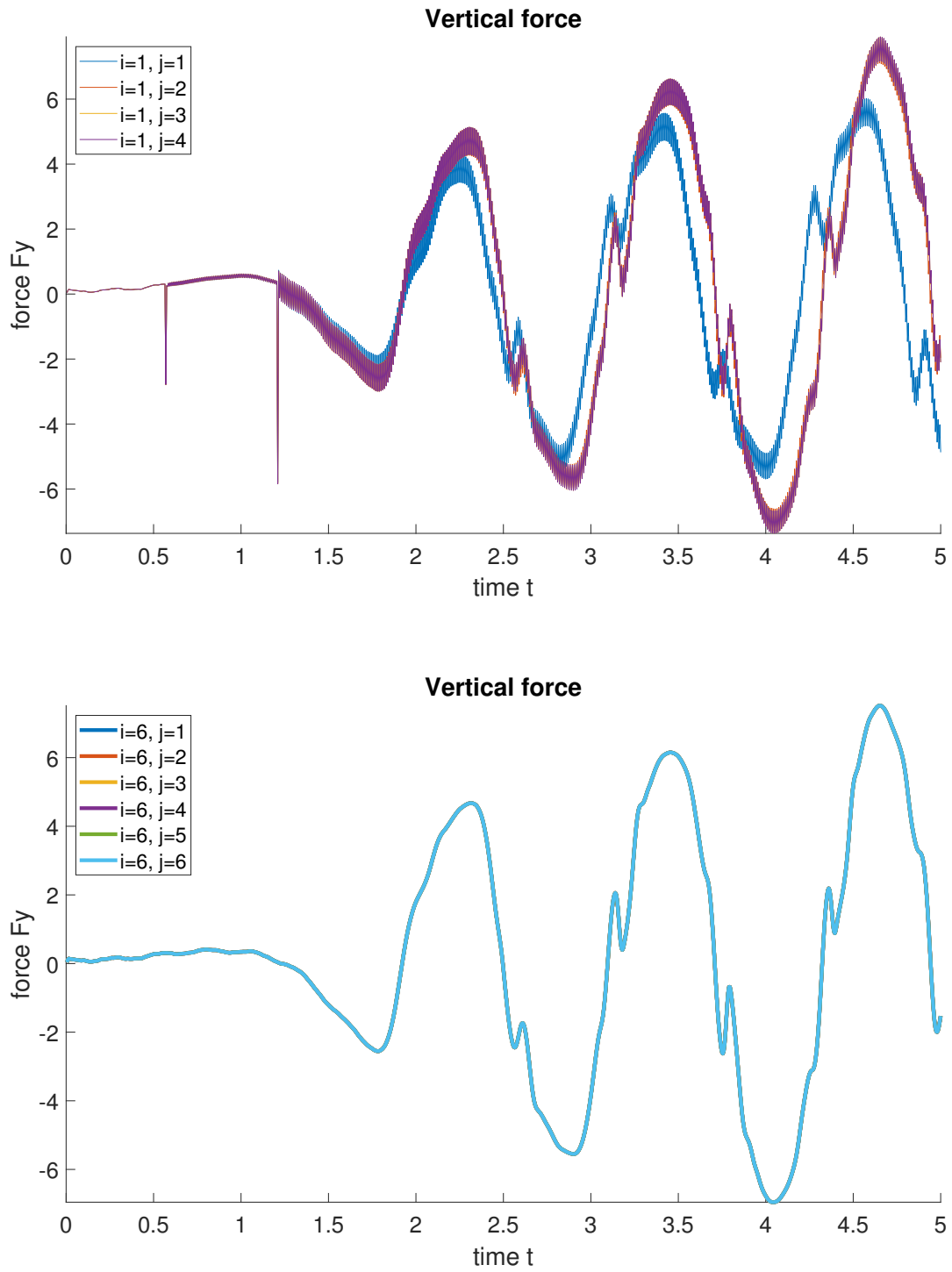


Fig. 34: Vertical force acting on the middle point of the right edge of the plate

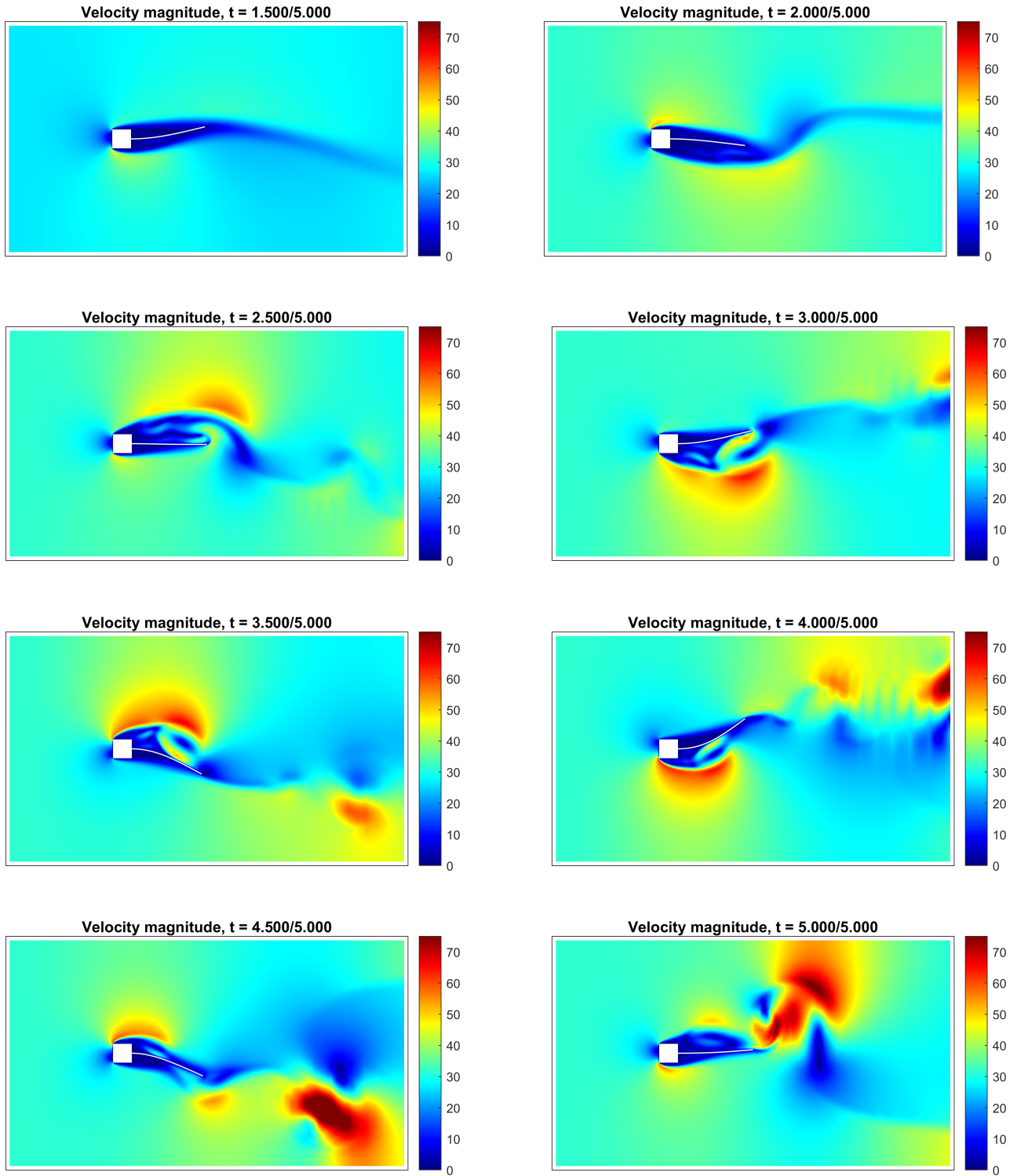


Fig. 35: Velocity field of reference case $\varepsilon_c = 10^{-6}$ and $\varepsilon_F = 10^{-2}$

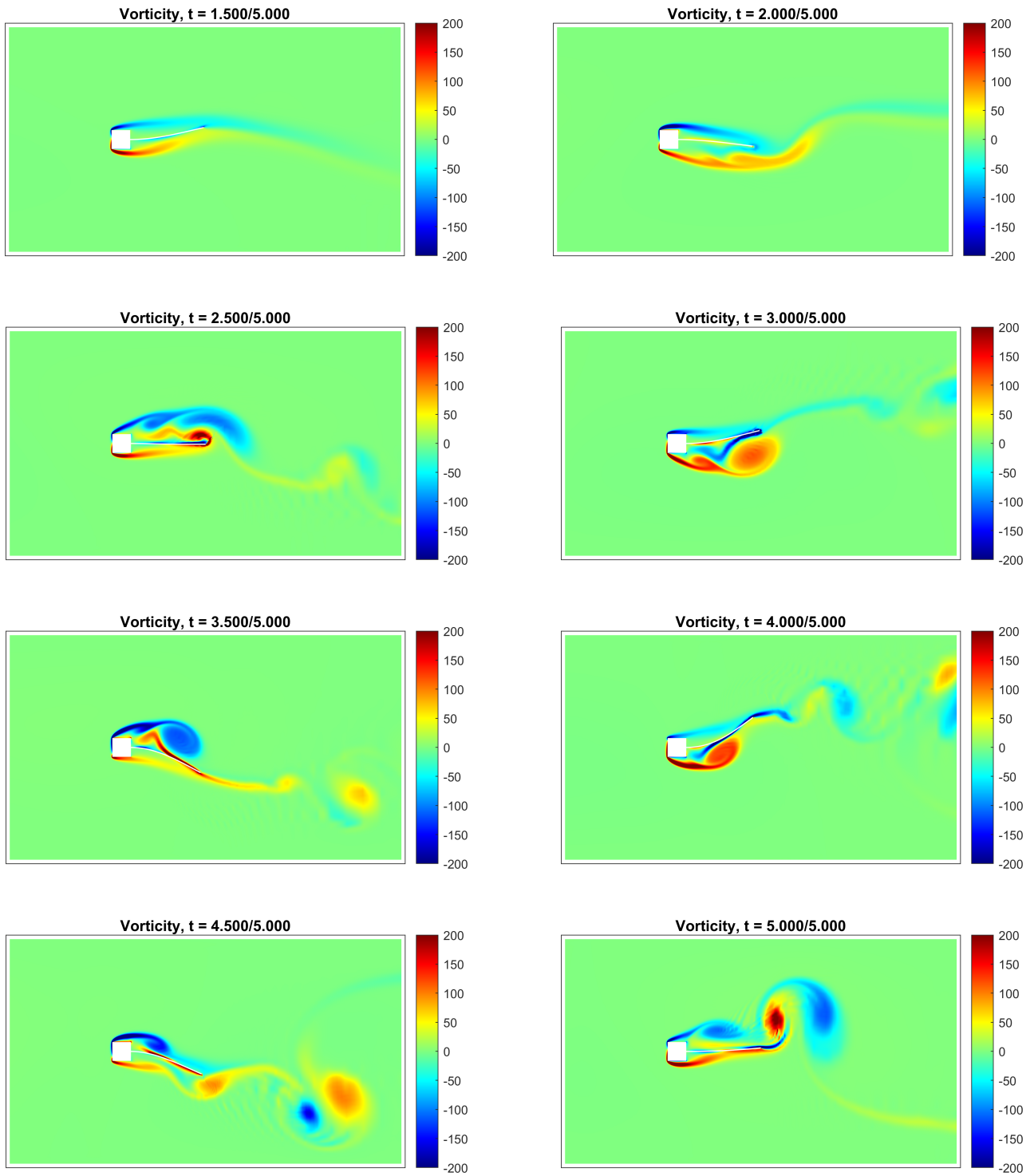


Fig. 36: Vorticity field of reference case $\varepsilon_c = 10^{-6}$ and $\varepsilon_F = 10^{-2}$

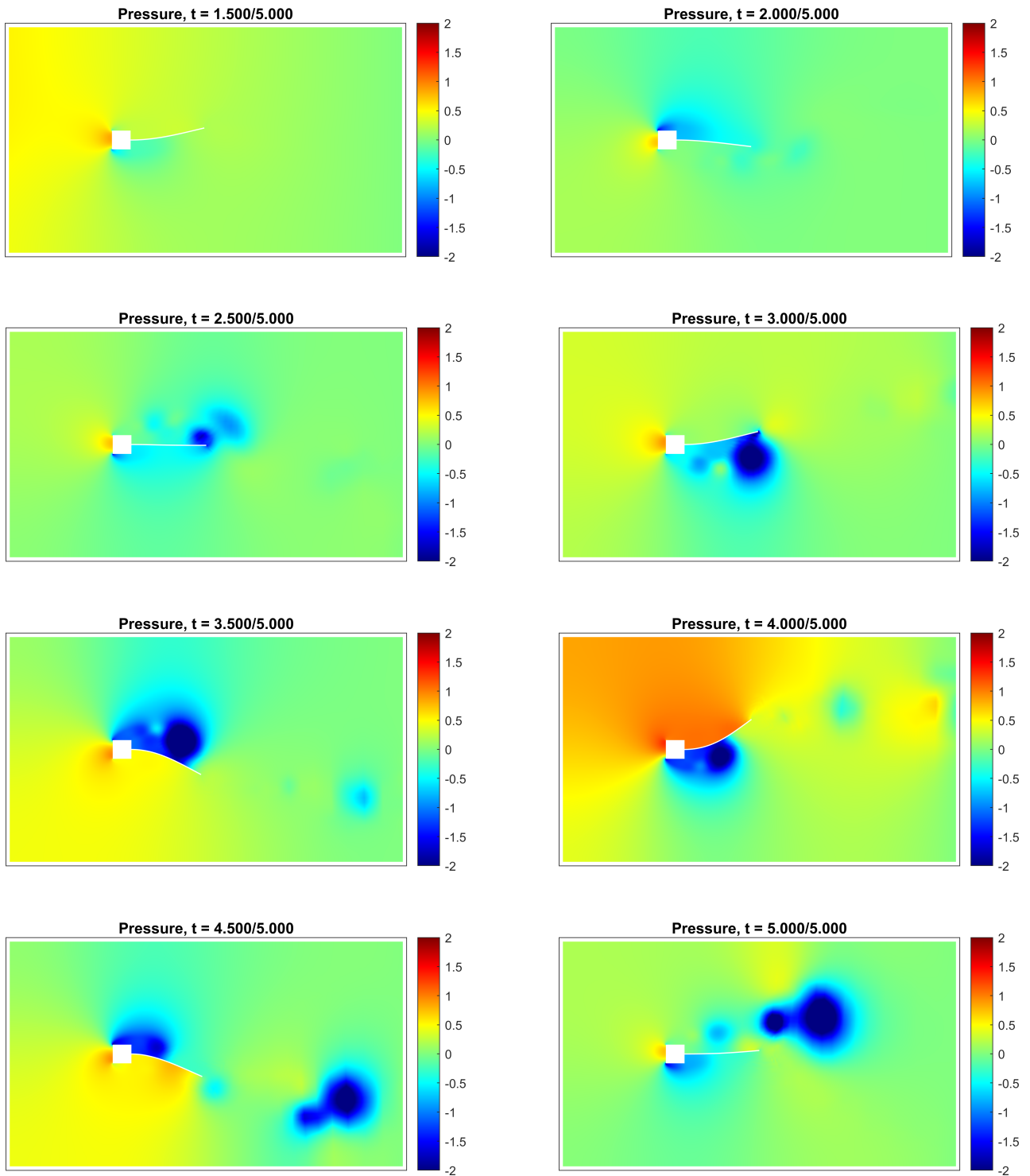


Fig. 37: Pressure field of reference case $\varepsilon_c = 10^{-6}$ and $\varepsilon_F = 10^{-2}$

5.2 Aitken's relaxation

The calculation time for the standard setting chosen in section 5.1 was 38.2 hours at the parallel computer for pre- and processing steps. The aim is to reduce the needed calculation time and get results within the same range of accuracy as before. One approach used and tested in this thesis is *Aitken's relaxation* or *Aitken's Δ^2 method* as described in [15].

Aitken's relaxation is used on the structural displacements \mathbf{d} . Algorithm 3 is an adaption of Algorithm 2 and shows how Aitken's relaxation is applied within the partitioned coupled loop. Figure 38 visualizes Algorithm 3.

Algorithm 3: FSI partitioned coupling loop for time step $n + 1$ using Aitken's relaxation

Input: From time step t_n : The fluid mesh Ω_n^{fluid} with velocity \mathbf{u}_n and pressure p_n , the time independent structural domain mesh Ω_0^{solid} and structural domains displacements \mathbf{d}_n .

initialization

```

while  $max(uvp_{conCrit}^c, d_{conCrit}^c) > MaxRes_c$  do
  solve fluid field - CFD to get  $\mathbf{u}_{n+1}$  and  $p_{n+1}$  using  $\Omega_{n+1}^{fluid}$ ,  $\Omega_n^{fluid}$ ,  $\mathbf{u}_n$ , and  $p_n$ 
  determine fluid forces  $\mathbf{f}_{n+1}$ 
  solve solid field - CSD using  $\Omega_0^{solid}$  to get  $\mathbf{d}_{n+1}$ 
  use Aitken's relaxation to get  $\mathbf{d}_{i+1}^{AR}$ 
  get new fluid mesh - CMD  $\Omega_{n+1}^{fluid}$  matching solid displacements  $\mathbf{d}_{i+1}^{AR}$ 
end

```

Output: obtain Ω_{n+1}^{fluid} , \mathbf{u}_{n+1} , p_{n+1} , and \mathbf{d}_{n+1}

Next time step if t_{end} has not been reached.

The general form of Aitken's relaxation for a variable \mathbf{x}_{i+1} where $i + 1$ is the actual iteration step and i the previous one is defined as

$$\mathbf{x}_{i+1} = (1 - \omega_{i+1})\mathbf{x}_i + \omega_{i+1}\tilde{\mathbf{x}}_{i+1} \quad (5.6)$$

with relaxation factor which is recursively defined as

$$\omega_{i+1} = -\omega_i \frac{\mathbf{r}_i \cdot (\mathbf{r}_{i+1} - \mathbf{r}_i)}{\|\mathbf{r}_{i+1} - \mathbf{r}_i\|^2} \quad (5.7)$$

where $\|\cdot\|$ is the Euclidean norm. It can be obtained for $i \geq 2$ and for $i = 1$ a defined value $\omega_{i=1} = \omega_{max} = 1$ is used. Another choice is to use the constraint parameter [15]

$$\omega_1^{n+1} = \max(\omega^n, \omega_{max}) \quad (5.8)$$

where ω^n is the relaxation factor of the last iteration of the partitioned coupled loop in the previous time step n .

The residuum r is defined as

$$\mathbf{r}_{i+1} = \tilde{\mathbf{x}}_{i+1} - \mathbf{x}_i \quad (5.9)$$

In the notation used within this thesis \boldsymbol{x} stands for the structural displacements \boldsymbol{d} and therefore follows $\boldsymbol{x}_{i+1} = \boldsymbol{d}_{i+1}^{AR}$ and $\tilde{\boldsymbol{x}}_{i+1} = \boldsymbol{d}_{i+1}$.

For the further procedure within the partitioned coupled loop (CMD and update of variables) the relaxation $\boldsymbol{d}_{i+1}^{AR}$ is used as the result of the solid field.

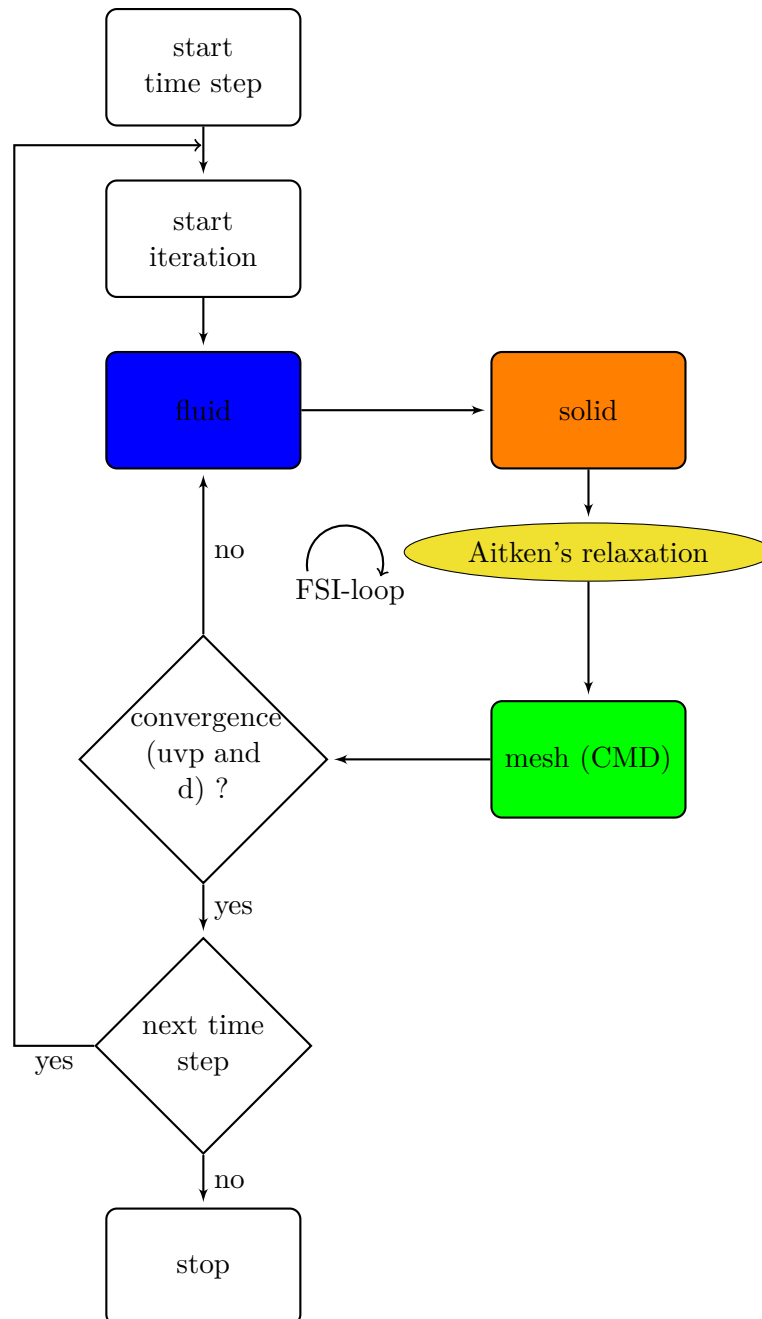


Fig. 38: Flow-diagram of FSI algorithm with Aitken's relaxation applied

Table 5 shows the number of iteration steps and needed time compared with the reference case with $\varepsilon_c = 1 \cdot 10^{-6}$ and $\varepsilon_F = 1 \cdot 10^{-2}$. AR stands for Aitken’s relaxation.

case	no AR			AR		
notation	FSI	F	S	FSI	F	S
min. iterations	5	5	11	5	5	11
max. iterations	8	11	20	8	11	20
avg. iterations	5.8	7.9	15.0	5.8	7.9	14.8
min. time FSI [s]	94.5			91.4		
max. time FSI [s]	190.5			194.3		
avg. time FSI [s]	137.7			132.3		
time [h]	38.2			36.8		

Tab. 5: Results of reference case left and Aitken’s relaxation applied on this case right.

Values written in **red** are worse in the actually considered case than in the reference case and values written in **green** are better than in the reference case. This is done for all further studies.

For this case about 1.4 hours can be saved for the entire calculation time which is about 3.7%. Consequently, not a big improvement can be achieved using Aitken’s relaxation to accelerate the fluid-structure iteration loop.

However, it is shown here that an improvement is possible. The iterations of the case without relaxation are already relatively low with an average number of FSI-iterations of 5.8 and maximum of three fluid iterations during one FSI iteration step in time steps 1 to 10, 495 to 505, and 990 to 1000 as shown in Appendix B¹⁴. Generally, it can be said according to the literature, e.g. [15], that relaxation is most effective when the number of iterations in the unrelaxed case would otherwise be quite large. Therefore, the small improvement achieved here is not surprising.

Figures 39 and 40 show the horizontal and vertical displacements, and the horizontal and vertical forces obtained with Aitken’s relaxation in blue over the plot of the reference case in green. Figures 41, 42, and 43 show in their left column the results of the fluid fields for the reference case and in their right column for the case where Aitken’s relaxation has been used. It is obvious that the solution is undistinguishable using Aitken’s relaxation so that there is no disadvantage resulting from relaxation.

¹⁴Only for the mentioned time steps an exact analysis of iteration numbers per FSI iteration steps has been done for each case. However, considering the summation it is obvious that the number of required iterations per time step and FSI iterations respectively is relatively low.

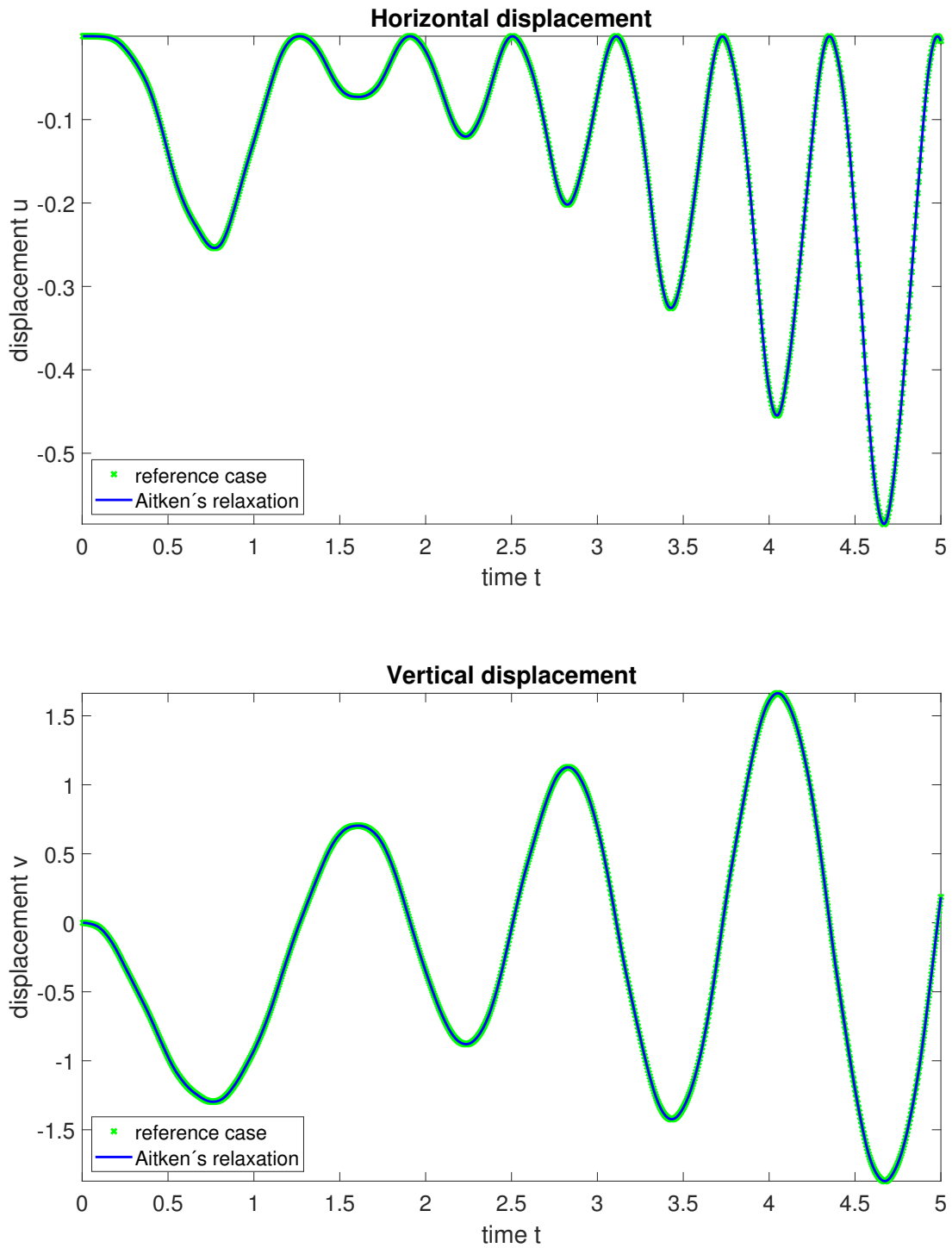


Fig. 39: Horizontal and vertical displacement of the middle point of the right edge of the plate

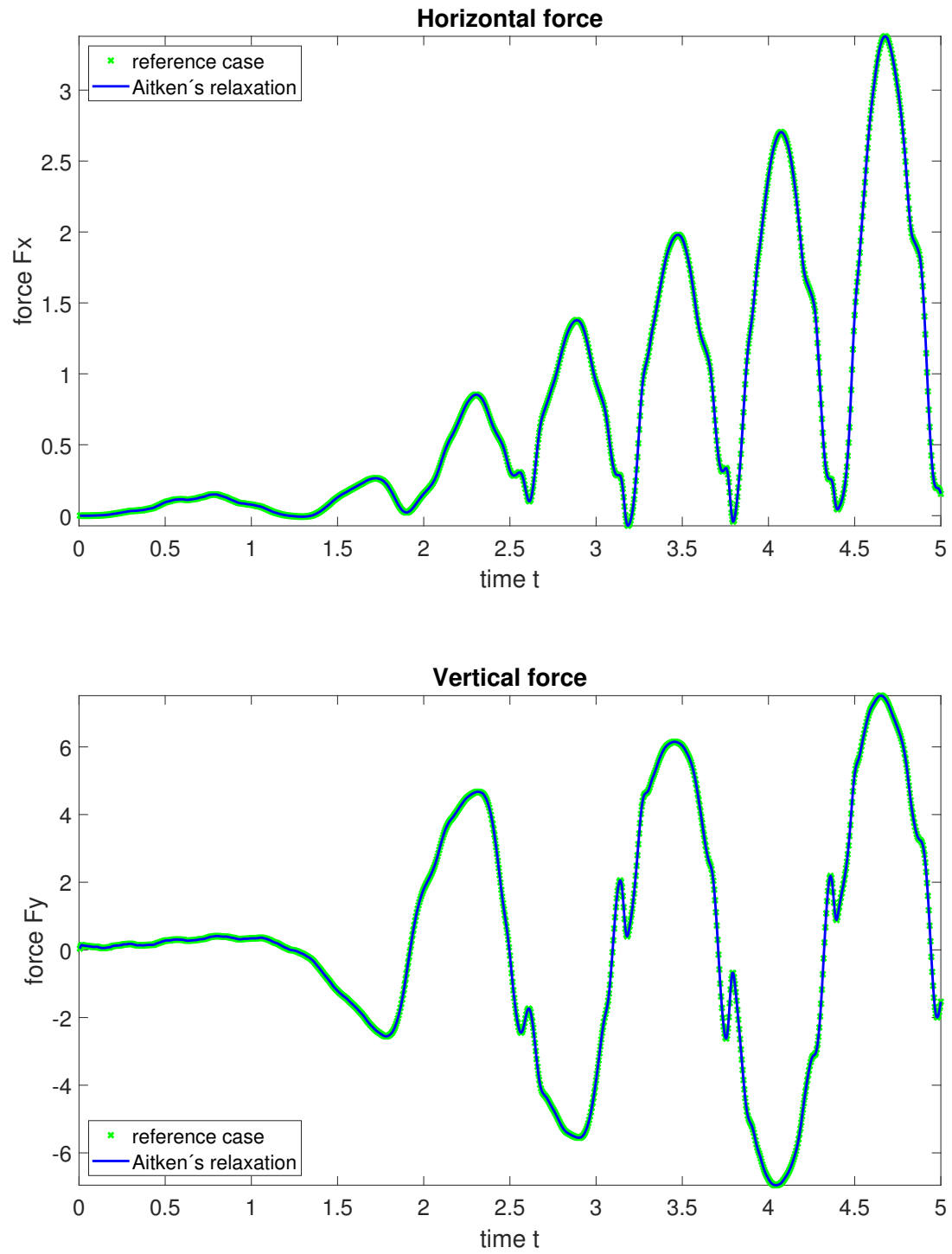


Fig. 40: Vertical and horizontal force of the middle point of the right edge of the plate

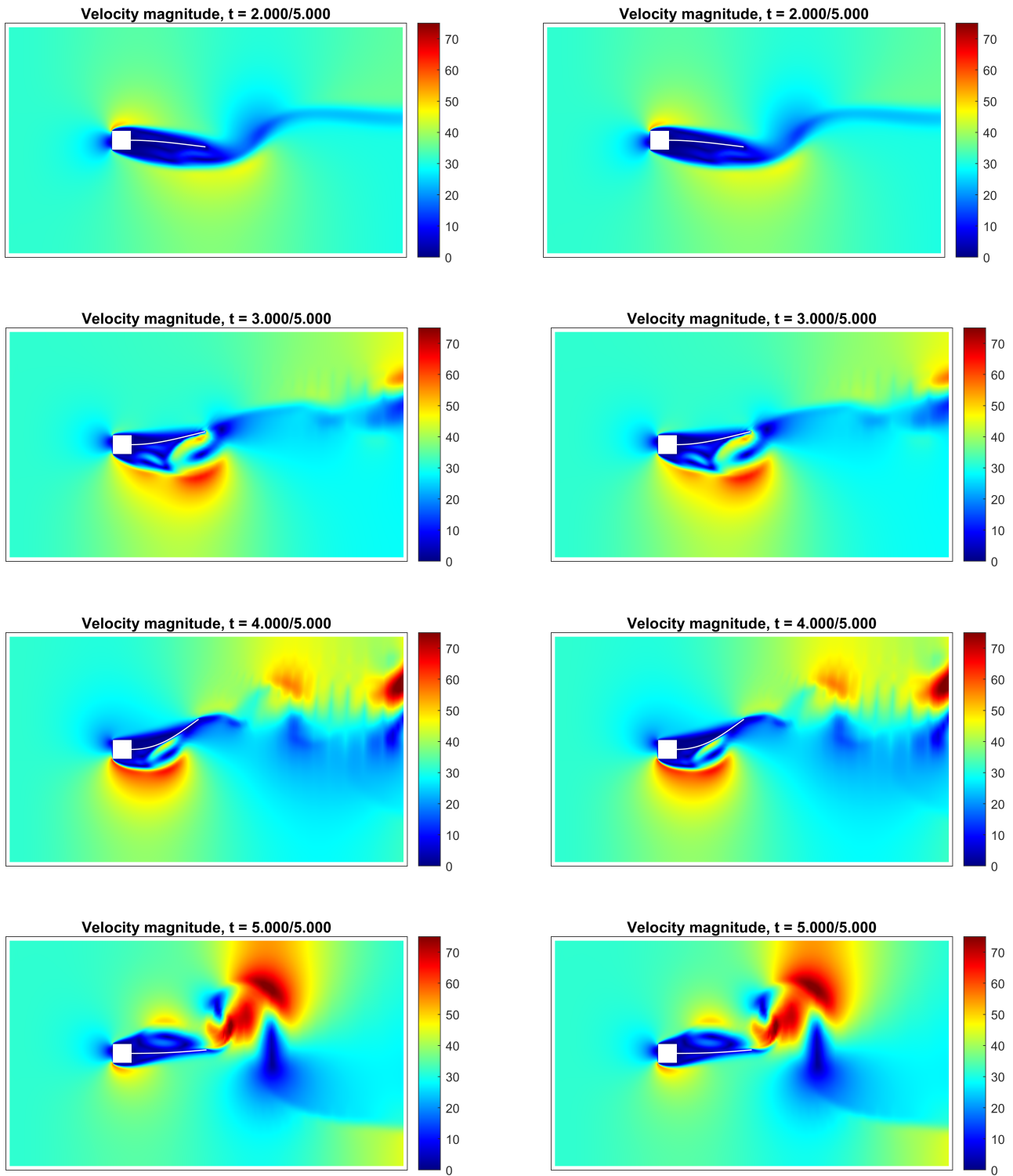


Fig. 41: Velocity field of reference case left and the study case for Aitken's relaxation right

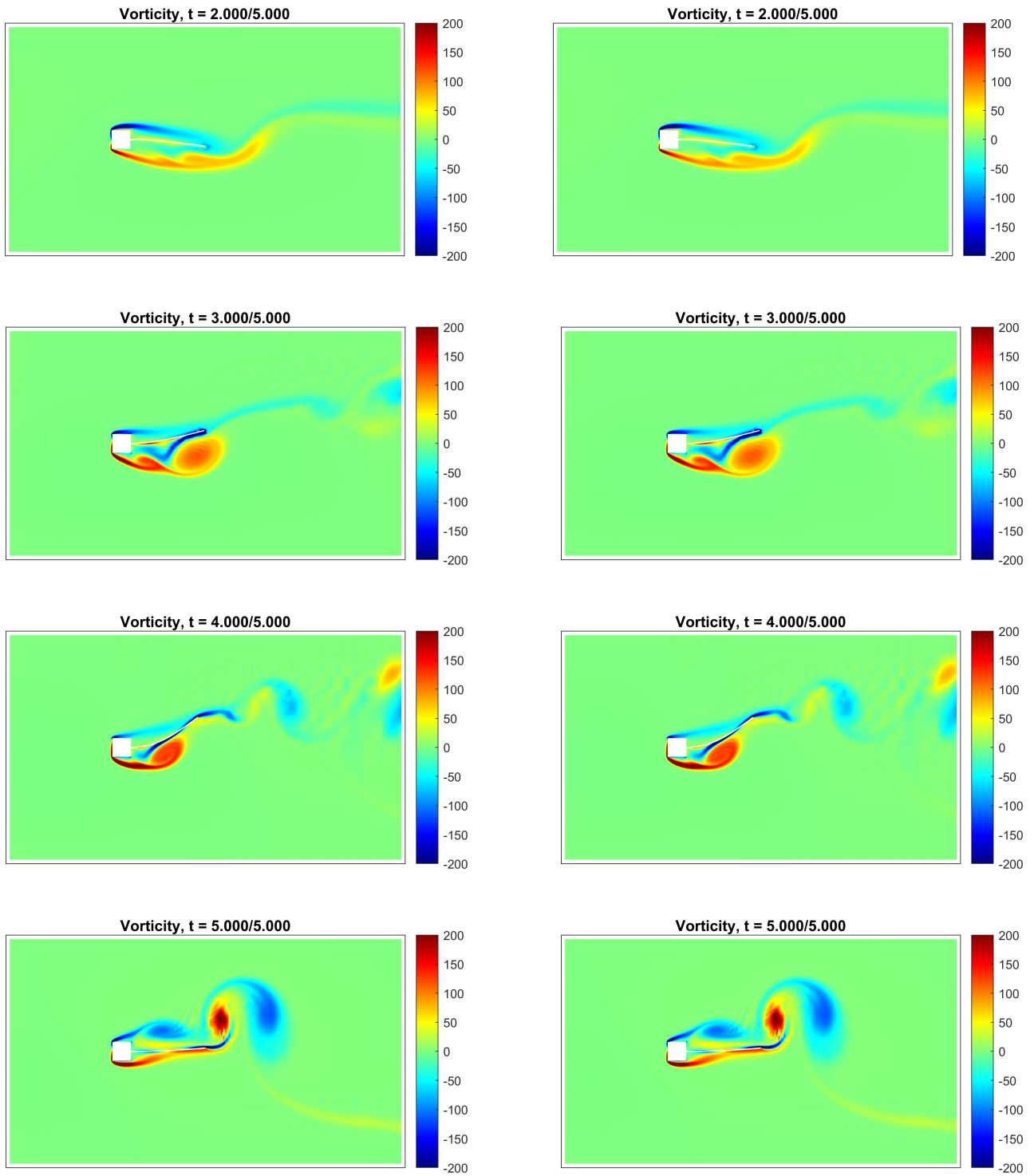


Fig. 42: Vorticity field of reference case left and the study case for Aitken's relaxation right

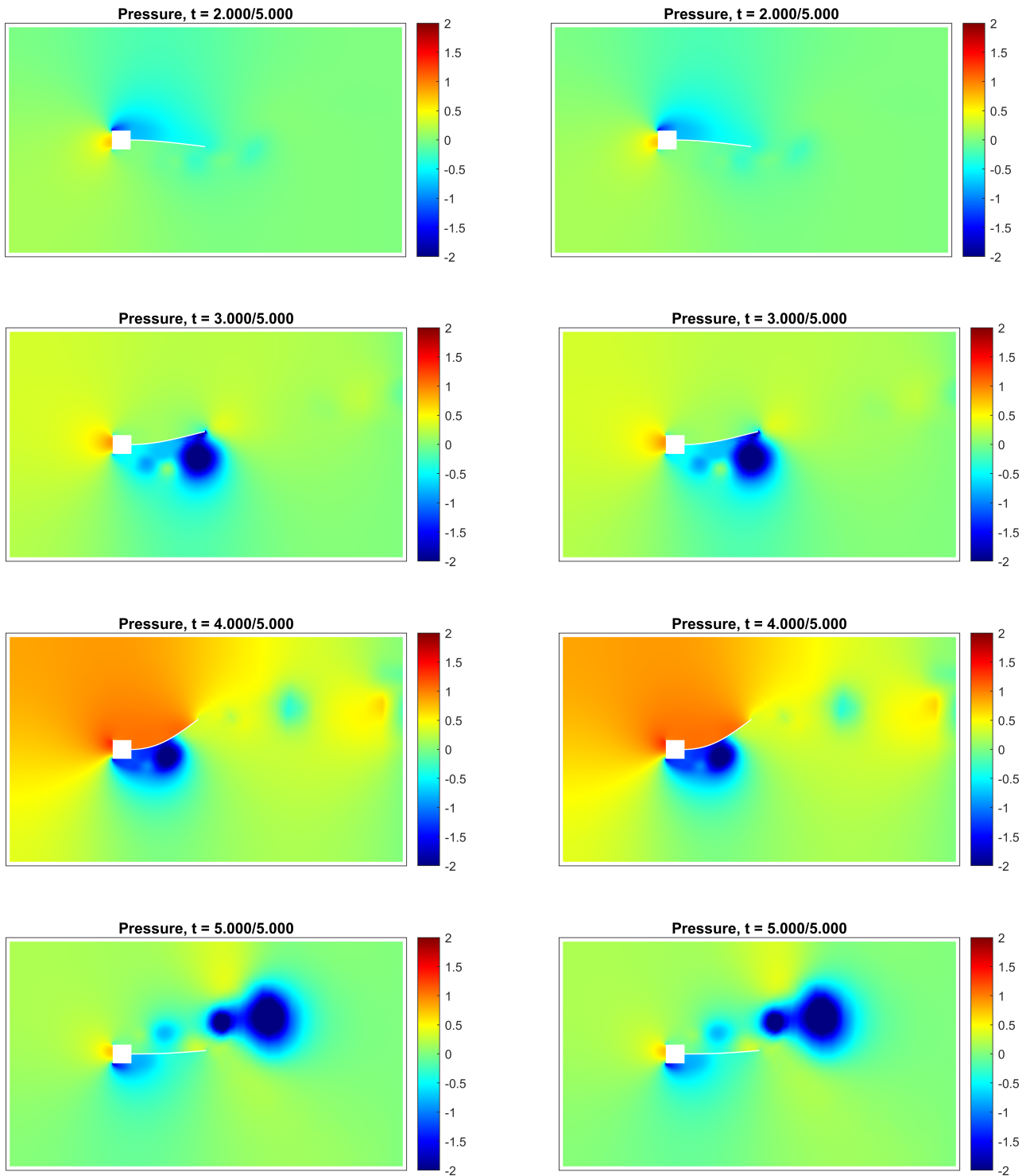


Fig. 43: Pressure field of reference case left and the study case for Aitken's relaxation right

5.3 Extrapolation

Another approach to accelerate the FSI algorithm is extrapolation which is investigated next. The extrapolation is applied in a new time step before the partitioned coupling loop starts. This is visualized in Figure 44.

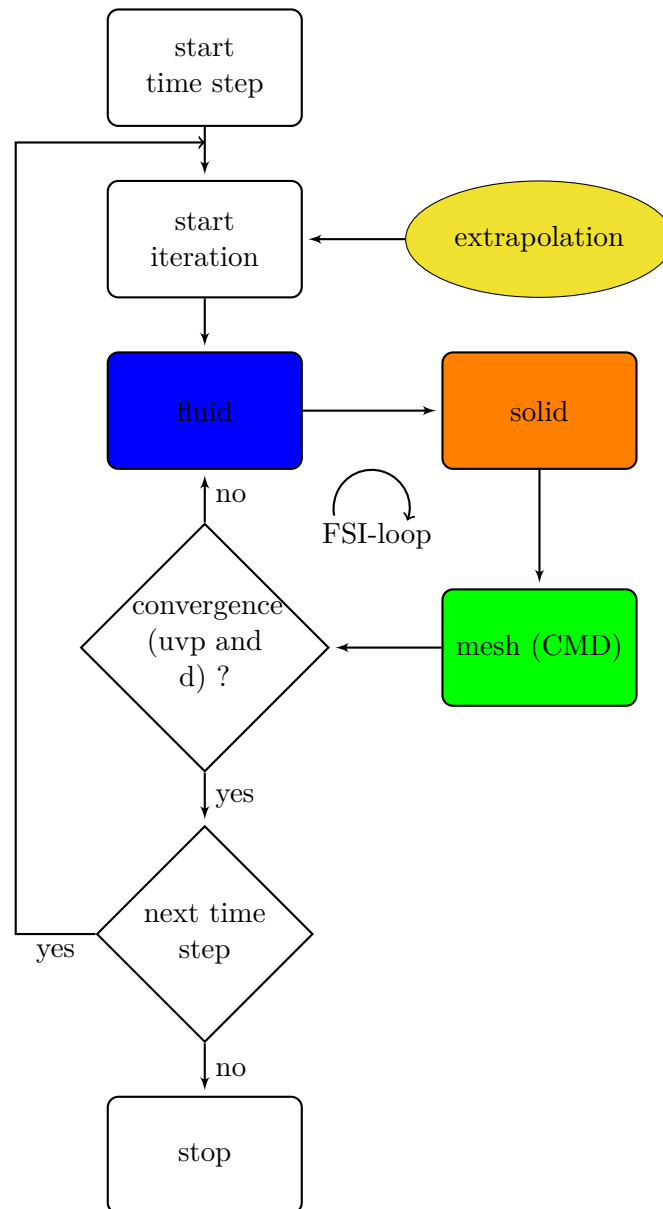


Fig. 44: Flow-diagram of FSI algorithm

Extrapolation has been used in context of fluid-structure interaction before, e.g. in [20]. The aim is to find out to which fields of the FSI procedure used in this thesis extrapolation should be applied and how large the improvement is.

The idea of extrapolation is to assume that an existing trend, known by considering history, e.g. solutions of the partitioned coupling loop of the previous time steps, continues and the procedure could be accelerated by better start values of partitioned coupled fluid-structure interaction loop cycles.

The extrapolation functions used in this thesis are easily obtained using finite differences based on the Taylor series expansions, see, e.g. [20].

The resulting extrapolation functions for different orders are given as:

- 1st order:

$$\mathbf{x}_{n+1} = -1 \cdot \mathbf{x}_{n-1} + 2 \cdot \mathbf{x}_n \quad (5.10)$$

- 2nd order:

$$\mathbf{x}_{n+1} = \mathbf{x}_{n-2} - 3 \cdot \mathbf{x}_{n-1} + 3 \cdot \mathbf{x}_n \quad (5.11)$$

- 3rd order:

$$\mathbf{x}_{n+1} = -1 \cdot \mathbf{x}_{n-3} + 4 \cdot \mathbf{x}_{n-2} - 6 \cdot \mathbf{x}_{n-1} + 4 \cdot \mathbf{x}_n \quad (5.12)$$

- 4th order:

$$\mathbf{x}_{n+1} = \mathbf{x}_{n-4} - 5 \cdot \mathbf{x}_{n-3} + 10 \cdot \mathbf{x}_{n-2} - 10 \cdot \mathbf{x}_{n-1} + 5 \cdot \mathbf{x}_n \quad (5.13)$$

- 5th order:

$$\mathbf{x}_{n+1} = -\mathbf{x}_{n-5} + 6 \cdot \mathbf{x}_{n-4} - 15 \cdot \mathbf{x}_{n-3} + 20 \cdot \mathbf{x}_{n-2} - 15 \cdot \mathbf{x}_{n-1} + 6 \cdot \mathbf{x}_n \quad (5.14)$$

\mathbf{x} is the quantity which is to be extrapolated at time $n+1$ based on already computed quantities of previous time steps n , $n-1$, etc. Of course, this is only a prediction for $n+1$ which is then actually determined based on the partitioned coupling loop. For Equation (5.10) at least two previous time steps are necessary, for Equation (5.14) six previous time steps. In the first time steps, the required number of computed time steps (according to the desired order) may not be available yet. Then, for the first time steps, always the best extrapolation rule is chosen based on the available data.

Table 6 shows the results. In the left column the field which is extrapolated is shown, the reference case is defined in section 5.1. Table 6 shows clearly that for this test case the extrapolation applied to a single field or result is not useful. There is not only no improvement but the performance of the calculation with respect to the number of iterations and calculation time is worse than for the reference case without any extrapolation. However, the results are correct as shown in Appendix C. If the extrapolation is applied to all fields, which are the vector of fluid velocities and pressure uvp , the structural displacements d , and the actual nodal coordinates of the deformed fluid mesh $mesh$ an improvement is achieved. For extrapolation functions of first order, the calculation time is about 21.2% lower than for the reference test case and for fifth order extrapolation functions, it is about 34.8% less.

uvp	extrapolation order	reference case			yes 1			yes 5		
	notation	FSI	F	S	FSI	F	S	FSI	F	S
	min iterations	5	5	11	5	7	14	5	7	14
	max iterations	8	11	20	8	18	30	8	18	30
	avg. iterations	5.8	7.9	15.0	6.7	13.6	21.4	6.7	13.6	21.4
	min time FSI [s]	94.5			115.4			119.2		
	max time FSI [s]	190.5			403.6			448.6		
	avg. time FSI [s]	137.7			240.6			244.9		
	time [h]	38.2			66.8 (174.9%)			68.0 (178.0%)		
d	extrapolation order	reference case			yes 1			yes 5		
	notation	FSI	F	S	FSI	F	S	FSI	F	S
	min iterations	5	5	11	5	8	14	5	8	14
	max iterations	8	11	20	8	18	23	8	18	23
	avg. iterations	5.8	7.9	15.0	6.7	13.7	18.4	6.7	13.7	18.4
	min time FSI [s]	94.5			133.4			128.3		
	max time FSI [s]	190.5			425.5			408.6		
	avg. time FSI [s]	137.7			246.0			240.8		
	time [h]	38.2			68.6 (179.6%)			66.9 (175.1%)		
mesh	extrapolation order	reference case			yes 1			yes 5		
	notation	FSI	F	S	FSI	F	S	FSI	F	S
	min iterations	5	5	11	4	5	11	4	5	10
	max iterations	8	11	20	7	9	29	7	9	28
	avg. iterations	5.8	7.9	15.0	5.5	7.4	17.7	5.3	7.1	15.7
	min time FSI [s]	94.5			88.7			89.6		
	max time FSI [s]	190.5			257.1			278.3		
	avg. time FSI [s]	137.7			138.9			130.4		
	time [h]	38.2			38.6 (101%)			36.2 (94.8%)		
d, uvp, mesh	extrapolation order	reference case			yes 1			yes 5		
	notation	FSI	F	S	FSI	F	S	FSI	F	S
	min iterations	5	5	11	4	4	9	3	3	7
	max iterations	8	11	20	7	9	17	7	9	16
	avg. iterations	5.8	7.9	15.0	5.2	5.5	12.9	4.3	4.6	9.9
	min time FSI [s]	94.5			78.4			58.5		
	max time FSI [s]	190.5			163.8			165.9		
	avg. time FSI [s]	137.7			108.5			89.7		
	time [h]	38.2			30.1 (78.8%)			24.9 (65.2%)		

Tab. 6: Extrapolation results and reference case

The reason for the worse results for extrapolations applied only to single quantities is probably, that the extrapolated quantity and the quantities which are not extrapolated do not fit together any more and therefore more iterations are necessary to reach convergence. Especially the deformed mesh, depending on the structural displacements which, in turn, depend on the fluid solution, does not match the other fields.

Figures 45 and 46 show the horizontal and vertical displacements, and the horizontal and vertical forces obtained with extrapolation of all fields d , uvp , and $mesh$ for fifth order extrapolation functions in blue over the plot of the reference case in green. Figures 47, 48, and 49 show in their left column the results of the fluid fields for the reference case and in their right column for the case where fifth order extrapolation on all three fields has been used. It is obvious that the solution is identical enough to say that there is no visible error made by using extrapolation. As shown in Appendix C this holds true for cases where more iteration steps and time are required if extrapolation is applied. There it is shown for first order extrapolation applied on the structural displacements because this is the worst case compared with the reference case.

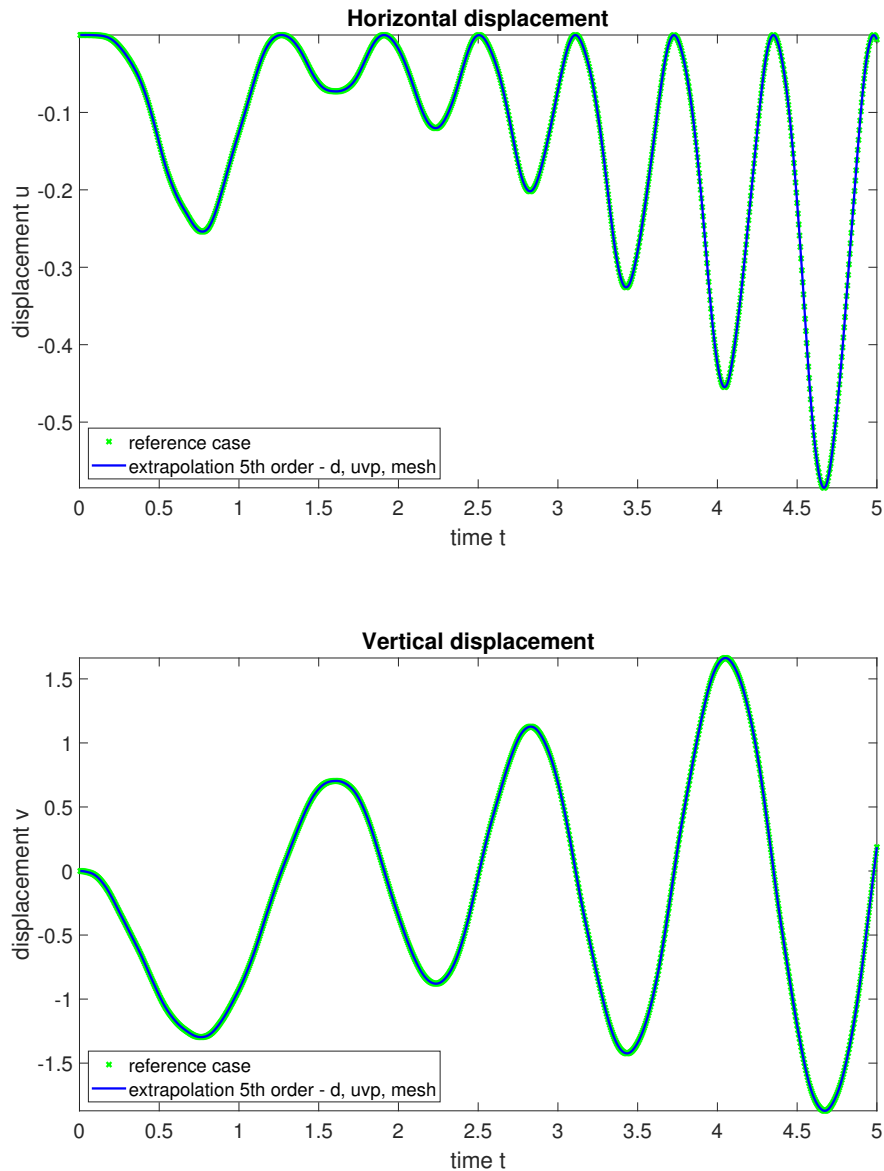


Fig. 45: Horizontal and vertical displacement of the middle point of the right edge of the plate

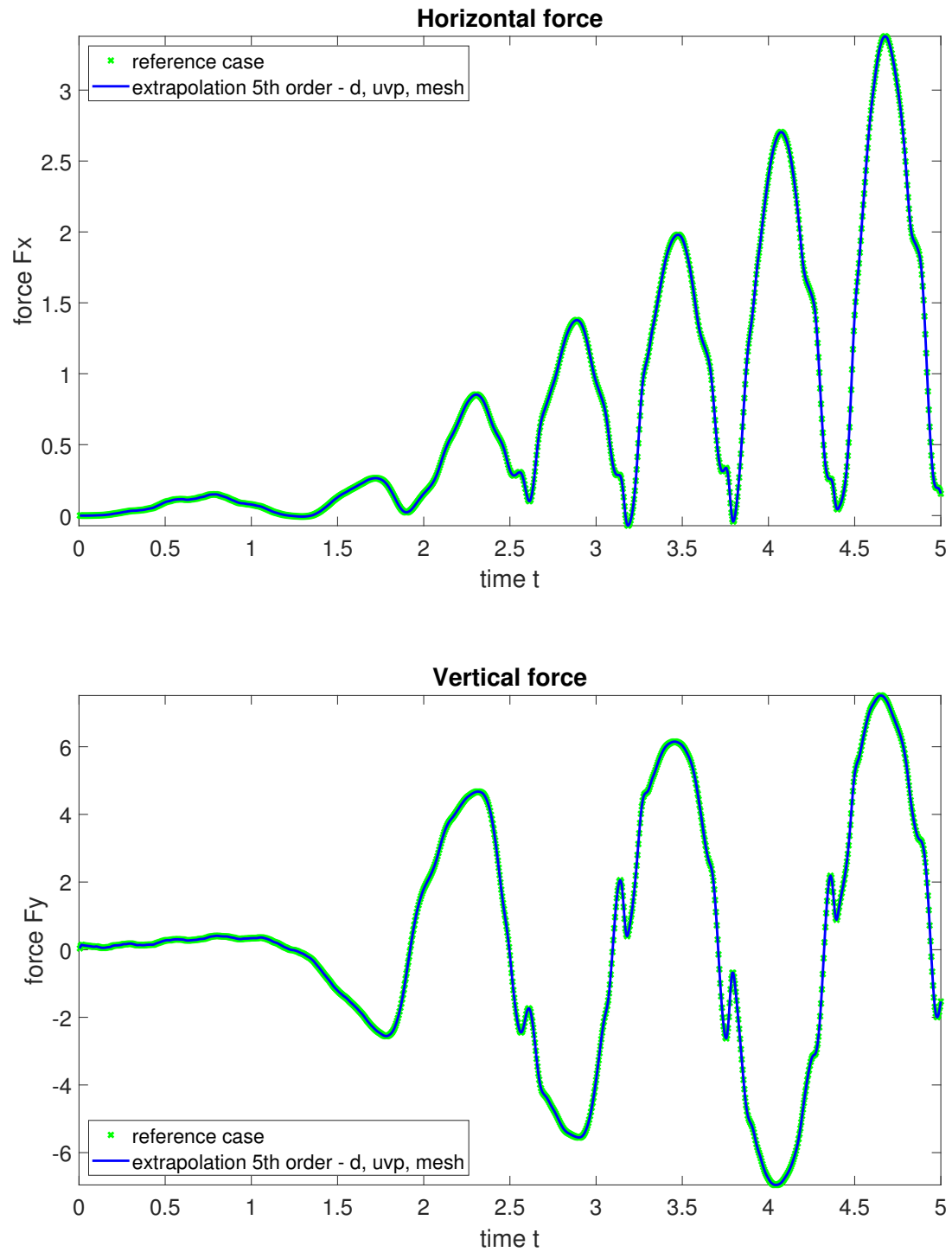


Fig. 46: Vertical and horizontal force of the middle point of the right edge of the plate

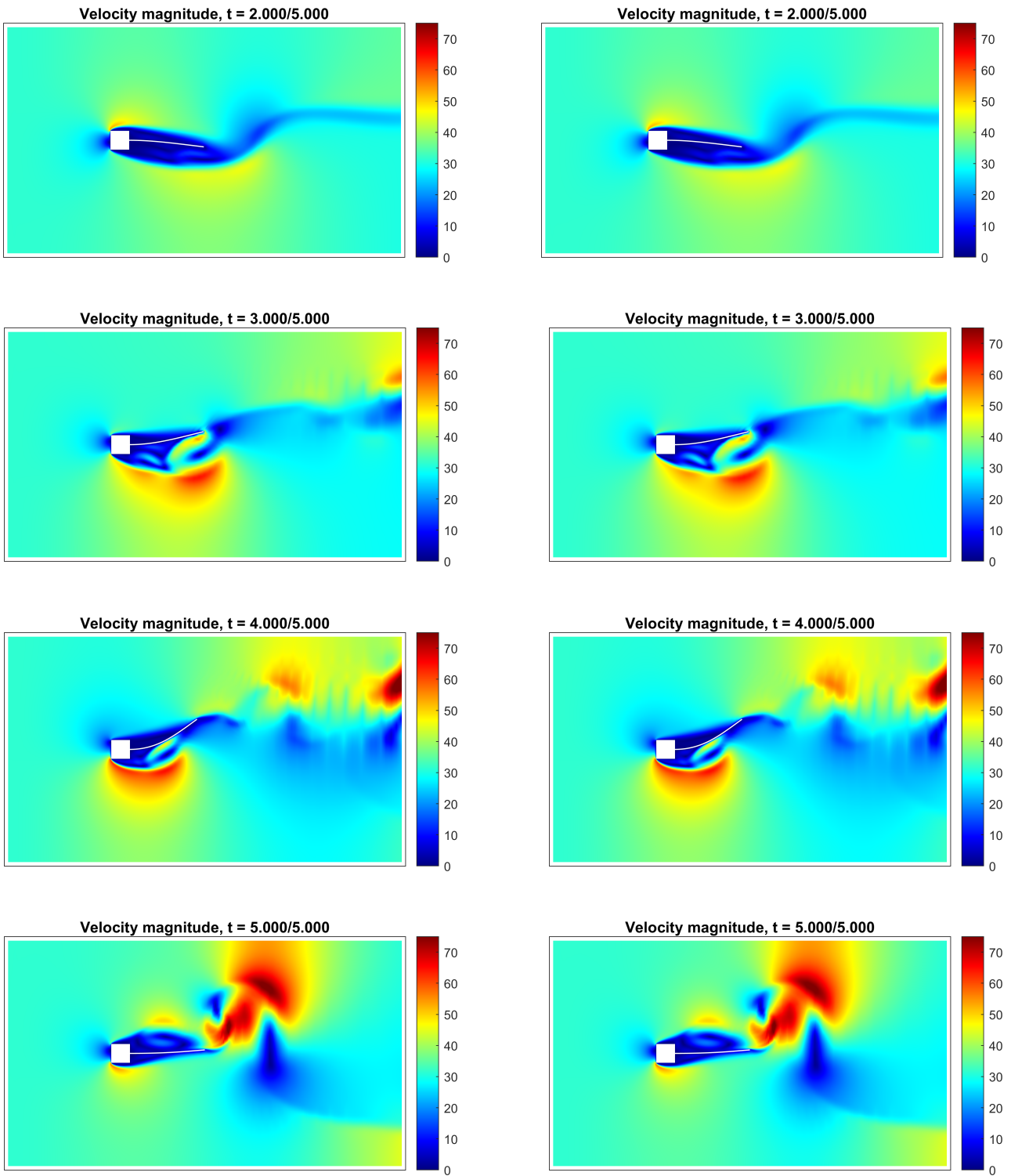


Fig. 47: Velocity field of reference case left and extrapolation right

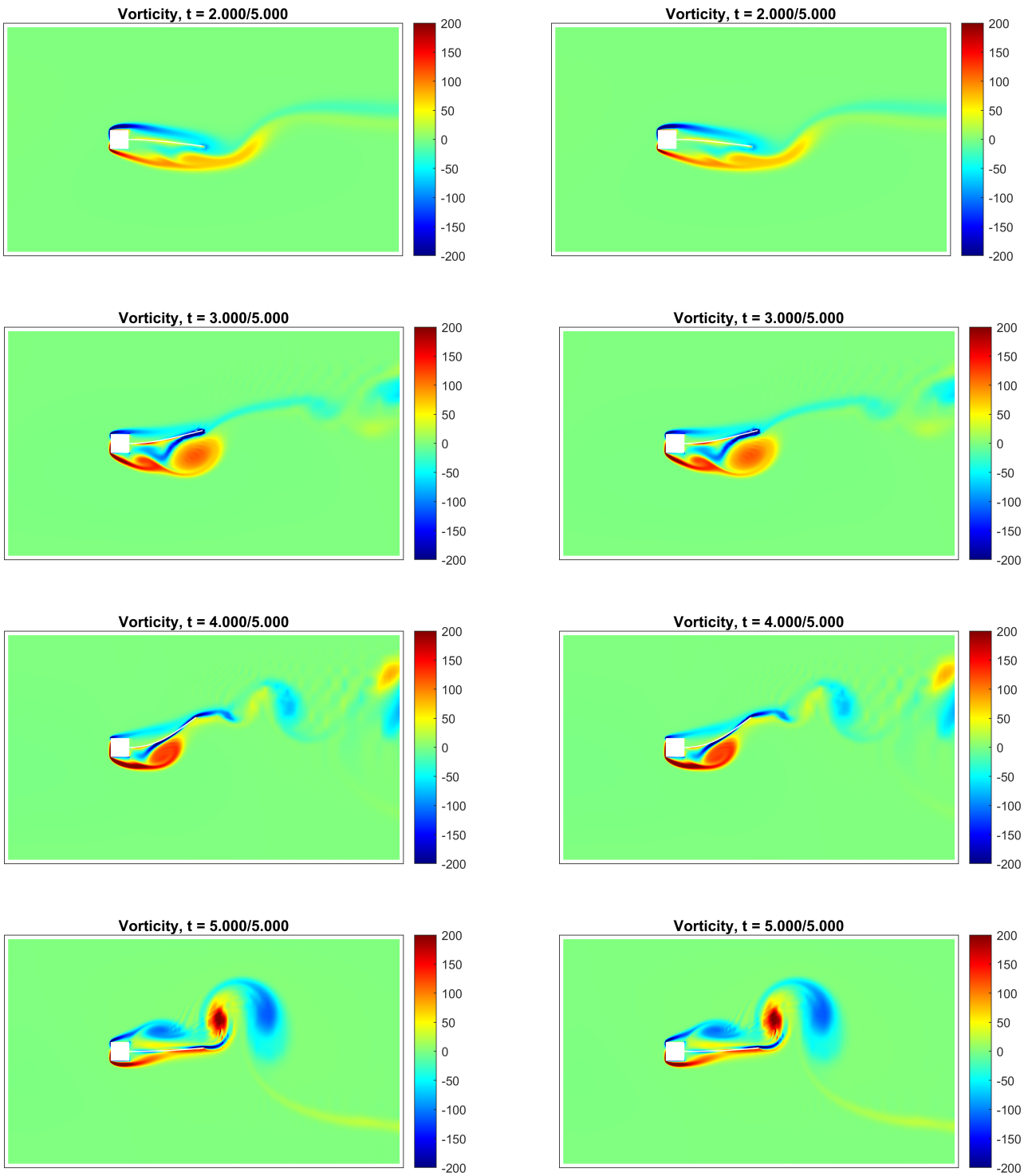


Fig. 48: Vorticity field of reference case left and extrapolation right

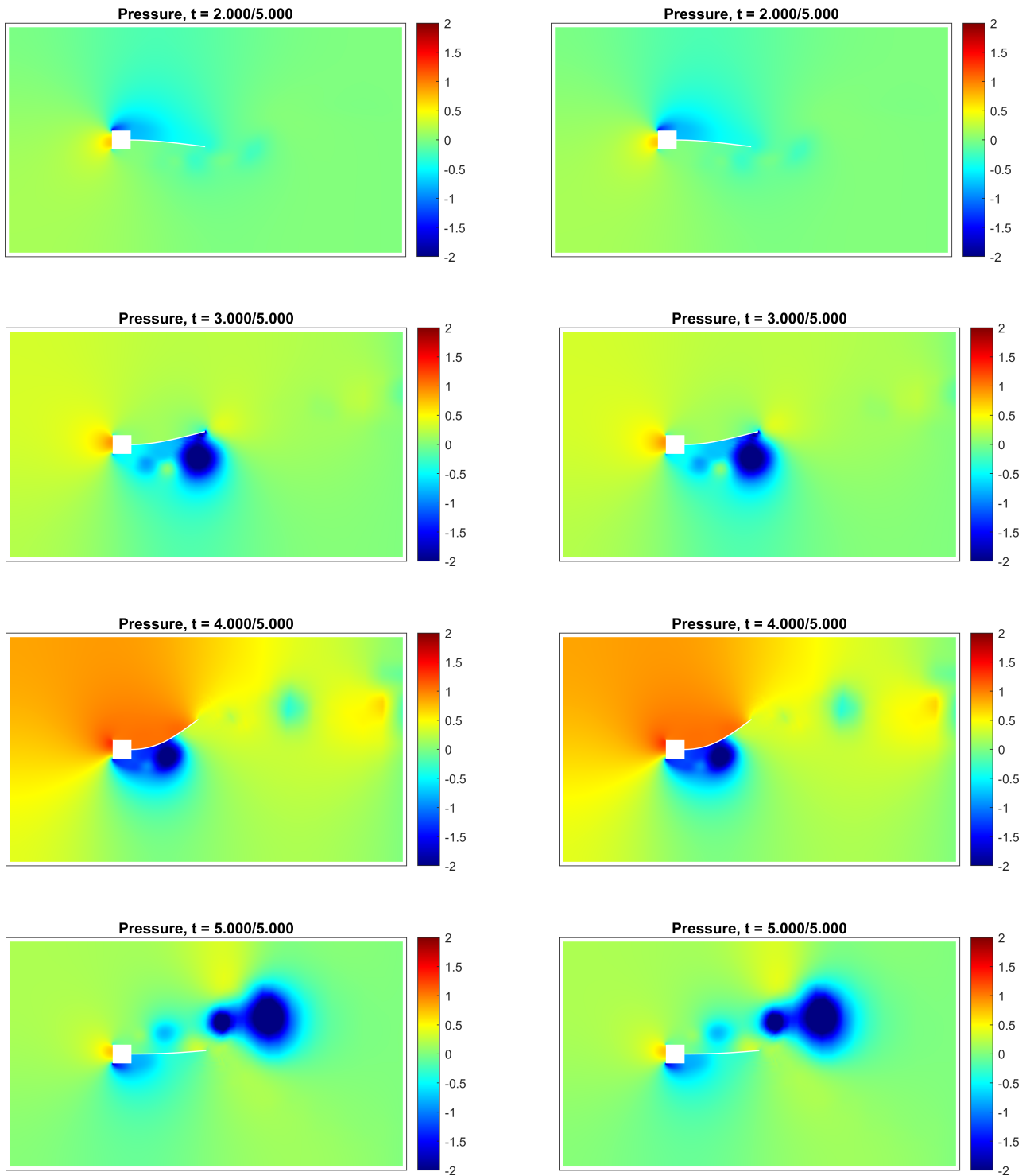


Fig. 49: Pressure field of reference case left and extrapolation right

Figure 50 shows the iteration history for the reference case (lower bar-plot) and the fifth order extrapolation function applied on the structural displacements d , the fluid solution uvp , and the mesh nodes of the deformed mesh. The green line is at four iterations and the pink line at nine iterations in both plots. It is obvious, that with extrapolation applied less iterations are necessary.

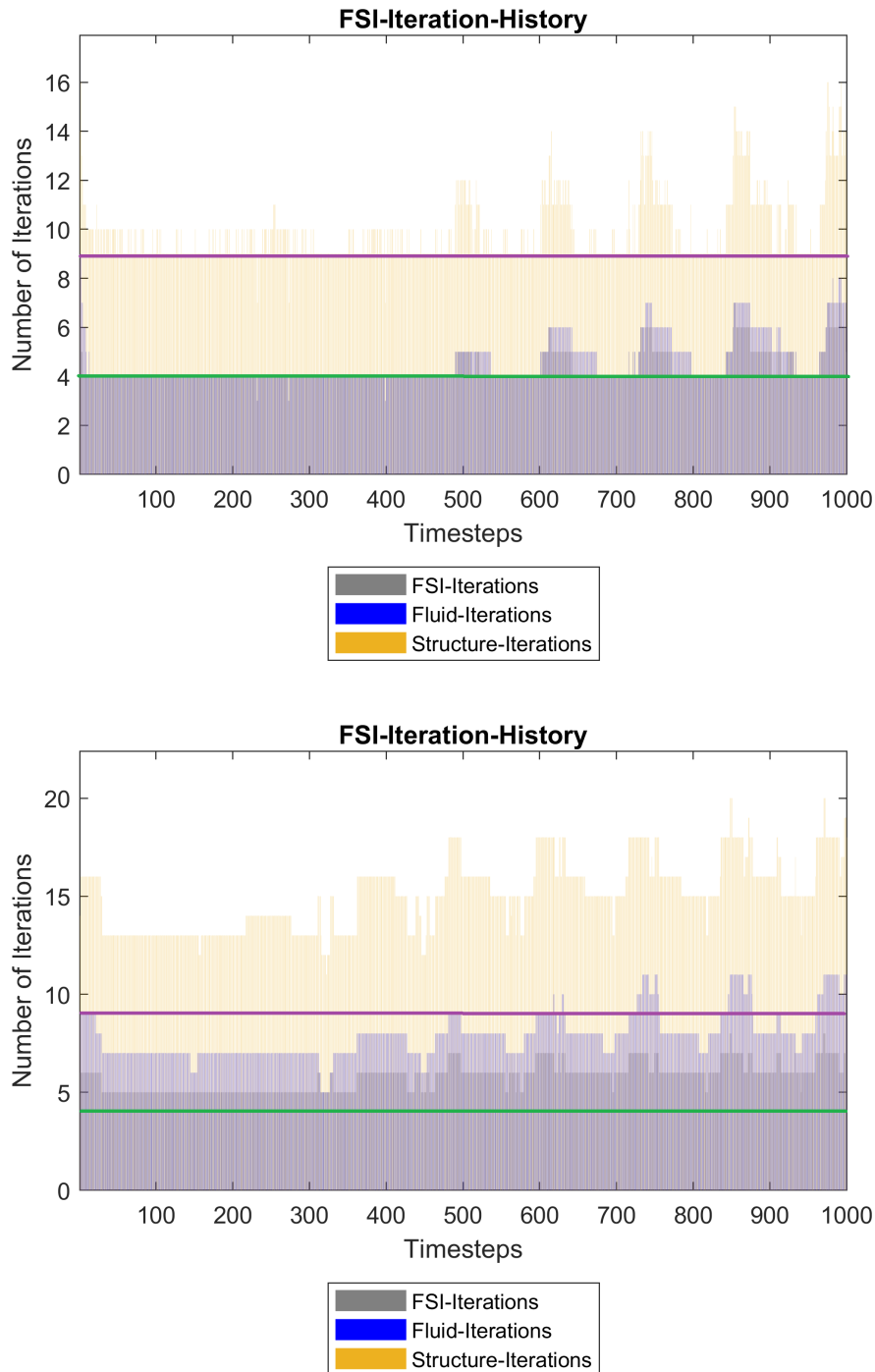


Fig. 50: Iterations over timesteps for reference case (lower bar-plot) and fifth order extrapolation applied on this case for uvp , d , and $mesh$

6 Bridge structure in FSI with wind

This bridge case is based on [8, pp. 99–113]. The model of the bridge describes a simplification of the Tacoma Narrows Bridge in Washington State, USA. This bridge collapsed in 1940 because of aeroelastic flutter [18, pp. 836–837]. FSI is a highly recommended tool to investigate structures with respect to their performance under wind loading. Tests of models of structures like towers or bridges in wind channels are common during the design process but these experiments are time consuming and expensive. Therefore computational FSI simulation is a practicable tool within the design process. However, the calculation time is still high for such cases and therefore the aim is again to find a reasonable parameter setting and to apply acceleration strategies on the chosen reference case analogously to the plate case described in section 5. Figure 51 shows the collapse of the Tacoma Narrows Bridge in 1940.



Fig. 51: Tacoma Narrows Bridge collapse [23]

Figure 52 shows the geometrical configuration of this two dimensional bridge test case as used in this thesis.

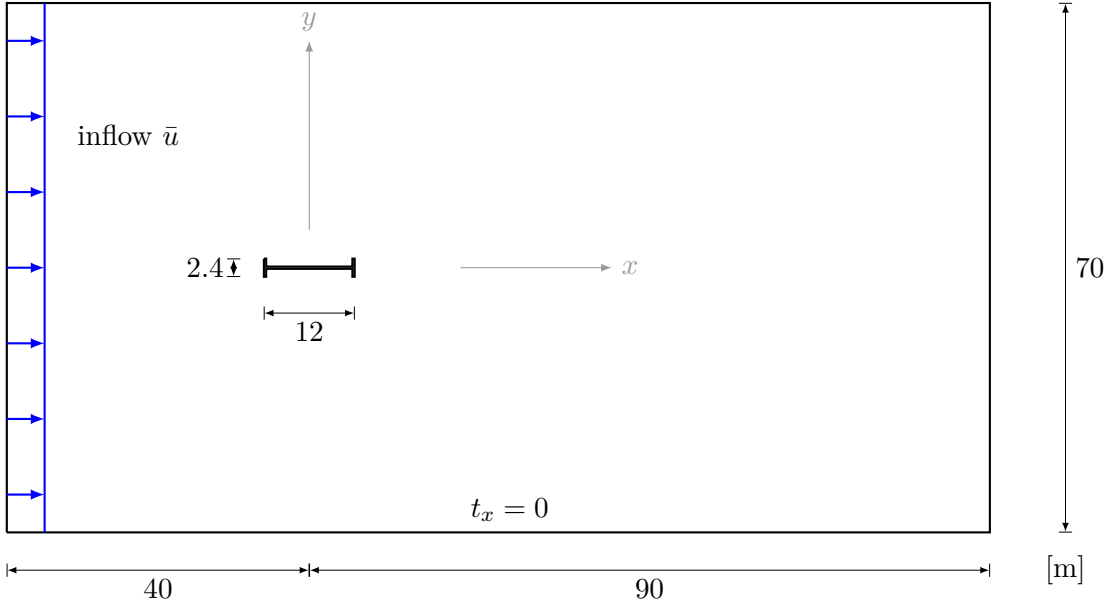


Fig. 52: Geometrical configuration and inflow condition of bridge test case

The bridge section is modelled as a rigid body which is supported horizontally. For the vertical and rotational support, springs are located at the geometric centre point of the section which is the point $(0, 0)$ in the used x - y -coordinate system. This is shown in Figure 53.

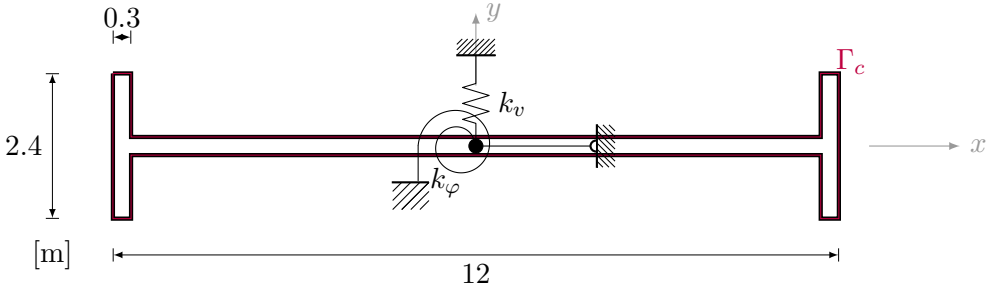


Fig. 53: Geometrical and mechanical configuration of bridge section as rigid body.

The prescribed inflow velocity is $\bar{u} = 10.0$ m/s in this case. This leads to a Reynolds number of $Re = 1500$.

The parameters used for the following studies for this case are given below.

General parameters: The considered time is 50 seconds and a time step size of 0.05 is chosen so 1000 time steps result. The tolerance for the partitioned coupled FSI loop is $\varepsilon_c = 1 \cdot 10^{-6}$, if not noted otherwise in the text.

The fluid parameters are listed below and given as:

- Fluid density $\rho_F = 1.25 \text{ kg/m}^3$
- Fluid dynamic viscosity $\mu = 0.1 \text{ Ns/m}^2$.
- $\theta = 0.5$ and $\theta_{cont} = 0.51$ for the time integration.
- Ramping is considered for the fluid due to the inflow conditions within the first four seconds.
- The tolerance boundary for the fluid is $\varepsilon_F = 1 \cdot 10^{-2}$, if not stated otherwise in the text.

For the bridge being a two-dimensional rigid body, the following parameters are defined:

- Solid mass $m = 4000 \text{ kg}$ and moment of inertia $\Theta = 80000 \text{ kg m}^2$.
- Stiffness of vertical spring is $k_v = 2467 \text{ N/m}$ and of the rotational spring $k_\varphi = 126330 \text{ Nm}$.
- Time discretization is done using Newmark's method.

The physical parameters are the same as given in [8, p. 105].

The spatial discretization is done in the same way for all studies and analogously to the descriptions in sections 4.2 and 5. Within the program code the spatial discretization is defined. At first a mesh containing several so-called super blocks is generated for the entire spatial domain. In a further step the fluid mesh and the solid mesh are split. For the fluid domain two meshes are generated because the element order for the mesh used to obtain the fluid pressure is one order lower than the mesh used for all other calculations as described above. These two meshes are used for the Taylor-Hood-elements $Q2/Q1$ [7] (see section 2.3), which means that for this test case again, if not clearly stated otherwise, the order of the pressure mesh is linear. For the entire spatial discretization quadrilateral elements are used. Figure 54 shows the fluid mesh used for this test case.

According to Hübner [8, p. 105] the chosen parameters for the rigid body leads to eigenfrequencies for the spring-mass-system of $f_v = 0.125 \text{ Hz}$ and $f_\varphi = 0.20 \text{ Hz}$ which are about the eigenfrequencies of the Tacoma Narrows Bridge.

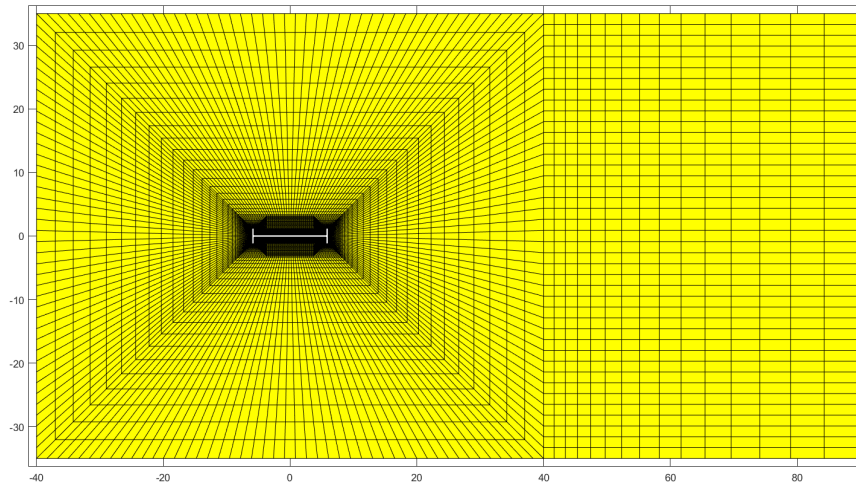


Fig. 54: FE-mesh for fluid domain

As stated in section 4.2 and used before for the plate test case in section 5 the mesh is finer near the fluid-structure interface Γ_c . This refined mesh is shown in a detailed view of Figure 54 in Figure 55.

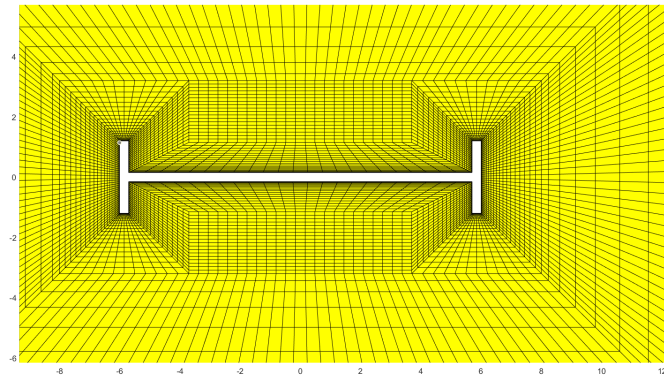


Fig. 55: FE-mesh for fluid domain around Γ_c around bridge H-section

6.1 Tolerance study

Analogously to 5.1 a tolerance study is done here. The aim is again to find a setting for the tolerances which is good enough to produce accurate results in reasonable time. The algorithm for the partitioned coupling loop and the fluid solver are the same as for the plate test case before. The solid domain is a rigid body and therefore another sub-solver is used here as described in section 3.1.

The only two parameters which are used systematically varied in contrast to those given above are the tolerances ε_c and ε_F . These two parameters are given as

$$\varepsilon_c = 1 \cdot 10^{-i} \quad (6.1)$$

with

$$i \in [1, 2, 3, 4, 5, 6]$$

and

$$\varepsilon_F = 1 \cdot 10^{-j} \quad (6.2)$$

with

$$j \in [1, 2, 3, 4]$$

These leads to 24 computations in a time interval of 50 seconds, i.e. $t \in [0, 50]$ in the configuration described above. The calculation times and numbers of iterations given in the result tables are here again with respect to the parallel computer specified in Appendix E. The calculation time includes pre-processing (meshing) and processing but not post-processing. The number of iterations for the partitioned coupling loop are the numbers for each time step. For fluid and solid for one partitioned coupling loop the iterations for all fluid iterations within the fluid solver are summed up. Table 7 shows the calculation time for the entire analysis on the parallel computer in hours.

$\varepsilon_c = 1 \cdot 10^{-i}$ is the tolerance boundary of the partitioned coupling loop and $\varepsilon_F = 1 \cdot 10^{-j}$ of the Picard iteration loop in the fluid solver used within the partitioned coupled loop. Figure 56 shows Table 7 visualized in a bar plot.

i \ j	1	2	3	4
1	25.4	34.1	44.2	56.8
2	28.4	36.9	46.8	60.8
3	32.3	39.6	50.0	64.0
4	58.7	63.3	72.4	75.1
5	65.5	68.4	75.6	87.5
6	73.4	76.9	81.8	92.8

Tab. 7: Calculation time to find parallel computed solution in hours

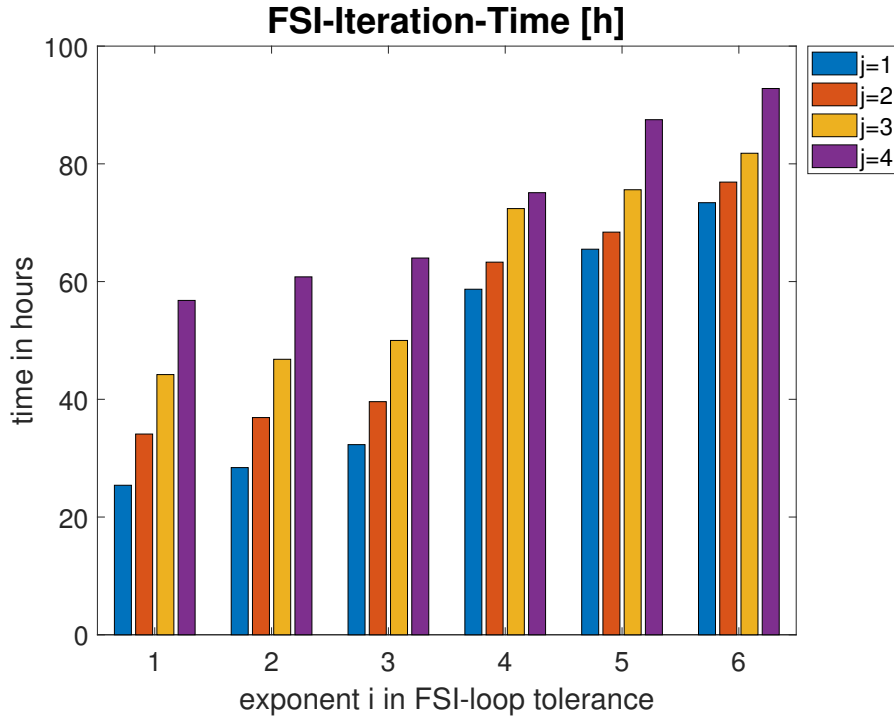


Fig. 56: Calculation time to find parallel computed solution in hours

Table 3 shows the average iterations for the partitioned coupled loop *FSI* and for the fluid solver *F*. This table is visualized in Figure 57 and Figure 58.

$j \rightarrow$	1		2		3		4	
$i \downarrow$	FSI	F	FSI	F	FSI	F	FSI	F
1	3.0	5.4	3.0	7.9	3.0	10.7	3.0	14.1
2	3.6	6.0	3.5	8.4	3.5	11.2	3.5	15.0
3	4.3	6.8	4.0	8.9	4.0	11.7	4.0	15.5
4	5.6	8.0	4.9	9.9	4.5	12.2	4.4	16.0
5	7.0	9.4	5.9	10.9	5.2	13.0	4.9	16.5
6	8.4	10.8	7.4	12.3	6.5	14.2	5.9	17.5

Tab. 8: Iteration steps to find parallel computed solution

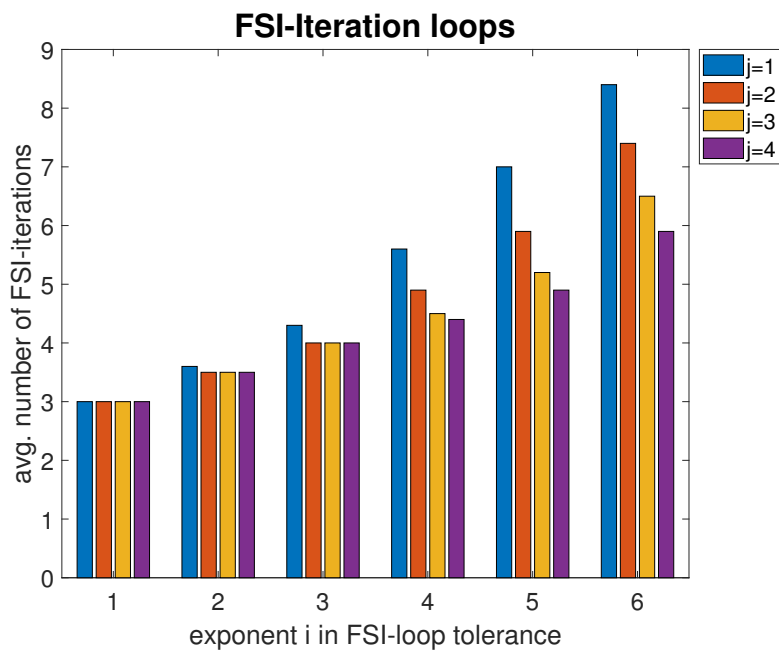


Fig. 57: Average number of FSI-Iteration loop iterations to find parallel computed solution

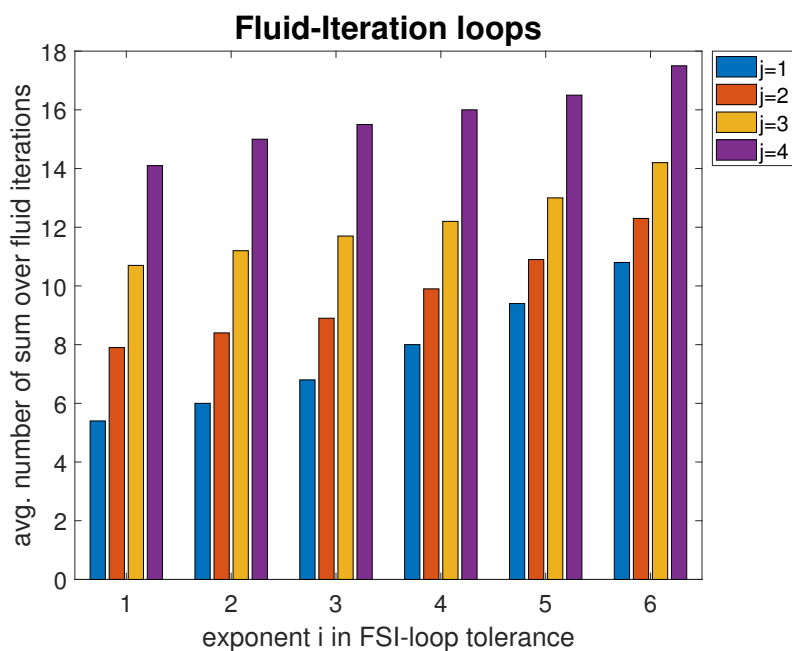


Fig. 58: Average number of summed fluid iterations to find parallel computed solution

Considering Table 7 and Figure 56 it can clearly be seen that higher exponents i and therefore smaller tolerances ε_c for the partitioned coupling loop need more time. This is expected because the higher

accuracy may need more iterations of the partitioned coupling loop and therefore more time to reach convergence. This was also observed for the previous considered plate case in section 5.1.

Figures 57 and 58 show similar results to Figures 29 and 30 in the analogous study for the plate case which is expected here. Again this leads to the interpretation that the tolerance boundary for the partitioned coupling loop is decisive as described in section 5.1. To find the best setting of parameters for this bridge case analogously to the plate case it is necessary to consider the quality of the results in addition to the amount of calculation time and number of iteration steps needed. Figures 59, 60, 61, 62, and 63 show the vertical fluid force, the vertical spring force, the fluid moment, the spring moment and the angle of rotation for $i = 1$ and appropriate $j \in [1, 2, 3, 4]$, and for $i = 6$ and appropriate $j \in [1, 2, 3, 4]$ over time t of analysis which is in this case 50 seconds. For the vertical fluid forces an oscillation occurs for $i = 1$ as shown in Figure 64. A numerical error is also seen in the fluid moment at about two seconds. These errors occur only for $i = 1$. For $i \geq 2$ no differences of the solution plots are visible.

Considering all results described here and the plots of the velocity, vorticity, and pressure fields of the fluid domain the setting for the tolerances of the partitioned coupling loop and the fluid solver are chosen as

$$\varepsilon_c = 1 \cdot 10^{-6} \quad (6.3)$$

and

$$\varepsilon_F = 1 \cdot 10^{-2} \quad (6.4)$$

as for the plate case before in section 5.1. Figures 65, 66, and 67 show the plots of the resulting fluid fields for this configuration.

Again, it should be noted that the results may be different for larger or smaller time steps and other physical parameters. Therefore further investigations including more parameter studies and a larger time range would have been necessary. This, however, is beyond the scope of this thesis for time reasons.

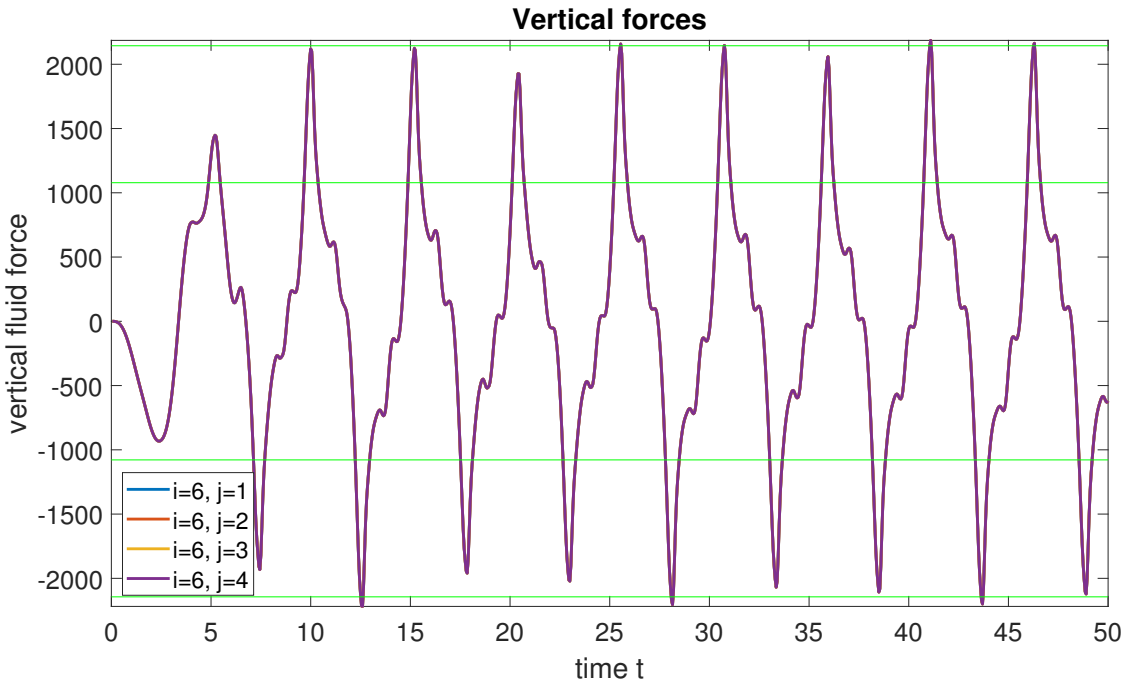
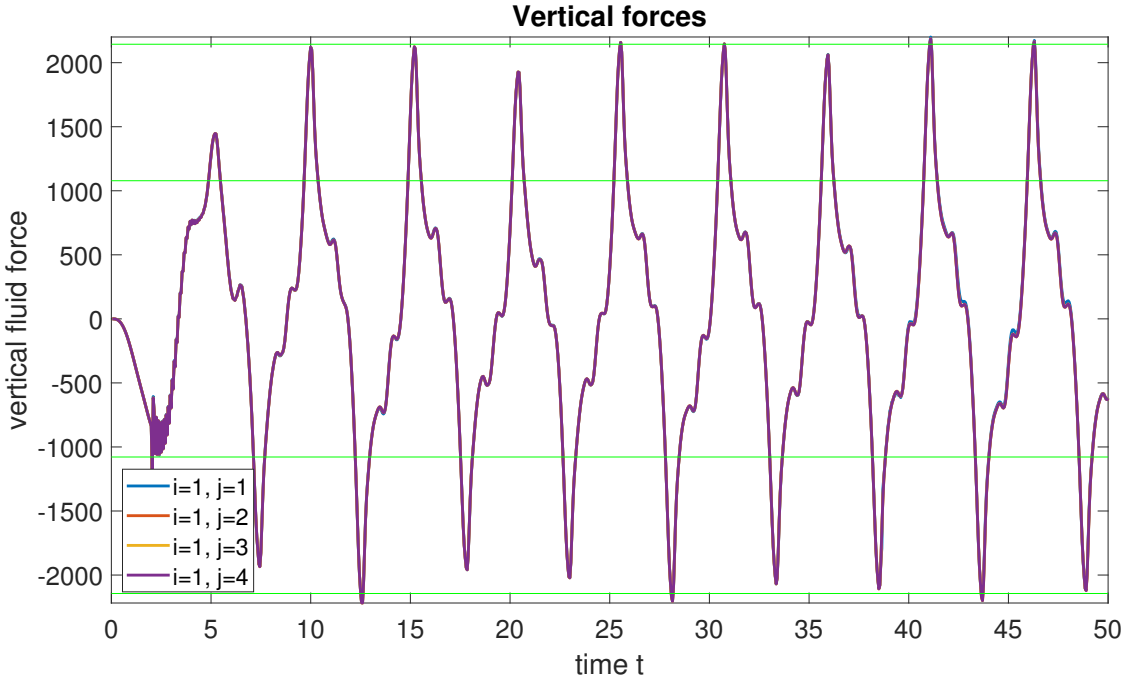


Fig. 59: Vertical fluid forces

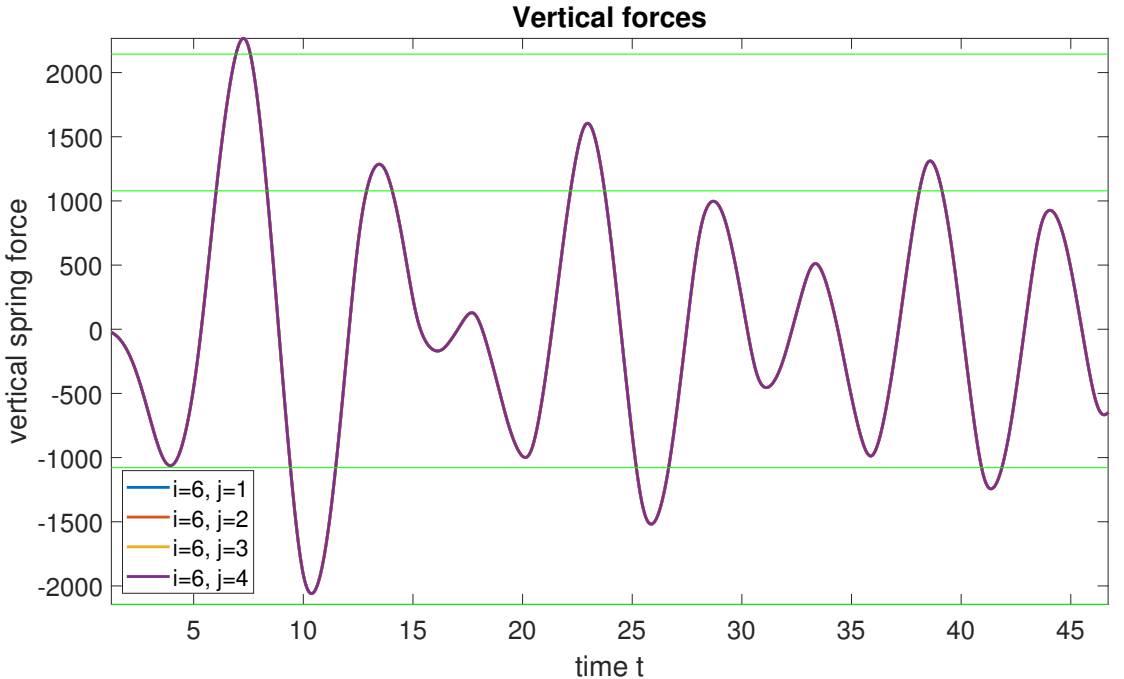
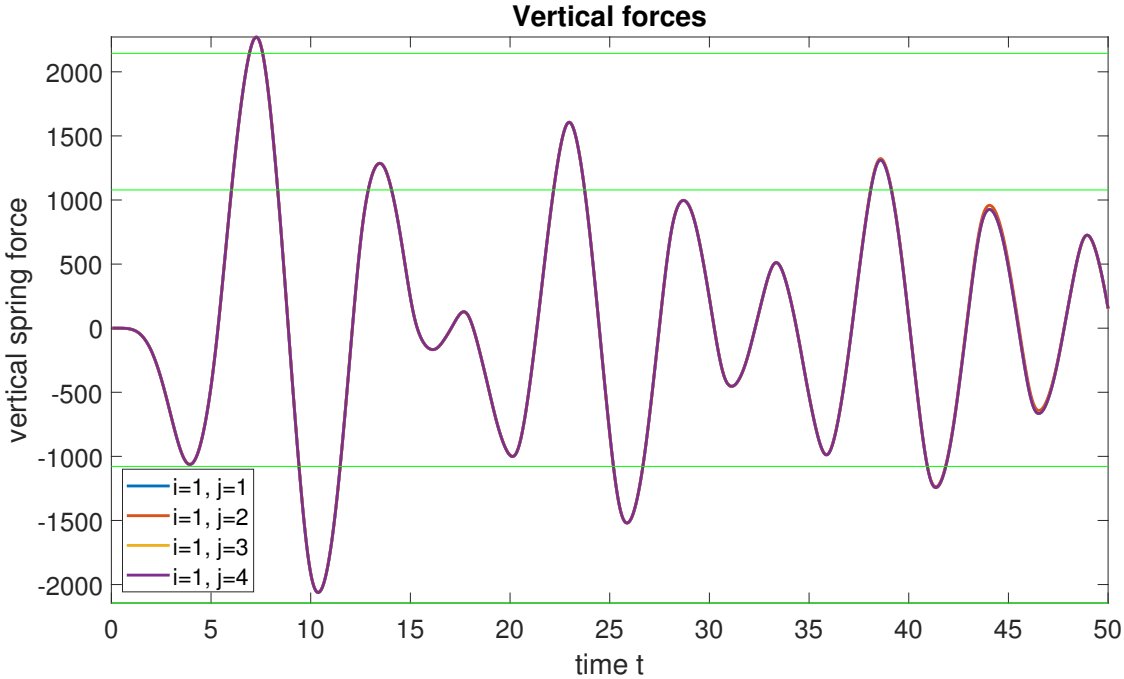


Fig. 60: Vertical spring forces

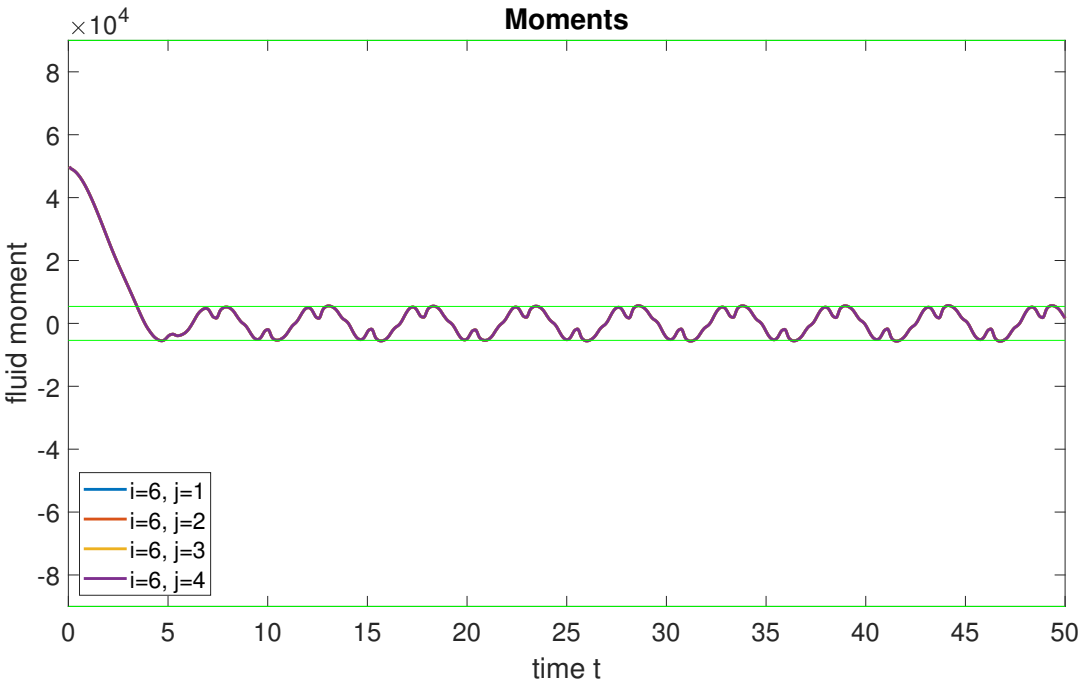
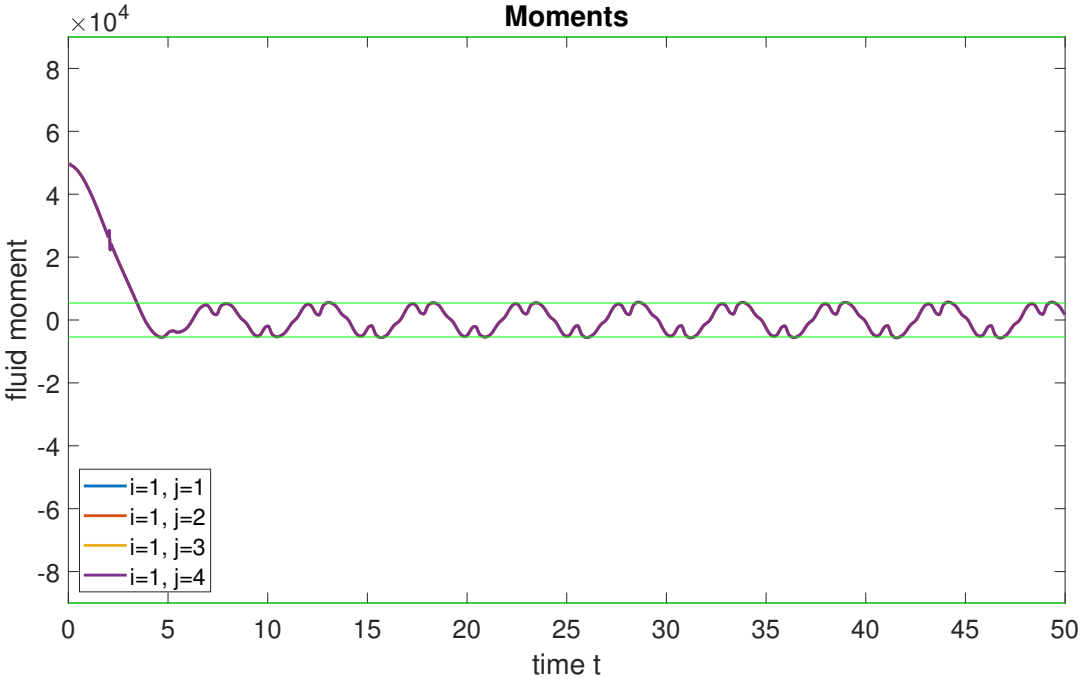


Fig. 61: Fluid moments

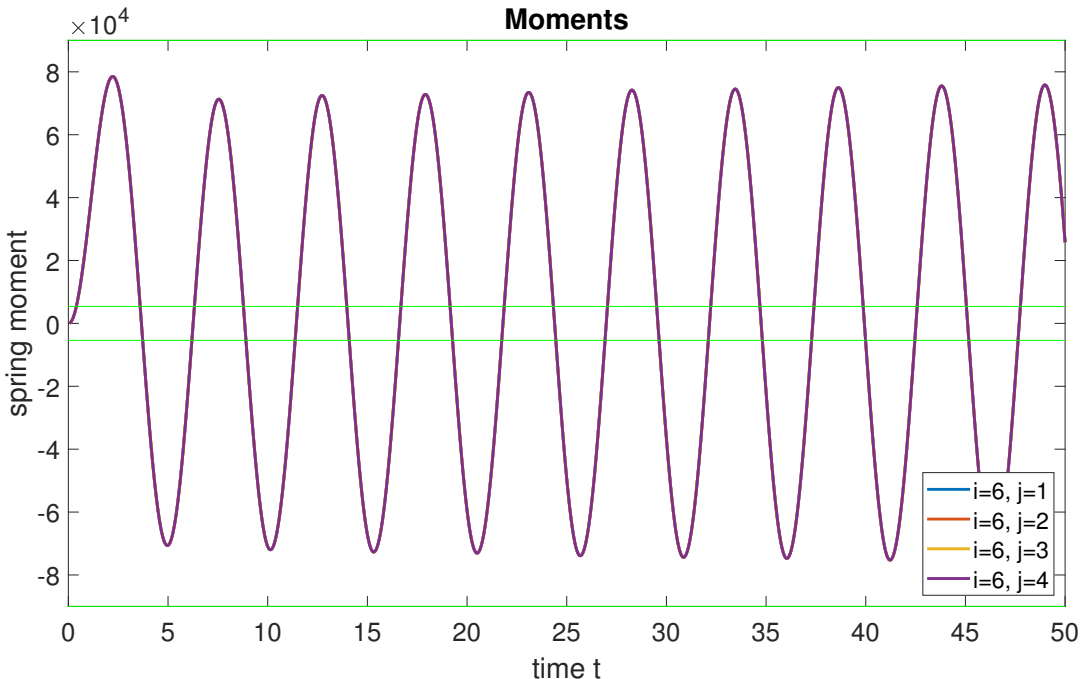
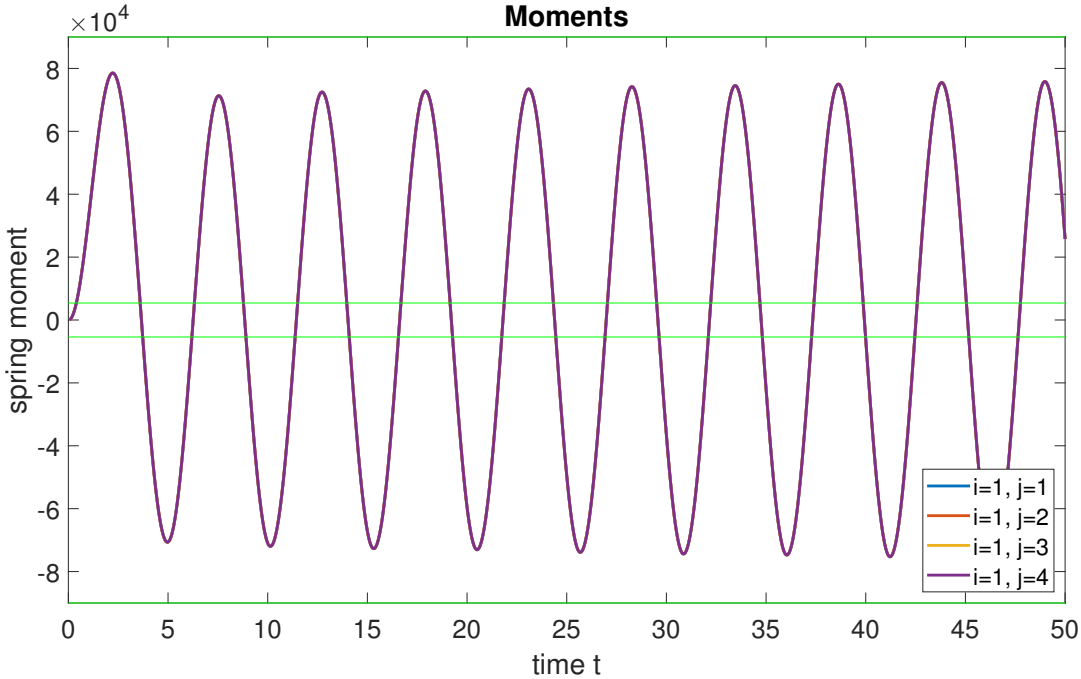


Fig. 62: Spring moments

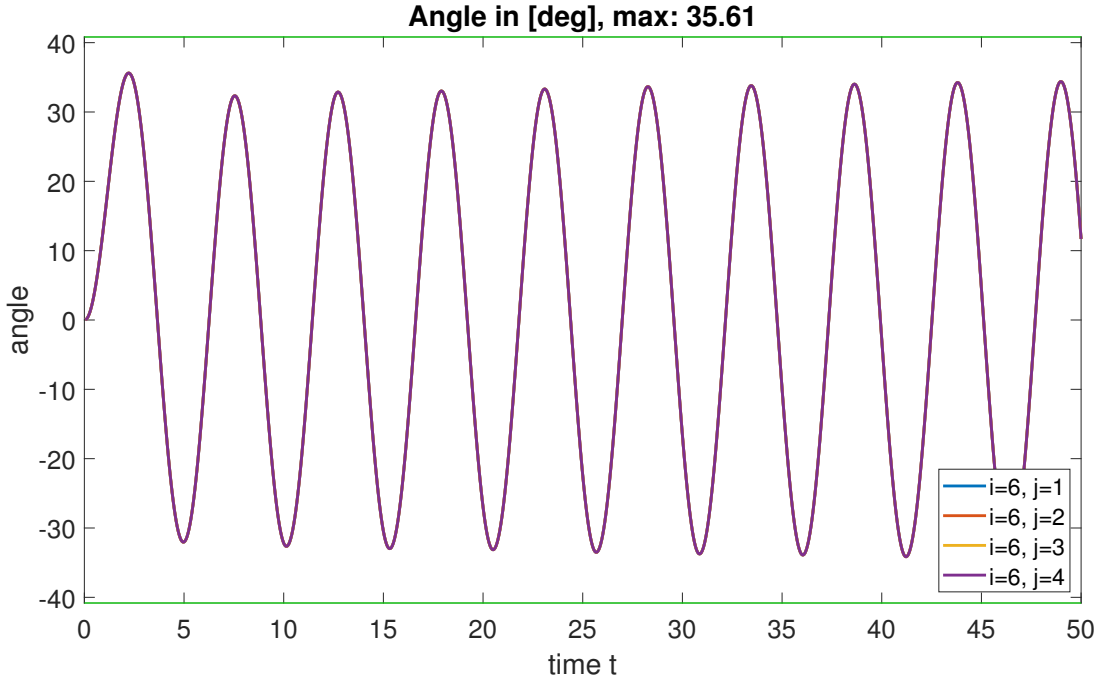


Fig. 63: Angle of rotation in degrees

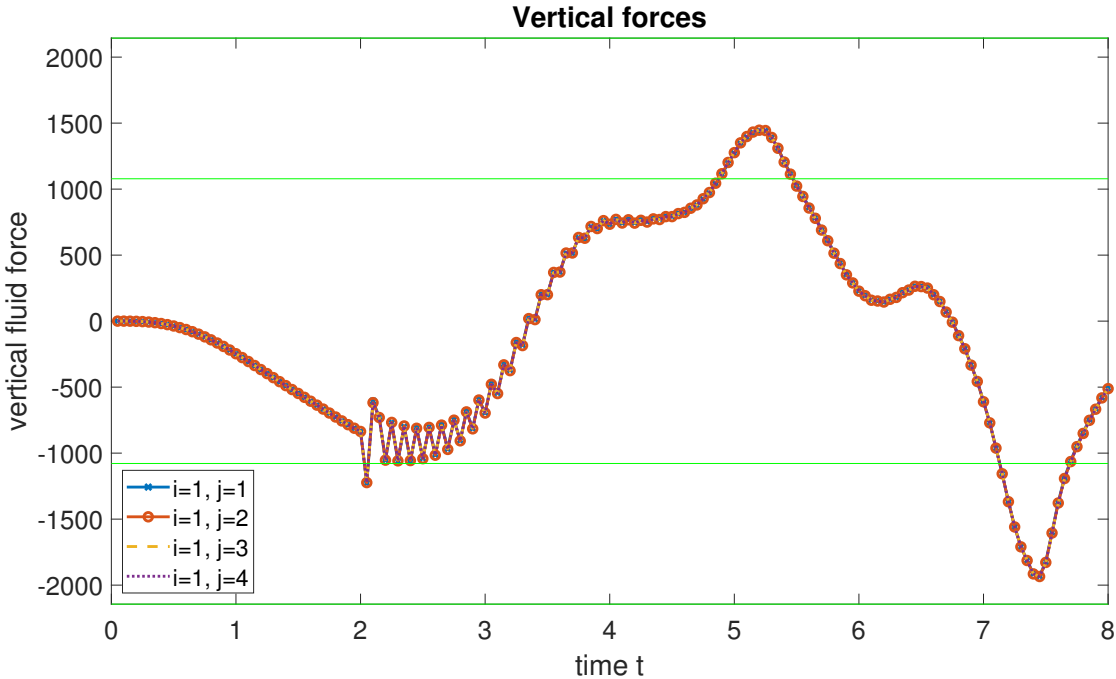


Fig. 64: Vertical fluid forces over first 8 seconds

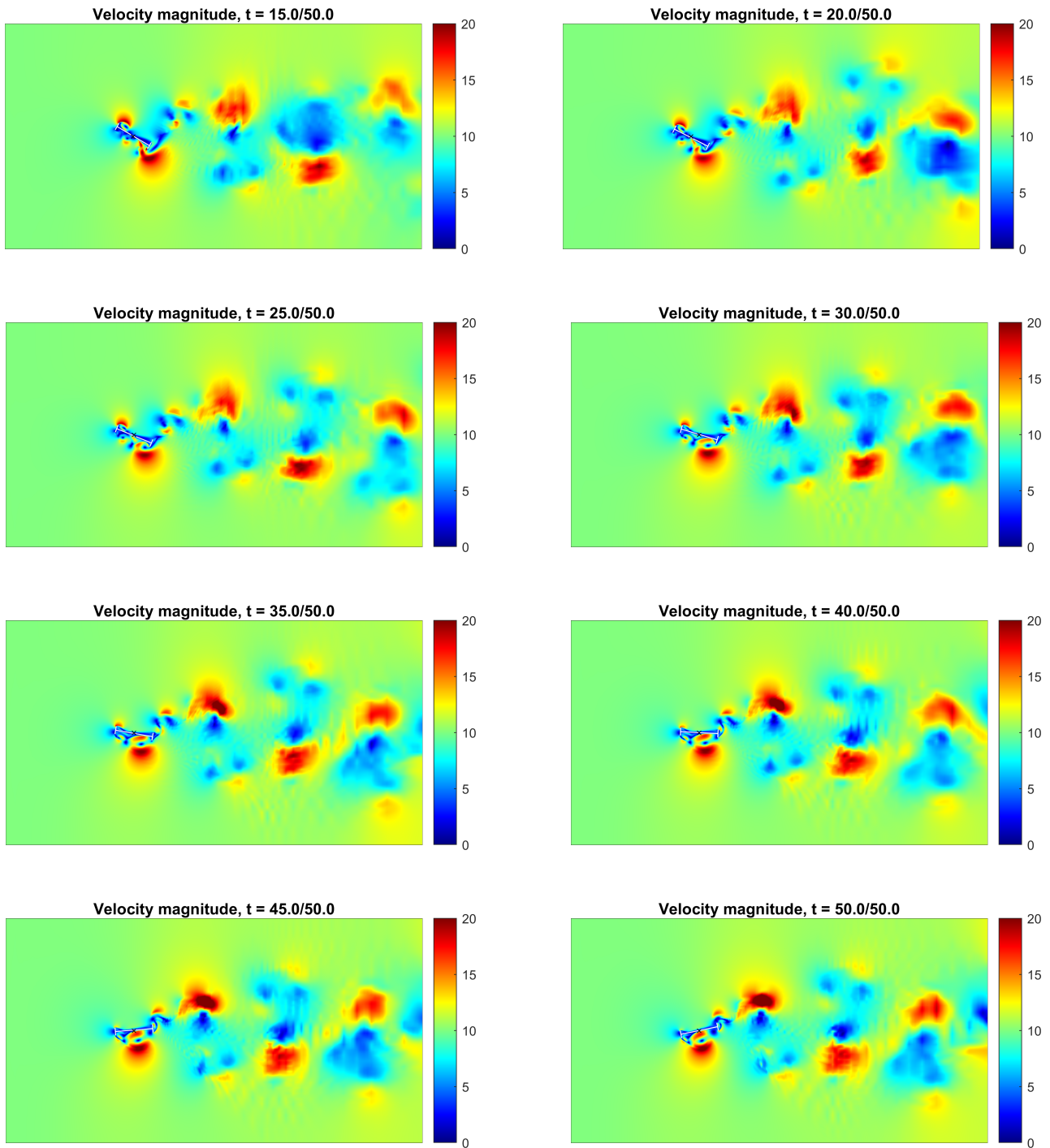


Fig. 65: Velocity field of reference case $\varepsilon_c = 10^{-6}$ and $\varepsilon_F = 10^{-2}$

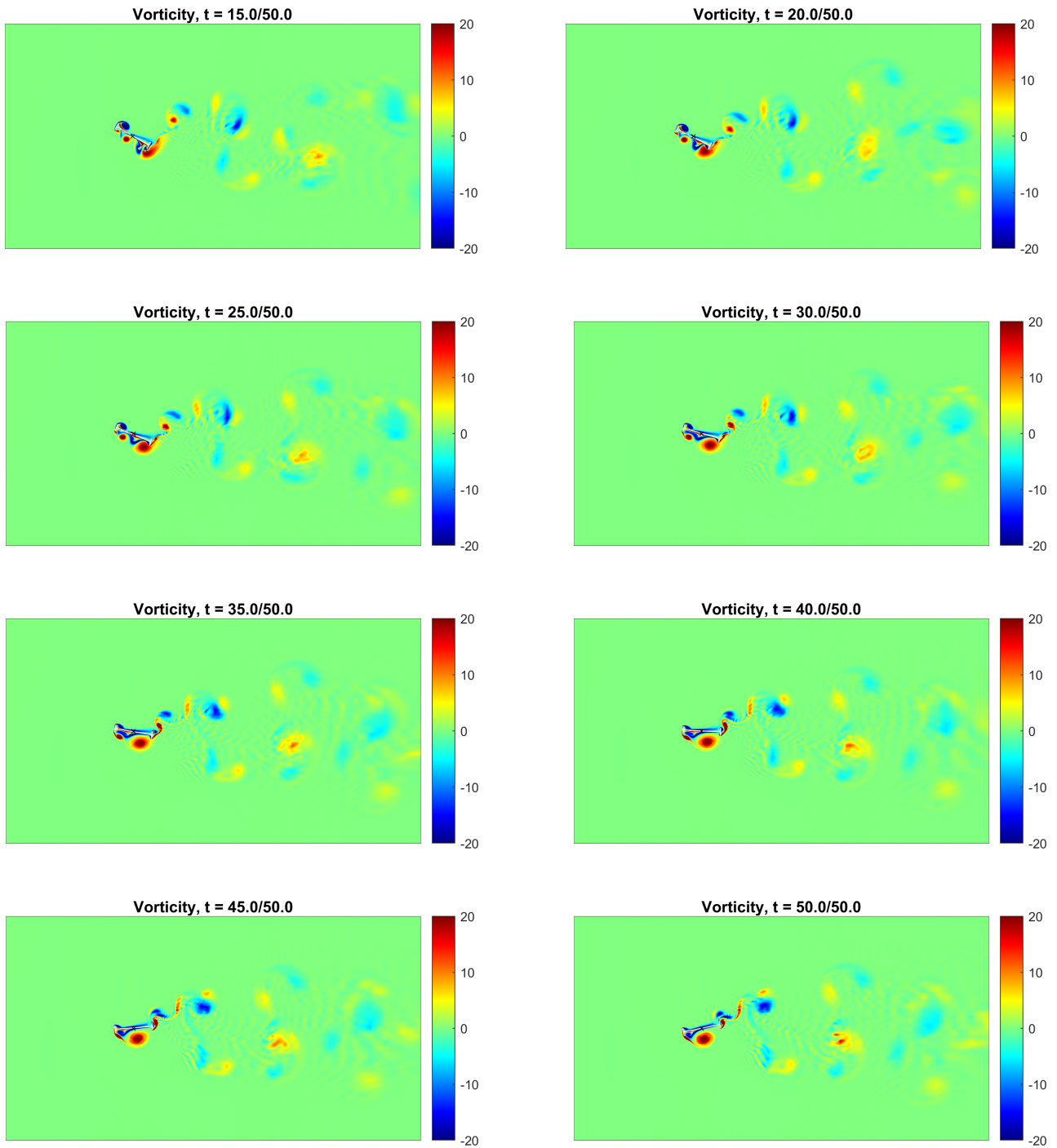


Fig. 66: Vorticity field of reference case $\varepsilon_c = 10^{-6}$ and $\varepsilon_F = 10^{-2}$

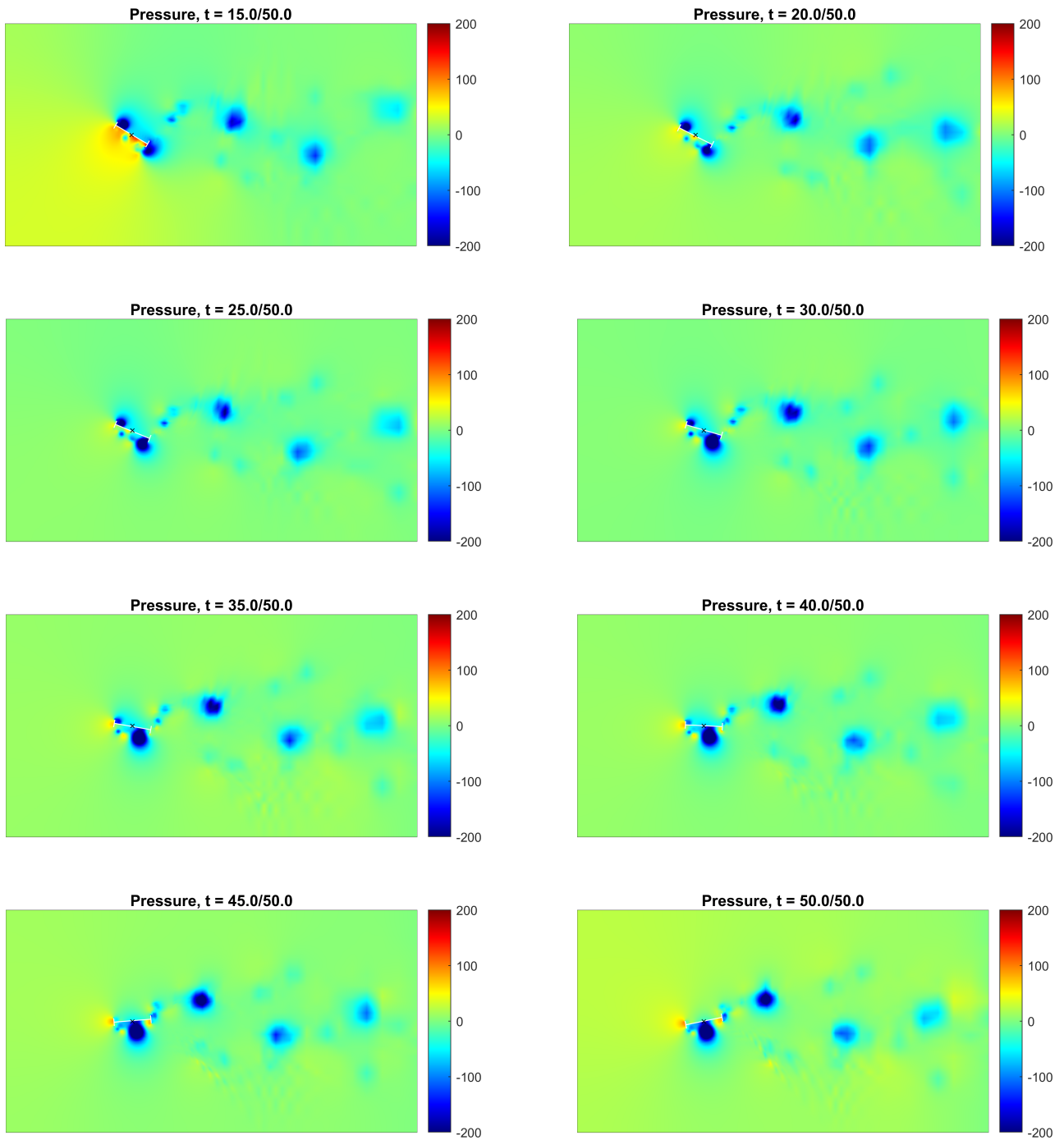


Fig. 67: Pressure field of reference case $\varepsilon_c = 10^{-6}$ and $\varepsilon_F = 10^{-2}$

6.2 Aitken's relaxation

The calculation time for the standard setting chosen in section 6.1 was 76.9 hours with the parallel computer for pre- and processing steps. The aim, as it was before for the plate case, is to reduce the needed calculation time and get results within the same range of accuracy than before. The first approach here is again *Aitken's relaxation* or *Aitken's Δ^2 method* as described in [15]. Aitken's relaxation is used on the structural displacements \mathbf{d} . The used Algorithm 3 is given in section 5.2 and Figure 38 visualizes this algorithm. The equations used in this procedure are also given in section 5.2.

Table 9 shows the number of iteration steps and required time compared to the reference case with $\varepsilon_c = 1 \cdot 10^{-6}$ and $\varepsilon_F = 1 \cdot 10^{-2}$. AR stands for Aitken's relaxation.

case	no AR		AR	
	FSI	F	FSI	F
min. iterations	4	6	4	6
max. iterations	10	15	10	15
avg. iterations	7.4	12.3	7.4	12.3
min. time FSI [s]	174.4		100.8	
max. time FSI [s]	436.0		296.5	
avg. time FSI [s]	276.7		210.4	
time [h]	76.9		58.4 (75.9%)	

Tab. 9: Results of reference case left and Aitken's relaxation applied on this case right.

For this case about 18.5 hours can be saved for the entire calculation time which is about 24.1%. This is much more than for the plate test case. The improvement achieved using Aitken's relaxation to accelerate the fluid-structure interaction for the bridge test case is 6.5 times higher compared with the plate test case but the calculation time for the reference case is about two times higher for the bridge case.

Figure 68 shows the fluid and spring forces, Figure 69 shows the fluid and spring moments, and Figures 70, 71, and 72 show in their left column the results of the fluid fields for the reference case and in their right columns for the case where Aitken's relaxation has been used. It is obviously to see that the solution is close enough to conclude that there is no visible error made by using Aitken's relaxation.

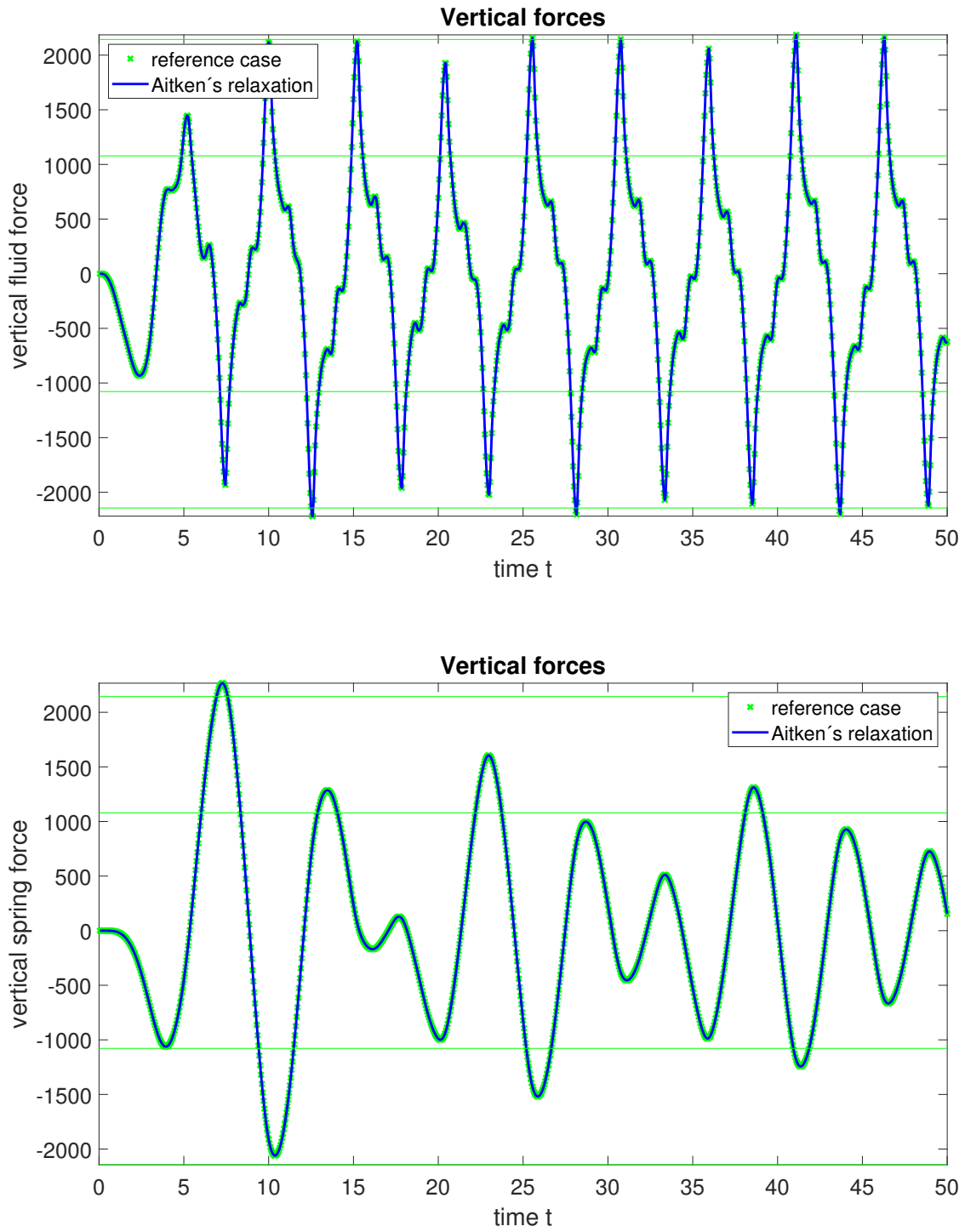


Fig. 68: Vertical forces

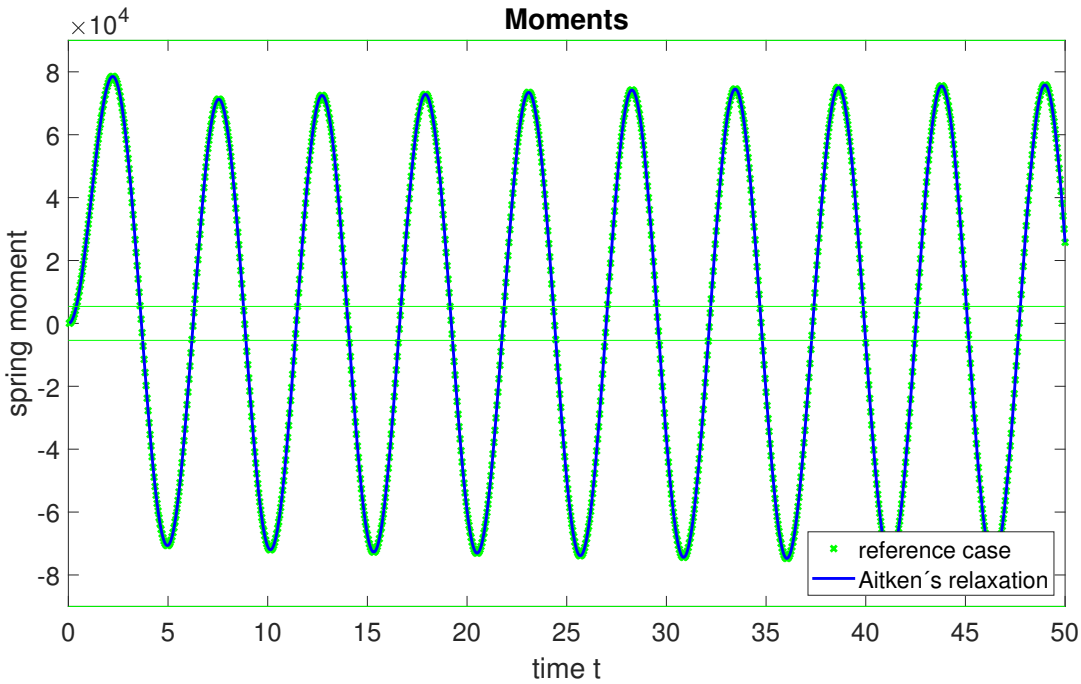
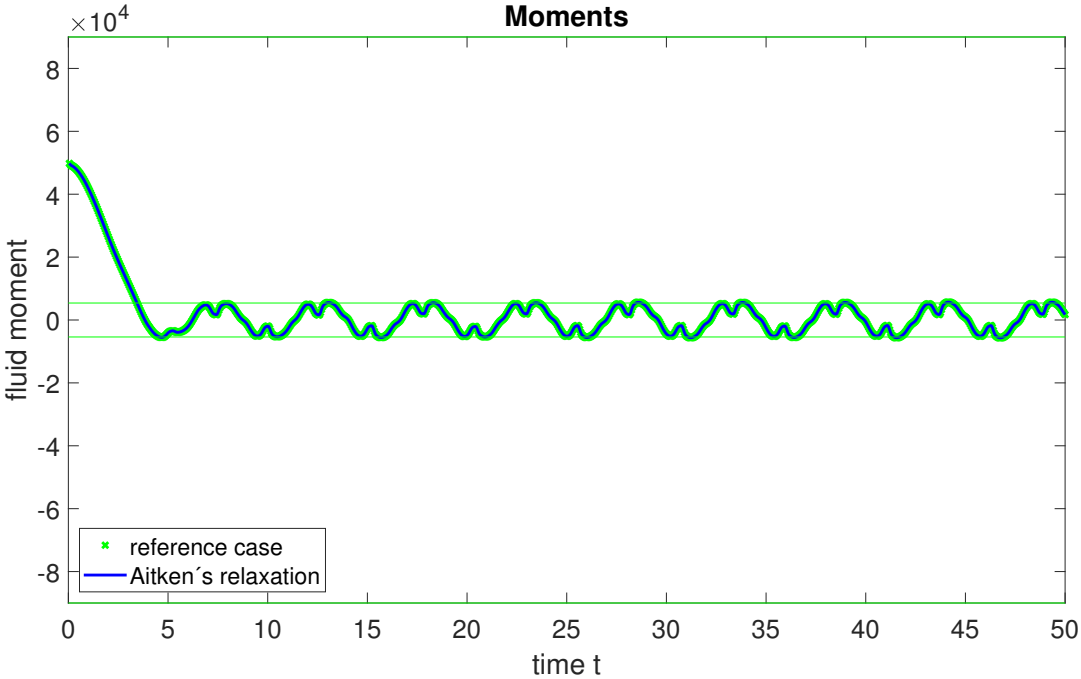


Fig. 69: Moments

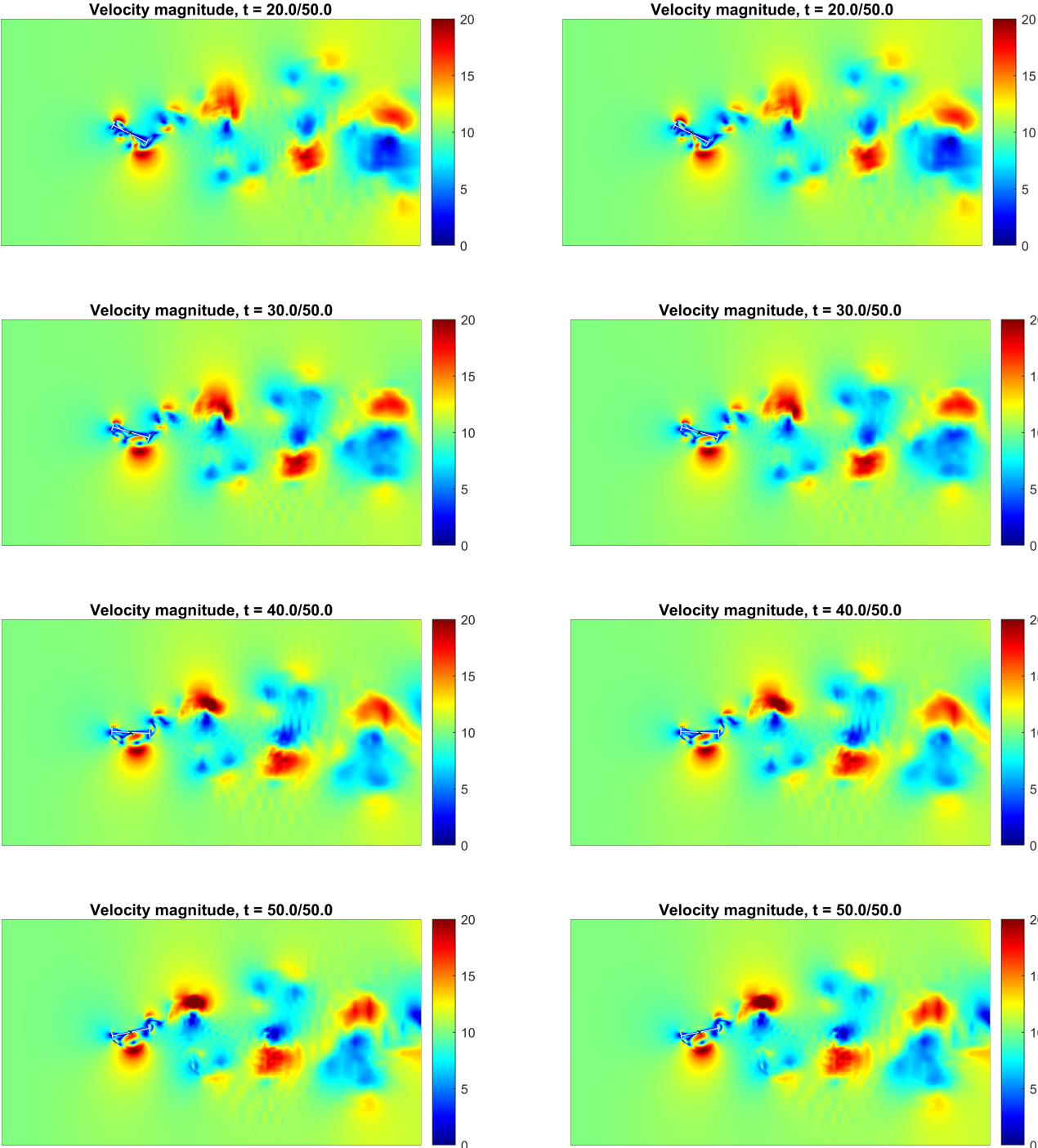


Fig. 70: Velocity field of reference case left and Aitken's relaxation applied on this case right

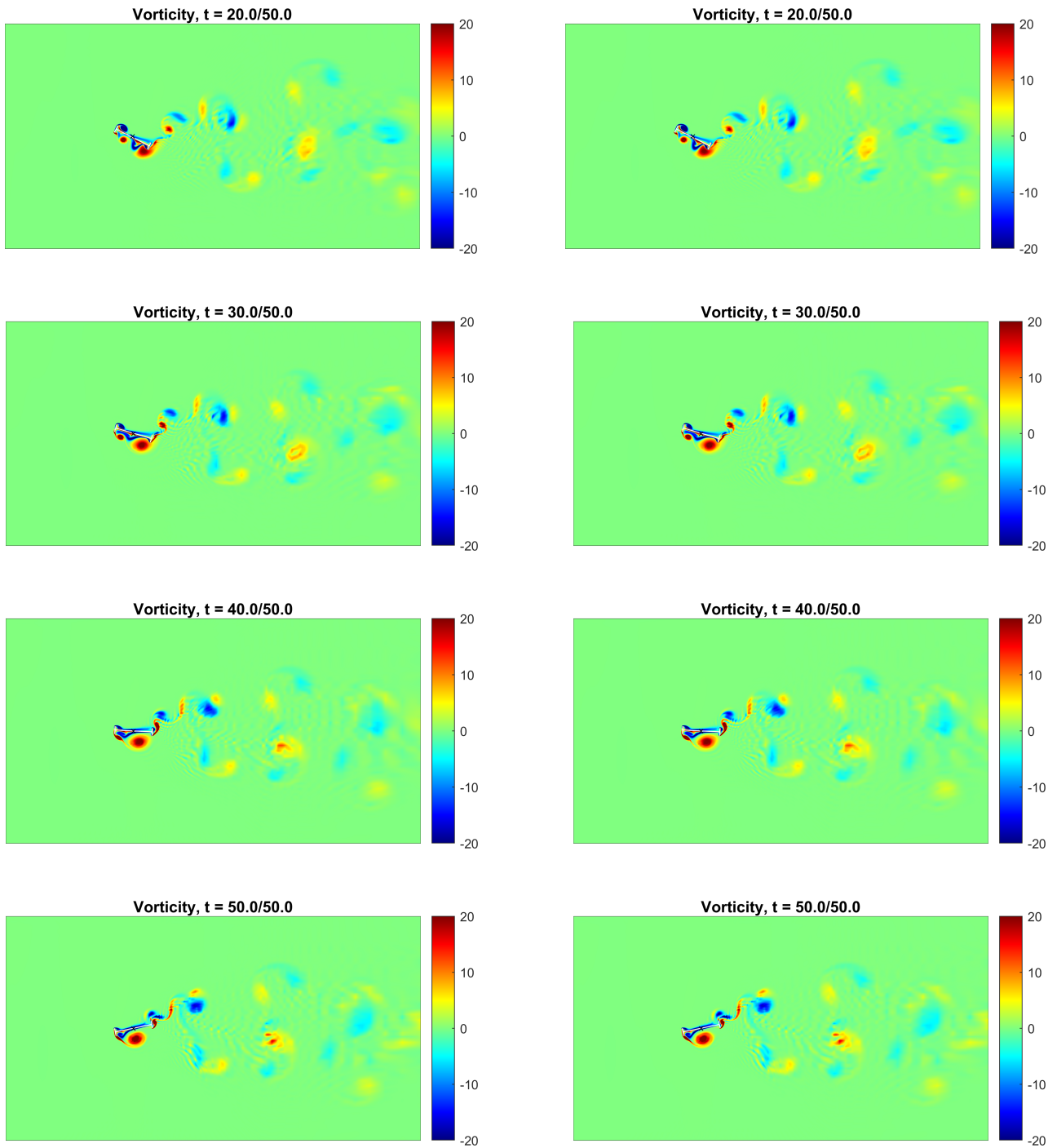


Fig. 71: Vorticity field of reference case left and Aitken's relaxation applied on this case right

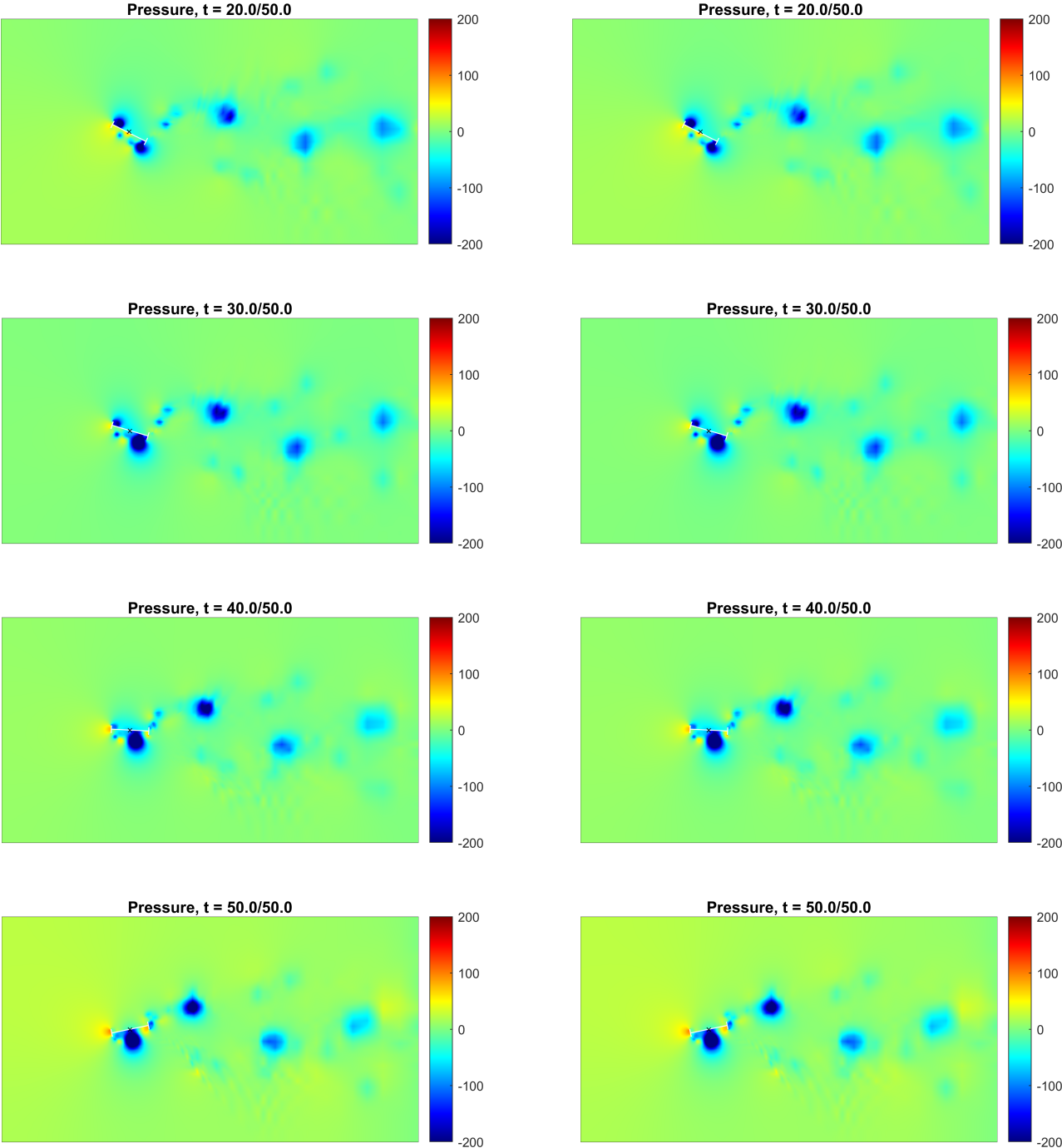


Fig. 72: Pressure field of reference case left and Aitken's relaxation applied on this case right

6.3 Extrapolation

As shown in section 5.3 another approach to accelerate the FSI simulation is extrapolation which is now studied for the bridge test case. The relevant background on extrapolation is given in section 5.3. There the approach is visualized in Figure 44 and the extrapolation formulas are given. Here first order and fifth order extrapolation formulas are used as before.

uvp	extrapolation order	reference case		yes 1		yes 5	
	notation	FSI	F	FSI	F	FSI	F
	min iterations	4	6	4	6	4	6
	max iterations	10	15	10	21	10	21
	avg. iterations	7.4	12.3	8.0	16.6	8.0	16.6
	min time FSI [s]	174.4		100.4		102.4	
	max time FSI [s]	436.0		355.3		362.3	
	avg. time FSI [s]	276.7		275.0		279.6	
	time [h]	76.9		76.4 (99.3%)		77.7 (101.0%)	
d	extrapolation order	reference case		yes 1		yes 5	
	notation	FSI	F	FSI	F	FSI	F
	min iterations	4	6	4	6	4	6
	max iterations	10	15	10	21	10	21
	avg. iterations	7.4	12.3	8.0	16.7	8.0	16.7
	min time FSI [s]	174.4		101.4		101.5	
	max time FSI [s]	436.0		372.4		367.6	
	avg. time FSI [s]	276.7		278.4		276.1	
	time [h]	76.9		77.3 (100.5%)		76.7 (99.7%)	
mesh	extrapolation order	reference case		yes 1		yes 5	
	notation	FSI	F	FSI	F	FSI	F
	min iterations	4	6	4	6	4	5
	max iterations	10	15	9	13	9	12
	avg. iterations	7.4	12.3	7.0	11.1	6.5	9.4
	min time FSI [s]	174.4		102.9		93.2	
	max time FSI [s]	436.0		292.7		253.8	
	avg. time FSI [s]	276.7		195.8		170.9	
	time [h]	76.9		54.4 (70.7%)		47.5 (61.8%)	
d, uvp, mesh	extrapolation order	reference case		yes 1		yes 5	
	notation	FSI	F	FSI	F	FSI	F
	min iterations	4	6	4	6	3	3
	max iterations	10	15	9	13	10	13
	avg. iterations	7.4	12.3	7.0	10.1	5.9	8.2
	min time FSI [s]	174.4		101.3		72.4	
	max time FSI [s]	436.0		270.5		302.3	
	avg. time FSI [s]	276.7		161.2		149.6	
	time [h]	76.9		50.3 (65.4%)		41.6 (54.1%)	

Tab. 10: Extrapolation results and reference case

d, uvp, mesh directly	extrapolation order	reference case		yes 1		yes 5	
	notation	FSI	F	FSI	F	FSI	F
	min iterations	4	6	4	5	2	3
	max iterations	10	15	9	13	10	13
	avg. iterations	7.4	12.3	6.9	9.9	5.9	8.2
	min time FSI [s]	174.4		102.1		53.3	
	max time FSI [s]	436.0		268.9		266.4	
	avg. time FSI [s]	276.7		177.6		149.0	
	time [h]	76.9		49.3 (64.1%)		41.4 (53.8%)	

Tab. 11: Extrapolation results and reference case

Table 10 shows the extrapolation results with the approach analogously to the plate case in section 5.3. It is obvious that the results are much better here. The calculation time is almost the same as for the reference case without extrapolation in the worst case and the best result is about twice as fast as the reference case.

Another approach considered here is shown in Table 11. There, the extrapolation is applied to the structural displacements and the fluid quantities. The extrapolated structural displacements are the input data for the computational mesh dynamics routine to get a deformed mesh based on these extrapolated displacements. For this configuration the CMD-module is already used before the first iteration step with the extrapolated structural displacement as input data. The difference between this approach and the approach where the mesh nodes are extrapolated is minimal but in this study the new approach considering extrapolated displacements within CMD leads to the best results.

Again, the results for forces, moments and fluid fields are virtually the same for all cases. Figure 73 shows the forces and Figure 74 shows the moments obtained with extrapolation of all fields *d*, *uvp*, and *mesh* for fifth order extrapolation functions in blue over the plot of the reference case in green. Figures 75, 76, and 77 show in their left column the results of the fluid fields for the reference case and in their right columns for the case where extrapolation is used.

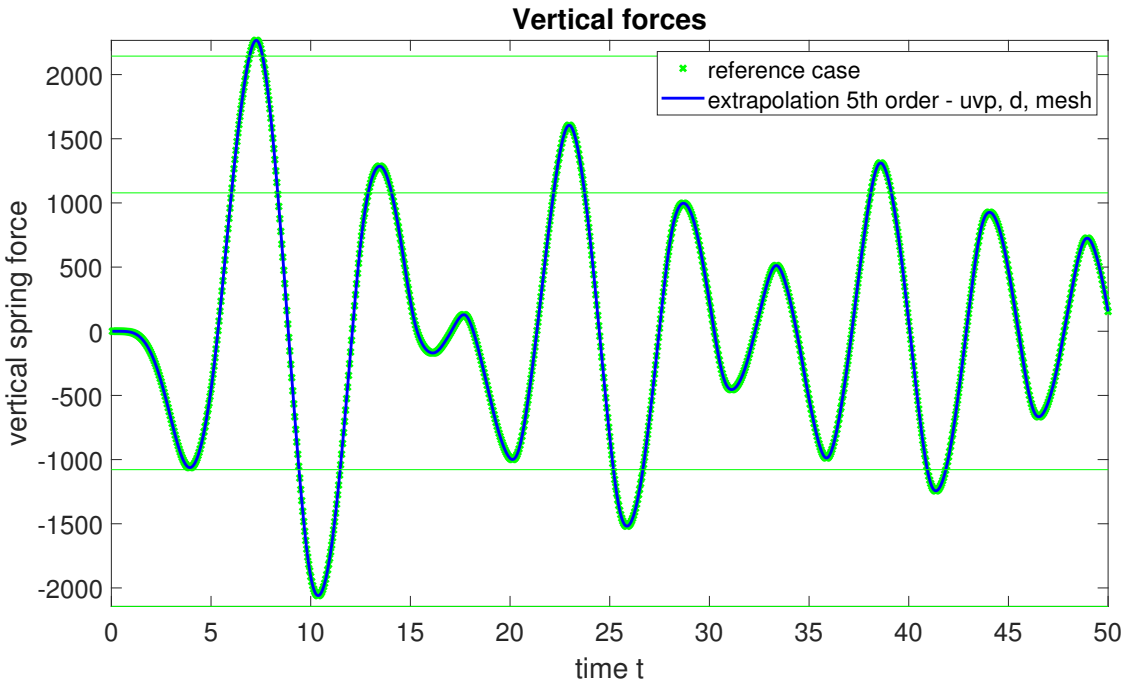
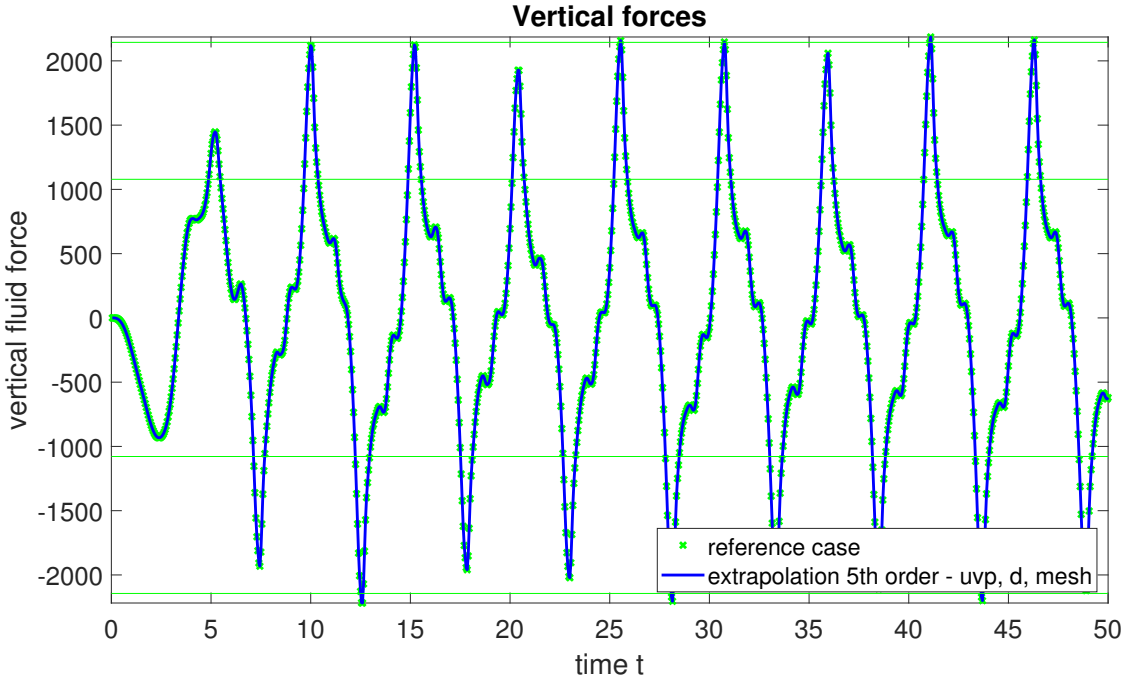


Fig. 73: Vertical forces

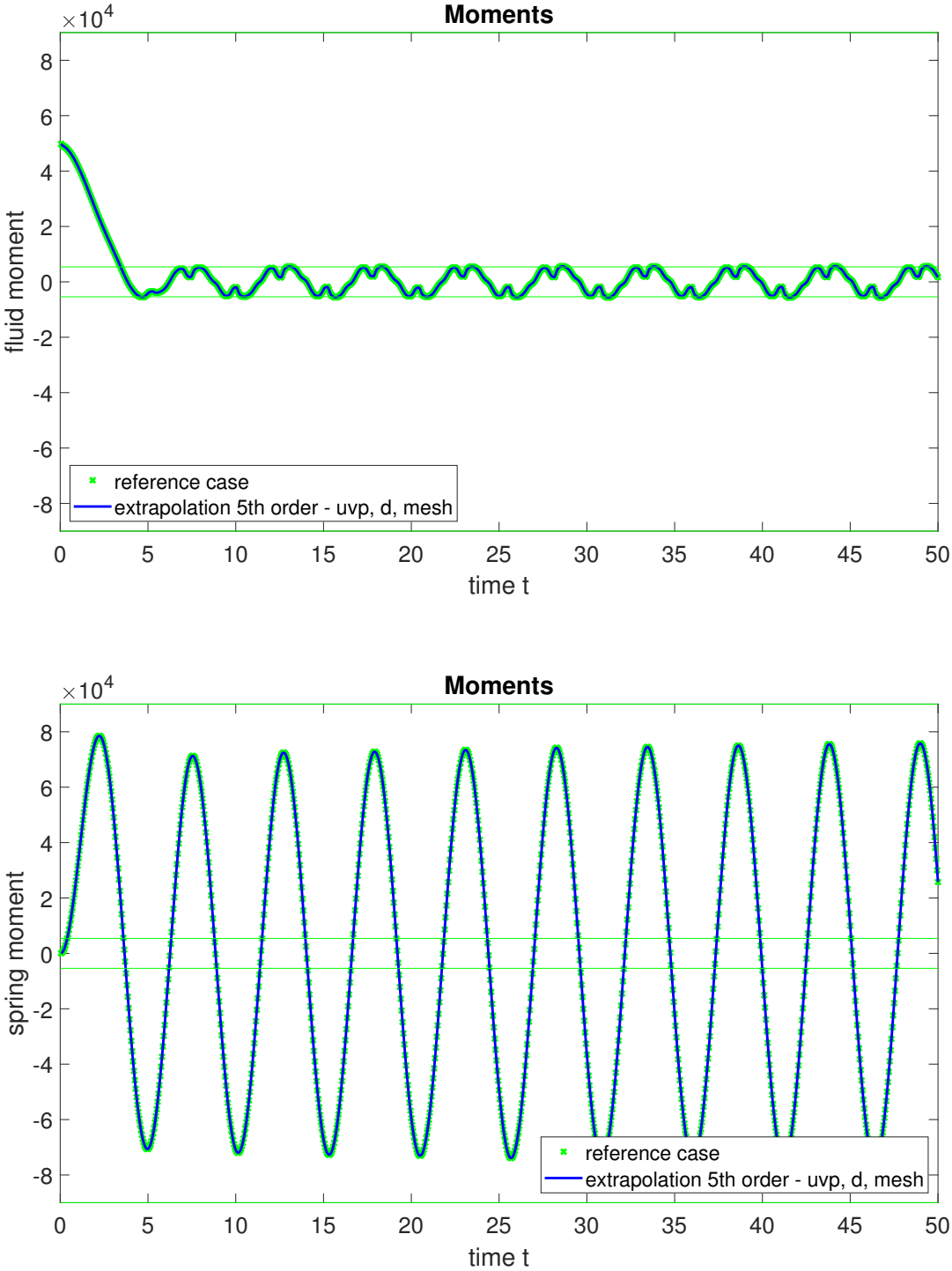


Fig. 74: Moments

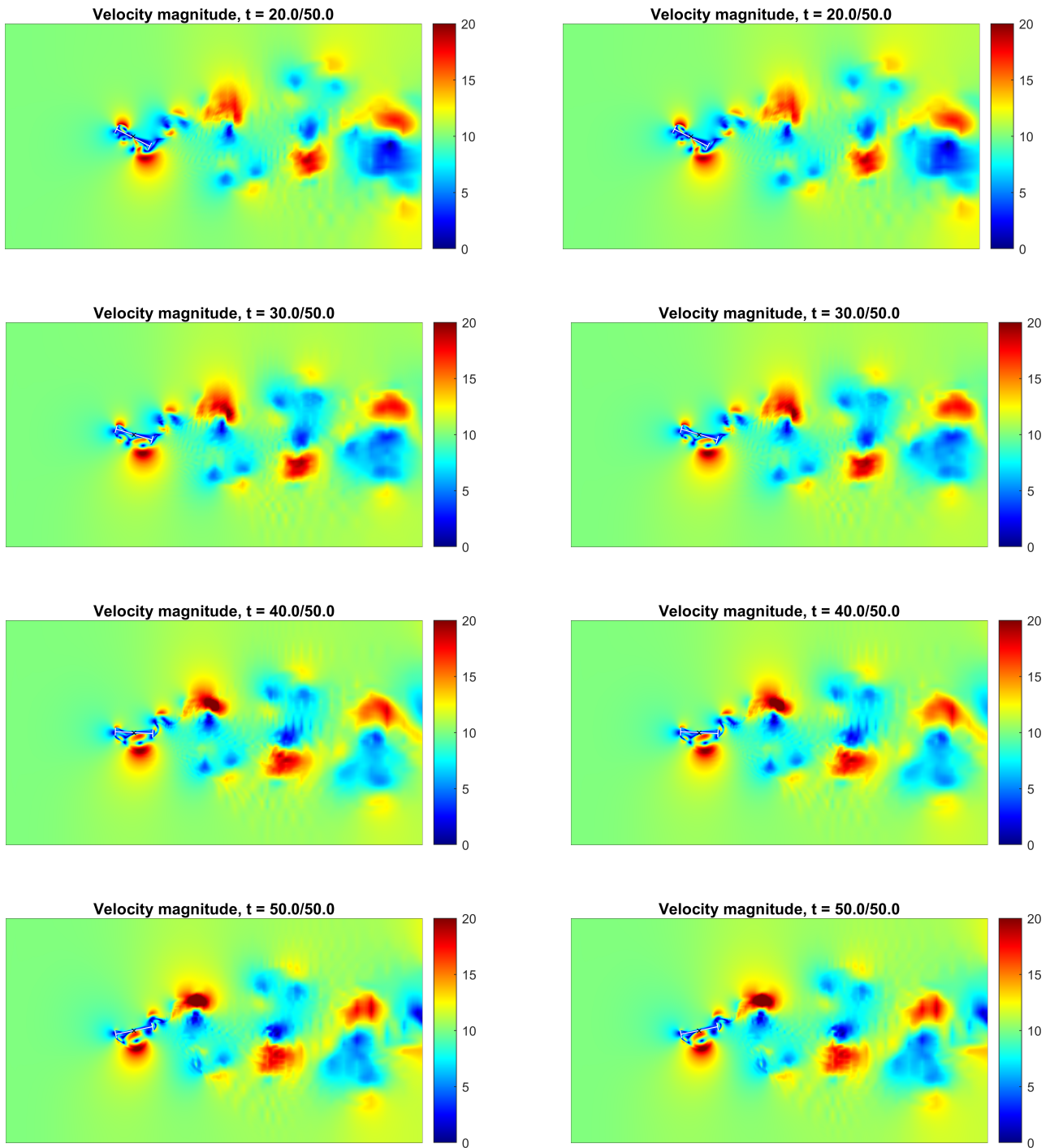


Fig. 75: Velocity field of reference case left and fifth order extrapolation applied on this case for fluid and solid solutions, and the mesh right

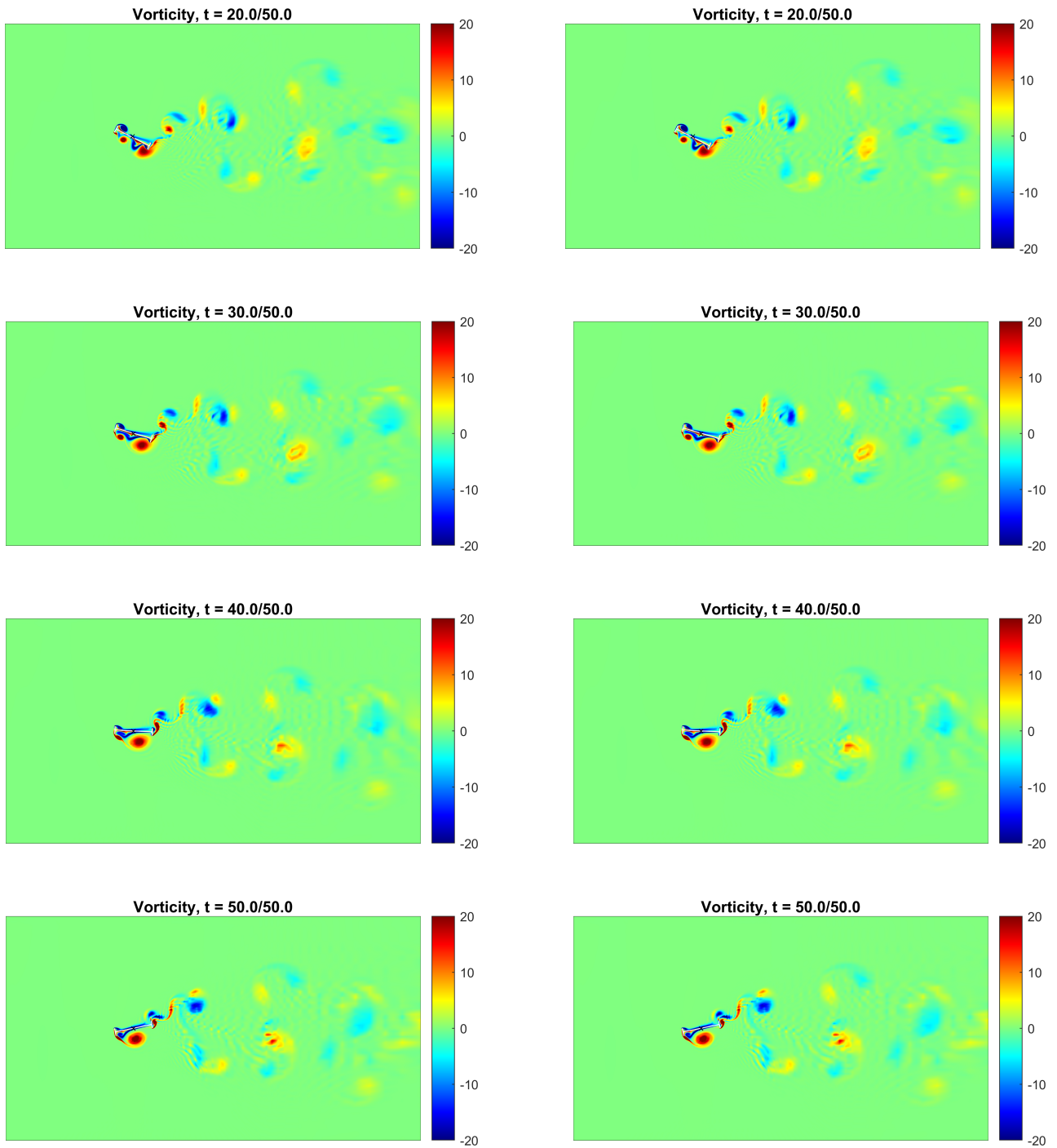


Fig. 76: Vorticity field of reference case left and fifth order extrapolation applied on this case for fluid and solid solutions, and the mesh right

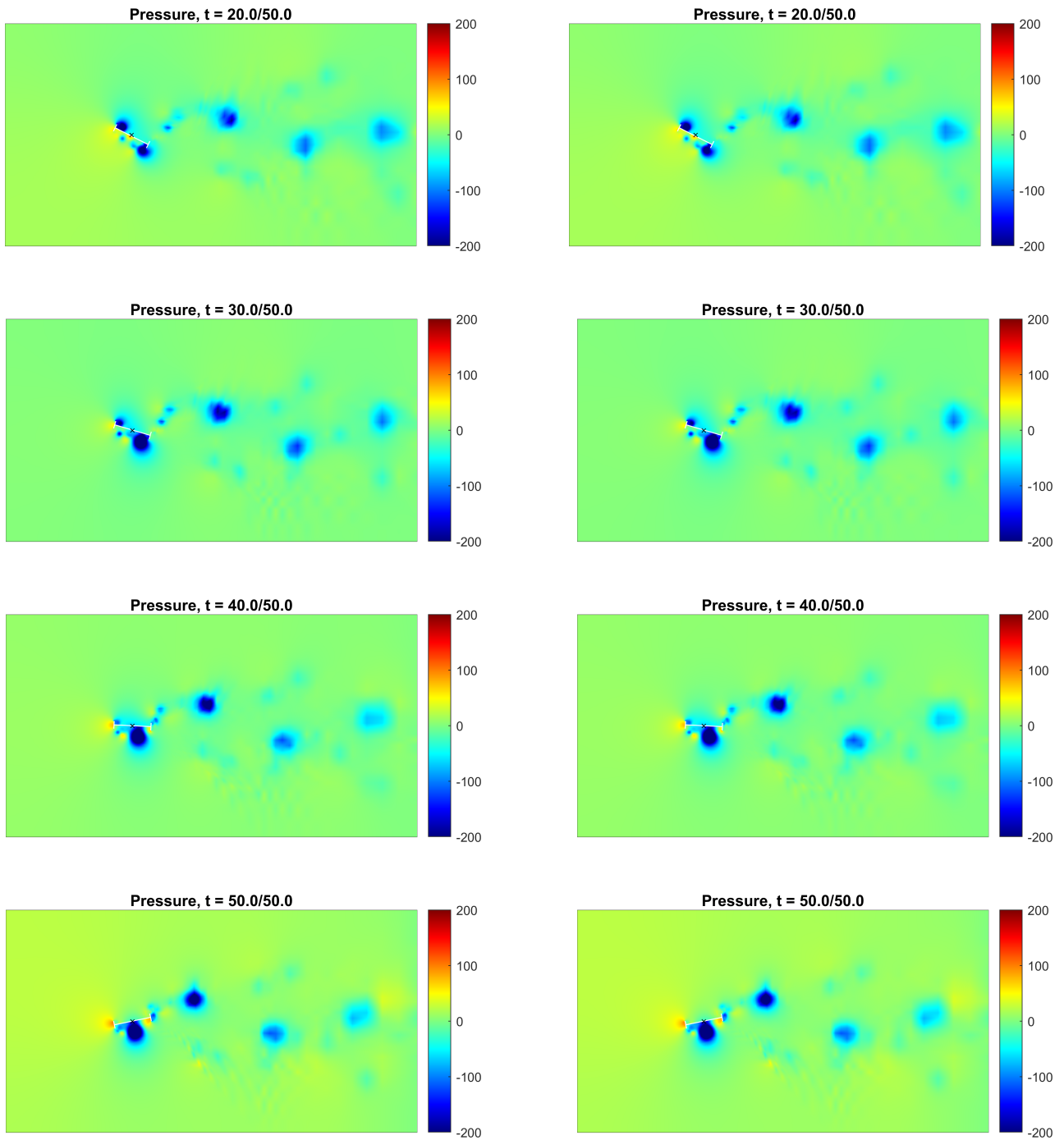


Fig. 77: Pressure field of reference case left and fifth order extrapolation applied on this case for fluid and solid solutions, and the mesh right

Figure 78 shows the iteration history for the reference case (lower bar-plot) and the fifth order extrapolation function applied on the structural displacements d , the fluid solution uwp , and the mesh nodes of the deformed mesh. The green line is at five iterations and the pink line at twelve iterations in both plots. It is obvious that with extrapolation applied less iterations are necessary.

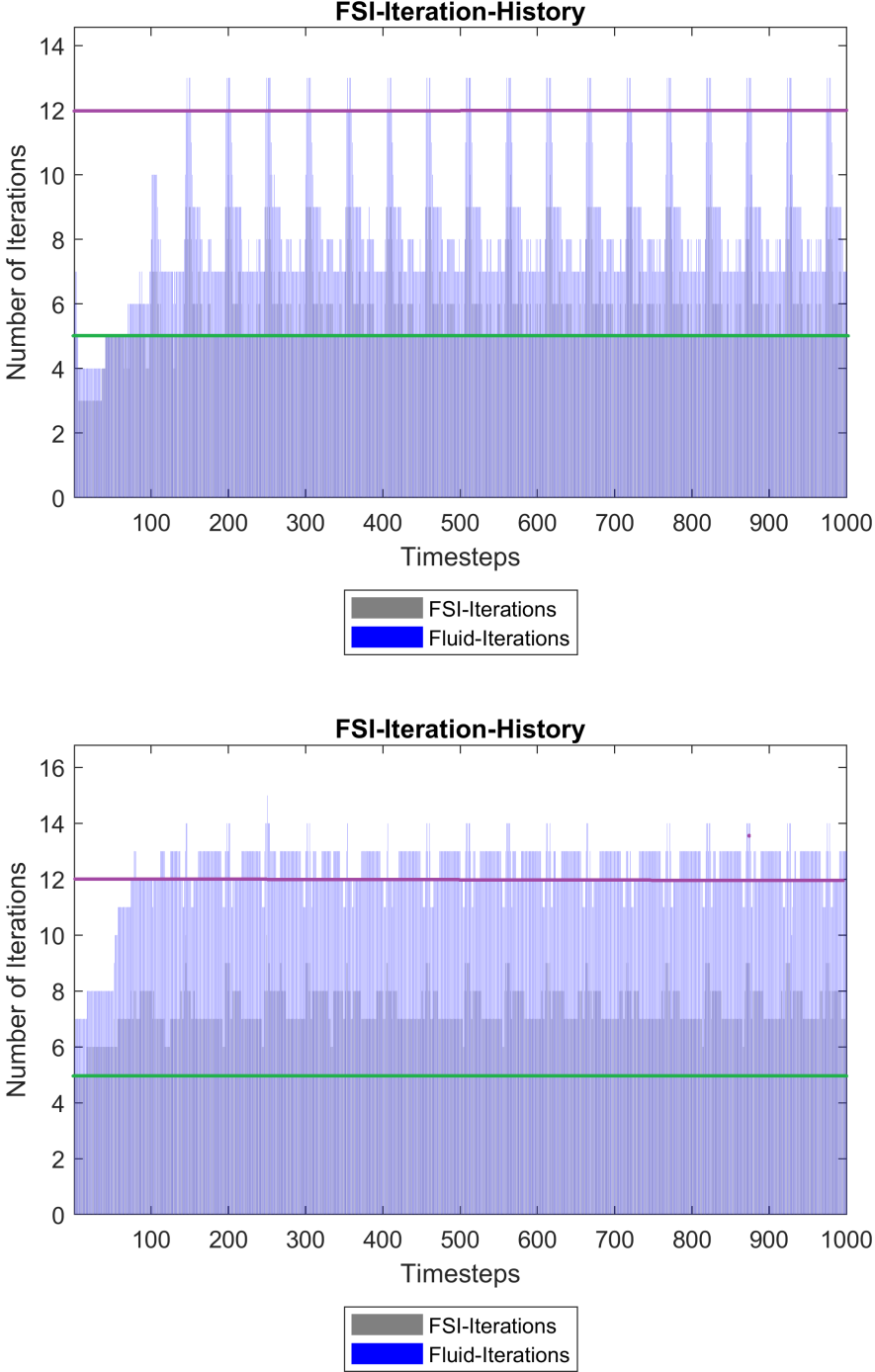


Fig. 78: Iterations over timesteps for reference case (lower bar-plot) and fifth order extrapolation applied on this case for uwp , d , and $mesh$

6.3.1 Extrapolation for $\varepsilon_c = \varepsilon_F = 1 \cdot 10^{-2}$

Here the reference case is the case with the tolerance boundaries $\varepsilon_c = 1 \cdot 10^{-2}$ and $\varepsilon_F = 1 \cdot 10^{-2}$. Table 12 shows the results for first and fifth order extrapolation of the deformed fluid mesh nodes (mesh), the solid field solution, the fluid field solution, and the deformed mesh (d, uvp, mesh), and the solid field solution, the fluid field solution, and the deformed mesh calculated using CMD (d, uvp, mesh directly).

mesh	extrapolation order	reference case		yes 1		yes 5	
	notation	FSI	F	FSI	F	FSI	F
	min iterations	3	5	3	3	2	3
	max iterations	4	10	3	8	3	6
	avg. iterations	3.5	8.4	3.0	7.0	2.0	4.9
	min time FSI [s]	85.2		89.5		53.7	
	max time FSI [s]	160.5		158.4		97.2	
	avg. time FSI [s]	133.0		116.5		79.4	
time [h]	36.9		32.4 (87.8%)		22.1 (59.9%)		
d, uvp, mesh	extrapolation order	reference case		yes 1		yes 5	
	notation	FSI	F	FSI	F	FSI	F
	min iterations	3	5	3	5	1	1
	max iterations	4	10	3	8	3	7
	avg. iterations	3.5	8.4	3.0	6.1	2.0	4.3
	min time FSI [s]	85.2		85.2		21.6	
	max time FSI [s]	160.5		126.6		108.6	
	avg. time FSI [s]	133.0		101.2		73.2	
time [h]	36.9		28.1 (76.2%)		20.3 (55.0%)		
d, uvp, mesh directly	extrapolation order	reference case		yes 1		yes 5	
	notation	FSI	F	FSI	F	FSI	F
	min iterations	3	5	1	1	1	1
	max iterations	4	10	3	8	3	7
	avg. iterations	3.5	8.4	3.0	6.0	2.0	4.3
	min time FSI [s]	85.2		26.1		21.5	
	max time FSI [s]	160.5		138.9		115.0	
	avg. time FSI [s]	133.0		102.5		72.4	
time [h]	36.9		28.5 (77.2%)		20.1 (54.5%)		

Tab. 12: Extrapolation results and reference case

The pattern of acceleration which is seen in Table 12 is similar to those shown in Tables 10 and 11 but the improvement is relatively smaller for first order extrapolation functions here. Calculation time can be accelerated with about the same relative values for fifth order extrapolation formulas for this reference case. The solution plots for the vertical forces and the moments are shown in Figures 94 and 95, and the three fluid fields are shown in Figures 96, 97, and 98 in Appendix D. For all other cases these plots look similar.

6.4 Aitken's relaxation and extrapolation

As shown above, high acceleration of the calculation time is possible using Aitken's relaxation or extrapolation for this test case. The aim is now to combine Aitken's relaxation and extrapolation in one algorithm. Table 13 compared with Tables 10 and 12 shows that the improvement is very similar to the case where extrapolation is used alone without Aitken's relaxation. For the upper part of Table 13 the tolerances are $\varepsilon_c = 1 \cdot 10^{-6}$ and $\varepsilon_F = 1 \cdot 10^{-2}$ and for the lower part of this table the tolerances are $\varepsilon_c = \varepsilon_F = 1 \cdot 10^{-2}$. The results and their plots are almost the same as before and are, therefore, not repeated here.

d, uvp, mesh dir. + AR	extrapolation order	reference case		yes 1		yes 5	
	notation	FSI	F	FSI	F	FSI	F
	min iterations	4	6	4	5	2	3
	max iterations	10	15	9	13	10	13
	avg. iterations	7.4	12.3	6.9	9.9	5.9	8.2
	min time FSI [s]	174.4		107.7		54.1	
	max time FSI [s]	436.0		235.8		240.2	
	avg. time FSI [s]	276.7		178.1		147.8	
	time [h]	76.9		49.5 (64.5%)		41.1 (53.4%)	
d, uvp, mesh dir. + AR	extrapolation order	reference case		yes 1		yes 5	
	notation	FSI	F	FSI	F	FSI	F
	min iterations	3	5	1	1	1	1
	max iterations	4	10	3	8	3	7
	avg. iterations	3.5	8.4	3.0	6.0	2.0	4.3
	min time FSI [s]	85.2		21.2		20.9	
	max time FSI [s]	160.5		127.5		120.7	
	avg. time FSI [s]	133.0		101.8		71.8	
	time [h]	36.9		28.3 (76.7%)		19.9 (53.9%)	

Tab. 13: Reference case without any acceleration and results for extrapolation used together with Aitken's relaxation for different loop tolerances

7 Conclusion

The findings for possible acceleration strategies in FSI-simulations are summarized according to the findings made in two different benchmark test cases. We have investigated tolerances of iterative loops, Aitken's relaxation and extrapolation schemes herein. It can clearly be seen that the used FSI-algorithm is quite stable and the results are good when the tolerance for the coupling loop is $\varepsilon_c \leq 1 \cdot 10^{-3}$. The chosen reference case with $\varepsilon_c = 1 \cdot 10^{-6}$ and $\varepsilon_F = 1 \cdot 10^{-2}$ leads to accurate results and computational times which are acceptable for both test cases. However, the computational time is still long for both cases and so acceleration strategies are important.

Aitken's relaxation leads to a good acceleration for the bridge case but for the plate case nearly no improvement has been achieved.

Applying the extrapolation functions leads to acceleration for both considered cases. The most noticeable difference is that in the plate case for some extrapolation configurations, when single fields are extrapolated only, the calculation time is much longer than without extrapolation and for the bridge test case the calculation time for the same configurations is almost the same than for the reference case. It should be clearly noted here that the main FSI algorithm is the same for both cases. The only difference is that the solid solver for the bridge only considers a rigid body whereas it is deformable in the plate test case. However, for both cases the solid solvers are fast and have almost no influence on the overall computing times.

This leads to the conclusion that the applied acceleration strategies may be used reliably to solve FSI-problems in various settings. However, it can clearly be seen that the quantities considered in this thesis, like numbers of iteration steps for different loops and computational time, depend on the cases which are to be solved. This means that the tolerances chosen based on the studies in this work represent a good default setting. It is thus seen that the aim of this work has been achieved successfully and recommended settings for tolerances and acceleration strategies such as Aitken's relaxation and extrapolation are suggested. Those are expected to work in a variety of FSI test cases.

Appendices

A More result plots for tolerance study of plate test case

Here the results of the plate test case are shown in plots which are not used in section 5.1 but are included in this thesis for completeness. Figure 79 shows the same as the lower plot in Figure 31 but with different line types plotted to show that all six lines are virtually identical and not just the result for $i = j = 6$ is shown. Figures 80 and 81 show the results for the horizontal displacements, Figure 82 and 83 those for the vertical displacements, Figure 84 and 85 for the horizontal forces, and Figures 86 and 87 for the vertical forces, for $i \in [2, 3, 4, 5]$.

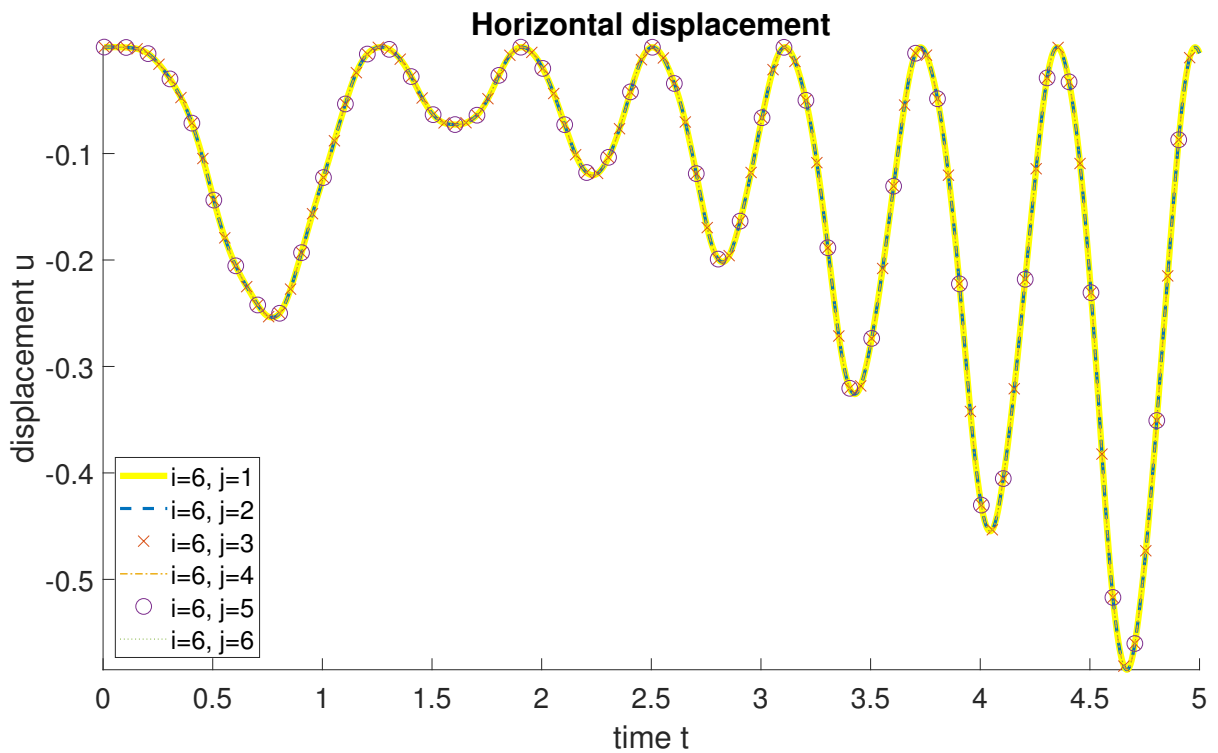


Fig. 79: Horizontal displacement of the middle point of the right edge of the plate with a different line type for each case, to show that all lines are laying over each other

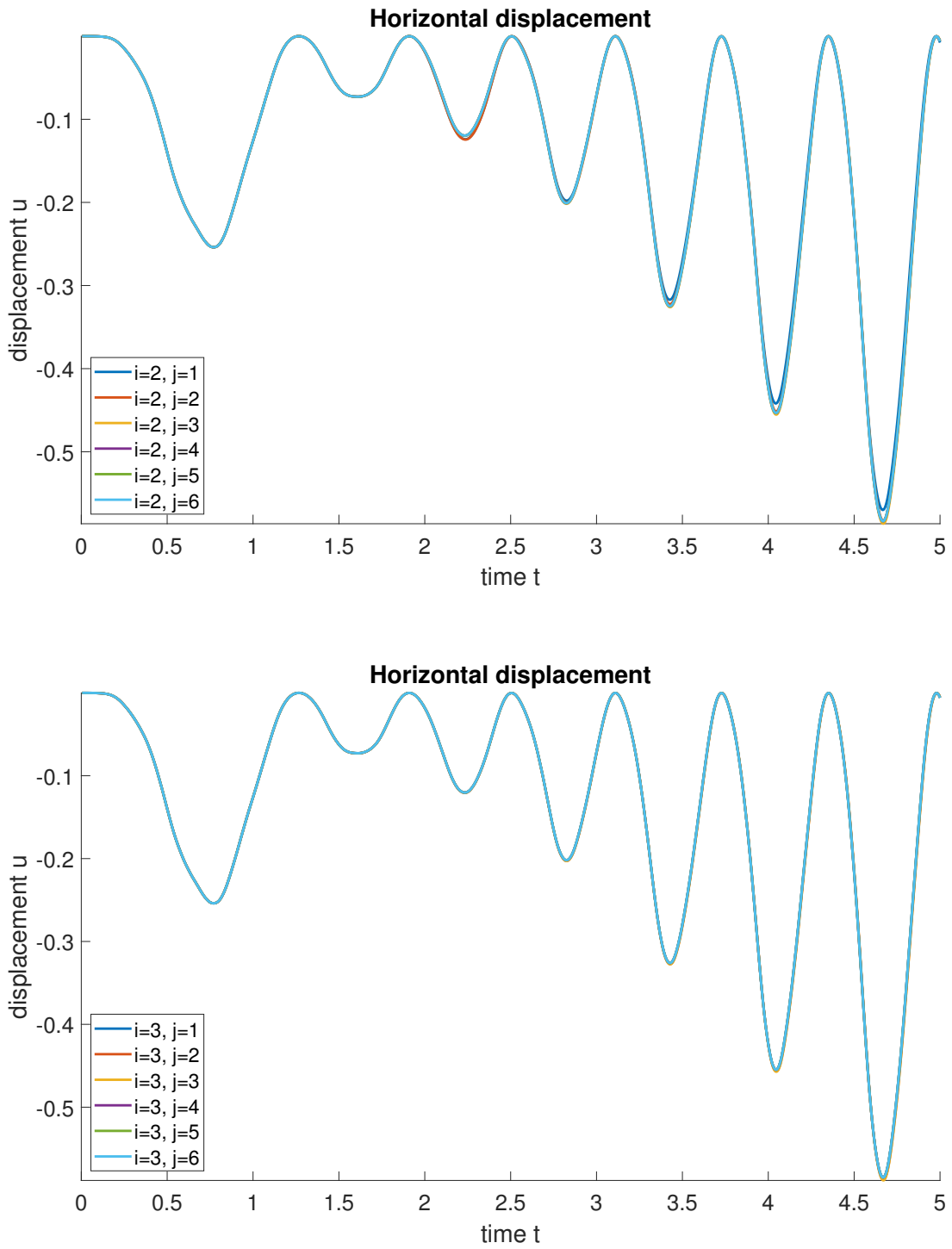


Fig. 80: Horizontal displacements of the middle point of the right edge of the plate

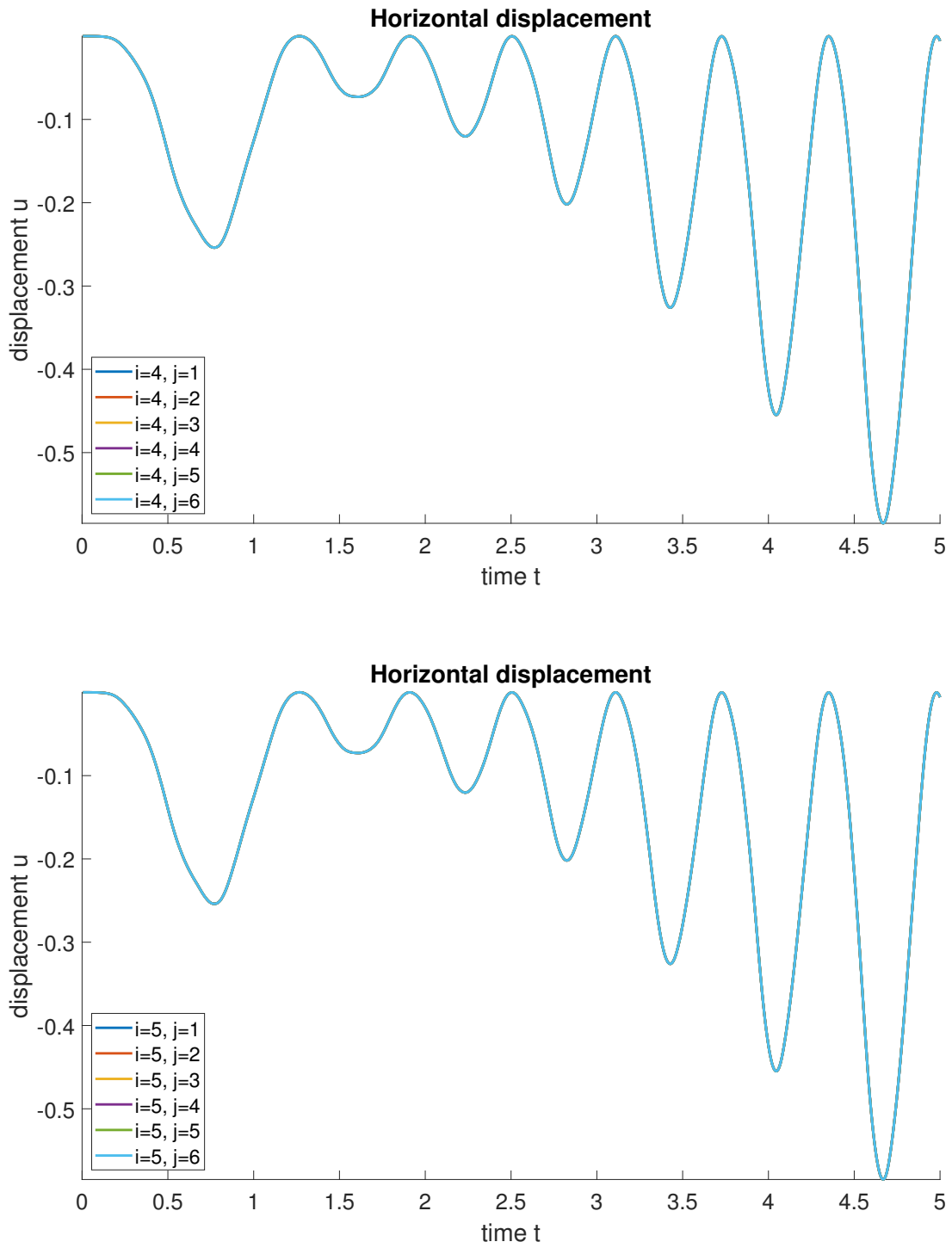


Fig. 81: Horizontal displacements of the middle point of the right edge of the plate

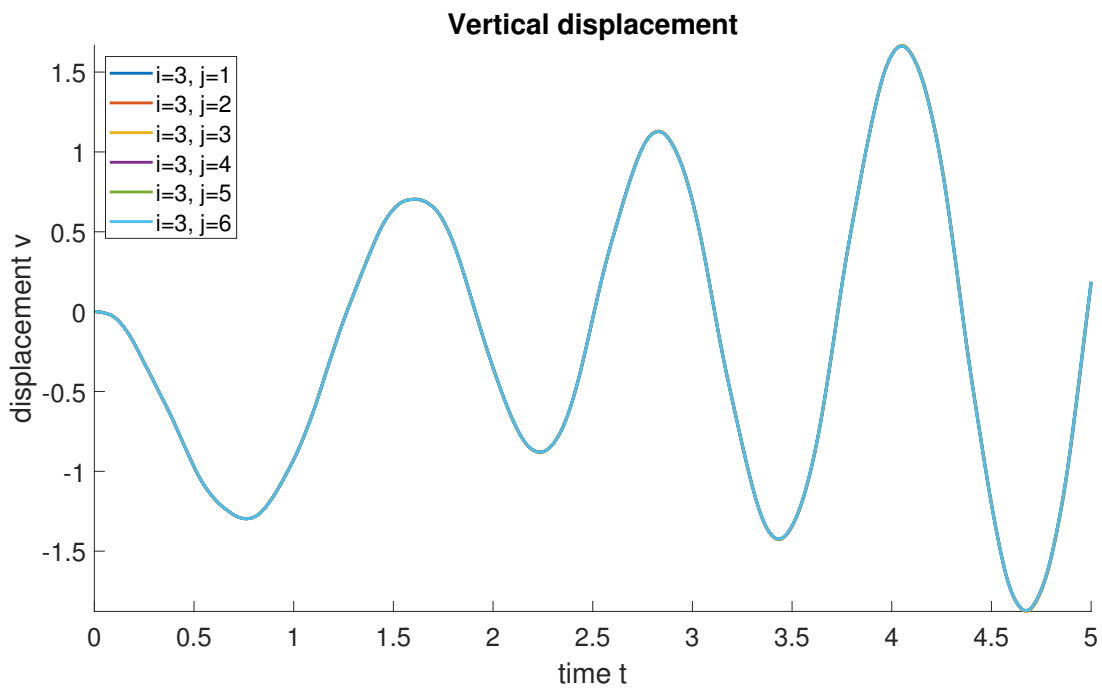
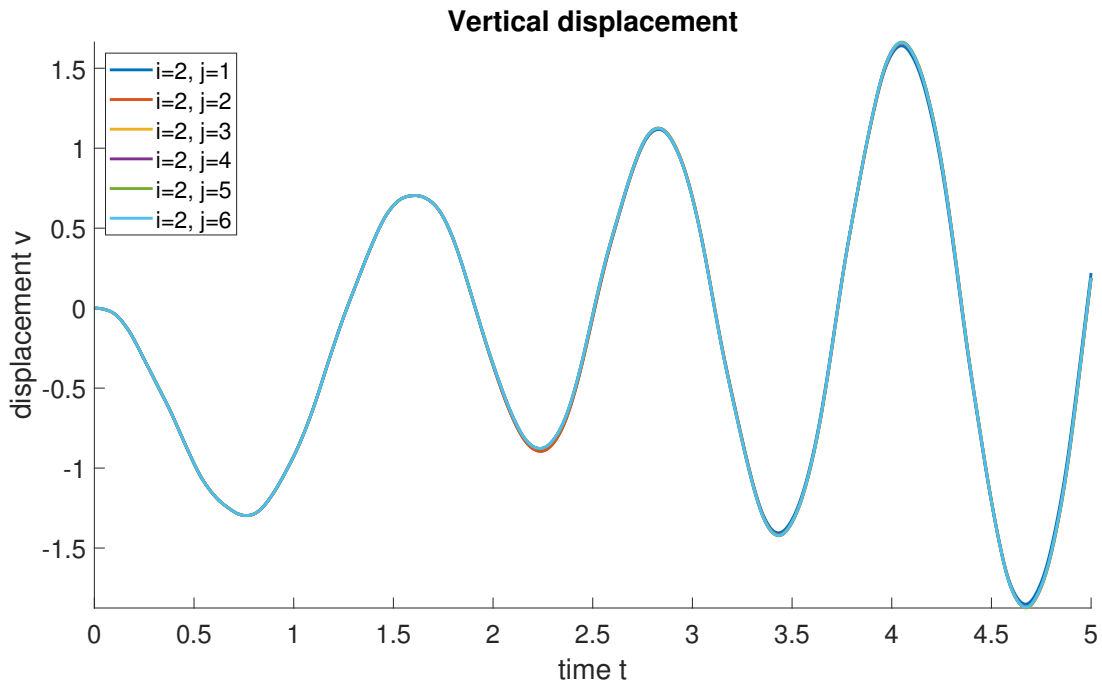


Fig. 82: Vertical displacements of the middle point of the right edge of the plate

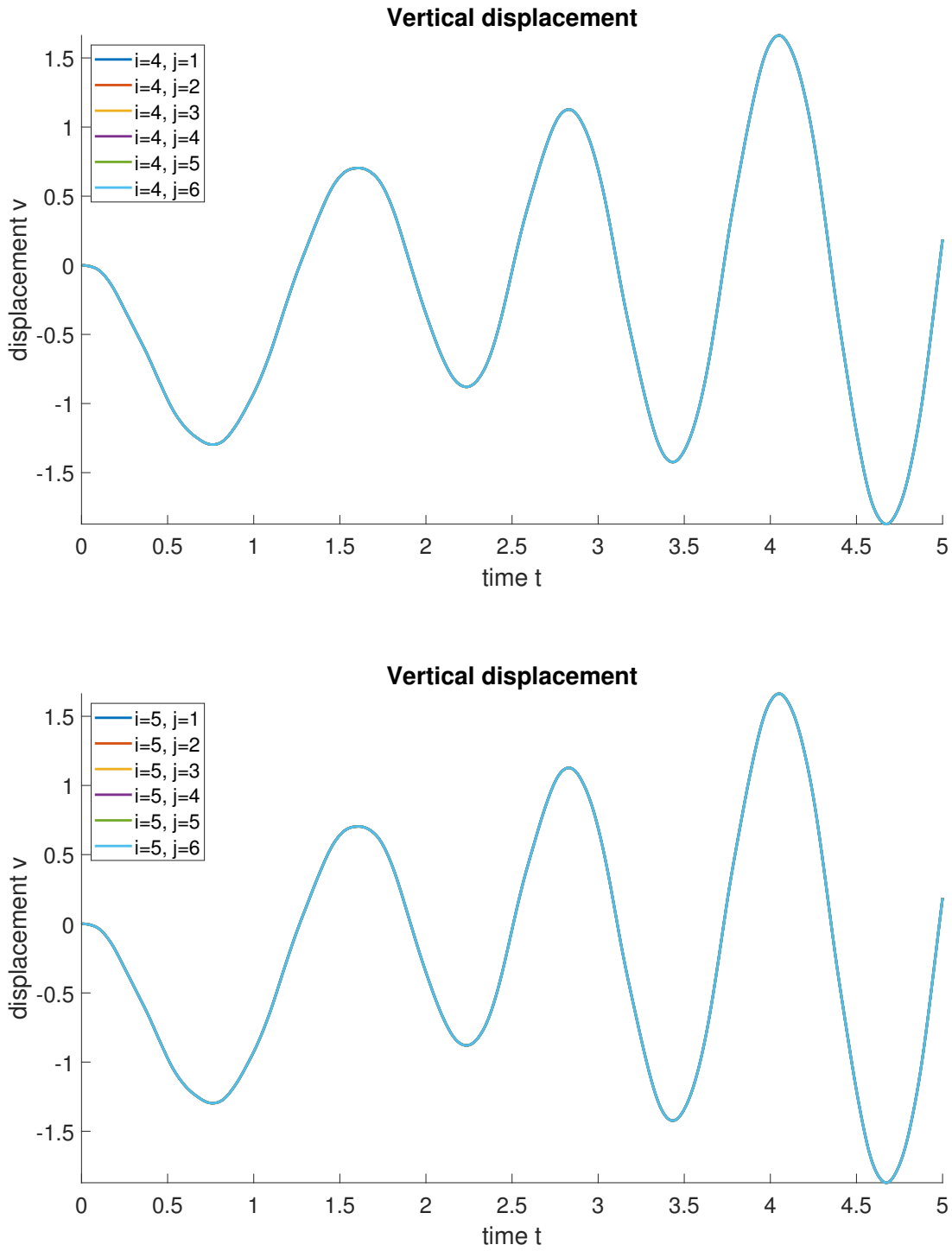


Fig. 83: Vertical displacements of the middle point of the right edge of the plate

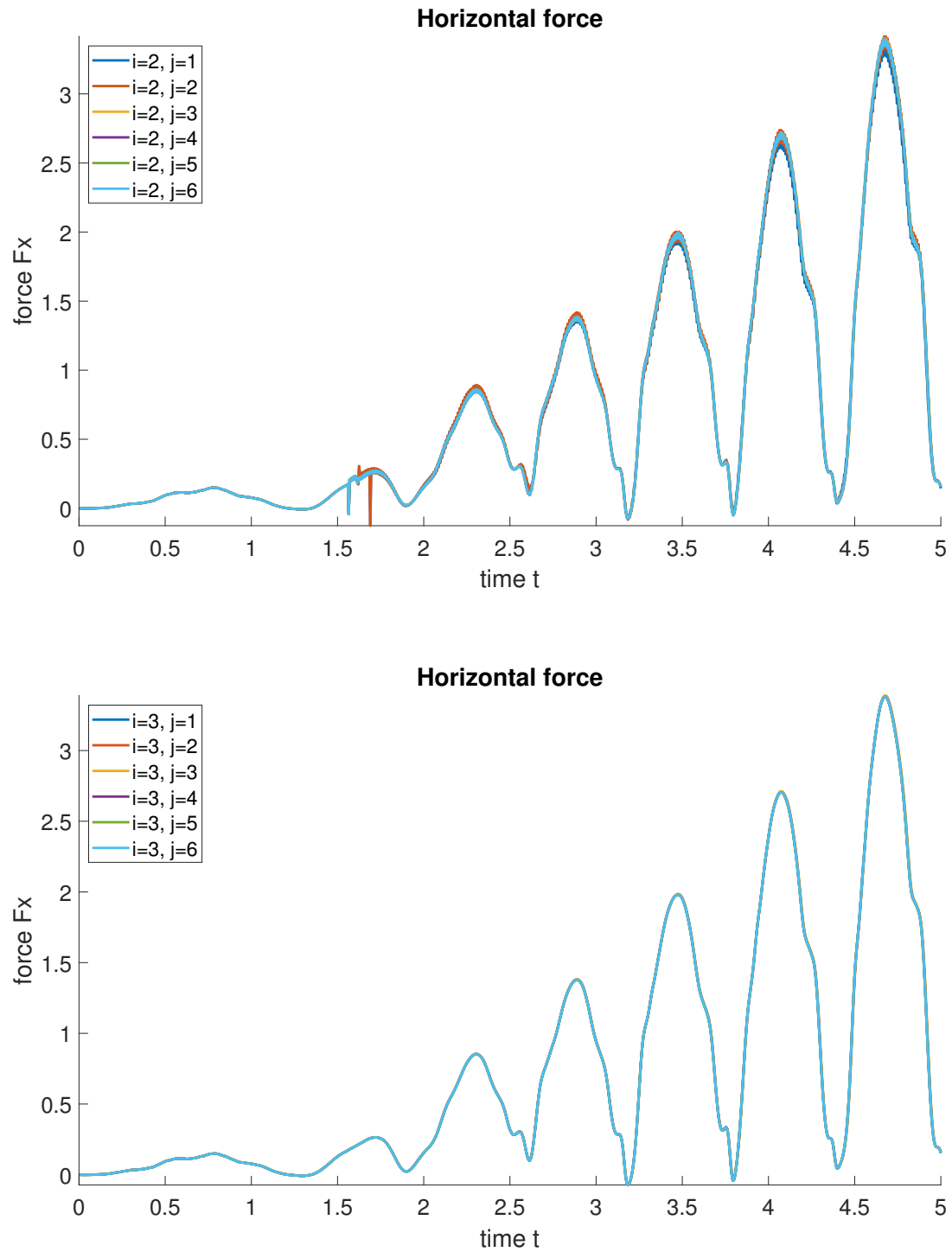


Fig. 84: Horizontal forces of the middle point of the right edge of the plate

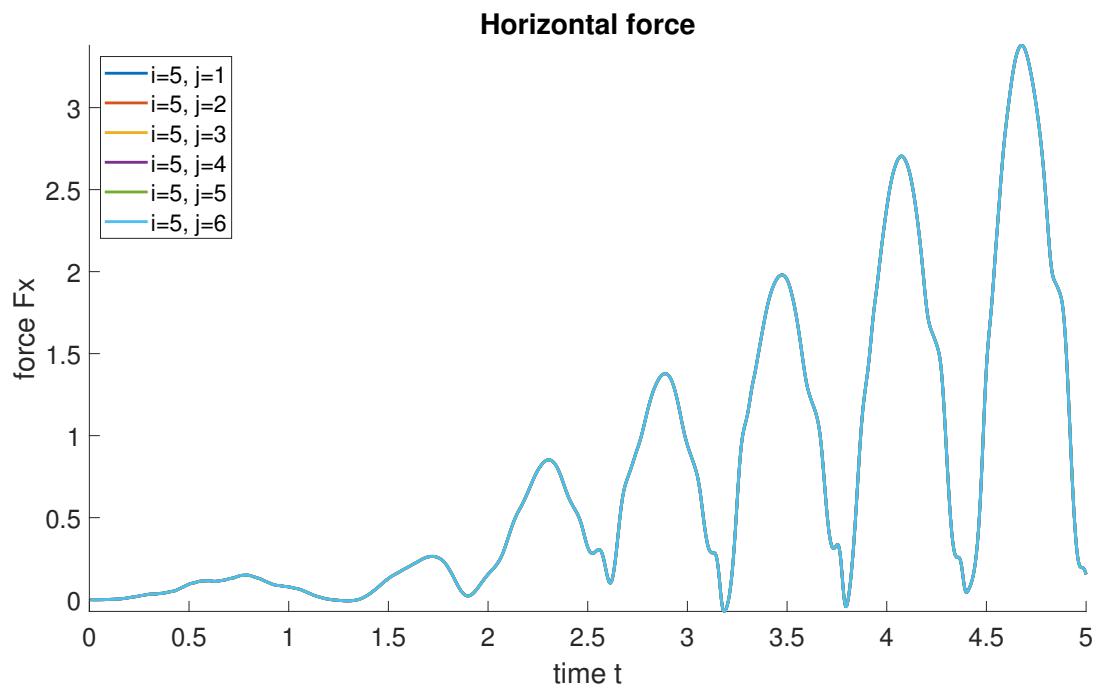
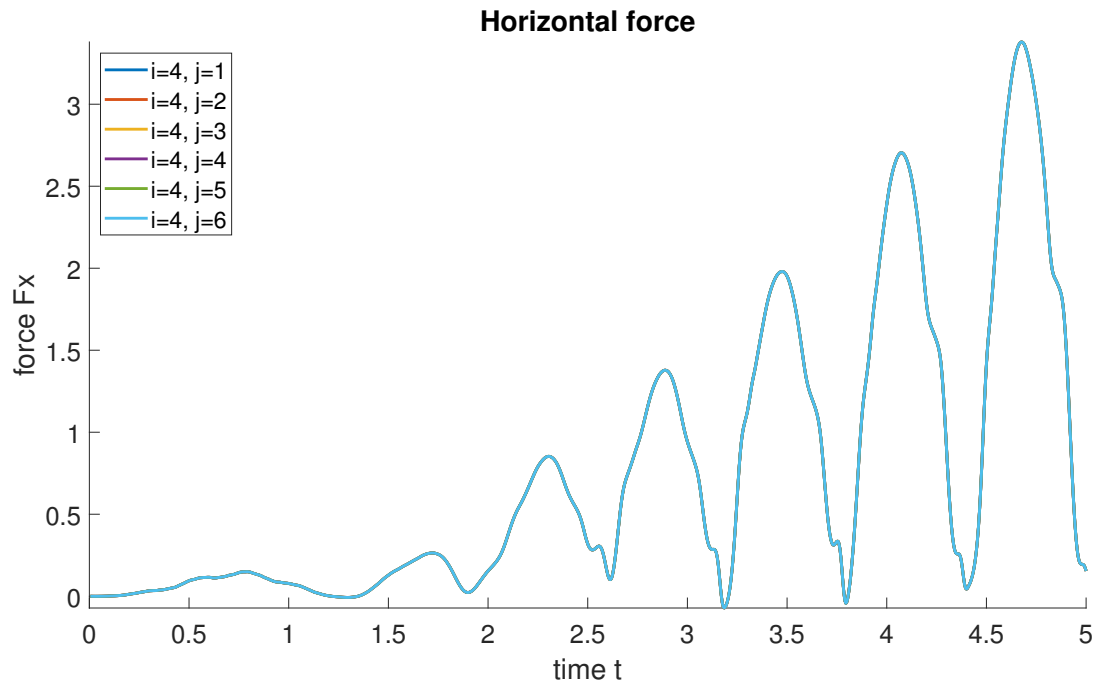


Fig. 85: Horizontal forces of the middle point of the right edge of the plate

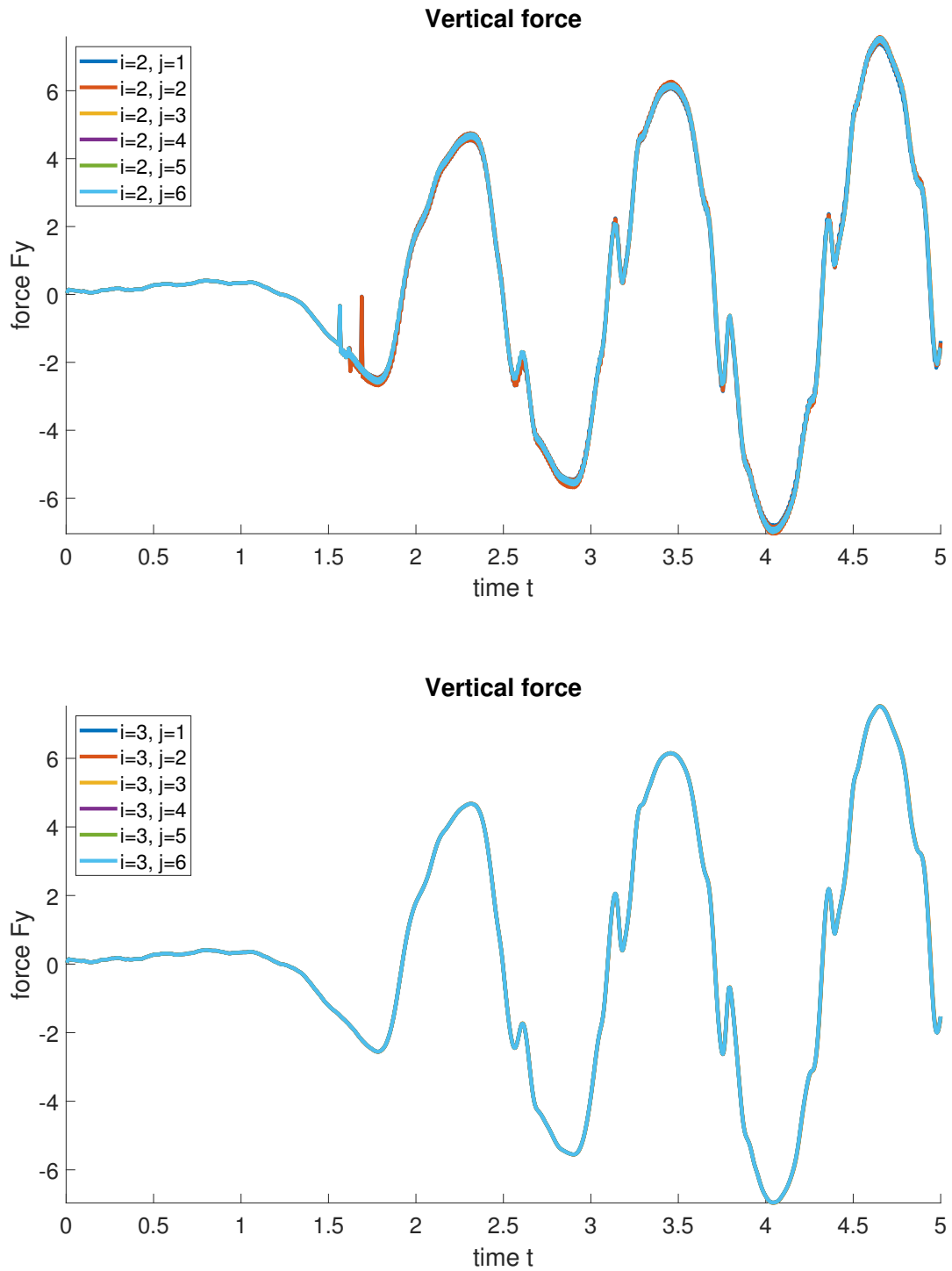


Fig. 86: Vertical forces of the middle point of the right edge of the plate

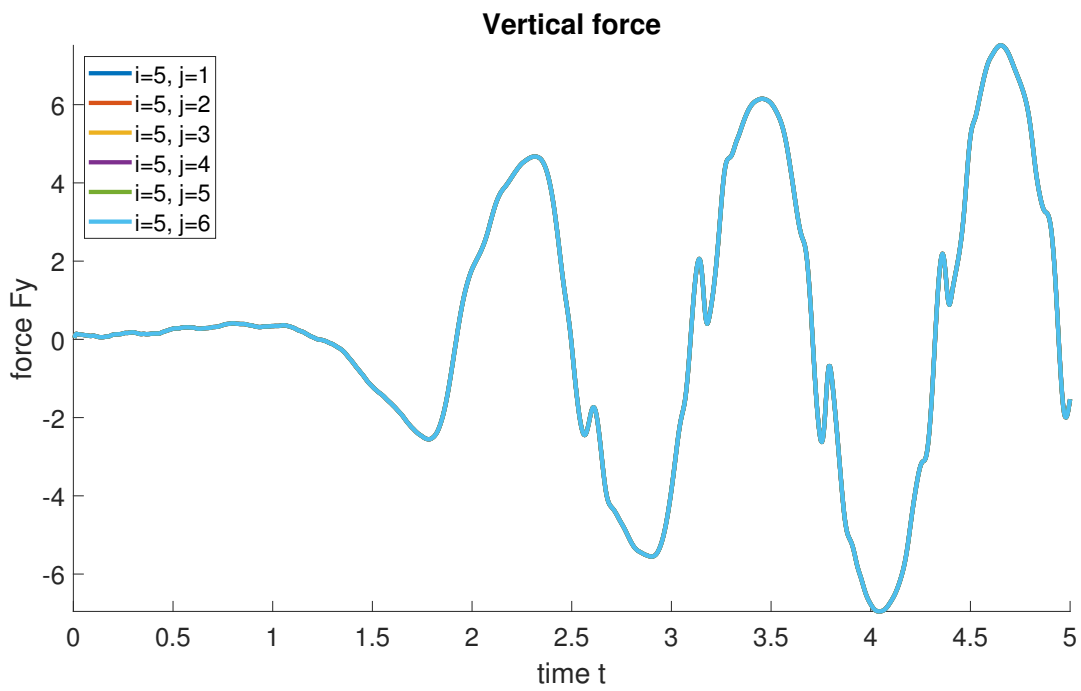
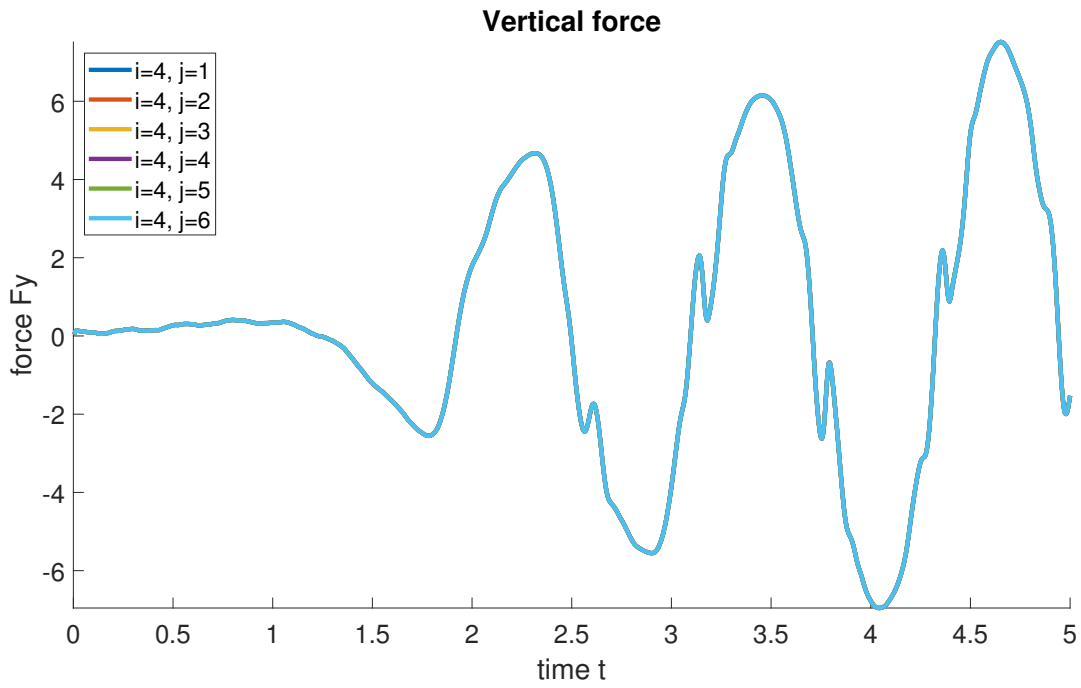


Fig. 87: Vertical forces of the middle point of the right edge of the plate

B Iteration history of plate study reference case

Here the iteration history is visualized for the reference test case. Figure 88 shows the iteration steps over time and the calculation time over time.

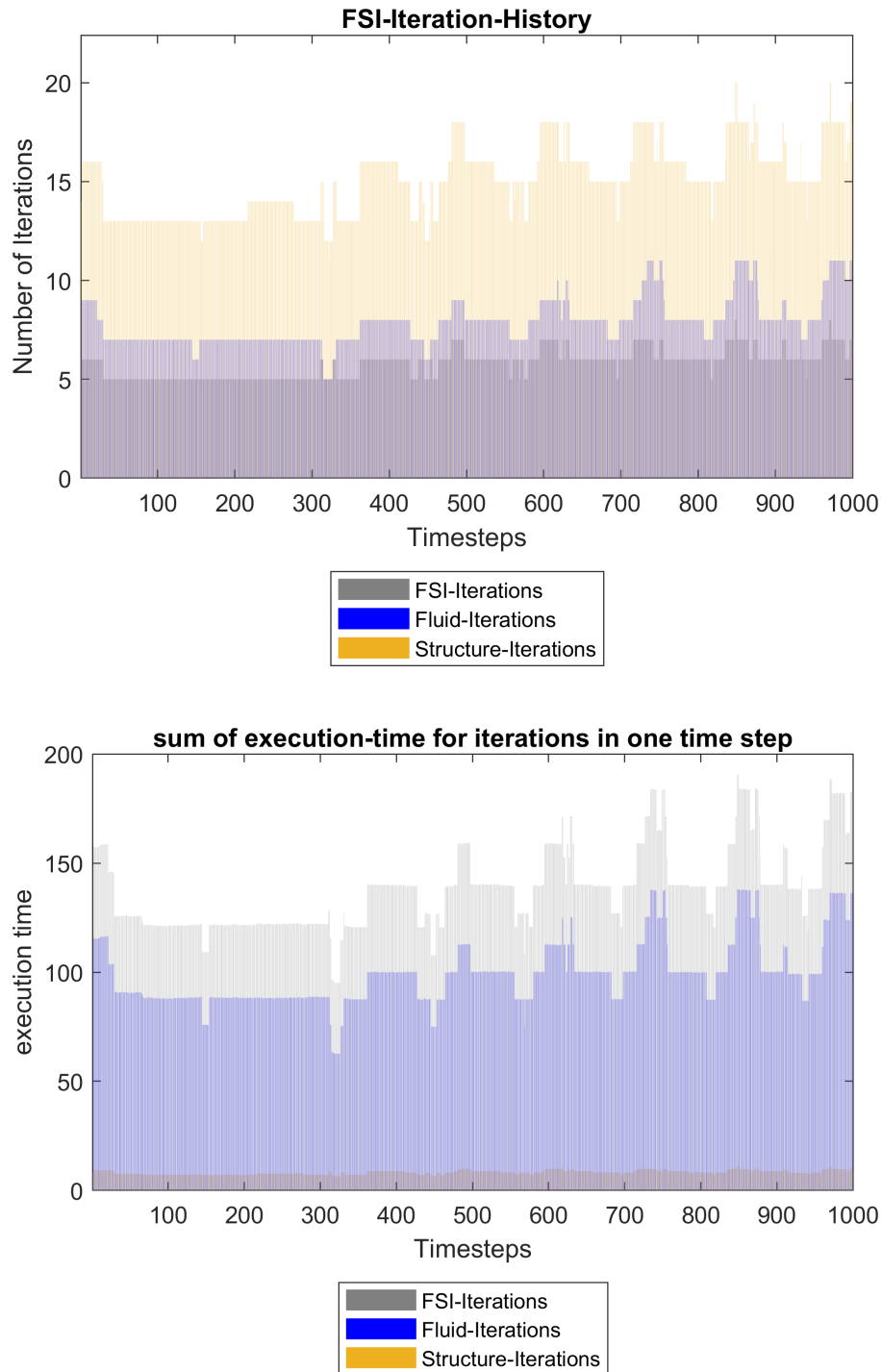


Fig. 88: Number of iterations and computational time over time steps

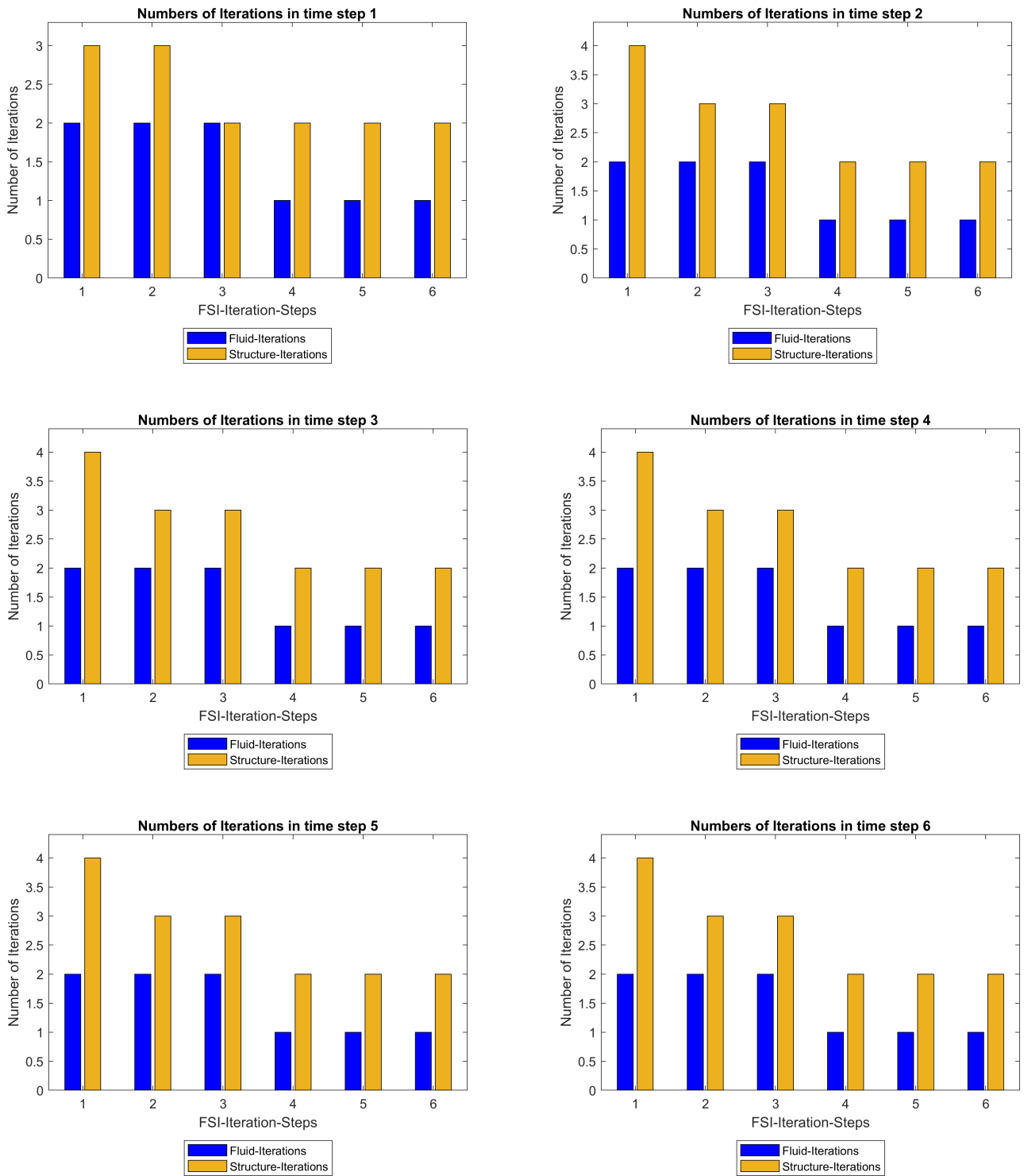


Fig. 89: Iteration steps of fluid and structure solvers within partitioned coupled loop for time step n

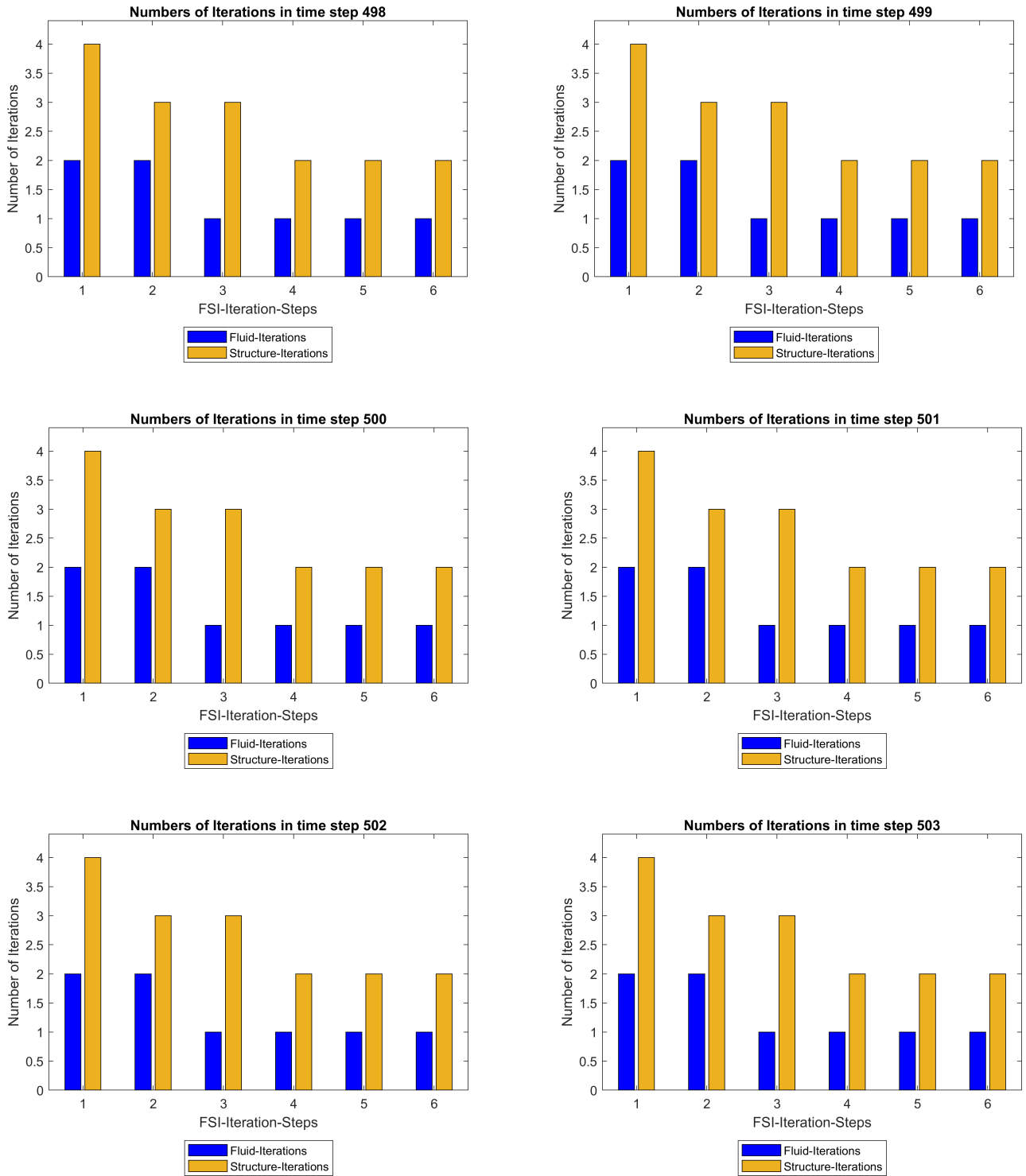


Fig. 90: Iteration steps of fluid and structure solvers within partitioned coupled loop for time step n

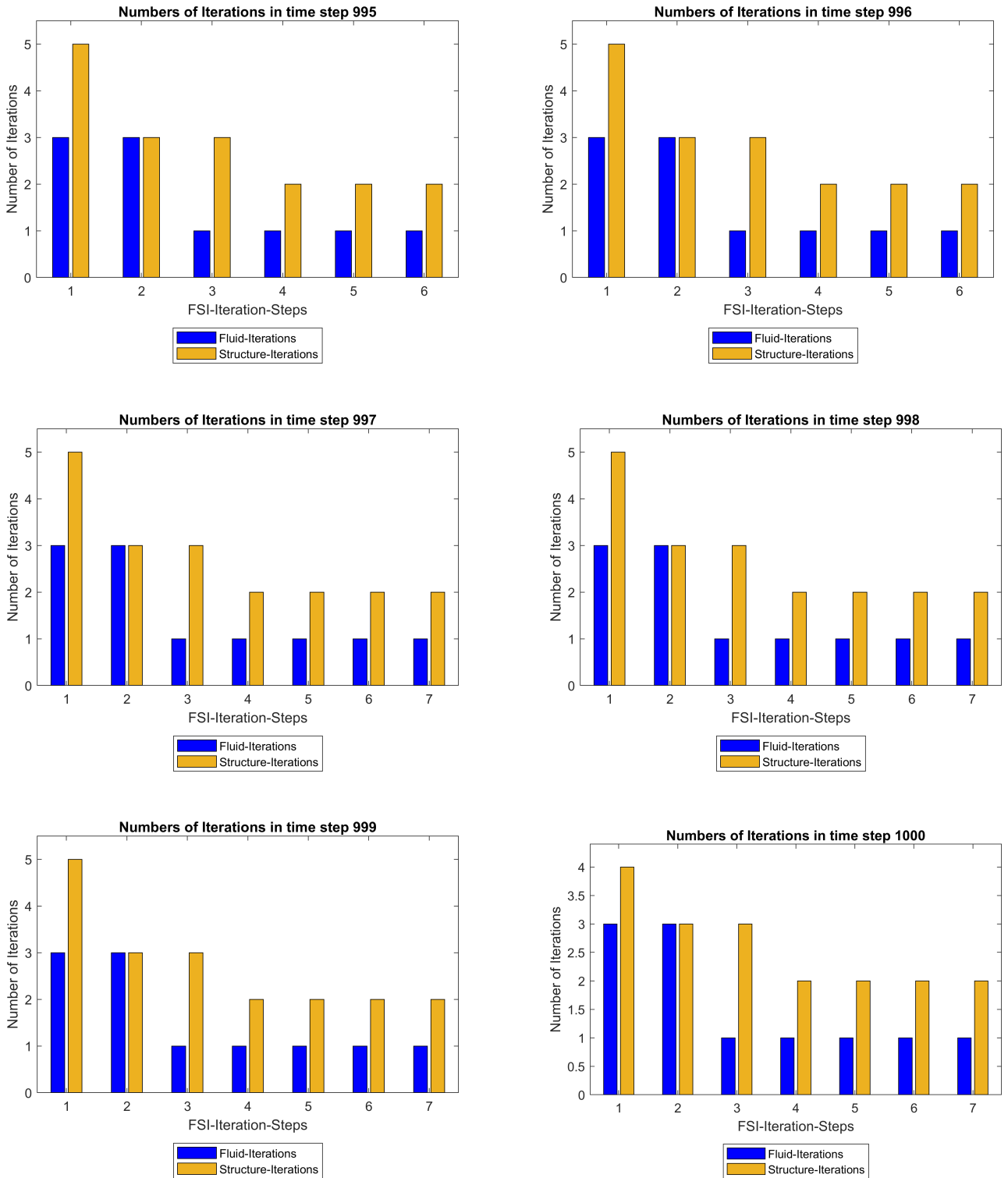


Fig. 91: Iteration steps of fluid and structure solvers within partitioned coupled loop for time step n

C Results for first order extrapolation applied on plate case

Here the results for the first order extrapolation applied on structural displacements d are shown in Figures 92 and 93.

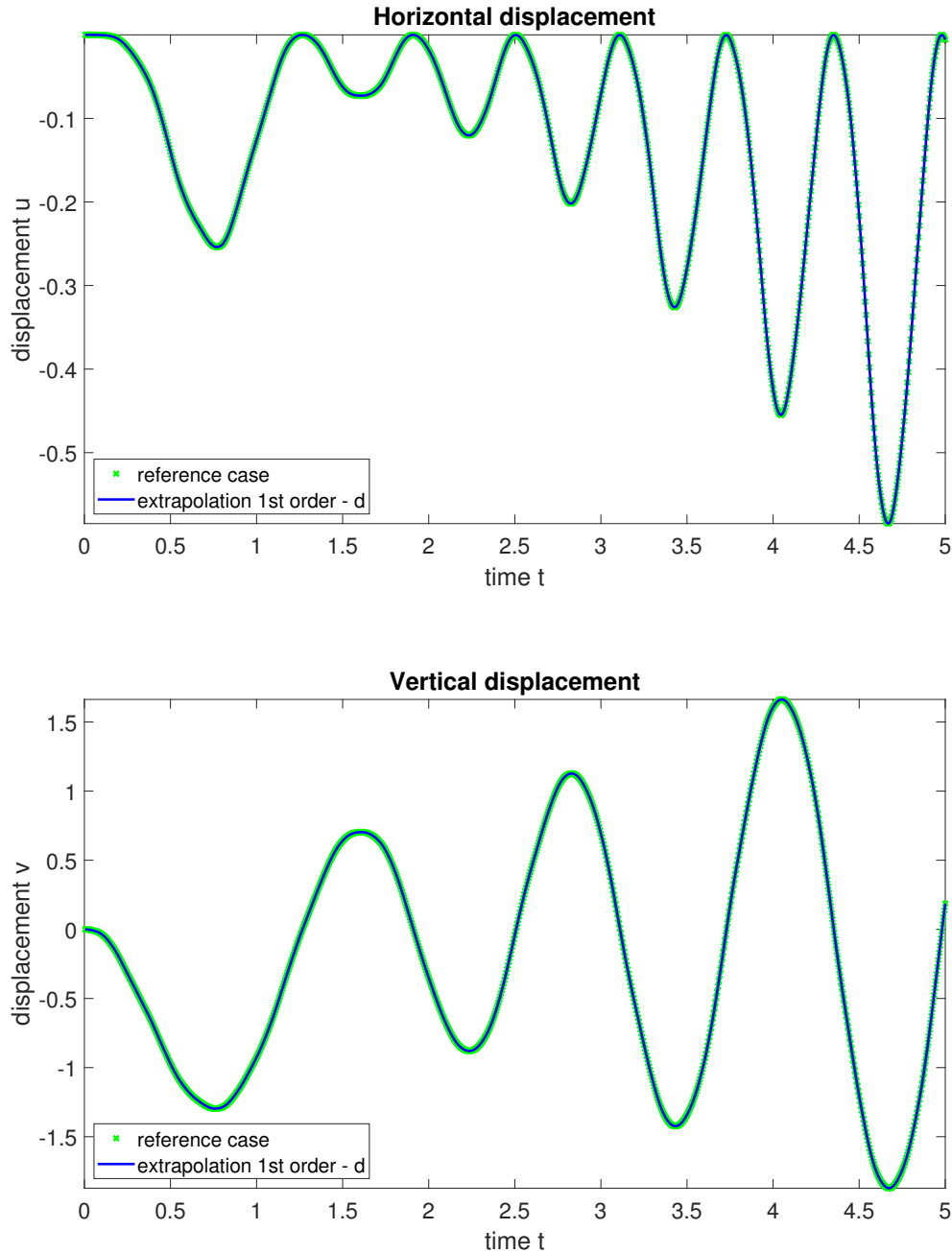


Fig. 92: Horizontal and vertical displacement of the middle point of the right edge of the plate

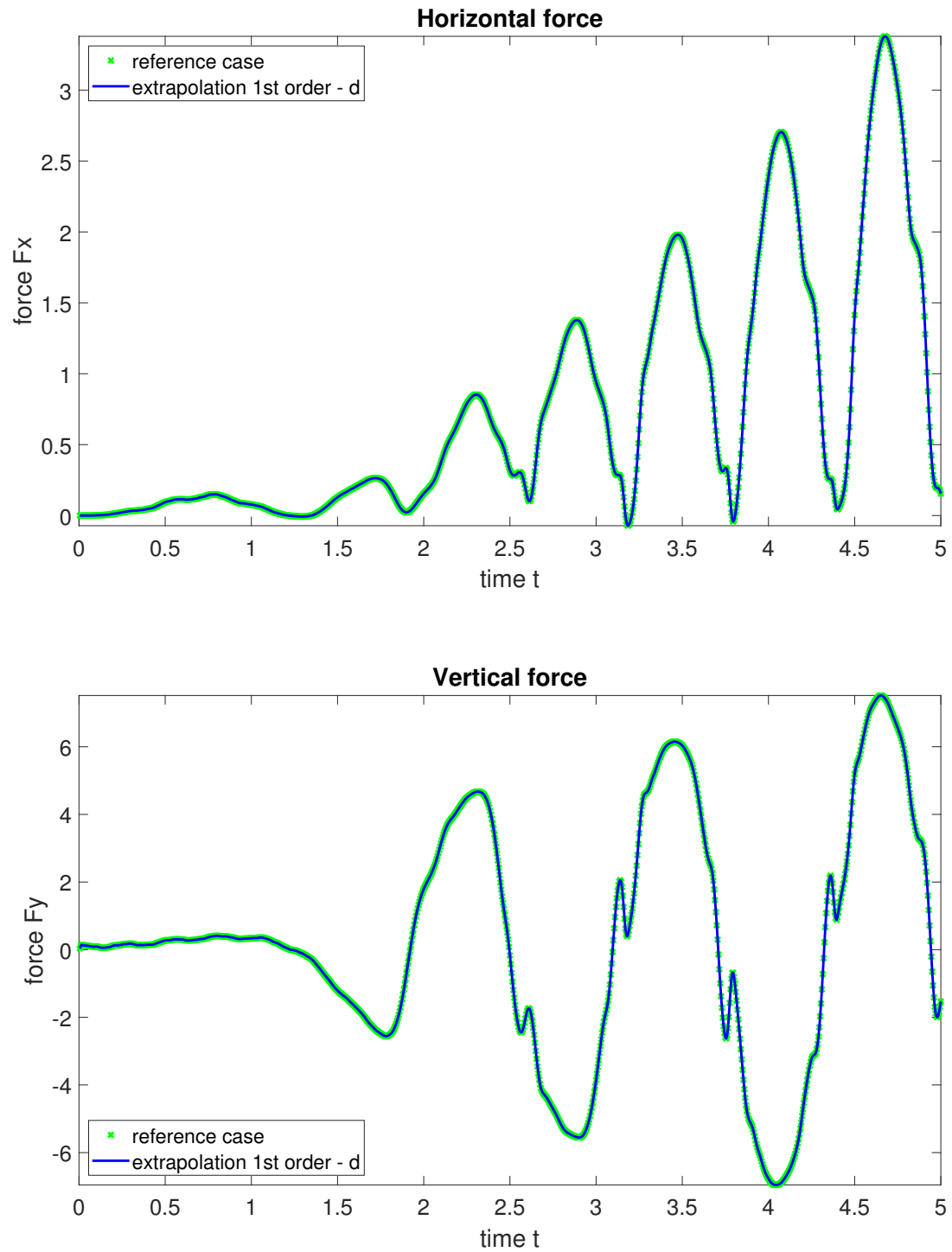


Fig. 93: Vertical and horizontal force of the middle point of the right edge of the plate

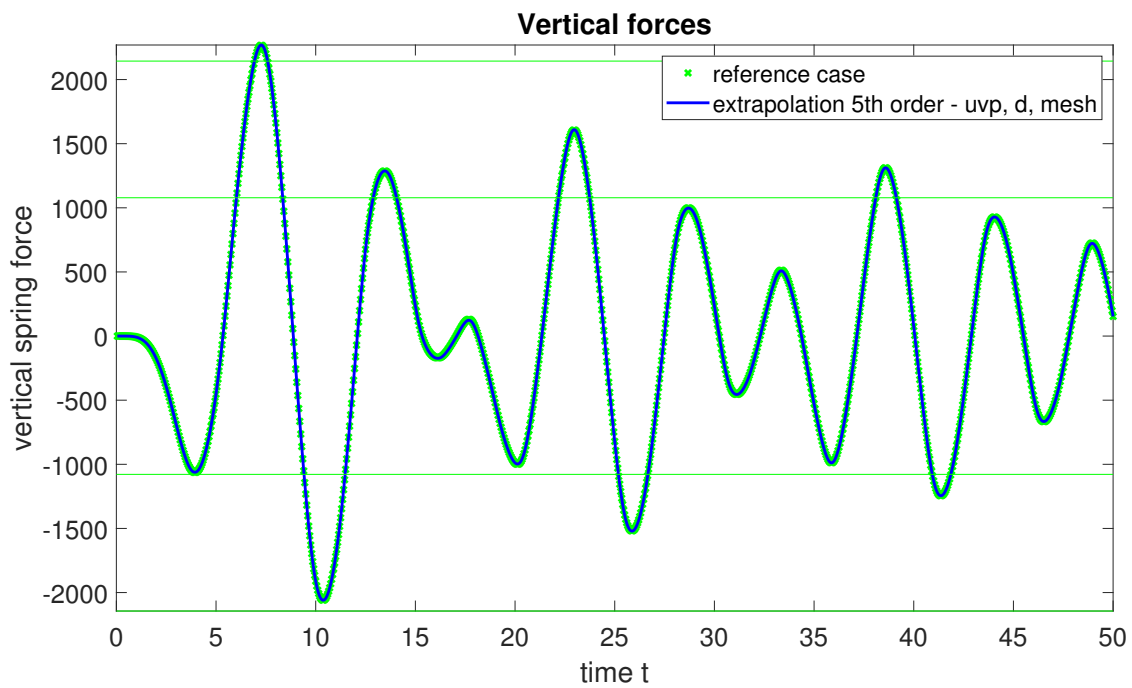
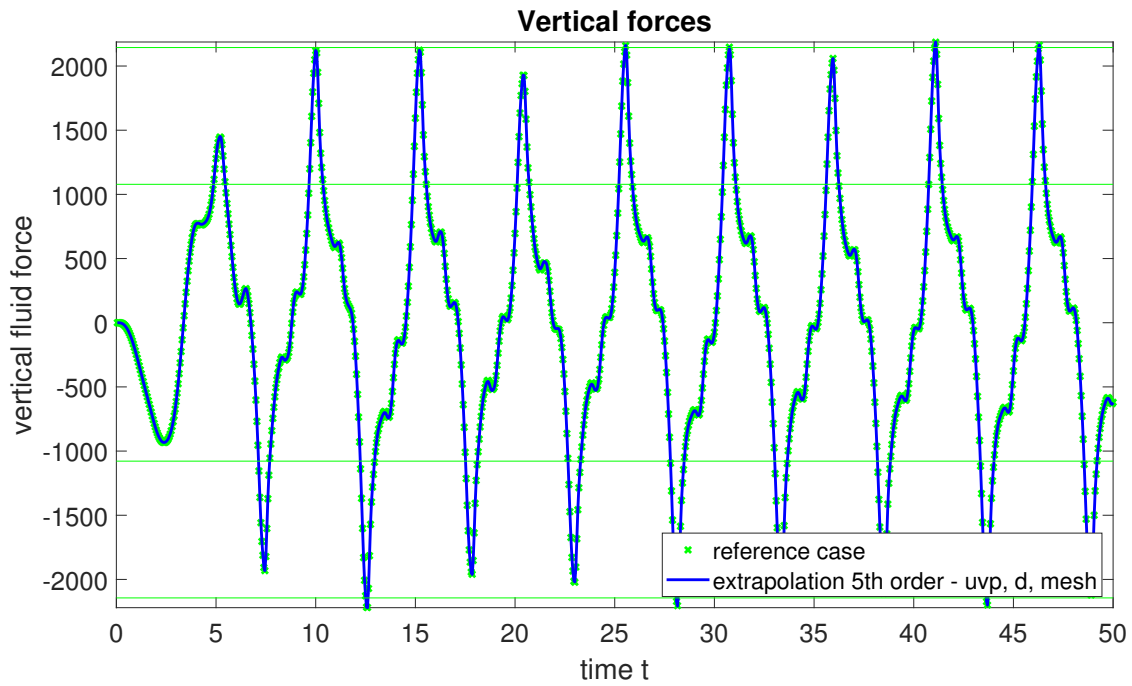
D Result plots for section 6.3.1

Fig. 94: Vertical forces

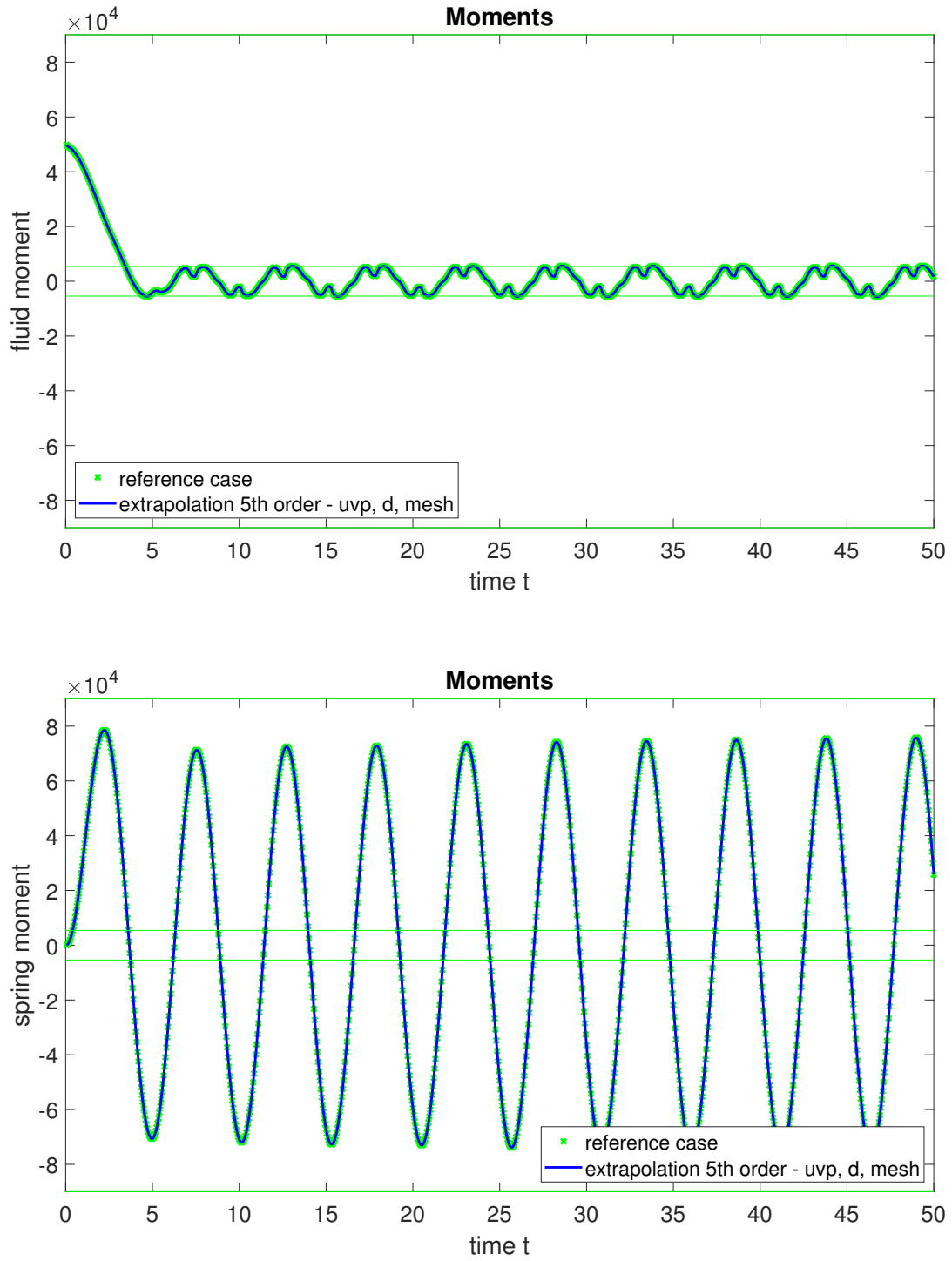


Fig. 95: Moments

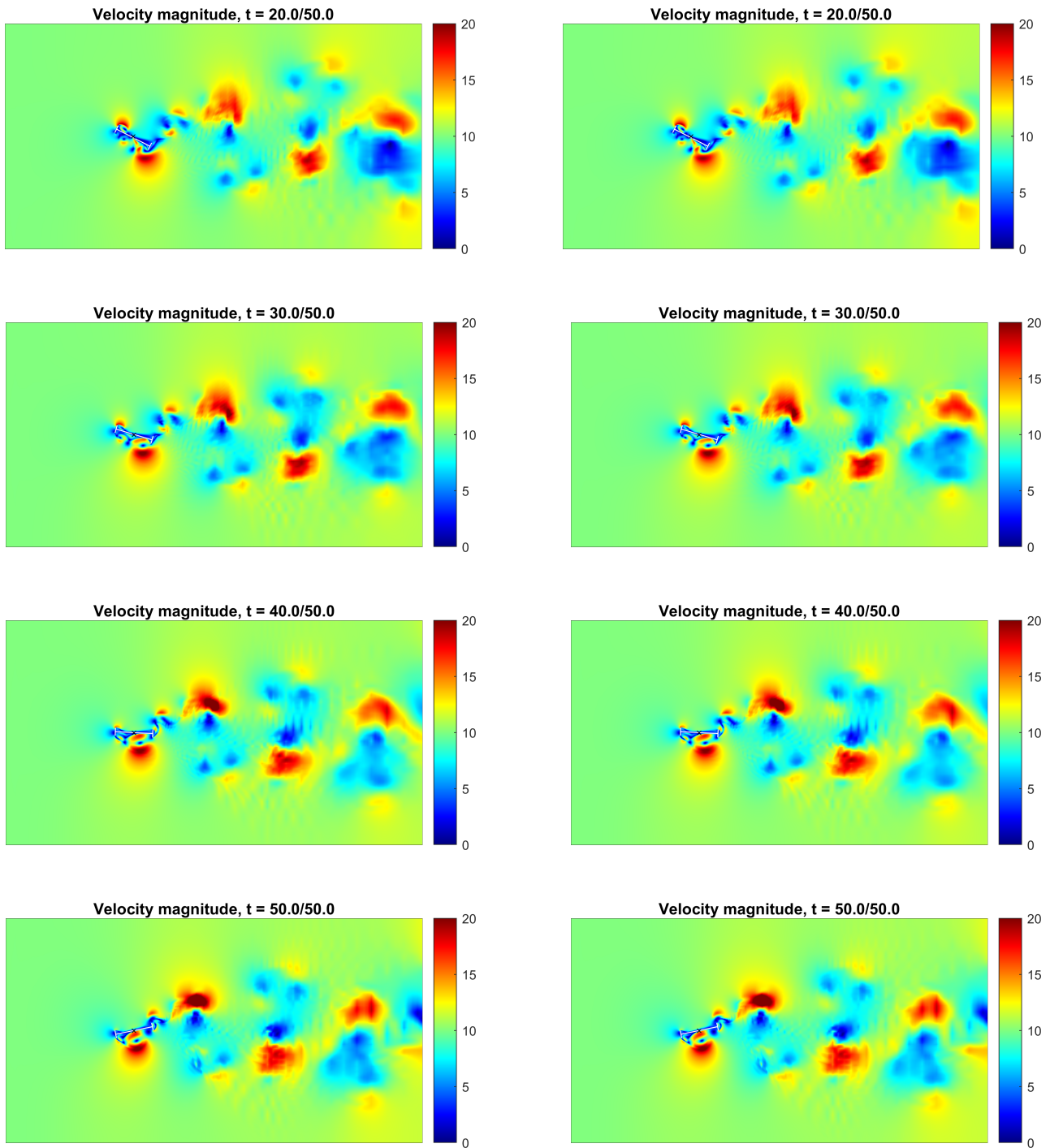


Fig. 96: Velocity field of reference case left and fifth order extrapolation applied on this case for fluid and solid solutions, and the mesh right

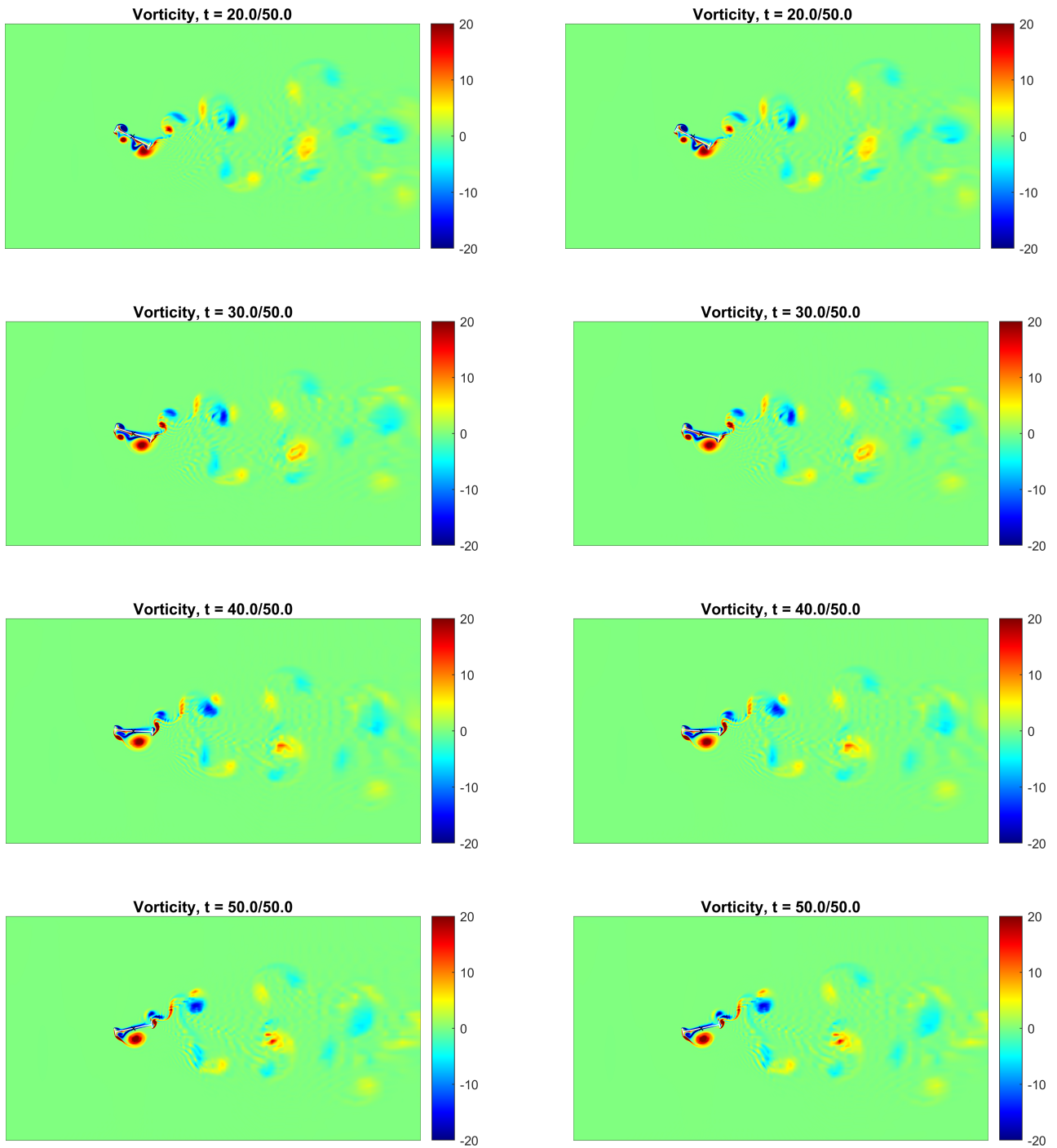


Fig. 97: Vorticity field of reference case left and fifth order extrapolation applied on this case for fluid and solid solutions, and the mesh right

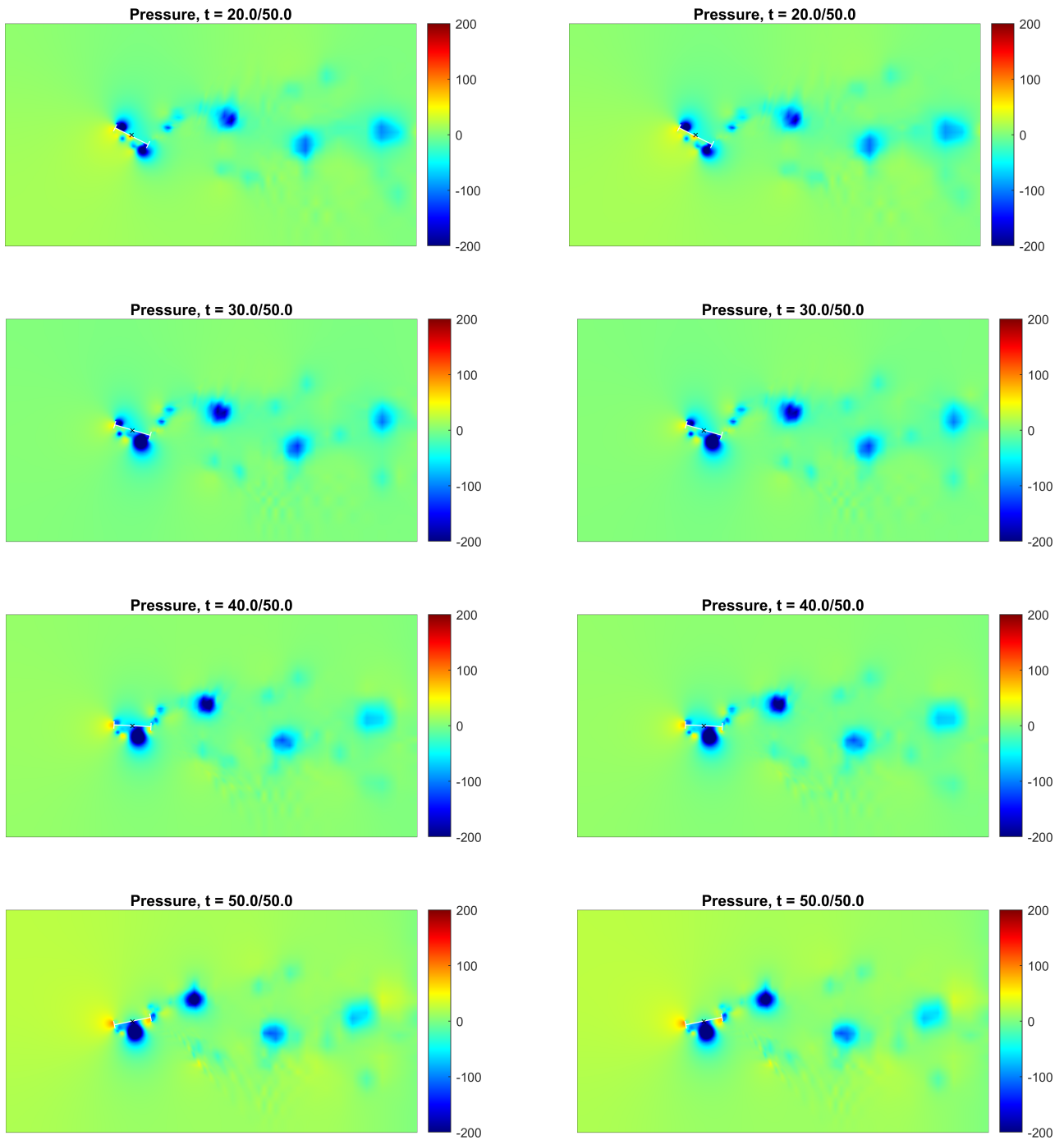


Fig. 98: Pressure field of reference case left and fifth order extrapolation applied on this case for fluid and solid solutions, and the mesh right

E Technical properties of used parallel computer

The used parallel computer is called ‘Sisyphus’ and specified below:

CALLEO Datacenter Server 2460

- 19” Quad-Socket Xeon E5-4600 Barebone, 2HE, SAS, 10GBE
- 4x Intel®Xeon®8-Core E5-4627v2 (3.3GHz, 7.2GT/s QPI, 130W)
- 32x 16 GB DDR3 SDRAM,1866 MHz, registered, ECC
- 2x 1 TB Enterprise SATA-3 hard drive, 7200 U/min
- Intel PCH 602 Onboard Controller
- Intel®X540 Dual Port 10GBase-T LAN onboard

List of Figures

1	Cartesian coordinate system	2
2	Flow-diagram of a simulation	6
3	Quadratic quadrilateral element in reference domain.	7
4	Quadratic quadrilateral element shape functions.	8
5	Mapping of quadratic element from reference to real domain.	9
6	FEM discretization for a tension bar using linear elements	11
7	Different configurations of the continuum	13
8	Mass flow on infinitesimal volume element dV	17
9	Momentum flow on infinitesimal volume element dV in x -direction	18
10	Normal and shear stresses on volume element dV in x -direction	19
11	Fluid domain Ω	21
12	Solid in material and spatial configuration	27
13	Rigid body with elastic support	31
14	Flow-diagram of FSI algorithm	33
15	Example case for explanation of FSI algorithm - Geometry and domain definition	36
16	FE-mesh for fluid domain	37
17	Detailed FE-mesh for fluid domain around flap	37
18	Ramping functions	39
19	Invalid linear quadrilateral element	41
20	Invalid fluid mesh	41
21	Stiffness distribution in pseudo-solid field	42
22	Deformed fluid and structural domain during an FSI-iteration	42
23	Vorticity, velocity, and pressure fields respectively of flap test case - at 1.84 seconds.	43
24	Geometrical configuration of plate test case	44
25	FSI configuration of plate test case	45
26	Detail of the configuration of plate test case	45
27	FE-mesh for fluid domain	47
28	Calculation time to find parallel computed solution in hours	49
29	Average number of FSI-Iteration loop iterations to find parallel computed solution	50
30	Average number of summed fluid iterations to find parallel computed solution	51
31	Horizontal displacement of the middle point of the right edge of the plate	53
32	Vertical displacement of the middle point of the right edge of the plate	54
33	Horizontal force acting on the middle point of the right edge of the plate	55
34	Vertical force acting on the middle point of the right edge of the plate	56
35	Velocity field of reference case $\varepsilon_c = 10^{-6}$ and $\varepsilon_F = 10^{-2}$	57
36	Vorticity field of reference case $\varepsilon_c = 10^{-6}$ and $\varepsilon_F = 10^{-2}$	58
37	Pressure field of reference case $\varepsilon_c = 10^{-6}$ and $\varepsilon_F = 10^{-2}$	59
38	Flow-diagram of FSI algorithm with Aitken's relaxation applied	61
39	Horizontal and vertical displacement of the middle point of the right edge of the plate	63
40	Vertical and horizontal force of the middle point of the right edge of the plate	64
41	Velocity field of reference case left and the study case for Aitken's relaxation right	65
42	Vorticity field of reference case left and the study case for Aitken's relaxation right	66
43	Pressure field of reference case left and the study case for Aitken's relaxation right	67
44	Flow-diagram of FSI algorithm	68

45	Horizontal and vertical displacement of the middle point of the right edge of the plate	71
46	Vertical and horizontal force of the middle point of the right edge of the plate	72
47	Velocity field of reference case left and extrapolation right	73
48	Vorticity field of reference case left and extrapolation right	74
49	Pressure field of reference case left and extrapolation right	75
50	Iterations over timesteps for reference case (lower bar-plot) and fifth order extrapolation applied on this case for u_{vp} , d , and $mesh$	76
51	Tacoma Narrows Bridge collapse [23]	77
52	Geometrical configuration and inflow condition of bridge test case	78
53	Geometrical and mechanical configuration of bridge section as rigid body.	78
54	FE-mesh for fluid domain	80
55	FE-mesh for fluid domain around Γ_c around bridge H-section	80
56	Calculation time to find parallel computed solution in hours	82
57	Average number of FSI-Iteration loop iterations to find parallel computed solution	83
58	Average number of summed fluid iterations to find parallel computed solution	83
59	Vertical fluid forces	85
60	Vertical spring forces	86
61	Fluid moments	87
62	Spring moments	88
63	Angle of rotation in degrees	89
64	Vertical fluid forces over first 8 seconds	89
65	Velocity field of reference case $\varepsilon_c = 10^{-6}$ and $\varepsilon_F = 10^{-2}$	90
66	Vorticity field of reference case $\varepsilon_c = 10^{-6}$ and $\varepsilon_F = 10^{-2}$	91
67	Pressure field of reference case $\varepsilon_c = 10^{-6}$ and $\varepsilon_F = 10^{-2}$	92
68	Vertical forces	94
69	Moments	95
70	Velocity field of reference case left and Aitken's relaxation applied on this case right	96
71	Vorticity field of reference case left and Aitken's relaxation applied on this case right	97
72	Pressure field of reference case left and Aitken's relaxation applied on this case right	98
73	Vertical forces	101
74	Moments	102
75	Velocity field of reference case left and fifth order extrapolation applied on this case for fluid and solid solutions, and the mesh right	103
76	Vorticity field of reference case left and fifth order extrapolation applied on this case for fluid and solid solutions, and the mesh right	104
77	Pressure field of reference case left and fifth order extrapolation applied on this case for fluid and solid solutions, and the mesh right	105
78	Iterations over timesteps for reference case (lower bar-plot) and fifth order extrapolation applied on this case for u_{vp} , d , and $mesh$	106
79	Horizontal displacement of the middle point of the right edge of the plate with a different line type for each case, to show that all lines are laying over each other	110
80	Horizontal displacements of the middle point of the right edge of the plate	111
81	Horizontal displacements of the middle point of the right edge of the plate	112
82	Vertical displacements of the middle point of the right edge of the plate	113
83	Vertical displacements of the middle point of the right edge of the plate	114
84	Horizontal forces of the middle point of the right edge of the plate	115
85	Horizontal forces of the middle point of the right edge of the plate	116

86	Vertical forces of the middle point of the right edge of the plate	117
87	Vertical forces of the middle point of the right edge of the plate	118
88	Number of iterations and computational time over time steps	119
89	Iteration steps of fluid and structure solvers within partitioned coupled loop for time step n	120
90	Iteration steps of fluid and structure solvers within partitioned coupled loop for time step n	121
91	Iteration steps of fluid and structure solvers within partitioned coupled loop for time step n	122
92	Horizontal and vertical displacement of the middle point of the right edge of the plate	123
93	Vertical and horizontal force of the middle point of the right edge of the plate	124
94	Vertical forces	125
95	Moments	126
96	Velocity field of reference case left and fifth order extrapolation applied on this case for fluid and solid solutions, and the mesh right	127
97	Vorticity field of reference case left and fifth order extrapolation applied on this case for fluid and solid solutions, and the mesh right	128
98	Pressure field of reference case left and fifth order extrapolation applied on this case for fluid and solid solutions, and the mesh right	129

Except Figure 51 which is a download from [23] all figures are made by Michael Kaiser with Matlab [16] or tikzpicture in L^AT_EX.

List of Tables

1	Order of ramping function and depending continuity	39
2	Calculation time to find parallel computed solution in hours	49
3	Iteration steps to find parallel computed solution for $j \in [1, 2, 3]$	50
4	Iteration steps to find parallel computed solution for $j \in [4, 5, 6]$	50
5	Results of reference case left and Aitken's relaxation applied on this case right.	62
6	Extrapolation results and reference case	70
7	Calculation time to find parallel computed solution in hours	81
8	Iteration steps to find parallel computed solution	82
9	Results of reference case left and Aitken's relaxation applied on this case right.	93
10	Extrapolation results and reference case	99
11	Extrapolation results and reference case	100
12	Extrapolation results and reference case	107
13	Reference case without any acceleration and results for extrapolation used together with Aitken's relaxation for different loop tolerances	108

Further acknowledgement

The used L^AT_EX-template is from DI Daniel Schöllhammer, BSc (Institute of Structural Analysis at Graz University of Technology).

References

- [1] I. N. Bronstein, K. A. Semendyayev, G. Musiol, and H. Mühlig. *Handbook of Mathematics*. 6th ed. Springer-Verlag Berlin Heidelberg New York Dordrecht London, 2015.
- [2] A. K. Chopra. *Dynamics of Structures - theory and applications to earthquake engineering*. New Jersey: Prentice Hall Inc., 1995.
- [3] W. Dahmen and A. Reusken. *Numerik für Ingenieure und Naturwissenschaftler*. 2nd ed. Berlin Heidelberg: Springer-Verlag, 2008.
- [4] T.-P. Fries. *A stabilized and coupled meshfree/meshbased method for fluid-structure-interaction problems*. Technische Universität Braunschweig, 2005.
- [5] T.-P. Fries. *EduFEM - a finite element method educational software*. TU Graz, 2019.
- [6] T.-P. Fries. *Finite Element Method, Lectures FEM I and FEM II*. TU Graz, 2019, unpublished.
- [7] P. Hood and C. Taylor. “Navier-Stokes equations using mixed interpolation”. In: *Finite element methods in flow problems* (1974), pp. 121–132.
- [8] B. Hübner. *Simultane Analyse von Bauwerk-Wind-Wechselwirkungen*. Technische Universität Braunschweig, 2002.
- [9] T. J. R. Hughes. *The Finite Element Method, Linear Static and Dynamic Finite Element Analysis*. New York: Dover Publications, 2000.
- [10] P. S. Huyakorn, C. Taylor, R. L. Lee, and P. M. Gresho. “A comparison of various mixed-interpolation finite elements in the velocity-pressure formulation of the Navier-Stokes equations”. In: *Computers & Fluids* 6.1 (1978), pp. 25–35.
- [11] M. Kaiser. *A finite element based topology optimization for structural design*. Hamilton: McMaster University, 2019, unpublished.
- [12] M. Kaiser. *Dynamically loaded tension bar, a time-stepping finite element method*. TU Graz, 2018/19, unpublished.
- [13] K. Knothe and H. Wessels. *Finite Elemente*. 5th ed. Berlin: Springer, 2017.
- [14] G. A. Korn and T. M. Korn. *Mathematical handbook for scientists and engineers: definitions, theorems, and formulas for reference and review*. New York: Dover Publications, 2000.
- [15] U. Küttler and W. A. Wall. “Fixed-point fluid-structure interaction solvers with dynamic relaxation”. In: *Computational Mechanics* 43.1 (2008), pp. 61–72.
- [16] <https://de.mathworks.com/help/matlab/index.html>.
- [17] A. Meister and T. Sonar. *Numerik - Eine lebendige und gut verständliche Einführung mit vielen Beispielen*. Berlin: Springer Spektrum/Springer Nature, 2019.
- [18] C. Petersen and Werkle H. *Dynamik der Baukonstruktionen*. 2nd ed. Wiesbaden: Springer Vieweg, 2017.
- [19] L. Prandtl and H. Oertel. *Führer durch die Strömungslehre*. 10th ed. Braunschweig: Vieweg, 2001.
- [20] S. Sachs, M. Streitenberger, D. Sternel, and M. Schäfer. “Extrapolation methods for accelerating unsteady partitioned fluid-structure interaction simulations”. In: *The International Journal of Multiphysics* 5.4 (2011), pp. 287–298.

-
- [21] H. Sigloch. *Technische Fluidmechanik*. 10th ed. Berlin: Springer, 2017.
- [22] P. Steinke. *Finite-Elemente-Methode*. 5th ed. Berlin: Springer, 2015.
- [23] <https://en.wikipedia.org/wiki/File:Tacoma-narrows-bridge-collapse.jpg>.
- [24] E. Walhorn. *Ein simultanes Berechnungsverfahren für Fluid-Struktur-Wechselwirkungen mit finiten Raum-Zeit-Elementen*. Technische Universität Braunschweig, 2002.
- [25] W. A. Wall. *Fluid-Struktur-Interaktion mit stabilisierten finiten Elementen*. Universität Stuttgart, 1999.
- [26] O. C. Zienkiewicz, R. L. Taylor, and P. Nithiarasu. *The Finite Element Method, Vol. 3 Fluid Dynamics*. 7th ed. Butterworth-Heinemann, Oxford, 2005.